



UNIVERSIDADE FEDERAL DO RIO DE JANEIRO

INSTITUTO DE FÍSICA

**Classical and Quantum Light:
Versatile tools for quantum foundations and quantum
information**

Thais de Lima Silva

arXiv:2011.05797v1 [quant-ph] 11 Nov 2020

Rio de Janeiro
Abril, 2020

UNIVERSIDADE FEDERAL DO RIO DE JANEIRO

INSTITUTO DE FÍSICA

**Classical and Quantum Light:
Versatile tools for quantum foundations and quantum
information**

Thais de Lima Silva

ORIENTADOR: Stephen Patrick Walborn

CO-ORIENTADOR: Gabriel Horacio Aguilar

*Tese apresentada como parte dos requisitos para
obtenção do título de doutora em Física pelo programa
de pós-graduação do Instituto de Física da Universidade
Federal do Rio de Janeiro.*

Rio de Janeiro
April, 2020

À memória de meu tio Oswaldo Vicente de Lima.

*Dedico-me sobretudo aos gnomos, anões,
sílides e ninfas que me habitam a vida.
Dedico-me à saudade de minha antiga
pobreza, quando tudo era mais sóbrio e digno
e eu nunca havia comido lagosta. O que me
atrapalha a vida é escrever. E não esquecer
que a estrutura do átomo não é vista mas
sabe-se dela. Sei de muita coisa que não vi.*

Clarice Lispector, “A hora da estrela”

AGRADECIMENTOS

Uma tese nasceu, com dores de parto e em meio a uma pandemia sem precedentes. Isolada no último mês de escrita, porém jamais sem o apoio distante de muitos que estiveram presentes durante esses quatro anos de doutorado e dez anos de física. Tantos são os que merecem dedicatórias e agradecimentos que incorro no risco de ser injusta e esquecer-me de alguns nomes ou até desprivilegiar alguém pela ordem em que os cito. Não sei se isso é de qualquer importância àqueles que me cercam, assim como não soube se a própria tese era de qualquer importância, por vezes ela perdeu o sentido: não salvaria vidas e parece ser só o que importa durante esses dias sombrios. Por outro lado, por que salvar vidas? Pelo número de vidas salvas ou pela individualidade de cada uma? Sendo assim, a minha vida também deve importar e as particularidades ligadas a ela também. Essa tese importa, nem que seja somente para mim. O conteúdo dela certamente não revoluciona a ciência, mas fornece alguns tijolinhos para sustentar essa enorme construção científica. E assim é feita a ciência: somente vez ou outra uma revolução, mas sempre se sustentando nos tijolinhos.

E eu sempre me sustentando na minha família. Meus pais, dona Ini e seu Magno, e minha irmã, Tina, sempre acreditaram em mim e nas minhas escolhas, mesmo quando elas envolveram me mudar para longe deles. Me mudando para longe, não pude participar ativamente do crescimento da minha sobrinha, Thayná, e de minha prima, Isa, espero que ao menos eu sirva de inspiração para essas criaturinhas. Devo me sentir orgulhosa e, família, vocês também devem se orgulhar do trabalho que fizemos. Meus pais, que sequer tiveram oportunidade de concluir o ensino fundamental, conseguiram me impulsionar para que eu agora tenha a oportunidade de concluir um doutorado! Muito obrigada pela dedicação de vocês, espero conseguir retribuir de alguma forma. Agradeço também a toda a família, tios e primos, a união dessa família sempre será uma motivação, em especial à Tinti e ao Uncle que sempre serviram de inspiração e também à Grangran, a avó mais teimosa e mais divertida que eu poderia ter.

Além da minha família original, não posso deixar de agradecer a uma família que me adotou e incorporou como se eu fosse um deles desde quando os conheci. Muito obrigada à família Zanco, especialmente ao Jônatas que por tanto tempo esteve ao meu lado, alguém que

me apoiou, me deu suporte e me ensinou tanta coisa para tornar a vida mais leve. Não poderia me esquecer também da minha mãe carioca, Druzila, que me recebeu em sua casa no primeiro ano de doutorado como a uma filha e me deu não somente abrigo, mas sua amizade e seus cuidados.

Muitas foram as amizades que os tantos anos de Física me trouxeram, algumas passageiras, outras que ficam pra vida. Quantas foram as vezes em que quase fomos roubados por macacos enquanto comíamos biscoito frito às 16h, Leandro? Companheiro de natação, de escrita de dissertação e agora de tese, de trabalhos de EaD, de finais de semana na universidade, de insolação... Obrigada pela amizade incondicional de quase dez anos e pela disposição em sempre ajudar e ouvir.

Assim que cheguei à UFRJ fui levada ao que seria meu escritório e que seria dividido com dois malucos. Como foram divertidos os primeiros dias, Kainã e Renato fizeram eu me sentir importante e acolhida, ganhava até paçoca e bolacha piraquê! Através deles e de sua capacidade incrível de socialização, conheci muitos colegas de instituto. Foi através deles que conheci uma pessoa incrível, uma mulher sonhadora, destemida e que domina as palavras como poucas vezes vi. Obrigada, Carol, pela amizade, pelas festas loucas, pelas trocas de segredinhos e por me fazer ver como feminilidade, força e conquista de respeito devem andar juntos. Não acho que já tenha te dito isso: te admiro muito, admiro sua determinação em não seguir a corrente, mas ir contra, ir bailando sobre pernas de pau ao encontro dos seus ideais. Falando em mulher forte e admiração, não posso deixar de mencionar e agradecer à Murielvis, a amiga mais surpreendente que jamais tive, de infância no canavial até paraquedismo, ela abarca tudo que a vida tem a oferecer com uma coragem e uma força que não parecem possíveis ao julgar erroneamente a aparência.

Obrigada a todos os colegas de laboratório e de grupo, sem vocês esses anos teriam sido pobres, até mesmo de inspiração para trabalhar. Foram muitas as festinhas de aniversário, confraternização aleatória ou celebrações de defesa, muitos imagem e ação, chocolates e outros doces compartilhados... Sem momentos de procrastinação pós almoço com Rodrigo ou com Márcio ou com Ranieri, ou com todos juntos, o doutorado não teria a leveza e a graça que teve. E claro que, sem a ajuda do Rani, nem mesmo o doutorado talvez fosse possível, após várias horas de discussões, misturadas com procrastinação baseada nos mais diversos temas e jogos, vários “Você pode ler isso aqui que eu escrevi?” seguidos de um trocadilho e um “sim”, após alguns aniversários de Thainery, diversas conversas sobre os questionamentos profundos da vida, só me resta agradecer e torcer para que nossa amizade e colaboração continuem por muitos anos mais. Agradeço ao Márcio também por me mostrar ridiculamente como é possível ter vida social, dominar várias línguas, traduzir vídeos do YouTube, dar ótimos churrascos, editar vídeos de memes e ainda ser super produtivo no trabalho. Esse agradecimento é o mais próximo que eu consigo chegar de um vídeo de aniversário com bolo de imagem e ação, considere retribuído.

Não posso também não agradecer ao Victor, mas honestamente não sei o que dizer. Sua importância durante esse período foi inegável, transformadora e por que não dizer nutritiva, dado que tudo se iniciou como uma troca de marmitas. E mesmo o seu afastamento me trouxe coisas maravilhosas, como esses dois amigos que não posso deixar de mencionar. Pedro e Matheus, vocês foram e são fundamentais na minha vida e mesmo no meu trabalho. A companhia de vocês, todos os jantares compartilhados e as besteiras ditas aliviaram minha carga e me ajudaram a me valorizar e confiar em mim. Obrigada por me integrarem em tão pouco tempo, a dedicação e o bom humor de vocês me inspira e não aceito que nossa amizade não seja pra sempre.

E como não citar os elementos fundamentais nessa trajetória: todos os professores que dela participaram. Muito obrigada a todos, tantos nomes fundamentais que não há espaço para citar todos. Desde antes de ingressar na universidade, um professor do instituto de Física da UFG já me influenciou na minha escolha. Ter invadido a sala do Caparica em uma visita à universidade foi fundamental, não só para a escolha, como também para não me frustrar com ela, já que ele me disse algo como “A vida, o trabalho e as conquistas de um cientista são muito diferentes da visão idealizada da ficção”. E meus primeiros passos como cientista foram guiados por meu primeiro orientador que me acompanhou na graduação e no mestrado, meu obrigada ao Ardiley. Obrigada também a todos os professores do grupo de Informação quântica da UFRJ pelos ensinamentos e pela amizade, em especial ao Fabricio que, à sua maneira às vezes rude, sempre se preocupou comigo, e ao Leandro que agora me acolhe para uma nova fase, o pós-doutorado. Finalmente, declaro minha gratidão ao meu orientador, Steve, e ao meu coorientador, Gabo, vocês acreditaram em mim, me acompanharam e me incentivaram, recebi não só ensinamentos e ajuda, mas confiança e amizade, e tive o melhor ambiente de trabalho possível.

Por último, gostaria de agradecer ao CNPq, sem a bolsa de doutorado não teria sido possível.

RESUMO

Feixes ópticos oferecem muitos graus de liberdade a serem explorados. Há graus de liberdade discretos como polarização, momento angular orbital e caminhos discretos. Existem também graus de liberdade contínuos, como frequência, momento e posição transversal. Além da possibilidade de emaranhar photons nesses muitos graus de liberdade, isso faz da luz uma ferramenta extremamente útil e versátil para investigações em fundamentos de mecânica quântica e em informação quântica. Desde o início da informação e da computação quântica, experimentos fotônicos têm tido um papel crucial que vai desde testes fundamentais da teoria até a implementação de protocolos de informação quântica. Nesta tese, essa importância e versatilidade é endossada apresentando novas contribuições que exploram tanto graus de liberdade discretos como contínuos. A tese inicia-se com dois experimentos que utilizam luz clássica e exploram a analogia entre a função de onda de sistemas quânticos e a amplitude da onda eletromagnética. O primeiro é uma simulação da dinâmica de uma partícula quântica relativística na qual utiliza-se a analogia entre campo próximo/distante e a função de onda em posição/momento, bem como a analogia entre spin e polarização. Esta simulação permite observar claramente o chamado *zitterbewegung*, movimento trêmulo de partículas livres, com boa visibilidade para valores ajustáveis de massa da partícula. O segundo trabalho é relacionado à teoria de medidas mutuamente imparciais que são efetivamente discretas, porém construídas a partir de variáveis contínuas, implementadas novamente no perfil transversal de um feixe luminoso clássico. Demonstra-se teoricamente que tais medidas não são compatíveis com variáveis discretas nem contínuas, uma vez que o número máximo de medidas mutuamente imparciais possível não se comporta como nenhuma das duas possibilidades. Na segunda parte desta tese, são apresentados três trabalhos utilizando graus de liberdade discretos de polarização e caminho de fótons. O primeiro trata da redefinição da correlação quântica não local chamada *steering* no cenário multipartido, baseada em uma inconsistência na definição anterior, a saber, a criação desta correlação através de operações que supostamente não seriam capazes de criá-la. Este fenômeno é chamado exposição de *steering* quântico. Neste trabalho, é construído um protocolo para geração de qualquer assemblage bipartido com *steering* a partir de um assemblage

tripartido sem a correlação. Em geral, tal protocolo não é realizável quanticamente, no entanto, apresentamos um exemplo obtido a partir de um estado quântico tripartido em que a exposição de *steering* ocorre e a observamos experimentalmente para fótons emaranhados. Os demais trabalhos são relacionados à implementação experimental de canais quântico de um qbit, um deles é um canal particular para o qual testamos não-Markovianidade usando uma medida operacional chamada correlação condicional de passado-futuro (CPF). É mostrado que, mesmo com erros e estatística finita inerente à implementação experimental, a correlação CPF é capaz de detectar efeitos de memória que vão além da capacidade de outros quantificadores. A tese é finalizada com uma proposta para a realização de qualquer canal quântico de um qbit, em que o qbit é representado pela polarização de fótons únicos. Diferentemente de outros trabalhos correlatos, nossa proposta não depende da implementação clássica de combinações convexas de canais, além de não requerer sistemas auxiliares adicionais, já que estes são providos por graus de liberdade de caminho do próprio fóton.

Palavras-chave: Ótica clássica e quântica; ótica paraxial; fótons emaranhados; simulação quântica e clássica; equação de Dirac; medidas mutuamente imparciais; *steering* quântico multipartido; não-markovianidade quântica; canais quânticos.

ABSTRACT

Light beams offer many degrees of freedom to be explored. There are discrete ones as polarization, angular orbital momentum and discrete paths. There are also continuous ones, like frequency, momentum and transverse position. In addition to the possibility of entangling photons in these many degrees of freedom, it makes light a very useful and versatile tool for quantum information and quantum foundation purposes. Since the very beginning of quantum information and quantum computation, photonic experiments have played a crucial role that ranges from testing the foundations of quantum theory to implementing quantum information protocols. In this thesis, we endorse its importance and versatility by presenting novel contributions that further explore both discrete and continuous degrees of freedom. It begins with two experiments that use classical light and explore its analogous behavior to quantum systems. The first one is a simulation of the dynamics of a relativistic quantum particle in which we use the analogy between near/far transverse fields and position/momentum wavefunctions as well as the analogy between spin and polarization. Our simulation enables us to clearly observe the so called zitterbewegung, the trembling motion of free particles, with good visibility and with a tunable value of particle mass. The second work is related to the theory of mutually unbiased measurements that are effectively discrete but constructed from continuous variables systems, which is again experimentally implemented on the transverse field profile of a classical light beam. We theoretically prove that these measurements are actually neither continuous or discrete, since the maximum number of mutually unbiased measurements possible does not behave like any of those. In the second part of the thesis, three works are presented that use the polarization and path discrete degrees of freedom. The first one is a redefinition of the quantum nonlocal correlation called steering in the multipartite scenario, based on an inconsistency in the previous definition, namely the creation of this correlation from scratch using operations that supposedly would not be able to do so. We call this exposure of quantum steering. In this work we build a protocol to generate any steerable bipartite assemblage from a tripartite unsteerable one, although this protocol is not realizable with quantum states, we come out with a quantum example for which this exposure phenomenon is observed with entangled photons. The other

two works are related to the experimental implementation of quantum channels of qubits, one of them is a particular channel for which we test for non-Markovianity using an operational measure called conditional past-future (CPF) correlation. We show that, even with finite statistics inherent to an experiment and with experimental errors, this CPF correlation is able to detect memory effects beyond other non-Markovianity quantifiers. The thesis finishes with a proposal for an experimental realization of any quantum channel of a single qubit, where the qubit is realized by the polarization of single photons. Differently from other works, our proposal does not rely on classical implementation of convex superposition, also it does not need any extra ancillary systems, since the ancillas are provided by path degrees of freedom of the photon itself.

Keywords: Quantum and classical optics; paraxial optics; entangled photons; quantum and classical simulation; Dirac equation; mutually unbiased measurements; multipartite quantum steering; quantum non-Markovianity; quantum channels.

CONTENTS

Introduction	1
I. Transverse spatial degree of freedom	4
1. Experimental techniques	6
1.1. Polarization transformations: wave plates	6
1.2. Paraxial approximation	9
1.3. Fractional Fourier transform and phase space variables	12
1.3.1. Optical Fourier transform	13
1.3.2. Optical fractional Fourier transform	15
1.4. Spatial Light Modulator	17
1.4.1. SLM calibration	20
1.4.2. Beam positioning in the SLM plane	21
1.4.3. Amplitude masks from phase modulation	23
2. Optical simulation of the free Dirac Equation	26
2.1. Introduction	26
2.2. Dirac Equation and position operator	28
2.3. Simulation Protocol and Experiment	29
2.4. Results	32
2.5. More spatial dimensions and potentials	35
2.5.1. Simulation of 2+1 dimensional Dirac Equation	36
2.5.2. Simulation of 3+1 dimensional Dirac Equation for a particular class of initial states	37
2.5.3. Simulation of 1+1 dimensional Dirac Equation for a particular class of potentials	38
2.6. Discussion and Conclusions	39

3. Mutual unbiasedness of coarse-grained measurements for an arbitrary number of phase space observables	41
3.1. Introduction	42
3.2. Mutually unbiased basis and measurements	43
3.3. Mutually unbiased periodic coarse grained measurements	46
3.4. Construction of several MUMs	48
3.4.1. Solution to equation (3.16)	49
3.4.2. Even dimensionality parameter	51
3.4.3. Examples for d odd	51
3.4.4. Experimental realization	52
3.5. Maximum number of MUMs: general case	55
3.6. Concluding remarks	58
II. Discrete degrees of freedom	60
4. Experimental techniques	62
4.1. Generating polarization entangled pairs of photons	62
4.1.1. Coherence length	65
4.1.2. Obtaining error bars: Poisson distribution	66
4.2. Generating path entanglement	67
4.3. Projective measurements	69
4.3.1. Path degree of freedom	72
4.4. Unitary transformations	72
5. Exposure of subtle multipartite quantum nonlocality	75
5.1. Introduction	75
5.2. Steering and the semi-DI setting	79
5.2.1. Multipartite steering	80
5.2.2. Post-quantum steering	82
5.2.3. Resource theory of steering	82
5.2.4. Steering detection, witnesses and quantifiers	84
5.2.5. Assemblage Fidelity	87
5.3. Steering exposure and super exposure of Bell-nonlocality	88
5.4. Experimental implementation	91
5.5. Redefinition of steering	96
5.6. Concluding remarks	99

6. Detection of quantum non-Markovianity close to the Born-Markov approximation	101
6.1. Introduction	101
6.2. Markov processes in classical Physics	103
6.3. Open quantum system dynamics and Markovianity	104
6.3.1. Born-Markov approximation	105
6.3.2. Quantum Markovianity	107
6.3.3. Conditional past future correlation	109
6.4. The spin-boson model	111
6.4.1. CPF correlation	113
6.5. Experiment	114
6.5.1. Results	117
6.5.2. Robustness of the experimental setup	119
6.6. Conclusions	120
7. Experimental realization of an arbitrary qubit channel: a proposal	123
7.1. Quantum maps	124
7.2. Quantum maps of qubits	126
7.3. Generalized amplitude damping channel	127
7.3.1. Accessing the environment state	130
7.4. General protocol	132
7.4.1. Examples	137
7.5. Quantum process tomography	139
7.6. Conclusion	141
Final Remarks	143
A. Birefringent materials	145
B. Further experimental results of several PCG MUM	149
C. Supplement to Steering Exposure	154
C.1. No-go theorem for multi-black-box universal steering bits	154
C.2. Redefinition of genuinely multipartite steering	158
C.3. On the sets of LHS assemblages, TO-LHS assemblages, and NS-LHS assemblages	159
D. Time evolution and CPF correlation for the decay of a two level system in a bosonic bath	163
D.1. Solution of Eq. (6.25) for initial separable states	163

D.2. Calculation of the CPF correlation	166
D.2.1. First scheme, measurements $\sigma_z - \sigma_z - \sigma_z$	167
D.2.2. Second scheme, $\hat{x}-\hat{z}-\hat{x}$	169
D.3. Map representation of the total unitary dynamics	172
Bibliography	174

INTRODUCTION

Optical experiments were at the heart of the two big revolutions in Physics that occurred in the beginning of the twentieth century. On one side, one can cite the interference experiment of Michelson and Morley which supported the Theory of Relativity [1]. On the other side, the discovery [2] and subsequent explanation [3] of photoelectric effect was one of the motivations for the development of quantum physics.

Ever since the first formulations of quantum theory, optics has played a central role in its development. Not only the theory itself has been initiated by the photoelectric effect, but also it was frequently an optics experiment that served as the most suitable platform for testing some non-intuitive features of the theory. For the latter, we can cite, for example, the incredible amount of experiments to test quantum nonlocality, with the first unambiguous experiments on violation of Bell inequalities [4] by quantum correlations realized by A. Aspect *et al.* [5–7] using photons produced by cascade emission, and subsequently many experiments using photons produced by parametric down conversion [8–10], only to cite a few. Also related to quantum correlations, we can mention the experiment proving the weirdness of entanglement for multipartite systems without the necessity of inequalities using Greenberger-Horne-Zeilinger states [11]. Furthermore, the first quantum teleportation implementation was performed with photonic states [12]; wave-particle complementarity has been tested many times with delayed choice experiments, and quantum erasers, for instance (see Ref. [13] and references therein); and the two-particles interference exhibiting a Hong-Ou-Mandel dip because of the symmetry in the quantum bosonic state of photons was also verified [14].

Moreover, with the advent of quantum information theory, photons have become a natural physical system for *quantum information transmission* because, first and foremost, they are the fastest carriers of information available and, due to their lack of charge and mass, they have a reduced interaction with the environment, making them able to transmit signals through large distances outside the protected environment of a laboratory [15]. Thus, many quantum key distribution protocols have been realized using photons [16, 17]. More recently, these protocols are becoming closer to practical application with many realizations of quantum information transmission through long distance fibers [18–20] and using Earth satellites [21, 22] or drones [23]. Photons have their limitations as a platform for *quantum information processing* because

of the difficulty to store them and also to build multipartite entangled states, due exactly to the feature that favors the transmission of information: the difficulty of producing interactions. However, even in this direction photonic experiments have contributed with the first attempts of proving the supremacy of quantum computers, by the use of many-photons interference in boson sampling [24, 25].

The enormous number of interesting results is ascribable to the versatility of light. It offers many degrees of freedom which can be explored independently or jointly, with the possibility of producing states with entanglement between different degrees of freedom. There are discrete ones such as polarization, angular orbital momentum, discrete spatial modes and number of photons [26]. There are also continuous ones, like frequency, momentum and transverse position [27].

After all these successful demonstrations of the power of optics as a tool for the study of quantum theory, there are still many challenges and room for new and interesting research. This thesis intends to give some additional contribution to the research field of quantum theory using optics experiments. It is divided in two parts according to the experimental platform used. Each part begins with an overview of the main experimental techniques and devices employed (chapters 1 and 4). Part I contains two experiments using continuous variables provided by the transverse degrees of freedom of a classical light beam. Part II contains three experiments that use discrete degrees of freedom of pairs of photons produced via spontaneous parametric down conversion. The experiments may be classified in three general topics: quantum kinematics (Chapter 3), quantum dynamics of a single system (chapters 2, 6, and 7) and quantum correlations (Chapter 5). Although sharing the same experimental platforms, the works presented here are substantially different in their theoretical support, thus each of them has its own technical introduction to the topic explored as self-contained as it is possible, such that the chapters can be read in any order. The five experiments presented approach different aspects of quantum theory in a fundamental or applied feature:

- In a slightly more applied direction, we present the optical simulation of a relativistic spin $1/2$ particle in Chapter 2. This experiment, although realized using a classical optical beam, goes along with the idea of quantum simulation in which a controllable system is used to mimic the dynamics of another system that one usually cannot access [28]. We observe the so-called *zitterbewegung*, the trembling motion of free relativistic particles predicted by Dirac equation.
- In Chapter 3 the description of a single continuous variable quantum system is explored by means of mutually unbiasedness (MU). Mutually unbiased bases refer to pairs of Hilbert space bases for which the projective measurement of any element of one basis on the other basis gives equiprobable outcomes [29]. This concept can be defined for

discrete or continuous variables systems and is directly related to complementarity of observables. In practice, MU is not directly observed for continuous variables systems, but can be recovered by discretizing the measurements through periodic coarse graining [30]. In this chapter, we investigate the construction of an arbitrary number of such periodic coarse grained measurements satisfying MU and how this construction resembles the discrete and continuous cases.

- If the system is composed of subsystems, then it may present correlations that are stronger than the ones allowed by classical physics. One such correlation is quantum steering, which appears in a scenario where some subsystems are not accessible at the quantum state level [31]. In Chapter 5, we explore multipartite quantum steering. It is shown that the current definition of this correlation can lead to inconsistencies, allowing for the creation of the correlation from scratch by applying some operations that admittedly should not be able to do so. We experimentally demonstrate this phenomenon, showing that it can be strong enough to be detected even under unavoidable experimental imperfections.
- The content of Chapter 6 is related to the dynamics of a single quantum system. Although the textbooks usually present the evolution of a quantum system as a unitary transformation, the general transformations are not unitary and given as the solution of master equations. Decoherence and dissipation are phenomena induced by the unavoidable coupling of an open quantum system with its environment. When describing this kind of system dynamics, some important approximations are usually considered. A paradigmatic example is the Born-Markovian approximation (BMA), which considers that the reservoir is not altered significantly due to the presence of the system. Nevertheless, even when a quantum master equation is obtained beyond the BMA, most of the indicators of quantum memory may indicate the absence of any non-Markovian (memory) effect. For example, dynamics characterized by positive time-dependent rates are usually classified as Markovian ones [32–34]. In this context, conditional past-future correlations (CPF) were shown to be good memory indicators, predicting non-Markovianity in dynamics usually considered as Markovian [35, 36]. In this chapter, we provide theoretical and experimental evidence on the feasibility of measuring and detecting departures from the BMA by using CPF correlations for the decay of a two level system (polarization of a photon) in a bosonic bath (spatial modes of the photon).
- Closing the thesis, in Chapter 7, a proposal for simulating the aforementioned general evolution for a qubit is presented, where the qubit is implemented in the polarization degree of freedom of single photons.

Part I.

Transverse spatial degree of freedom

EXPERIMENTAL TECHNIQUES

In this chapter, the experimental techniques and devices common to the following two chapters are presented. In these two works the experiments are realized using classical light beams, and we will be interested in the continuous variables coming from the beam transverse position and discrete variables coming from the polarization degree of freedom. The first section presents the functioning of the waveplates used to manipulate the polarization. We use collimated light beams satisfying the paraxial approximation, which is presented in Section 1.2. It is possible to change to which phase space representation we are looking to by performing optical Fourier transforms (to go from position to momentum representation and vice versa) or optical fractional Fourier transforms (to change between two arbitrary phase space direction representations), this is the subject of Sec. 1.3. Finally, in the last section we present the device used to manipulate the spatial profile of the light beam, it is known as a spatial light modulator and enables one to imprint programmable position dependent phases to the wave fronts.

1.1. Polarization transformations: wave plates

Birefringent crystals (App. A) have different properties for different electric field directions. Because of this anisotropy, they are ideal to manipulate the polarization of electromagnetic waves, by transforming the polarization of a beam or even to separate different polarization components. Wave plates are slabs of a birefringent crystal cut to have their optical axis perpendicular to the incidence direction. This way it is guaranteed that no walk-off between two orthogonal polarization directions occurs. The effect of the wave plate is to set a phase difference between ordinary and extraordinary polarization directions. For fixed refractive indexes n_e (x polarization) and n_o (y polarization), the phase difference and accordingly the polarization transformation is manipulated by changing the crystal width d and rotation angle θ around the z axis.

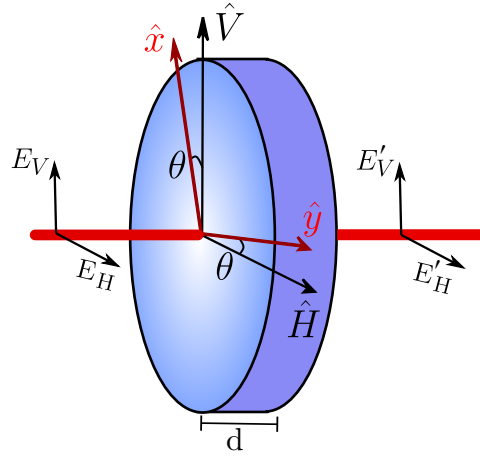


Figure 1.1.: A wave plate: a piece of a uniaxial crystal of width d cut such that its optical axis \hat{x} lie on the incidence plane face. By changing the rotation angle θ and the width of the plate, the transformation relative to the convenient polarization basis $\{\hat{H}, \hat{V}\}$ can be selected.

Let us consider the plane wave solutions for a given frequency ω_0 propagating in the \hat{z} direction. Because the optical axis is perpendicular to the propagation direction, so is the electric field inside the material. The most general plane wave with this features reads

$$\mathbf{E}(z, t) = \left(E_x e^{i\omega_0 t - i2\pi \frac{n_e}{\lambda_0} z} \hat{x} + E_y e^{i\omega_0 t - i2\pi \frac{n_o}{\lambda_0} z} \hat{y} \right) = e^{i\omega_0 t - i2\pi \frac{n_e}{\lambda_0} z} \left(E_x \hat{x} + E_y e^{-i2\pi \frac{n_o - n_e}{\lambda_0} z} \hat{y} \right), \quad (1.1)$$

with E_x and E_y the field amplitudes in the extraordinary and ordinary directions, respectively, and $\lambda_0 = \frac{2\pi c}{\omega_0}$ is the wavelength of the beam in vacuum.

It is convenient to define the laboratory coordinate system in the horizontal and vertical directions. The crystal and laboratory references are related by

$$\hat{x} = \cos \theta \hat{H} + \sin \theta \hat{V} \quad \hat{y} = -\sin \theta \hat{H} + \cos \theta \hat{V}. \quad (1.2)$$

A plane wave in the imminence of entering the wave plate ($z = 0$) has field amplitude $\mathbf{E}_0 = E_H \hat{H} + E_V \hat{V}$. After crossing the wave plate $z = d$, according to (1.1), it is transformed to

$$\mathbf{E}(d) = e^{-i2\pi \frac{n_e}{\lambda_0} d} \left\{ \left[(E_H \cos \theta + E_V \sin \theta) \cos \theta - (-E_H \sin \theta + E_V \cos \theta) \sin \theta e^{-i2\pi \frac{n_o - n_e}{\lambda_0} d} \right] \hat{H} \right. \\ \left. \left[(E_H \cos \theta + E_V \sin \theta) \sin \theta + (-E_H \sin \theta + E_V \cos \theta) \cos \theta e^{-i2\pi \frac{n_o - n_e}{\lambda_0} d} \right] \hat{V} \right\}. \quad (1.3)$$

If the wave plate width is such that $d = (2m + 1)\lambda_0/2(n_1 - n_2)$, with m an integer number, then it is called a *half wave plate* (HWP). The phase difference caused by a HWP is π and $e^{-i2\pi \frac{n_o - n_e}{\lambda_0} d} = -1$. It can be seen from (1.3) that the resultant transformation $(E_H, E_V) \rightarrow (E'_H, E'_V)$ resulting from a HWP set at angle θ in the $\{\hat{H}, \hat{V}\}$ basis is given by the transforma-

tion matrix

$$H\hat{W}P(\theta) = \begin{bmatrix} \cos(2\theta) & \sin(2\theta) \\ \sin(2\theta) & -\cos(2\theta) \end{bmatrix}. \quad (1.4)$$

Thus, a half wave plate transforms linear polarization into linear polarization because it does not introduce any complex phase between the field amplitude components. Particularly, if $\theta = 45^\circ$, the HWP transforms horizontal into vertical polarization and vice versa. Another interesting particular configuration is $\theta = 22.5^\circ$. In this case, horizontally (vertically) polarized light is transformed into a beam with diagonal (antidiagonal) polarization $\hat{D} = \frac{\hat{H} + \hat{V}}{\sqrt{2}}$ ($\hat{A} = \frac{\hat{H} - \hat{V}}{\sqrt{2}}$).

If the plate width is related to the light wavelength by $d = (4m + 1)\lambda_0/4(n_1 - n_2)$, with m an integer number, it is called *quarter wave plate* (QWP). The phase difference between ordinary and extraordinary waves after crossing the plate is then $e^{-i2\pi\frac{n_\theta - n_e}{\lambda_0}d} = i$, considering that $n_e > n_\theta$ as is the case of quartz, the material composing the wave plates we use. If the angle between the crystal axis and the vertical direction is θ the resulting transformation in the $\{\hat{H}, \hat{V}\}$ basis is given by the operator

$$Q\hat{W}P(\theta) = \frac{1}{\sqrt{2}}e^{i\frac{\pi}{4}} \begin{bmatrix} 1 - i\cos(2\theta) & i\sin(2\theta) \\ i\sin(2\theta) & 1 + i\cos(2\theta) \end{bmatrix}, \quad (1.5)$$

as can be obtained from Eq. (1.3). In particular, when $\theta = 45^\circ$, the QWP transforms linear to circular polarization and vice versa

$$\hat{H} \xrightarrow{QWP} \hat{R} = e^{i\frac{\pi}{4}} \frac{(\hat{H} - i\hat{V})}{\sqrt{2}} \quad \hat{V} \xrightarrow{QWP} \hat{L} = e^{-i\frac{\pi}{4}} \frac{(\hat{H} + i\hat{V})}{\sqrt{2}}, \quad (1.6)$$

\hat{R} and \hat{L} are complex unity vectors for right and left polarization, respectively.

For both types, the integer m defines the order of the wave plate. For applications with classical laser light with a big coherence length such as the one discussed in the next chapter, the order of the wave plates used does not degrade the interference between ordinary and extraordinary light. In the second part of this thesis, however, the experiments are made with down converted photons which have a short coherence length comparable with the possible optical path difference inside the wave plate. In that case, it is desirable to work with zero order plates ($m = 0$).

For this part of the thesis, we only consider the special angles mentioned above. In Sec. 4.3, we show that any polarization projection can be performed by a pair QWP-HWP. In Sec. 4.4 we also show that any unitary transformation in polarization can be realized by a set HWP-QWP-HWP.

1.2. Paraxial approximation

The electric field of an electromagnetic wave propagating in vacuum satisfies the wave equation

$$\nabla^2 \mathbf{E}(t, \mathbf{x}) - \frac{1}{c^2} \frac{\partial^2}{\partial t^2} \mathbf{E}(t, \mathbf{x}) = 0, \quad (1.7)$$

where c is the light velocity. The simplest solution to this equation is a plane wave $E_0 \exp[i\omega_{\mathbf{k}}t - i\mathbf{k} \cdot \mathbf{x}]$ with frequency ω and wave vector \mathbf{k} satisfying $\omega_{\mathbf{k}} = c|\mathbf{k}| = ck$. A plane wave itself does not represent a physical field since it is spread all over space and time, but the set of plane wave functions is a complete set of solutions of the wave equation such that

$$\mathbf{E}(t, \mathbf{x}) = \int d^3k \tilde{\mathbf{A}}(\mathbf{k}) e^{i\omega_{\mathbf{k}}t - i\mathbf{k} \cdot \mathbf{x}}$$

is the most general solution possible, $\tilde{\mathbf{A}}(\mathbf{k})$ is a complex vector perpendicular to the wave vector \mathbf{k} . We are interested in describing the monochromatic collimated light beam emitted by a laser. This solution has the property of being well localized in space, it has a well defined propagation direction and it does not diverges much during the propagation. This features allows for the so called paraxial approximation which leads to the Helmholtz equation, as we describe next, whose solutions are well known.

A monochromatic paraxial wave propagating in the z direction is a solution composed by plane waves with frequency ω whose transverse wave vector components are much smaller than the component in the direction of propagation, i.e. $k_x, k_y \ll k$ and $k_z \sim k$ or writing $k_z = k - \Delta k$

$$\Delta k = k - \left(k^2 - k_x^2 - k_y^2\right)^{\frac{1}{2}} \ll k = \frac{2\pi}{\lambda}. \quad (1.8)$$

The electric field can be rewritten as

$$\mathbf{E}(t, \mathbf{x}) = \left[\int d^2k \tilde{\mathbf{A}}(\mathbf{k}) e^{-i(k_x x + k_y y + \Delta k z)} \right] e^{i\omega t - ikz} = \mathbf{A}(\mathbf{x}) e^{i\omega t - ikz}, \quad (1.9)$$

that is, a plane wave propagating in the z direction with envelope $\mathbf{A}(\mathbf{x})$. Because of the paraxial condition (1.8), the envelope varies slowly with the propagation distance. The substitution of solution (1.9) into the wave equation shows that the envelope satisfies

$$\nabla_t^2 \mathbf{A}(\mathbf{x}) - 2ik \frac{\partial \mathbf{A}(\mathbf{x})}{\partial z} + \frac{\partial^2 \mathbf{A}(\mathbf{x})}{\partial z^2} = 0, \quad (1.10)$$

∇_t^2 stands for the Laplacian operator in the transverse coordinates x and y . Considering the slow variation with the propagation distance, the Taylor series of the envelope

$$\mathbf{A}(x, y, z + \Delta z) = \mathbf{A}(\mathbf{x}) + \frac{\partial \mathbf{A}(\mathbf{x})}{\partial z} \Delta z + \frac{1}{2} \frac{\partial^2 \mathbf{A}(\mathbf{x})}{\partial z^2} \Delta z^2 + \dots$$

can be approximated by the first order expansion for $\Delta z \sim \lambda$, regarding that

$$\frac{1}{2} \left| \frac{\partial^2 \mathbf{A}(\mathbf{x})}{\partial z^2} \right| \lambda^2 \ll \left| \frac{\partial \mathbf{A}(\mathbf{x})}{\partial z} \right| \lambda,$$

or equivalently

$$\left| \frac{\partial^2 \mathbf{A}(\mathbf{x})}{\partial z^2} \right| \ll 2k \left| \frac{\partial \mathbf{A}(\mathbf{x})}{\partial z} \right|.$$

Applying this approximation to Eq. (1.10) give us the paraxial Helmholtz equation

$$\nabla_t^2 \mathbf{A}(\mathbf{x}) + 2ik \frac{\partial \mathbf{A}(\mathbf{x})}{\partial z} = 0 \quad (1.11)$$

satisfied by the envelope field in the paraxial condition. This equation is completely analogous to the free Schrödinger equation for a unit-mass particle if we make the associations $z \rightarrow t$ and $k \rightarrow 1/\hbar$. In this analogy, the complex amplitude of the field is associated to the particle wavefunction, and the beam intensity distribution to the probability density of detecting the particle. This analogy has been widely used in many experiments emulating quantum systems using light [37, 38].

The Hermite-Gauss functions form a particular complete set of solutions to the Helmholtz equation for each component of the vector $\mathbf{A}(\mathbf{x})$ [39]. The output of the monomode laser we use in our experiments is a Hermite-Gauss function of zero order expressed as

$$A_{0,0}(x, y, z) = A_0 \frac{w_0}{w(z)} \exp \left[\frac{-\rho^2}{w^2(z)} \right] \exp \left[-ik \frac{\rho^2}{2R(z)} + i\zeta(z) \right],$$

where:

- A_0 is a complex constant, $\rho^2 = x^2 + y^2$ is the distance to the center of the beam;
- $w(z) = w_0 \left[1 + \left(\frac{z}{z_0} \right)^2 \right]^{1/2}$ is the beam width in position z , were $z_0 = \frac{w_0^2 \pi}{\lambda}$ is known as the Rayleigh range;
- The origin of the z axis is defined such that the beam waist, that is the position is which the beam width has the smallest value possible w_0 , is located at $z = 0$;
- $R(z) = z \left[1 + \left(\frac{z_0}{z} \right)^2 \right]$ is the radius of curvature of the wave fronts in position z ;
- $\zeta(z) = \text{tg}^{-1} \left(\frac{z}{z_0} \right)$ is called Gouy phase.

Free space propagation: Let us consider only one component of the electric field of a paraxial wave propagating in the z direction and that this component distribution on the plane $z = z_1$ is equal to a function $f_1(x, y) = E(x, y, z_1)$. We want to relate this initial transverse profile to

the field distribution $f_2(x, y) = E(x, y, z_2)$ in a posterior position $z = z_2$ if the electromagnetic wave is propagating in free space. The paraxial approximation applied to Eq. (1.8) gives

$$\Delta k \approx \frac{k_x^2 + k_y^2}{2k}. \quad (1.12)$$

Thus, defining the Fourier transform of the initial distribution

$$f_1(x, y) = \frac{1}{(2\pi)^2} \int dk_x \int dk_y F_1(k_x, k_y) e^{-ik_x x - ik_y y}$$

and defining the propagation distance $d = z_2 - z_1$, the field distribution in position $z = z_2$ is obtained with Eq. (1.9) as

$$f_2(x, y) = \frac{e^{-ikd}}{(2\pi)^2} \int dk_x \int dk_y F_1(k_x, k_y) e^{-ik_x x - ik_y y} e^{-i \frac{k_x^2 + k_y^2}{2k} d}, \quad (1.13)$$

but this is the inverse Fourier transform of the product $F_1(k_x, k_y) e^{-i \frac{k_x^2 + k_y^2}{2k} d}$, and by the convolution theorem [40] it can be written as

$$f_2(x, y) = e^{-ikz} \int dx' \int dy' f_1(x', y') h(x - x', y - y'), \quad (1.14)$$

where we defined $h(x, y) = \frac{i}{\lambda d} \exp \left[-ik \frac{x^2 + y^2}{2d} \right]$ as the Fourier transform of the free space transfer function $e^{-i \frac{k_x^2 + k_y^2}{2k} d}$.

Propagation through a thin lens: Consider a monochromatic paraxial wave crossing a lens with central width Δz made of a homogeneous isotropic material whose refractive index is n . While inside the lens, the wave vector changes its modulus due to the change in the refractive index. The lens width and thus the optical path difference acquired by the beam depend on the transverse position relative to the center of the lens. If $f_1(x, y) = E(x, y, z_1)$ is the electric field amplitude in the plane immediately before the lens, the net effect in the electric field amplitude in the plane immediately after the lens $f_2(x, y) = E(x, y, z_1 + \Delta z)$ is a quadratic phase

$$f_2(x, y) = e^{-ink\Delta z} \exp \left[ik \frac{x^2 + y^2}{2f} \right], \quad (1.15)$$

where f is the focal distance of the lens which relates to the refractive index of the lens material and to the curvature of the lens depending on its exact shape. This expression is obtained under some assumptions: that the incident beam is narrow compared to the lens curvature, and that the lens is thin and the incidence is almost normal, such that direction changes in the wave vector are neglected. The last condition is valid for all wave vectors composing the beam and is equivalent to requiring the beam to be paraxial.

1.3. Fractional Fourier transform and phase space variables

The fractional Fourier transform is a generalization of the ordinary Fourier transform and can be defined in the context of rotations in the phase space of a continuous variables system. As a mathematical tool it has applications in classical signal processing, quantum physics and in the solution of differential equations [41].

Let us consider the adimensional position and momentum operators of a continuous variables system satisfying the canonical commutation relation $[\hat{x}, \hat{p}] = i$. Let $|x\rangle$ be the eigenstate of the position operator \hat{x} with eigenvalue x . The eigenstates of the position operator satisfy the completeness relation $\int dx |x\rangle\langle x| = \mathbb{1}$, such that any pure state $|\psi\rangle$ of the system can be uniquely represented by its position representation or wavefunction $\psi(x) = \langle x|\psi\rangle$ as

$$|\psi\rangle = \int dx \psi(x)|x\rangle. \quad (1.16)$$

The same statements are valid for the momentum eigenstates $\{|p\rangle\}$, being $\tilde{\psi}(p) = \langle p|\psi\rangle$. Because of the commutation relation between position and momentum, the scalar product of eigenstates of the two operators is given by $\langle p|x\rangle = \frac{e^{ipx}}{\sqrt{2\pi}}$ and thus

$$\tilde{\psi}(p) = \int dx \langle p|x\rangle\langle x|\psi\rangle = \frac{1}{\sqrt{2\pi}} \int dx e^{-ipx}\psi(x), \quad (1.17)$$

that is, momentum and position representations are connected via a Fourier transform (FT). Accordingly, the position representation is obtained as the inverse Fourier transform of the momentum wavefunction.

Analogously, we can consider the eigenstates $\{|q_\theta\rangle\}$ of any operator defined as

$$\hat{q}_\theta = \cos \theta \hat{x} + \sin \theta \hat{p}. \quad (1.18)$$

The operator \hat{q}_θ can be seen as a rotated position in phase space, a two dimensional space which orthogonal axis are defined by the position and momentum values. The eigenstates of \hat{q}_θ satisfy [41]

$$\langle q_\theta|x\rangle = \mathcal{F}^\theta = \sqrt{\frac{1 - i \cot \theta}{2\pi}} e^{i \frac{\cot \theta}{2} (x^2 + q_\theta^2) - ixq_\theta \csc \theta}, \quad (1.19)$$

they form a basis for the space of states and satisfy $\int dq_\theta |q_\theta\rangle\langle q_\theta| = \mathbb{1}$ such that any state can be written as

$$|\psi\rangle = \int dq_\theta \bar{\psi}(q_\theta)|q_\theta\rangle. \quad (1.20)$$

The q_θ representation and the position representation are related through the integral transfor-

mation

$$\bar{\psi}(q_\theta) = \langle q_\theta | \psi \rangle = \int dx \psi(x) \langle q_\theta | |x \rangle \quad (1.21)$$

with kernel given by (1.19). This transformation is called fractional Fourier transform (FrFT). The FrFT is linear and additive, meaning that realizing two subsequent transformations with angles θ_1 and θ_2 is equivalent to realizing only one transformation with angle $\theta_1 + \theta_2$. In the particular case of $\theta = \pi/2$, it is possible to see that the FrFT consistently reduces to the ordinary FT. Analogously, any rotation in phase space from q_θ to $q_{\theta'}$ representations is obtained through a FrFT with kernel $\mathcal{F}^{\Delta\theta}$, with $\Delta\theta = \theta' - \theta$.

The FrFT has many optical realizations and even one of its first treatments came in the context of classical optics [42, 43]. We show next the methods we use in our experiments to realize FTs and FrFT. Although the FT is contained in the FrFT, we present the two transformations separately as we use a simpler method to realize FTs when position and momentum are the only phase space variables needed.

1.3.1. Optical Fourier transform

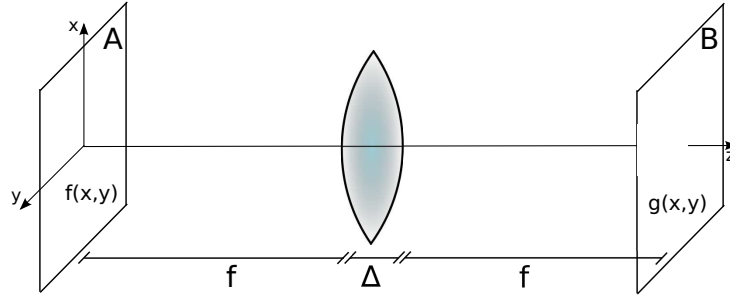
As was mentioned before, the transverse electric field distribution of a paraxial wave is analogous to the wavefunction of a quantum particle in position representation. In the same way, the Fourier transform of the field distribution can be regarded as the analogous to the momentum representation of the state. The Fourier transform of the transverse field distribution can be obtained experimentally by the apparatus shown in Fig. 1.2 as is described in what follows.

Let us consider again a monochromatic paraxial beam with wavelength λ , propagating in the z direction, which is perpendicular to a lens of focal distance f and width Δ , located one focal distance apart from the plane $z = 0$. In a plane A located in the origin of the z axis, a component of the electric field is described by a function $f(x, y) = E(x, y, 0)$ with Fourier transform $F(k_x, k_y)$. We are interested in relating $f(x, y)$ and the field distribution $g(x, y) = E(x, y, 2f + \Delta)$ after the beam has propagated in free space by a distance f , traversed the lens and then again freely propagated by another focal distance.

After the first free space propagation, according to Eq. (1.13), the field distribution becomes

$$E(x, y, f) = \frac{e^{-ik_0 f}}{(2\pi)^2} \int dk_x \int dk_y F(k_x, k_y) e^{if \frac{k_x^2 + k_y^2}{2k_0}} e^{-ik_x x - ik_y y}. \quad (1.22)$$

The wave then crosses the lens acquiring a quadratic phase (Eq. (1.15)) and becoming



figurename? 1.2.: Configuration using a lens to implement the optical Fourier transform between the two focal planes.

$$\begin{aligned} E(x, y, f + \Delta) &= e^{-ik_0\Delta} e^{ik_0 \frac{x^2+y^2}{2f}} E(x, y, f) \\ &= \frac{e^{-ik_0(f+\Delta)}}{(2\pi)^2} e^{ik_0 \frac{x^2+y^2}{2f}} \int dk_x \int dk_y F(k_x, k_y) e^{if \frac{k_x^2+k_y^2}{2k_0}} e^{-ik_x x - ik_y y}. \end{aligned} \quad (1.23)$$

It is now easier to directly use Eq. (1.14) rather than the Fourier propagation to obtain the field distribution in the focal plane B after the last free space propagation as¹

$$g(x, y) = \frac{i e^{-2ik_0 f}}{\lambda_0 f} F\left(\frac{k_0 x}{f}, \frac{k_0 y}{f}\right), \quad (1.24)$$

that is, the wave amplitude in the position (x, y) on plane B is proportional to the Fourier transform of the initial amplitude, evaluated for the transverse wave vector ($k_x = \frac{k_0 x}{f}, k_y = \frac{k_0 y}{f}$). Thus, we can regard the first and second focal planes as the position and momentum spaces, respectively.

The “inverse” Fourier transform is obtained replicating the lens system as shown in

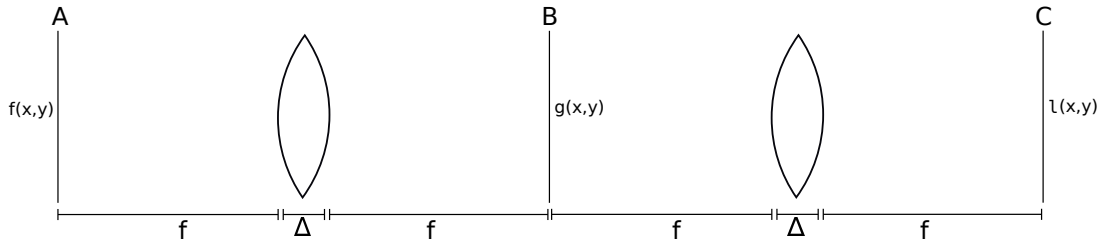
¹Plugging Eq. (1.23) into Eq. (1.14) gives

$$\begin{aligned} g(x, y) &= \frac{i}{\lambda_0 f} \frac{e^{-ik_0(2f+\Delta)}}{(2\pi)^2} \int dx' \int dy' \int dk_x \int dk_y e^{-\frac{ik_0}{2f}((x-x')^2+(y-y')^2)} e^{\frac{ik_0}{2f}(x'^2+y'^2)} \\ &\quad e^{\frac{if}{2k_0}(k_x^2+k_y^2)} e^{-i(k_x x' + k_y y')} F(k_x, k_y) \\ g(x, y) &= \frac{i}{\lambda_0 f} \frac{e^{-ik_0(2f+\Delta)}}{(2\pi)^2} e^{-\frac{ik_0}{2f}(x^2+y^2)} \int dk_x \int dk_y \left[\int dx' e^{i\left(\frac{k_0 x}{f} - k_x\right)x'} \right] \left[\int dy' e^{i\left(\frac{k_0 y}{f} - k_y\right)y'} \right] \\ &\quad e^{\frac{if}{2k_0}(k_x^2+k_y^2)} F(k_x, k_y). \end{aligned}$$

The lens width can be neglected in comparison with the focal distance and the position integrals are identified as Dirac delta functions since $\delta(k) = \frac{1}{2\pi} \int dx e^{ikx}$, giving

$$g(x, y) = \frac{i}{\lambda_0 f} e^{-ik_0 2f} e^{-\frac{ik_0}{2f}(x^2+y^2)} \int dk_x \int dk_y \delta\left(\frac{k_0 x}{f} - k_x\right) \delta\left(\frac{k_0 y}{f} - k_y\right) e^{\frac{if}{2k_0}(k_x^2+k_y^2)} F(k_x, k_y),$$

which leads to Eq. (1.24) after integration.



?figurename? 1.3.: The optical Fourier transform scheme duplicated.

Fig. 1.3. As the Fourier transform of $g(x, y)$ is given by

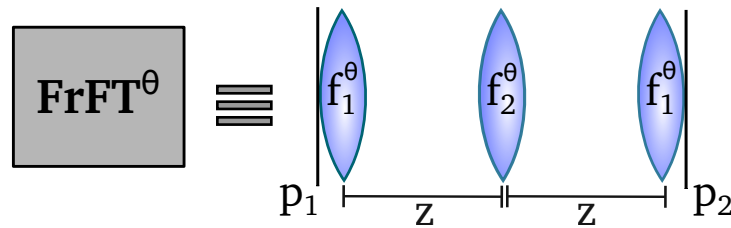
$$\begin{aligned}
 G(k_x, k_y) &= \int dx \int dy g(x, y) e^{ik_x x + ik_y y} \\
 &= i e^{-2ik_0 f} f \lambda_0 f \left(-\frac{f}{k_0} k_x, -\frac{f}{k_0} k_y \right),
 \end{aligned}
 \tag{1.25}$$

then the field amplitude in plane C is the inverted image of plane A

$$l(x, y) = e^{-2ik_0 f} f(-x, -y),
 \tag{1.26}$$

what allow us to say that in plane C we have again the position space although it is inverted.

1.3.2. Optical fractional Fourier transform



?figurename? 1.4.: Three lenses scheme for optical FrFT: the field distribution in the transverse plane p_2 is equals to the FrFT of the field distribution in the input plane p_1 .

In what follows it is shown that the three lenses configuration illustrated in Fig. 1.4 realizes a FrFT of the transverse field distribution between the input (p_1) and output (p_2) planes, with any phase-space rotation-angle θ if the lenses focal lengths are suitably chosen as

$$\frac{1}{f_1^\theta} = \frac{1}{z} \left(1 - \frac{\cot(\theta/2)}{2} \right)
 \tag{1.27}$$

$$1 - \frac{z}{2f_2^\theta} = \sin \theta.
 \tag{1.28}$$

Let us consider a monochromatic light beam with wavelength λ propagating in the z direction perpendicular to the lenses coming from the left to the right. The spatial electric field

distribution is given in any point of space by $E(x, y, z)$. In the plane p_1 immediately before the first lens the field is a function $E(x, y, 0) = f(x, y)$ of the coordinates on the plane. For simplicity, the lenses are considered to be cylindrical, such that the curvature in y direction is infinity and the lens acts only in the x direction. We can forget about the dependence in coordinate y since the beams we use are separable in the transverse variables and the y -dependent part is only affected by the free propagation divergence. Also for simplicity, the propagation phases e^{ikz} are ignored throughout the calculation. So, after the first lens the field amplitude becomes (Eq. (1.15))

$$E(x, \Delta_1) = f(x) \exp\left(\frac{i\pi x^2}{\lambda f_1^\theta}\right), \quad (1.29)$$

where Δ_1 and f_1 are the width and the focal length of this lens. Then the wave freely propagates by a distance z after which the field distribution is given by the convolution (Eq. (1.14))

$$E(x, \Delta_1 + z) = \frac{1}{\lambda z} \int dx' f(x') \exp\left(\frac{i\pi x'^2}{\lambda f_1^\theta}\right) \exp\left[-i\pi \frac{(x - x')^2}{\lambda z}\right]. \quad (1.30)$$

Another quadratic phase is imprinted by the second lens whose width is Δ_2 and whose focal length is f_2 . The field becomes

$$E(x, \Delta_1 + z + \Delta_2) = \frac{1}{\lambda z} \int dx' f(x') \exp\left(\frac{i\pi x'^2}{\lambda f_1^\theta}\right) \exp\left(\frac{i\pi x^2}{\lambda f_2^\theta}\right) \exp\left[-i\pi \frac{(x - x')^2}{\lambda z}\right]$$

After the second free space propagation, using again the convolution (1.14), the field amplitude transforms to

$$E(x, \Delta_1 + 2z + \Delta_2) = \frac{1}{(\lambda z)^2} \int dx'' \int dx' f(x') \exp\left(\frac{i\pi x'^2}{\lambda f_1^\theta}\right) \exp\left(\frac{i\pi x''^2}{\lambda f_2^\theta}\right) \exp\left[-i\pi \frac{(x'' - x')^2}{\lambda z}\right] \exp\left[-i\pi \frac{(x - x'')^2}{\lambda z}\right]$$

Let us take a look at the integral in the variable x''

$$\int dx'' \exp\left[\frac{i\pi x''^2}{\lambda f_2^\theta} - \frac{2i\pi x''^2}{\lambda z} + \frac{2i\pi x''(x + x')}{\lambda z}\right]. \quad (1.31)$$

Substituting (1.28) and solving the Gaussian integral it becomes

$$\int dx'' \exp\left[-\frac{2i\pi \sin \theta x''^2}{\lambda z} + \frac{2i\pi x''(x + x')}{\lambda z}\right] = \sqrt{\frac{\lambda z}{2i \sin \theta}} \exp\left[\frac{i\pi(x' + x)^2}{2\lambda z \sin \theta}\right]. \quad (1.32)$$

The field amplitude is then given by

$$E(x, \Delta_1 + 2z + \Delta_2) = \frac{1}{(\lambda z)^2} \sqrt{\frac{\lambda z}{2i \sin \theta}} \int dx' f(x', y') \exp \left(\frac{i\pi x'^2}{\lambda f_1^\theta} + \frac{i\pi(x' + x)^2}{2\lambda z \sin \theta} - \frac{i\pi x'^2}{\lambda z} - \frac{i\pi x^2}{\lambda z} \right), \quad (1.33)$$

Finally, using (1.27) and the trigonometric relation $\cot(\theta/2) = \frac{1}{\sin \theta} + \cot \theta$ all the undesired phases in x' are canceled out. The remaining spurious phases in x are removed by the last lens. The field at the output plane is given by

$$E(x, 2\Delta_1 + 2z + \Delta_2) = \frac{1}{(\lambda z)^2} \sqrt{\frac{\lambda z}{2i \sin \theta}} \int dx' f(x', y') \exp \left\{ \frac{i\pi}{2\lambda z} \left[\cot \theta (x'^2 + x^2) - 2xx' \csc \theta \right] \right\}, \quad (1.34)$$

that is precisely the FrFT of angle θ of the field amplitude in the input plane $f(x)$. The scaling factor $\sqrt{2\lambda z}$ is common to both phase space variables and does not depend on the FrFT order. If there are no further transformations after the second free propagation, then the last lens is not required, since it just corrects the phase.

This scheme was proposed in Ref. [44] and is not the only way to perform an optical FrFT. For example, a simpler scheme using only one lens could be used [42], but then the free propagation distances must be changed for each phase space direction one wants to access. The three-lenses scheme allows one to keep the free space propagation distances fixed. That is, the lenses can have fixed positions, if the focal lengths are changed accordingly. As we show in the next section, since the lens effect is to imprint a position dependent phase to the wave front, a spatial light modulator can be used to mimic a lens of any focal length. Thus the three-lenses scheme provides a method to realize optical FrFT in a programmable way.

1.4. Spatial Light Modulator

Spatial light modulator (SLM) is a common term used to identify devices that modulate the phase, the amplitude, or the polarization of a light beam by means of diverse physical phenomena like acousto-optic and electro-optic effects, and liquid crystal anisotropy [39]. In this section the basic operation of a liquid crystal SLM is explained.

Basically, liquid crystals (LC) are materials which are in a fluid phase as liquids, being able to adapt their shapes to the recipient, at the same time that they present anisotropic features like crystals [45]. Typically, materials which present a LC phase are composed by elongated molecules. The anisotropy then comes from the alignment of the long molecule axis in a preferred direction. When the molecules are in average all aligned in the same direction, but their centers are randomly distributed, the LC has only one anisotropic axis. In this case, the LC is called nematic and it behaves like a uniaxial crystal with optic axis in the same direction as the

molecule orientation.

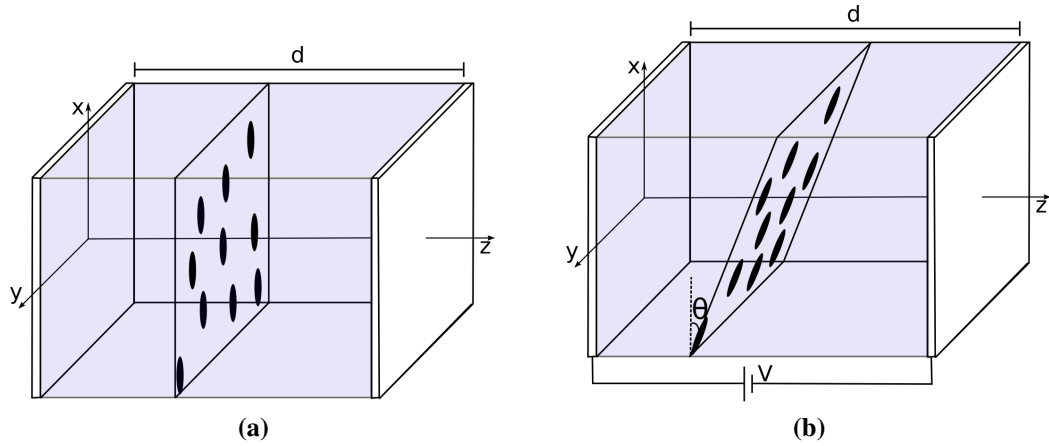


Figure 1.5: (a) Nematic liquid crystal cell with width d , enclosed by two glass plates which keep the LC molecules aligned with the x direction. (b) If a potential difference V is applied through the cell in the z direction, it generates a dipole force that tilts the molecules by an angle θ in the steady position.

Let us consider a cell of a nematic LC with thickness d and a square face as shown in Fig. 1.5-a). Because of the interaction with the two glass plates involving the LC material, the molecules tend to align with the x direction. A transverse field can be applied with a electric potential difference V across the cell, generating a dipole force in the z direction which cause the molecules to rotate until they reach a steady position at angle θ relative to the x axis (Fig. 1.5-b)). The inclination of the molecules is given as a function of the potential difference by [39]

$$\theta = \begin{cases} 0, & V < V_c \\ \frac{\pi}{2} - 2\text{tg}^{-1} \left[\exp \left(-\frac{V-V_c}{V_0} \right) \right], & V > V_c \end{cases}, \quad (1.35)$$

where V_0 is a constant characterizing the material, and V_c is the critical potential above which the molecules start tilting.

The direction of the molecules long axis is the extraordinary direction of the crystal with index of refraction n_e , while the two perpendicular directions have refractive index n_o . When an electromagnetic wave propagates inside the LC cell in the z direction, it feels the ordinary refractive index n_o if it is y -polarized, while the refractive index will be

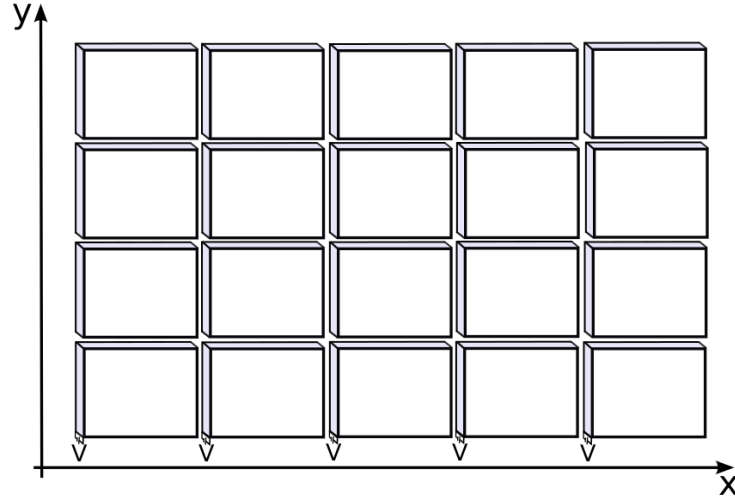
$$\frac{1}{n(\theta)^2} = \frac{\cos^2 \theta}{n_o^2} + \frac{\sin^2 \theta}{n_e^2} \quad (1.36)$$

for x -polarized waves (App. A). Thus, the optical path of the x -polarized component inside the LC cell can be manipulated by changing the applied voltage. Analogously to Eq. (1.1), this optical path difference results in a phase difference between the two orthogonal polarizations

given by

$$\phi(\theta) = 2\pi \frac{n_2 - n(\theta)}{\lambda_0} d, \quad (1.37)$$

that is, an electrically-controlled phase modulation occurs.



?figurename? 1.6.: Many LC identical cells disposed side by side composing a SLM screen. Each cell's voltage is individually controlled such that a position dependent phase is imprinted to the wave front of the x -polarized component of an electromagnetic wave.

A SLM is a screen composed of thousands of microscopic LC cells arranged side by side as shown in Fig. 1.6. The voltage across each cell is individually electronic controlled. So it is possible to program the SLM to apply any position depend phase $f(x, y)$ by changing the voltages as to make $2\pi \frac{n_2 - n(\theta(x, y))}{\lambda_0} d = f(x, y)$, where $\theta(x, y)$ is the inclination of the molecules inside the cell located at position (x, y) on the screen plane. The refractive index in the y direction is fixed and the phase aquired by the x -polarized component is relative between the two components of polarization. The action of a SLM in the $\{\hat{x}, \hat{y}\}$ basis is given by the position dependent operator

$$\hat{P}[f(x, y)] = \begin{bmatrix} e^{if(x, y)} & 0 \\ 0 & 1 \end{bmatrix}, \quad (1.38)$$

disregarding the global phase. Of course the applied phase is not the spatially continuous function $f(x, y)$ but a discretized version of it, whose resolution is given by the size of the LC cells.

In our experiments, we use Holoeye SLMs, which have the long molecule axis is in the horizontal and thus the horizontal polarization is modulated. The resolution of these SLMs is 1920×1080 pixels, with $8 \mu\text{m}$ pixel pitch. Therefore, if a phase function varies considerably in a interval smaller than $8 \mu\text{m}$, then the SLM does not capture its detailed features. These devices are build on a silicon matrix in which lies the electronic control parts, thus the light is not transmitted through the cells but it is reflected passing twice through the LC [46]. These

SLMs have a fill factor of 92% meaning that 8% of the total active area is empty space between neighbor cells. This causes part of the incident light to scatter by diffraction and approximately 40% of the light is lost in each SLM use. This kind of SLM works coupled to a computer as an additional screen. The phase function is converted to a gray scale image which is projected in the SLM. Each value of the gray scale number of 8 bits (natural numbers from 0 to 255) is associated to a value in the phase interval usually with a roughly linear correspondence, which can be adjusted manually for each SLM. Ideally, if the phase interval is $[0, 2\pi]$, then the color 0 corresponds to applied phase 0 and color 255 corresponds to apply a phase of 2π . For each of the 256 gray scale values, a voltage is assigned. This operation mode discretize also the values of phase possible, since only the values of the form $(n - 1) \frac{2\pi}{255}$ can be set, with $n = 1, 2, \dots, 256$.

1.4.1. SLM calibration

A SLM typically works for a large range of wavelengths imprinting phases in an adjustable phase interval. To assure that, for a fixed wavelength (632.8 nm produced by a He-Ne laser in our case), the right phase interval is reached, a calibration process is needed. To find out what is the phase imprinted for each gray tone we interfere a modulated wave with one that has not been applied a phase difference. As the SLM modulates only the horizontal polarization, we interfere the incoming horizontal and vertical polarizations in a HWP as is illustrated in Fig. 1.7. First of all a horizontally polarized beam is prepared from a continuous wave laser using a polarizing beam splitter (PBS), a device that transmits horizontal polarization while reflecting the vertical polarized component. The beam then passes through a QWP set to -45° which transforms the polarization to circular

$$E_0 \hat{\mathbf{H}} \xrightarrow{QWP_{@45^\circ}} E_0 \frac{\hat{\mathbf{H}} + i\hat{\mathbf{V}}}{\sqrt{2}}, \quad (1.39)$$

E_0 is the field amplitude after the PBS. The light is then reflected by the SLM whose screen uniformly projects the same grayscale which corresponds to some unknown phase θ . The correspondent transformation is given by

$$E_0 \frac{\hat{\mathbf{H}} + i\hat{\mathbf{V}}}{\sqrt{2}} \xrightarrow{SLM_{@ \theta}} E_0 \frac{\hat{\mathbf{H}} e^{i\theta} + i\hat{\mathbf{V}}}{\sqrt{2}}. \quad (1.40)$$

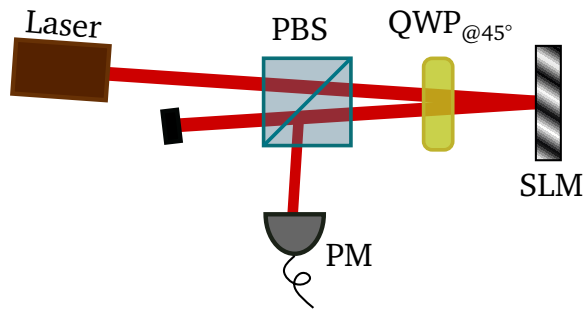
After that , the beam goes back through the same path passing again through the QWP which mixes modulated and unmodulated components

$$E_0 \frac{\hat{\mathbf{H}} e^{i\theta} + i\hat{\mathbf{V}}}{\sqrt{2}} \xrightarrow{QWP_{@45^\circ}} E_0 \frac{\hat{\mathbf{H}} (e^{i\theta} - 1) + i\hat{\mathbf{V}} (e^{i\theta} + 1)}{2}. \quad (1.41)$$

Finally, the polarization components of the beam are separated by the PBS and the vertical component intensity is measured by a power meter. For a given θ the measured intensity I is proportional to the modulus square of the vertical electric field and thus

$$I \propto \cos^2 \frac{\theta}{2} \quad (1.42)$$

what allows us to determine the phase θ corresponding to a given grayscale level.



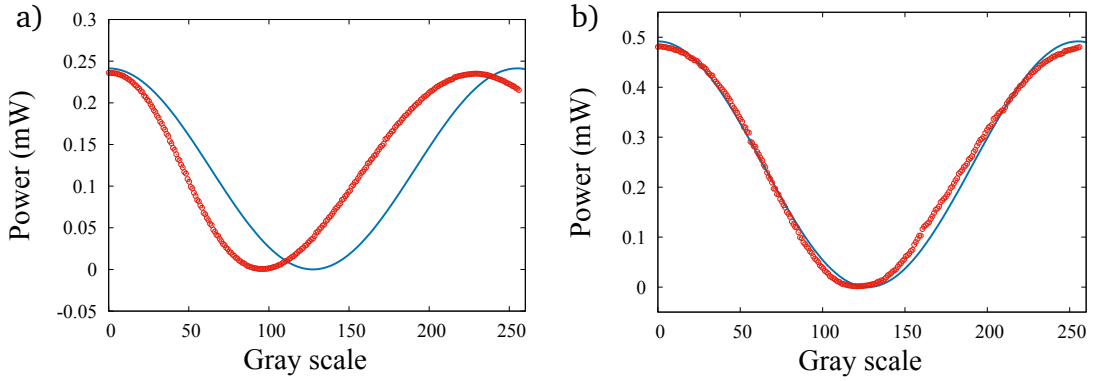
?figurename? 1.7.: Set up for an SLM calibration: a light beam at the frequency the SLM is going to be calibrated for passes through a polarizing beam splitter (PBS) which lets only the horizontally polarized component be transmitted. A HWP set to 22.5° transforms the light to diagonal polarization. Only the horizontal component is modulated by the SLM. Horizontal and vertical polarization interfere when passing again through the HWP and the intensity of vertical polarization component reflected by the PBS is measured by a power meter (PM).

If the SLM is set to work in the range $[0, 2\pi]$ with linear correspondence between grayscale values and angles, then the measured power as a function of the color should behave like Eq. (1.42), with maximums at 0 and 255. To calibrate the SLM we vary the grayscale along all 256 possible values, measuring the power of the vertically polarized component for each one. When using the factory setting, we obtain the red dots shown in Fig. 1.8-a), a behavior similar to the expected (blue solid line in the figure) but with a slightly larger frequency. We use this measurements to determine a new correspondence function between color and voltage across the LC cells. After the reconfiguration, the power measurement returns the correct behavior (Fig. 1.8-b)).

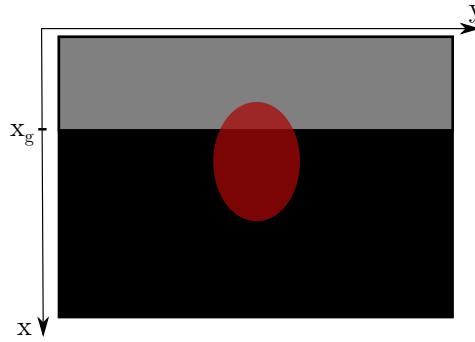
1.4.2. Beam positioning in the SLM plane

Besides of assuring that the correct phase value is imprinted, a proper coordinate system on the SLM plane must be defined, what means to find a physically meaningful origin point since the direction of the axes is defined by the rectangular array of LC cells. The origin is defined relatively to the center of the light beam without any previous spatial alteration².

²In the case when the beam hits other SLM screens before the one that is being calibrated, all the previous ones must be kept with uniform phase such that the position of the beam is not altered.



?figurename? 1.8.: Measured power as a function of the gray color projected on the SLM screen in a calibration process: a) with the factory setting, b) after adjusting the voltage configuration to wavelength 632.8 nm and phase range $[0, 2\pi]$. In both plots the blue solid line is the expected cosine function and the red dots are measured power values.



?figurename? 1.9.: SLM screen projecting the image for positioning the beam. Part of the red light beam gets the phase given by black color and part gets the phase associated to the gray tone.

We consider only one coordinate on the plane, let us say the vertical position, and ignore the dependence on the second one, as it is the case in our experiments. The laser produces a Gaussian mode with amplitude proportional to $f(x, y) = \exp\left[-\frac{(x-x_0)^2}{2\Delta_x^2}\right] \exp\left[-\frac{(y-y_0)^2}{2\Delta_y^2}\right]$. Let us consider a setup as the one used for phase calibration (Fig. 1.7) but instead of a uniform grayscale in the entire screen, the SLM projects an image as shown in Fig. 1.9 with the screen divided into two colors. When we wrote the field amplitude in Eq. (1.40), we were not concerned with the spatial distribution since the whole beam was receiving the same phase and the spatial distribution would be integrated to give the total power. Now, after the SLM action and after the QWP, instead of Eq. (1.41), we have two phase regions and we can write for the field amplitude

$$\mathbf{E} \propto \begin{cases} f(x, y) \frac{\hat{\mathbf{H}}(e^{i\theta_1}-1) + i\hat{\mathbf{V}}(e^{i\theta_1}+1)}{2} & x < x_g \\ f(x, y) \frac{\hat{\mathbf{H}}(e^{i\theta_2}-1) + i\hat{\mathbf{V}}(e^{i\theta_2}+1)}{2} & x \geq x_g \end{cases}, \quad (1.43)$$

θ_1 and θ_2 are the phases of each color region. Consequently, the total power measured when

selecting only vertical polarization is proportional to

$$\int_{-\infty}^{\infty} dy \left[\int_{-\infty}^{x_g} dx f(x, y)^2 \cos^2 \frac{\theta_1}{2} + \int_{x_g}^{\infty} dx f(x, y)^2 \cos^2 \frac{\theta_2}{2} \right]. \quad (1.44)$$

If the colors are chosen such that $\theta_1 = \pi$ and $\theta_2 = 0$, because the beam is Gaussian, the power will be a displaced complementary error function of $x_g \operatorname{erfc}(x_g - x_c)$ which center x_c coincides with the center of the Gaussian beam x_0 . So, by varying the position of the gray π -phase stripe from pixel 0 to the 1080th pixel we can reconstruct the complementary error function and determine the central position of the beam on the SLM as shown in Fig. 1.10. In general, we cannot use exactly the setup of Fig. 1.7 because the beam positioning must be done with the whole experimental setup for the actual experiment mounted, but any configuration able to interfere horizontal and vertical polarization after the SLM action will behave as a error-like function when the screen is scanned by the π -phase region.

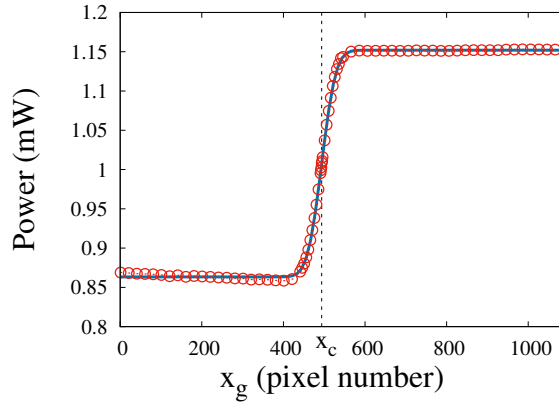


Figure 1.10. Power of vertical polarization component as a function of the end position of the gray stripe. The dots are the measured values and the blue line is the fitted complementary error function.

1.4.3. Amplitude masks from phase modulation

It is possible to produce amplitude masks from phase modulation by using a phase-only SLM as a diffraction grating. A diffraction grating is an optical element that periodically modulates the phase of an incident beam. Thus, setting a SLM to imprint a periodic phase $\exp[i f(y)]$ makes it work as a diffraction grating in the y direction. Consider a paraxial incident beam making a small angle θ_i with the plane xz , where z is the normal direction to the SLM plane. If the imprinted phase has a period Λ which is much larger than the beam wavelength λ , then the reflection of the beam by the SLM generates several beams at angles [39]

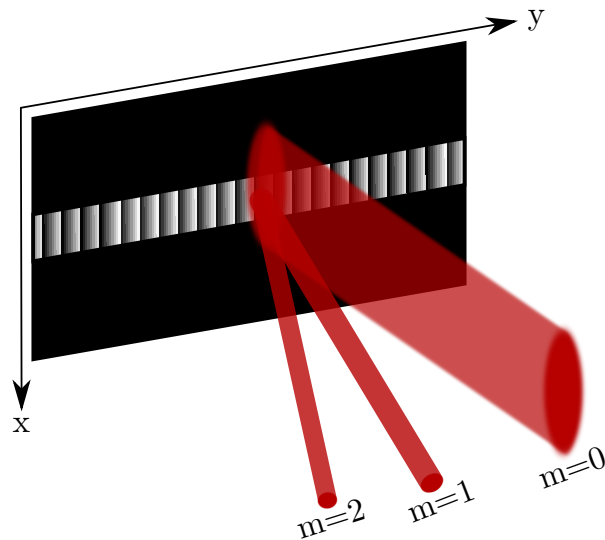
$$\theta_m = \theta_i + m \frac{\lambda}{\Lambda}, \quad m \in \mathbb{Z}.$$

Thus, the smaller the period of the phase function, the larger is the separation between two consecutive diffracted beams. However, the period, and consequently the beam separation, is limited by the SLM pixel size. The relative power in each diffraction order is determined by the shape of the phase function.

Now, let us consider that the y -direction periodic phase is multiplied by a mask

$$M(x) = \begin{cases} 1 & x \in R \\ 0 & \text{otherwise,} \end{cases}$$

that is, the mask vanishes outside the region R of the x axis, which could be the union of several disconnected intervals. An example of the resultant phase pattern is shown in Fig. 1.11. The effect is to select the portion of the beam incident in the desired region, that is, the beam falling outside R is reflected to the zero order of diffraction and the higher orders of diffraction contain only the beam incident inside R . Different mask functions may also be used, allowing for a more general amplitude modulation. The diffraction grating can also be summed to any other phase function varying with the x coordinate, such that this coordinate can be independently manipulated. The advantage of using only the higher order diffracted beams is to ensure that the whole beam has been modulated, otherwise it would not be diffracted. However, it is worth noting that this application of an SLM only works for beams linearly polarized in the direction of the LC molecules, and thus cannot be used in experiments which tangle polarization and spatial degrees of freedom.



?figurename? 1.11.: SLM used as an amplitude mask: only the portion of the incident beam (not shown in the picture) that hits the SLM in the graded region will be present in order $m \geq 1$ of diffraction. The beam with the order $m = 0$ of diffraction also contains the portion reflected in the non-graded region.

OPTICAL SIMULATION OF THE FREE DIRAC EQUATION

In this chapter, I present a classical optics simulation of the one-dimensional Dirac equation for a free particle. For this purpose we use both discrete and continuous degrees of freedom. Positive and negative energy components are represented by orthogonal polarizations of a free propagating beam, while the spatial profile represents the spatial wave function of the particle. Using a completely tunable time parameter, we observed the oscillation of the average value of the Dirac position operator—known as *Zitterbewegung* (ZB). We are also able to measure the so called mean-position operator which is a single-particle observable and presents no oscillations. Our work opens the way for optical simulation of interesting phenomenon of relativistic systems, as well as condensed-matter physics, without any requirement for specially engineered medium.

This work was done in collaboration with Ardiley T. Avelar, Rafael M. Gomes and Emile R.F. Taillebois from Federal University of Goiás, and Stephen P. Walborn. My contribution to this work was devising the simulation protocol, designing the experiment, setting the experiment up, and also to do the data analysis and help writing the paper which is now published in Phys. Rev. A [47].

2.1. Introduction

Although the Dirac equation [48] represents a historical landmark in the quantum description of relativistic systems – satisfactorily explaining the origin of spin and predicting the existence of antimatter [49] – it still provokes a lot of discussion about its interpretation, even when applied to describe the simplest physical system, that is, a free particle. In this case, the Dirac equation predicts intriguing phenomena, for instance the ZB [50] and Klein’s paradox [51], which impede the single-particle (SP) interpretation of the Dirac equation. As fundamental ef-

fects in the understanding of relativistic influence over quantum theory, they have contributed to the transition to the many-body quantum field approach [52].

The important technical difficulties involved in the direct observation of several relativistic quantum predictions have led to an increased interest in their simulations in trapped ions [53, 54], photonic crystals [55], confined light [56], graphene [57], optical superlattices [58], Bose-Einstein condensates [59, 60] and ultracold atoms [61]. Among the unexpected effects of Dirac equation, the ZB – the flickering motion of a free relativistic quantum particle described by a Dirac wavefunction with positive and negative energy components – is one of most investigated due to its interesting counterintuitive nature.

From a SP perspective, Dirac's equation must be interpreted as the simultaneous solving of two independent problems, for instance, the single free evolution of both electron (positive energy sub-space) and positron (negative energy sub-space). Therefore, there is no meaning in assigning a physical interpretation to an operator that is not SP, that is, an operator that mixes positive and negative subspaces. In the SP approach, physical results must be obtained by projecting SP observables over the subspace corresponding to the problem of interest. Despite the previous studies [53, 58, 60], an important feature was not explored: the Dirac position operator related to the flickering motion is not a SP observable, i.e. it cannot be written as the direct sum of its positive and negative energy projections.

For Dirac's theory, a SP position observable exists and is obtained using the so-called Foldy–Wouthuysen transformation (FWT) [62] – a momentum dependent unitary transformation that diagonalizes Dirac's Hamiltonian and is at the kernel of important algorithms used to obtain quantum relativistic corrections [63, 64]. This observable is often called mean-position operator and does not exhibit the oscillatory behavior characteristic of the ZB, a result that generates doubts concerning its actual existence.

Here, the simulation of the Dirac one-dimensional free evolution and the ZB is performed using the transverse degrees of freedom of a paraxial light beam, where different components of the spinor are represented by different polarization components of the beam. This physical setup is well suited for the purpose of quantum simulation, as it allows for implementation of the dynamical phases with easy tuning of the important physical parameters [38]. Besides being a proof-of-concept for the optical simulation of Dirac particles, the present approach differs from others in the theoretical procedure adopted to perform the simulation. Previous works perform a direct simulation of the 1+1D Dirac Hamiltonian, while the present approach performs the evolution in the diagonalized Foldy–Wouthuysen representation (FWR) and permits one to switch back and forth between this and Dirac's representation, allowing us to investigate the behavior of both the Dirac position and the mean-position operators.

2.2. Dirac Equation and position operator

Consider the 1D Dirac equation

$$i\hbar\frac{\partial}{\partial t}\psi_D = \hat{\mathcal{H}}_D\psi_D = (c\hat{p}\sigma_1 + mc^2\sigma_3)\psi_D, \quad (2.1)$$

where c is the speed of light, \hat{p} is the momentum operator, m is the mass of the particle, and σ_i are the usual Pauli matrices. The information of this system is encoded in the spinor ψ_D that has only two components which are related to positive and negative energy states in the particle's rest frame, i.e. spin degrees of freedom are eliminated by the dimensional constrain [65]. In Dirac's coordinate representation, the momentum operator \hat{p} assumes the usual form $-i\hbar\frac{\partial}{\partial x}$, where x is the so-called Dirac coordinate associated to the multiplication operator $\hat{x}_D\psi_D(x) = x\psi_D(x)$. Since the Hamiltonian operator is not diagonal in this representation, the positive and negative energy eigenstates are non-trivial and assume, respectively, the forms $\psi_p^+(x, t) = u(p)e^{-i\varepsilon(p)t/\hbar}e^{ipx/\hbar}$ and $\psi_p^-(x, t) = v(p)e^{i\varepsilon(p)t/\hbar}e^{-ipx/\hbar}$, with $\varepsilon(p) \equiv \sqrt{(mc^2)^2 + (pc)^2}$, $u(p) = [2mc^2(\varepsilon(p) + mc^2)]^{-1/2} (\varepsilon(p) + mc^2 \quad cp)^T$ and $v(p) = [2mc^2(\varepsilon(p) - mc^2)]^{-1/2} (cp \quad \varepsilon(p) - mc^2)^T$.

The non-diagonal form of $\hat{\mathcal{H}}_D$ in Dirac's representation is evinced by the commutator $[\hat{\mathcal{H}}_D, \hat{x}_D] = -i\hbar c\sigma_1$ and leads to the Heisenberg picture evolution given by [66]

$$\hat{x}_D(t) = \hat{x}_D(0) + c^2\hat{p}\hat{\mathcal{H}}_D^{-1}t - \frac{c\hbar\hat{\mathcal{H}}_D^{-1}}{2i} (e^{2i\hat{\mathcal{H}}_Dt/\hbar} - 1) (c\hat{p}\hat{\mathcal{H}}_D^{-1} - \sigma_1). \quad (2.2)$$

The first two terms on the right represent the expected linear time evolution of a free particle, the last term being associated to the ZB. This flickering motion is accompanied by other particularities of the \hat{x}_D operator. Indeed, the evolution given in (2.2) is derived from the equation of motion $\dot{\hat{x}}_D = \frac{i}{\hbar}[\hat{\mathcal{H}}_D, \hat{x}_D] = c\sigma_1$, which implies that, although $\langle \hat{x}_D \rangle = \langle c^2\hat{p}\hat{\mathcal{H}}_D^{-1} \rangle$, the eigenvalues associated to the velocity $\dot{\hat{x}}_D$ are restricted to $\pm c$, a remarkable result which contributes to raise doubts as to the correct interpretation of \hat{x}_D as definition of position. These peculiarities of the operator \hat{x}_D arise from the fact that this is not a SP observable, i.e. $\hat{x}_D \neq \hat{P}_+\hat{x}_D\hat{P}_+^\dagger + \hat{P}_-\hat{x}_D\hat{P}_-^\dagger$, where $\hat{P}_\epsilon = \frac{1}{2mc^2} \begin{pmatrix} mc^2 + \epsilon\varepsilon(p) & -\epsilon cp \\ \epsilon cp & mc^2 - \epsilon\varepsilon(p) \end{pmatrix}$ is the projection operator over the subspace of states with energy sign ϵ .

To obtain a SP position, the FWT must be applied to diagonalize the Dirac Hamiltonian. For the 1D Dirac free particle, this canonical transformation is given by the momentum dependent unitary operator

$$\hat{U}(\hat{p}) = e^{i\hat{S}(\hat{p})}, \quad \text{with } \hat{S}(\hat{p}) \equiv \frac{\sigma_2}{2} \text{tg}^{-1} \left(\frac{\hat{p}}{mc} \right). \quad (2.3)$$

In the resulting FWR, the original Dirac Hamiltonian is given by $\hat{\mathcal{H}}'_D = \sigma_3 \varepsilon(\hat{p})$, and the former \hat{x}_D operator by $\hat{x}'_D = \hat{x}_{FW} + \frac{\hbar mc^3}{2\varepsilon(\hat{p})^2} \sigma_2$, where \hat{x}_{FW} is the new multiplication operator in the FWR. The operator \hat{x}_{FW} is the so called mean-position operator and, unlike the operator \hat{x}_D , it is a SP observable since $\hat{x}_{FW} = \hat{P}'_+ \hat{x}_{FW} \hat{P}'_+ + \hat{P}'_- \hat{x}_{FW} \hat{P}'_-$, where $\hat{P}'_\epsilon = \begin{pmatrix} \delta_{\epsilon+} & 0 \\ 0 & \delta_{\epsilon-} \end{pmatrix}$ are the energy projectors in the new representation.

Aside from being SP, the operator \hat{x}_{FW} also satisfies the equation $\dot{\hat{x}}_{FW} = c^2 \hat{p} \hat{\mathcal{H}}'_D$, resulting in the Heisenberg picture evolution [66]

$$\hat{x}_{FW}(t) = \hat{x}_{FW}(0) + c^2 \hat{p} \hat{\mathcal{H}}'^{-1}_D t \quad (2.4)$$

that is linear in time, as expected for a free particle. Thus, as stated before, the ZB does not occur for this operator.

Here, as a proof-of-concept for the simulation of relativistic systems using free propagating light beams, the simulation of both the Dirac and FWRs will be performed in a single setup. This difference with other simulation procedures open the possibility for future investigations on more complex FWTs associated to relativistic scenarios involving interactions.

2.3. Simulation Protocol and Experiment

One way to simulate the dynamics associated to Eq. (2.1) is to directly implement the evolution operator $\exp\left(-\frac{i\hat{\mathcal{H}}_D t}{\hbar}\right)$, which is usually a tough task due to the non-diagonal character of $\hat{\mathcal{H}}_D$. This difficulty can be overcome by using the FWT, since this transformation allows the time evolution operator to be written as $\exp\left(-\frac{i\hat{\mathcal{H}}_D t}{\hbar}\right) = \hat{U}^{-1}(\hat{p}) \exp\left(-\frac{i\hat{\mathcal{H}}'_D t}{\hbar}\right) \hat{U}(\hat{p})$, and $\hat{\mathcal{H}}'_D$ is a diagonal operator. This operator can be implemented in an optical beam by considering the vertical coordinate on the transverse plane as the particle's position and the horizontal (vertical) polarization as the superior (inferior) component of the spinor. The horizontal spatial degrees of freedom on the transverse plane play no relevant role in the experiment. Although a spinor is a mathematical object which transforms very specifically under a reference frame change, it is not a concern for this simulation since the reference frame is assumed to be fixed.

The optical transformations required for the simulation are polarization transformations (acting as nondiagonal operators) and phase shifts (used to introduce momentum dependent phases). The former are obtained with the suitable application of wave plates and the last are realized by SLMs, which are able to imprint programmable position dependent phases $\exp[i f(x, y)]$ in the horizontal polarization. The momentum-dependent phases are applied in the momentum space defined as the optical Fourier transform of the position space where the initial state is prepared. The position plane is shown as a dashed line in Fig. 2.1, the SLMs are placed such that the optical Fourier transform connects position and momentum planes as

presented in Sec. 1.3.1. The action of a quarter wave plate (QWP) set to 45° is given by the operator $\hat{Q} := Q\hat{W}P(45^\circ) = e^{i\frac{\pi}{4}}/\sqrt{2}(\mathbb{1} - i\sigma_1)$ [see Eq. (1.5)], while $\hat{H} := H\hat{W}P(45^\circ) = \sigma_1$ describes a half wave plate at 45° [see Eq. (1.4)]. The action of a SLM is equivalent to applying $\hat{P}[f(x, y)] = \exp[i f(x, y)]\sigma_+\sigma_- + \sigma_-\sigma_+$ over the transverse profile spinor., as can be seen from Eq. (1.38). Using this operator representation for the optical devices, it follows that the operator (2.3) can be written in momentum representation as

$$\hat{U}(p) = \hat{Q}\hat{P}[-\theta(p)]\hat{H}\hat{P}[\theta(p)]\hat{Q}, \quad (2.5)$$

with $2\theta(p) = \tan^{-1}\left(\frac{p}{mc}\right)$. We express the inverse FWT in an analogous fashion. As the Hamiltonian is diagonal in the FWR, the transformed time evolution operator is achieved via the application of the dynamical phase $\exp[\pm it\varepsilon(p)/\hbar]$ in each spinor component using waveplates and the SLM, which concludes the simulation. A summary of the analogy between the optical simulator and the simulated system is given in Table I.

Table 2.1.: Summary of the optical analogy

Optical System	Simulated System
Vertical transverse position	x
Transverse profile of horizontal polarization	$\psi_{D_1}(x)$
Transverse profile of vertical polarization	$\psi_{D_2}(x)$
QWP@ 45°	$\hat{Q} = e^{i\frac{\pi}{4}}/\sqrt{2}(\mathbb{1} - i\sigma_1)$
HWP@ 45°	$\hat{H} = \sigma_1$
SLM printing phase $f(x, y)$	$\hat{P}[f(x, y)] = \exp[i f(x, y)]\sigma_+\sigma_- + \sigma_-\sigma_+$
Normalized horizontal polarization intensity at x	$ \psi_{D_1}(x) ^2$

The experimental scheme is shown in Fig.2.1. A He-Ne laser with wavelength 632.8 nm and two Holographic reflective SLMs, each of which divided into halves to operate twice, are used. As in this experiment we use both vertical and horizontal polarizations, we need to use the zero order diffraction of the SLM although not all the light is modulated in this order. The Fourier transforms are made by plano-convex cylindrical lenses with 150 mm focal distance such that the position space (mirrors and camera) is in one focal plane and the momentum space is in the opposite focal plane where the SLM is located. The reason to use cylindrical lenses is that only the vertical transverse coordinate is used and thus only this direction must be transformed. The momentum p and the position on the SLM, X , are connected by $X = \frac{\lambda f}{h}p$, where f is the focal distance and λ is the laser wavelength [39]. In terms of X , the applied

phases become $2\theta(X) = \tan^{-1}\left(\frac{h}{mc} \frac{X}{\lambda_f}\right)$ and $t\varepsilon(p)/\hbar = 2\pi t \sqrt{\left(\frac{X}{\lambda_f}\right)^2 + \left(\frac{mc}{h}\right)^2}$, so the parameters we need to set are the speed of light c and the Compton wavelength $\lambda_C = h/mc$, which are easily tunable since they enter as programmable parameters in the imprinted phases. Notice that contrary to what is usual in optical simulations [38], the time in our simulation does not correspond to the propagation distance of the beam as it would come in a direct analogy between Schrödinger and paraxial Helmholtz equations [67]. Since the time coordinate also comes up as a programmable parameter, we could in principle take measurements for as many time values as we wish inside a time interval. This also implies that the unit of measurement for time is an arbitrary τ . In this realization we chose $\Delta t/\tau = 1$.

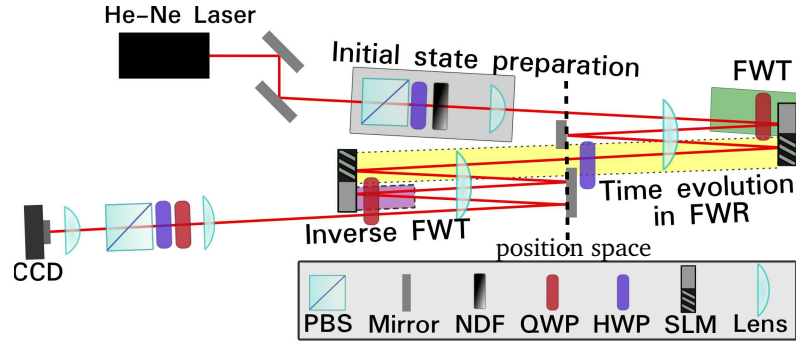


Figure 2.1.: A He-Ne laser, prepared with an initial gaussian profile and anti-diagonal polarization state, is sent through an optical system designed to implement the Dirac Hamiltonian. The grey shaded regions of the SLMs implement the FWTs, while the striped regions implement the free-evolution. Lenses are used to map the field profile among the different planes of the SLMs, and wave plates to control the polarization state. A CCD camera is used to register the intensity profile of the output field. Additional details are provided in the text.

The laser produces a Gaussian spatial profile separable in the x and y coordinates, so the initial spinor is

$$\psi_D(x, t = 0) = \frac{e^{-i\pi x^2/(\lambda R)} e^{-x^2/(4\Delta^2)}}{(\sqrt{2\pi}2\Delta)^{1/2}} \begin{pmatrix} a \\ b \end{pmatrix}, \quad (2.6)$$

where a and b are the normalized horizontal and vertical polarization coefficients ($|a|^2 + |b|^2 = 1$), Δ is the beam width in the vertical direction, and R is the vertical radius of curvature of the beam in the initial position plane. The propagation and Gouy terms of the Gaussian beam only introduce global phases which do not affect the dynamical evolution [39]. We start with $a = -b = 1$, but changing a and b would enable us to prepare different positive and negative energy superpositions. Two cylindrical lenses are placed before the first position space in order to manipulate the initial momentum distribution which depends on R and therefore on Δ . Using a beam profiler, we determined the initial state parameters to be $\Delta = 48,6 \mu m$ and $\lambda R/\pi = (2.2\Delta)^2$.

The average position of the simulated particle is calculated as

$$\langle \hat{x}_D \rangle(t) = \sum_{i=1,2} \int dx x |\psi_{Di}(x, t)|^2,$$

where $|\psi_{Di}(x, t)|^2$ is proportional to the light intensity of polarization component i at position x on the transverse plane measured by a CCD camera placed at the output position space. Each instant of time corresponds to one programmable-phases configuration and one intensity-profile measurement. It is worth noting that the evolved state is accessible for any time value.

2.4. Results

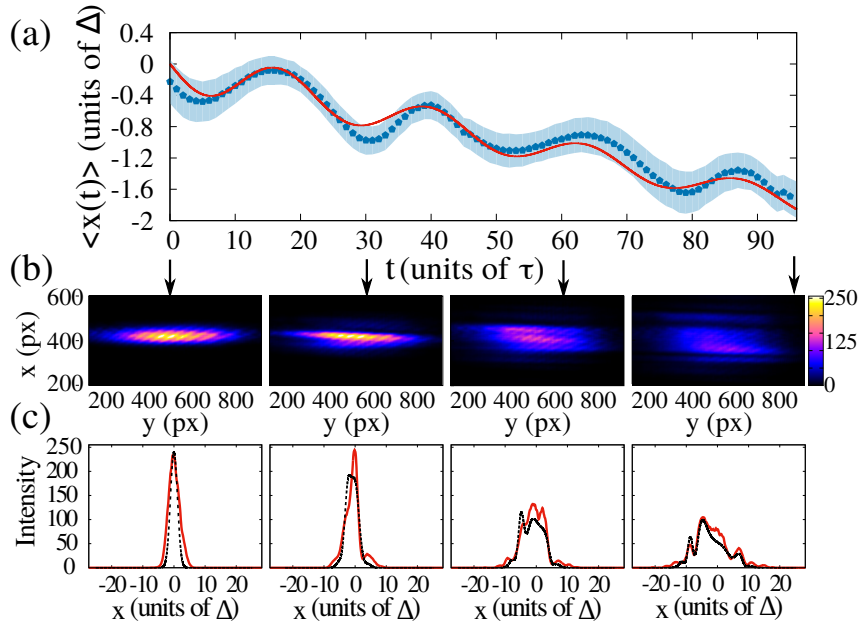


Figure 2.2.: (a) Mean position $\langle \hat{x}_D \rangle(t)$ as a function of the time parameter t for Compton length $\lambda_C/\Delta = 5$. Points are experimental data, the dashed line is the numerical solution and filled band is the experimental error of one σ . (b) The camera image and (c) the one dimensional state got from marginalizing the intensity measured by the camera over y for four values of the parameter t , namely $t/\tau = 0, 30, 60$ and 95 , are shown. In (c) red solid lines are experimental data and black dashed curves are numerical solutions.

A summary of our experimental procedure for the particular case $\lambda_C = 5\Delta$ is depicted in Fig.2.2. In Fig.2.2-a we present the mean position $\langle \hat{x}_D \rangle(t)$ as a function of t , the ZB being evidenced by the oscillatory behavior. The solid red line is the theoretical prediction, while points are experimental results obtained from the images shown in Fig.2.2-b). The shaded region represents uncertainty of one σ . Fig.2.2-b) shows samples of the data collected by the CCD camera for some instants of time, the x distribution being obtained by considering only

a fixed y coordinate at the center of the beam. The x distributions used to calculate $\langle \hat{x}_D \rangle(t)$ are shown in Fig.2.2-c). This procedure assumes that x and y intensity distributions remain separable throughout all the apparatus. This is true in the ideal case, however the cylindrical lenses can introduce some non-separability as one can see in the slightly tilted elliptical intensity pattern shown in Fig. 2.2-b). The non-separability causes the initial state to be not entirely pure. Since our experimental results agree well with theory, we conclude that these effects are negligible for the present experiment.

For a fixed initial state and speed of light $c = 0.1 \Delta/\tau$, we measured the average position in Dirac's representation for different values of the Compton wavelength, as shown in Fig.2.3. We fitted the average position with the function $vt + A \sin(\omega t + \delta)$ for each λ_C to estimate the mean velocity, amplitude and frequency of the oscillation. These quantities are shown in Fig.2.4. Our experimental results are in agreement with the expected linear dependence of amplitude and inverse dependence of frequency on λ_C ¹, as can be seen in Fig.2.4-b). This is consistent with the fact that the ZB visibility in Fig.2.3 increases for smaller values of λ_C .

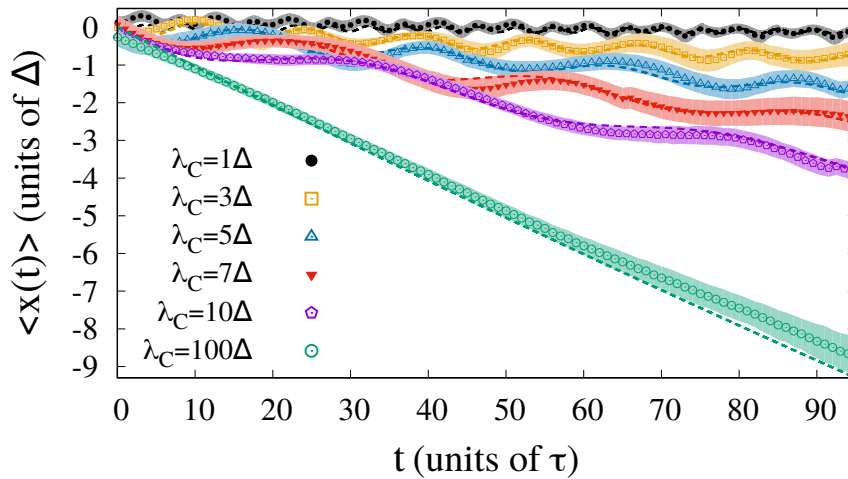


Figure 2.3.: Average position $\langle \hat{x}_D(t) \rangle$ as a function of the time parameter t for Compton lengths $\lambda_C/\Delta = 1, 3, 5, 7, 10, 100$. Dashed lines are numerical predictions of the theory using Eq. (2.1), while points are experimental results. The filled bands are experimental errors of one σ .

The different inclinations exhibited in Fig.2.3 are due to the fact that each mass, i.e. Compton wavelength, is associated to a different velocity distribution, even the momentum distribution being the same for all values of λ_C . Although the initial state (2.6) has zero average momentum, this is not true for the mean velocity in Fig.2.4-a). As is expected, the mean velocity falls quadratically with λ_C for large masses (small λ_C), while it is close to the speed of light for very small masses ($\lambda_C = 100$).

¹From Eq.(2.2) we have that the amplitude of oscillations for a given momentum eigenstate is proportional to $ch/\epsilon(p)$, which for small λ_C , i.e., large mass, can be approximated by λ_C . On the other hand, the frequency is proportional to $\epsilon(p)/h$, that approaches c/λ_C for large masses.

The agreement between the experimental ZB data and the theoretical predictions confirm that our optical setup is well suited for the study of 1+1D relativistic dynamical systems, the theoretical extension to larger dimensions being discussed in the Sec. 2.5. Beside serving as a proof-of-concept, the proposed setup permits to investigate the system in the FWR, an interesting possibility since it allows to describe the dynamics of the system according to the single-particle perspective, i.e. assigning physical sense only to the projections of single-particle operators over the subspaces of definite sign of energy.

From the SP perspective, operators that are not block-diagonal in the FWR, as is the case for \hat{x}_D , have no physical meaning, since they mix components of positive and negative energy that are associated to two distinct problems. On the other hand, operators that are block-diagonal in the FWR, as \hat{x}_{FW} or the Dirac Hamiltonian, may have a physical sense assigned to their positive and negative projections. In this sense, the correct description of the dynamics of a single electron (positron), for example, should be given by $\hat{x}_{FW,+} = P'_+ \hat{x}_{FW} P'_+$ ($\hat{x}_{FW,-} = P'_- \hat{x}_{FW} P'_-$). In our setup, the average $\langle \hat{x}_{FW} \rangle$ measured using both positive and negative components of the spinor can be obtained by measuring the transverse profile of the beam before the inverse FWT. However, since the positive and negative components of the spinor are encoded in the horizontal and vertical polarizations of the beam in the FWR, the single-particle position dynamics described by $\hat{x}_{FW,+}$ (particle) and $\hat{x}_{FW,-}$ (anti-particle) is also accessible by simply selecting one of the polarizations prior to the CCD measurement in the FWR.

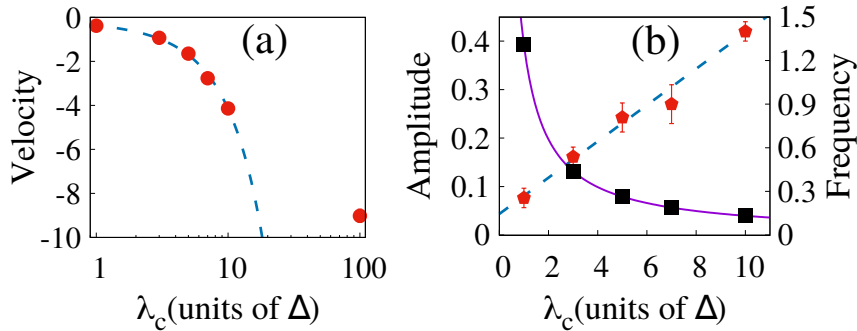


Figure 2.4.: (a) Mean velocity, (b) amplitude (red circles) and frequency (black squares) of ZB obtained by fitting a sinusoidal function to the average position $\langle \hat{x}_D(t) \rangle$ for each Compton wavelength. For small values of Compton wavelength (large masses) the mean velocity falls quadratically with λ_C (dashed blue line) and for a large value of Compton wavelength (vanishing mass) it approximates the speed of light set on the experiment. The amplitude dependence with λ_C is in well agreement with linear behavior (dashed blue line) while frequency is proportional to $1/\lambda_c$ (solid purple line).

Experimental results for the mean-position operator are shown in Fig. 2.5 for $\lambda_C = 5\Delta$. The experimental data concerning the ZB effect for the \hat{x}_D operator is also plotted for comparison (blue points). Measurements of $\langle \hat{x}_{FW,+}(t) \rangle$ and $\langle \hat{x}_{FW,-}(t) \rangle$ are shown as black dots. As is expected from the independence of the two problems in the SP description, we

have two independent mean trajectories corresponding to the free evolution of the particle and the corresponding anti-particle. The ZB is not present for these mean trajectories and a linear behavior in time is observed, as it was expected. As mentioned earlier, we were also able to measure the mean value of the FW mean-position operator \hat{x}_{FW} . The results are plotted as the red circles and represent an average of the positive and negative projections cases. The small deviation from a perfect linear behavior can be explained assuming that the SLMs do not modulate all the incident light but a fraction of it, as is shown in the inset picture which shows the same mean values as the experimental plot but obtained from a numerical simulation of the experiment for modulation efficiency of 95% in each SLM.

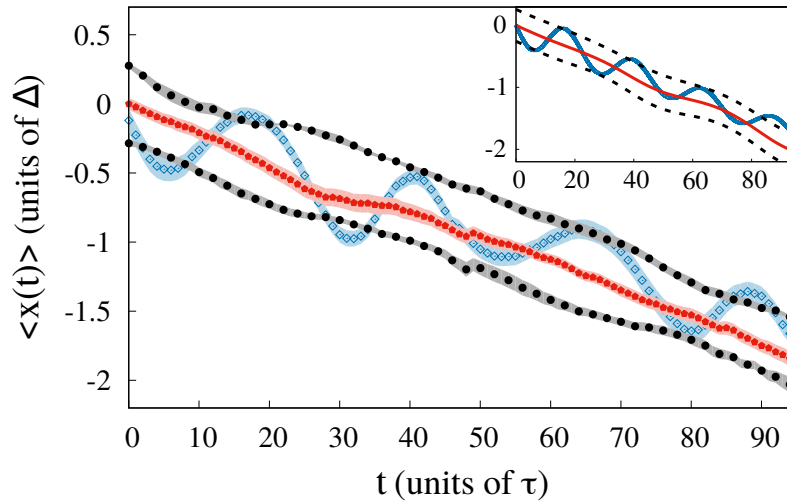


Figure 2.5.: Experimental mean positions $\langle \hat{x}_D(t) \rangle$ (blue dots) and $\langle \hat{x}_{FW}(t) \rangle$ (red circles) for $\lambda_C/\Delta = 5$. Measurements of $\hat{x}_{FW}(t)$ projected over positive energy components (horizontal polarization in FWR) as well as negative energy components (vertical polarization in FWR) are shown as black dots. The shaded regions are the mean value uncertainties. The $\langle \hat{x}_{FW}(t) \rangle$ data presents no ZB and fits a linear dependence with $R^2 = 99.6\%$. The inset picture shows the result of a numeric simulation of the experimental setup assuming ideal devices except that the SLMs have efficiency of 95%.

2.5. More spatial dimensions and potentials

The goal of this section is to show the simulation protocols for particles in two and three spatial dimensions. Because we use the transverse spatial degrees of freedom of a light beam, we only have at disposal two coordinates to play the role of particle position. Also, the polarizations used as spinor components, allows us to simulate only a two-components spinor. Thus, this restricts our simulation protocol to one and two spatial dimensions, the last one is presented in Section 2.5.1. Despite the apparent impossibility of simulating a particle existing in a three dimensional space using our scheme, in Section 2.5.2 we show that the simulation is

possible for some particular cases.

Finally, it would be desirable to include interactions in the particle Hamiltonian. The drawback of using a simulation based on the FWT is that this transformation is not exact for most of the potential functions [62]. But for a particular class of potentials it is possible to include interactions in our simulation as we show in Section 2.5.3.

2.5.1. Simulation of 2+1 dimensional Dirac Equation

Consider the Dirac Hamiltonian for a free particle existing in a 2D space

$$H = c(\sigma_1 p_x + \sigma_2 p_y) + mc^2 \sigma_3. \quad (2.7)$$

The unitary transformation $e^{iS_2} = e^{-i \frac{\sigma_1 p_x - \sigma_2 p_y}{|\mathbf{p}|} \theta(\mathbf{p})}$ is the FWT which diagonalizes the Hamiltonian in this case, with $\theta(\mathbf{p}) = \frac{1}{2} \text{tg}^{-1} \frac{|\mathbf{p}|}{mc}$. For the same reasons as in the 1D situation, there is no spin if the space is restricted to two dimensions and the particle state is a spinor with two components. Once we manage to construct FWT from optical device operators, the simulation protocol is made possible identifying again the transverse profile of a laser beam in the two orthogonal polarizations with the spinor components and identifying the two transverse coordinates with particle position. To show that in fact there is such a decomposition let us define a new momentum dependent phase

$$\theta'(\mathbf{p}) = \begin{cases} \text{tg}^{-1}(p_y/p_x), & p_y > 0 \text{ or } p_y = 0, p_x > 0 \\ \pi + \text{tg}^{-1}(p_y/p_x), & p_y < 0 \text{ or } p_y = 0, p_x < 0, \end{cases} \quad (2.8)$$

motivated by the polar expression $p_x - ip_y = |\mathbf{p}|e^{-i\theta'}$. In terms of the two phase functions the FWT reads

$$e^{iS_2} = \begin{pmatrix} \cos \theta(\mathbf{p}) & e^{-i\theta'} \sin \theta(\mathbf{p}) \\ -e^{i\theta'} \sin \theta(\mathbf{p}) & \cos \theta(\mathbf{p}) \end{pmatrix}. \quad (2.9)$$

Using the definitions given in the main text it is easy to see that the operator sequence

$$\hat{P}[-\theta'(\mathbf{p})] \hat{Q} \hat{P}[-\theta(\mathbf{p})] \hat{H} \hat{P}[\theta(\mathbf{p})] \hat{Q} \hat{P}[\theta'(\mathbf{p})]$$

is equal to the FW unitary. The transformed diagonalized time evolution is then given by the product $\hat{H} \hat{P}[i\varepsilon(\mathbf{p})t/\hbar] \hat{H} \hat{P}[-i\varepsilon(\mathbf{p})t/\hbar]$. Just to conclude the protocol, the inverse FWT is given analogously by the same set of devices as the FWT with different imprinted phases and different angles for the wave plates.

2.5.2. Simulation of 3+1 dimensional Dirac Equation for a particular class of initial states

Let us consider the 3+1 Dirac equation

$$i\hbar \frac{\partial \psi(\mathbf{x}, t)}{\partial t} = [c\boldsymbol{\alpha} \cdot \mathbf{p} + mc^2\beta] \psi(\mathbf{x}, t) \quad (2.10)$$

with the standard choice of Dirac matrices $\beta = \begin{pmatrix} \mathbb{1}_{2 \times 2} & 0 \\ 0 & -\mathbb{1}_{2 \times 2} \end{pmatrix}$, $\alpha_k = \begin{pmatrix} 0 & \sigma_k \\ \sigma_k & 0 \end{pmatrix}$. The four components of the spinor $\psi(\mathbf{x}, t)$ accounts for the two signs of the energy and for the two spin projections along a fixed direction. The FWT reads $e^{iS_3} = \cos \theta(\mathbf{p}) + \beta \frac{\boldsymbol{\alpha} \cdot \mathbf{p}}{|\mathbf{p}|} \text{sen } \theta(\mathbf{p})$ with the same definition for $\theta(\mathbf{p})$ as before.

A general simulation of the above equation, besides of requiring a four dimensional object to emulate the four spinor components, it would also require three spatial degrees of freedom, while the presented setup allows for just two. Instead of proposing a complete simulation, let us consider only the particular family of initial states given by

$$\psi(\mathbf{x}, t = 0) = \begin{cases} \frac{1}{\sqrt{L}} \begin{pmatrix} \tilde{\phi}_1(x, y) \\ \vdots \\ \tilde{\phi}_4(x, y) \end{pmatrix} & -\frac{L}{2} < z < \frac{L}{2} \\ 0 & \text{elsewhere} \end{cases}. \quad (2.11)$$

In momentum space this state becomes

$$\tilde{\psi}(t = 0, \mathbf{p}) = \begin{pmatrix} \tilde{\phi}_1(p_x, p_y) \\ \vdots \\ \tilde{\phi}_4(p_x, p_y) \end{pmatrix} \sqrt{\frac{L}{2\pi\hbar}} \left(\frac{\text{sen } \frac{p_z L}{2\hbar}}{\frac{p_z L}{2\hbar}} \right), \quad (2.12)$$

which dependence on p_z behaves like a $\delta(p_z)$ for large values of L .

Thus we can approximate the FW transformed state by

$$\tilde{\psi}'(\mathbf{p}, t = 0) \approx \left(\cos(\theta(p_x, p_y, 0)) + \beta \frac{\alpha_x p_x + \alpha_y p_y}{|(p_x, p_y, 0)|} \text{sen } \theta(p_x, p_y, 0) \right) \tilde{\psi}(\mathbf{p}, t = 0), \quad (2.13)$$

and all the momentum dependent phases only depend on two coordinates and can be applied with SLMs.

The transformed state is explicitly written as

$$\psi'(\mathbf{p}, t = 0) = \begin{pmatrix} \cos \theta & 0 & 0 & \frac{p_x - ip_y}{|\mathbf{p}|} \text{sen } \theta \\ 0 & \cos \theta & \frac{p_x + ip_y}{|\mathbf{p}|} \text{sen } \theta & 0 \\ 0 & \frac{-p_x + ip_y}{|\mathbf{p}|} \text{sen } \theta & \cos \theta & 0 \\ \frac{-p_x - ip_y}{|\mathbf{p}|} \text{sen } \theta & 0 & 0 & \cos \theta \end{pmatrix} \begin{pmatrix} \phi_1 \\ \phi_2 \\ \phi_3 \\ \phi_4 \end{pmatrix} \sqrt{\frac{L}{2\pi\hbar}} \left(\frac{\text{sen } \frac{p_z L}{2\hbar}}{\frac{p_z L}{2\hbar}} \right) \quad (2.14)$$

we notice that the FWR only mixes the components two by two what makes possible to simulate it using two beams without any joint transformation between them. Then we can address the transverse profiles of horizontal and vertical polarizations of the first beam to ϕ_1 and ϕ_4 and the FWR as well as the subsequent diagonal time evolution do not mix this components with the two remaining. Moreover, each pair of mixed components transforms like the two spatial dimensions case (Eq. (2.9)) with the suitable phase signs.

The interesting thing about three spatial dimensions simulation is that it would enable us to investigate also spin effects like the spin analogous to *Zitterbewegung*.

2.5.3. Simulation of 1+1 dimensional Dirac Equation for a particular class of potentials

Employing the strategy of [68], we show in this subsection that, if the initial state is conveniently prepared, our approach is able to simulate the Dirac equation for a particular class of potentials. To this end, consider the 1D Dirac equation

$$i\hbar \frac{\partial}{\partial t} \psi_D = (c\hat{p}\sigma_1 + mc^2\sigma_3 + V(x))\psi_D, \quad (2.15)$$

where $V(x)$ is a spinorial potential of the form

$$V(x) = V_1(x)\sigma_1. \quad (2.16)$$

For the above particular case, we define ϕ_D such that

$$\psi_D = e^{-i\frac{1}{\hbar c} \int V_1(x') \mathbb{1} dx'} \phi_D. \quad (2.17)$$

The substitution of this state on Eq.(2.15) shows that the spinor ϕ_D evolves according to the free Dirac equation (Eq.(2.1)). Thus, if we want to simulate the time evolution of the initial state $\psi_D(x, t = 0)$, we need to prepare the state $\phi_D(x, t = 0) = \exp \left[i\frac{1}{\hbar c} \int V_1(x') \mathbb{1} dx' \right] \psi_D(x, t = 0)$ and the dynamics of the free evolution. From the experimental point of view, this corresponds to applying a local phase in position space to all the components of the spinor before performing the free evolution in the way as it is shown in the main text.

2.6. Discussion and Conclusions

Our experiment demonstrates how relativistic dynamics can be studied using classical optics, and opens the way to more sophisticated investigations. For this purpose it would also be desirable to produce more general initial states. This can be accomplished using intensity and phase masks in the initial state preparation. The state produced in this experiment had zero average momentum, but simply shifting the momentum in all SLMs phases by the same Δp can be interpreted as if the state has non-vanishing average momentum.

In principle the method implemented in this simulation using the FWT could be applied for other simulation schemes of the Dirac equation, however this transformation requires applying a phase shift that is proportional to the inverse tangent of momentum. In our approach the application of this phase is fairly easy, thanks to the spatial light modulator (SLM). However, in other systems, this is quite challenging. Typically in continuous variable quantum simulators one can implement Gaussian Hamiltonians, but non-Gaussian operations (third order and above) are quite difficult [37]. Thus, we believe that our approach is quite interesting in this regard, as it allows one to employ the FWT and investigate relevant aspects of it.

Albeit here we focused 1+1D case, the extension for 2+1D and for some initial states in 3+1D is straightforward as shown in the Sec. 2.5. The first is a direct extension considering the second transverse coordinate of the beam as the second spatial degree of freedom of the simulated particle. A 2+1D simulation also allows for investigation of electronic behavior in bidimensional condensed matter systems such as graphene [57], but still do not present any spin effect. For a general 3+1D simulation it would be necessary a third beam coordinate what is not available in this scheme. In spite of this limitation, we showed a class of initial states which dependence on the third coordinate does not alter the time evolution. In this case, the two extra spinor components are provided by the polarization components of a second beam.

It is well known that there is no exact FWT for the non-free Dirac equation, i.e., if we add a potential to the free Dirac equation (2.1) the Dirac Hamiltonian becomes no longer diagonalizable with one single unitary transformation [65]. This seems to be a very limiting factor of our simulation technique and indeed it is if we try to implement the actual FWT for a potential problem. Instead of doing so, we can try to find other kinds of unitary transformations which reproduce the time evolution and are experimentally feasible with the available optical elements. Up to now we know that at least for a particular class of potentials it is possible to break the time evolution operator into a position dependent phase which carries all the information about the potential followed by the free evolution presented in this work. This particular case was also discussed in Sec. 2.5.

In conclusion, we have presented an all-optical simulation of the dynamics of a one-dimensional relativistic free point particle, where the beam's spatial profile plays the role of the particle's wavefunction, and its orthogonal polarization components are associated to spinor

components. Our experiment is based on the diagonalization of the Dirac Hamiltonian using the FWT, which allowed for the decomposition of the unitary evolution into operations that are realizable with off-the-shelf optical components. Adjusting the tunable time parameter we observed the oscillatory ZB phenomenon for Dirac's position operator. Using our experimental FWT, we were also able to address this phenomenon from a single-particle perspective, where the position description is given by the positive and negative energy projections of the single-particle mean-position operator. This approach allowed us to observe the absence of ZB oscillations for the particle and anti-particle single-particle dynamical evolutions.

MUTUAL UNBIASEDNESS OF COARSE-GRAINED MEASUREMENTS FOR AN ARBITRARY NUMBER OF PHASE SPACE OBSERVABLES

Observables of continuous quantum variables can be made discrete by binning them together, resulting in an observable with a finite number d of outcomes. These operators allow one to reproduce some properties of measurements on discrete quantum systems. One example is mutual unbiasedness, which continuous variable operators satisfy only in limits that are unphysical, but physical discretized operators can satisfy perfectly, as in the discrete case. In this chapter, it is shown that binning of continuous observables can lead to operators that are in a sense neither continuous nor discrete. In particular, it is shown that the maximum number of mutually unbiased measurements is three for even d , which is analogous to the continuous case. However, for prime d we can find $d + 1$ mutually unbiased observables, surpassing the continuous case and in partial analogy to the discrete case. To illustrate this, an optical experiment is presented showing four mutually unbiased measurements with $d = 3$ outcomes. For odd non-prime d , it is shown theoretically that the maximum number of unbiased measurements follows neither the discrete nor the continuous regimes.

This work was done in collaboration with Łukasz Rudnicki from the Center for Theoretical Physics in Poland, Daniel Tasca from Fluminense Federal University, and Stephen Walborn. My contribution to this work is both theoretical and experimental. In the theoretical part, I showed the solution for the possible angle between phase space directions, showed that the pair dimensions are forbidden for 4 or more phase space directions, and also demonstrated the maximum number of directions in the odd dimension case. In the experimental part, I designed and built the experiment and made the data analysis. This work is being prepared for publication.

3.1. Introduction

Quantum physics separates itself from classical physics in a number of ways. One of these is the incompatibility of measurements, which lies at the heart of the complementarity principle [69], uncertainty relations [70], quantum contextuality [71], the violation of Bell's inequalities [72], quantum random number generation [73], among other topics. Mutual unbiasedness (MU) plays a fundamental role in incompatibility. Two observables are mutually unbiased if measurements of one observable on the eigenstates of the other observable produce a set of equiprobable outcomes. The bases of the underlying Hilbert space associated to two mutually unbiased observables are said to be mutually unbiased basis (MUB).

For practical purposes, it is of fundamental importance to know what is the maximum number of simultaneously MUBs for a given Hilbert space dimension and also how to build a set of MUBs with the maximum number of elements. By a set of simultaneously MUBs we mean that any pair of bases taken from the set satisfies MU conditions. Besides the fundamental mathematical interest in MU, many quantum information protocols rely on the use of more than two simultaneously MUBs. It is known, for example, that measuring a quantum system in the maximal set of MUBs is the minimal and optimal set of measurements to completely determine the quantum state of the system [74]. For a discrete variables system with dimension d , the maximum number of MUBs possible is $d + 1$. Although this upper bound is valid for any d , only if $d = q^m$, with q a prime number and m a positive integer, the maximal set with $d + 1$ elements is known to exist [74]. If d is not the power of a prime number, few things are known about the existence or construction of a MUB set even for the smallest dimension possible $d = 6$, and numerical [29, 75–78] as well as analytical [79, 80] evidences point to the existence of only three MUBs in this case .

In contrast to finite dimensional systems, continuous variables (CV) systems also have MUBs, the position and momentum operators bases being standard examples. However, instead of allowing for the construction of infinitely many simultaneously MUBs as would be if the limit of discrete case were valid, it allows for only three simultaneously MUBs [81]. On the other hand, because of the finite resolution of CV detectors and the impossibility of producing eigenstates of CV operators, the unbiasedness is not observed in practice. Recently, it was proposed that a periodic coarse graining (PCG) of the CV measurements can recover the unbiasedness relations if the period of the measurements in different phase space directions is adequately chosen [30]. In this scheme, the CV system is mapped to a effective DV system with dimension d equals to the number of possible outcomes of the measurement. In this case, it is referred to as mutually unbiased measurements (MUM) instead of bases. The natural questions are: *how many MUMs one can have in this PCG scheme? And knowing that a certain number of MUMs is possible, how to construct them? Is there a "scaling rule" as a function of d ? Do these measurements resemble more their continuous or discrete counterparts?* The previous

works showed the existence of pairs [30] and triples [82] of such PCG MUMs. Here we answer these questions, first providing a general recipe to construct mutually unbiased measurements (MUMs) together with their experimental realization in an optical setup. We then show that PCG observables display a behavior that is reminiscent of both continuous and discrete variables systems. For even dimensionality d , it is shown that there are at most three MUMs, as in the continuous case. On the other hand, for odd d there is some agreement with the discrete case. We show that for prime d there are at most $M = d + 1$ MUMs, like the discrete case. However, when d odd and not prime then there is no correspondence with neither the continuous nor the discrete case.

The chapter is organized as follows. In Sec. 3.2 the concept of MUBs in DV and CV variables is presented. In Sec. 3.3 the construction of PCG MUM of Ref. [30] is revised for only one pair of measurements. Our contribution is contained in Secs. 3.4 and 3.5 with a method to construct several PCG MUMs for any dimension parameter, including its experimental realization, and a proof of the maximum number of PCG MUMs depending on the number of outcomes, respectively. Sec. 3.6 concludes this chapter.

3.2. Mutually unbiased basis and measurements

Consider first a system with a finite dimensional Hilbert space which dimension is d . Consider also two orthonormal bases $\{|a_j\rangle\}_{j=0,\dots,d-1}$ and $\{|b_j\rangle\}_{j=0,\dots,d-1}$ that may be regarded as the set of eigenstates of the two observables $A = \sum_j a_j |a_j\rangle\langle a_j|$ and $B = \sum_j b_j |b_j\rangle\langle b_j|$, respectively. The bases are said to be mutually unbiased if the absolute value of the inner product of any pair of states, one from each basis, is a fixed number, that is

$$|\langle a_j | b_k \rangle| = d^{-1/2} \quad \forall j, k = 0, \dots, d-1, \quad (3.1)$$

where the value $d^{-1/2}$ is due to the normalization of the states [29]. In other words, if the system is initially prepared in an eigenstate of A , any outcome of a subsequent measurement of B is equally probable, and vice-versa. A and B are said to be extreme complementary observables: if one of them is known, the other is completely unknown. The statement in terms of measurements is useful to extend the concept of unbiasedness to more general measurement processes. Consider two positive-operator valued measurements $\{\hat{\Omega}_j^{(a)}\}$ and $\{\hat{\Omega}_j^{(b)}\}$, they are said to be mutually unbiased measurements if, for any state ρ satisfying $p_{j'}^{(a)} = \text{Tr} \left[\hat{\Omega}_{j'}^{(a)} \rho \left(\hat{\Omega}_{j'}^{(a)} \right)^\dagger \right] = \delta_{jj'}$ for some j , we have

$$p_k^{(b)} = \text{Tr} \left[\hat{\Omega}_k^{(b)} \rho \left(\hat{\Omega}_k^{(b)} \right)^\dagger \right] = \frac{1}{d} \quad \forall k = 0, \dots, d-1, \quad (3.2)$$

where d in this case is the number of outcomes, $p_{j'}^{(a)}$ ($p_k^{(b)}$) is the probability of outcome j' (k) when performing measurement a (b). In other words, if the measurement a is determin-

istic in the sense that only outcome j is detected with unity probability, then the outcomes of measurement b on the same state are equiprobable. This statement is also valid if a and b are interchanged.

Maybe the most celebrated pair of complementary observables is position and momentum, two continuous variable operators. Indeed, most quantum mechanics textbooks highlight the fact that MU between position (\hat{x}) and momentum (\hat{p}) operators can be demonstrated by $|\langle x|p\rangle| = 1/\sqrt{2\pi}$ (we set $\hbar = 1$ throughout). What is somewhat less well-known is the fact that *any* two non-parallel phase space operators \hat{q}_θ and $\hat{q}_{\theta'}$ (Eq. (1.18)) are mutually unbiased, which can be demonstrated via

$$|\langle q_{\theta'}|q_\theta\rangle| = (2\pi|\sin \Delta\theta|)^{-1/2}, \quad (3.3)$$

where we assume that q_θ and $q_{\theta'}$ are characterized by angles θ and θ' in phase space, and $\Delta\theta \equiv \theta' - \theta$ is the angle between them¹, as illustrated in Fig. 3.1.

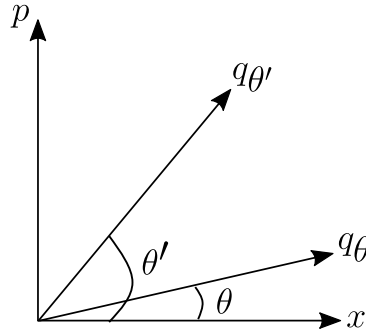


Figure 3.1.: Phase space directions and angles.

Mutually unbiasedness (MU) brings up one major difference between continuous variable and discrete variable quantum systems. Discrete and finite d -dimensional quantum systems admit at most $d + 1$ mutually unbiased bases [74]. This means that the maximal set for which any pair of bases are mutually unbiased has at most $d + 1$ elements. When d is the power of a prime number the existence of such a maximal set is guaranteed [74, 83–85]. On the other hand, it was shown in Ref. [81] that there are at most three MU bases for a CV system (also known as a “qumode”). MU for three phase space operators can be achieved by defining the relative angle $\Delta\theta = 2\pi/3$, such that all pairs of operators satisfy Eq. (3.3) with the same right-hand side (RHS) [81, 86].

Observables of continuous quantum variables can be discretized by a “binning” procedure, dividing the Hilbert space into a finite number of discrete parts, as exemplified in Fig. 3.2. One common example is the parity operator, with eigenstates that are symmetric or anti-symmetric with respect to the origin. There are a number of reasons to pursue this type of discretization. For example, it is well known that it is difficult to employ phase space operators

¹We note that in the limit $\theta_j k \rightarrow 0$, the limit must be taken before the absolute value to recover the normalization to the usual Dirac delta function

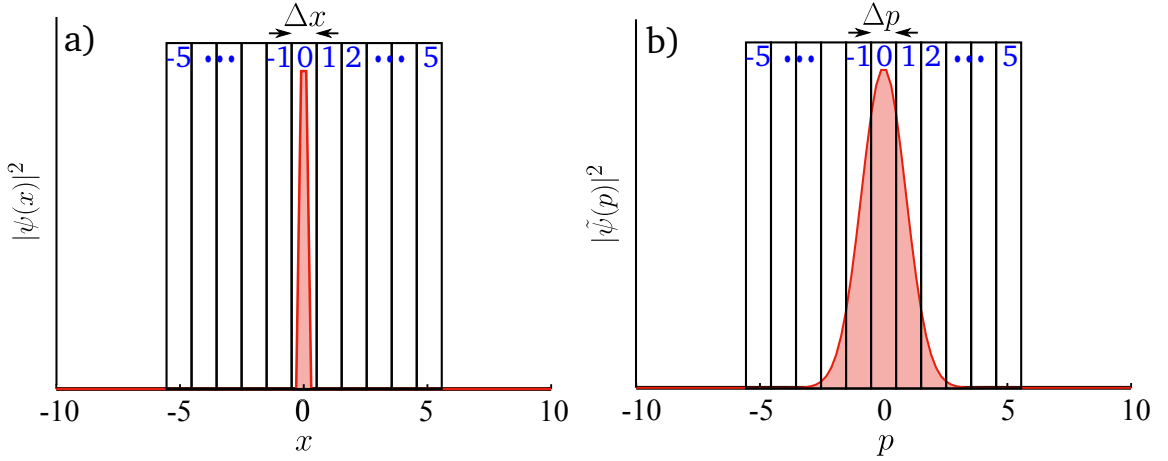


Figure 3.2.: Coarse grained measurements in a) position and b) momentum over a state $|\psi\rangle$.

to demonstrate quantum non-locality [87]. This has led to a number of binning schemes of measurements or states [88–92]. More fundamentally, the continuous variable eigenstates in (3.3) are not physical [27]. In real-world experiments, they are approximated by states that are localized around some mean value, which renders these physical eigenstates no longer mutually unbiased. In addition, measurements in any quantum system suffer from some amount of coarse graining, which follows from the fact that any measurement device has some finite resolution. In this way, the measurements are not projections over an eigenstate of the CV observable, but a projection on the region of each detector

$$\hat{\Omega}_k^{(q_\theta)} = \int_{(k-\frac{1}{2})\Delta q_\theta}^{(k+\frac{1}{2})\Delta q_\theta} dq_\theta |q_\theta\rangle\langle q_\theta|, \quad (3.4)$$

where k is an integer and Δq_θ is the detector aperture. For example, consider a very localized Gaussian state in position representation, such that the probability of detecting the particle out of detector 0 is negligible, as the one represented in Fig. 3.2-a). The more localized the state is, it still has a finite width in position, and consequently a finite width in momentum as well [Fig. 3.2-b)]. Therefore, although we may have unity probability of detecting the system in the detector 0 when measuring position, we do not have equal probability of detecting the system in any detector when measuring momentum, and the MU for this real measurement process is lost. In other words, the measurements of Eq. (3.4) for position and momentum are not MUM. The coarse-grained observables describing these measurements though satisfy uncertainty relations [70], but they are not complementary in the sense of MU. This inherent coarse graining of real-world states, as well as real-world measurements, motivates the search for coarse-grained mutually unbiased observables.

3.3. Mutually unbiased periodic coarse grained measurements

It has been shown recently that one path to MU is through the definition of periodic coarse grained (PCG) observables, where physical mutually unbiased measurement pairs [30] and mutually unbiased measurement triples [82] were demonstrated theoretically and experimentally. An schematic representation of the PCG measurement is shown in Fig. 3.3. The continuum of values for the phase space observable q_θ is binned uniformly, according to the size of the detectors. Instead of associating an outcome to each detector, the bins are labeled periodically with natural numbers from 0 to $d - 1$. Anytime the quantum system is detected in a box labeled by j , the outcome j is attributed to that measurement. In this formulation there naturally appears a “dimensionality” parameter d , given by the number of possible measurement outcomes. The period of the coarse grained measurement, T_θ , is equal to the size of the detectors times the dimension.

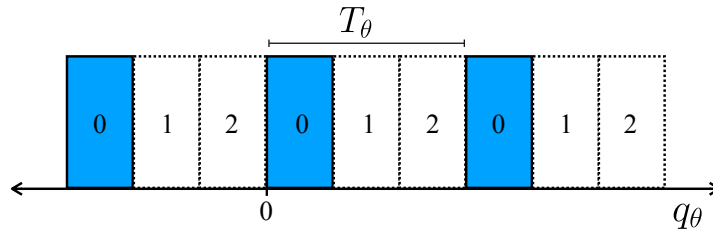


Figure 3.3.: The periodic coarse graining scheme for $d = 3$ and period T_θ . Anytime a particle is detected in the blue regions, the measurement is attributed the outcome value 0. The solid line represents the mask function $M_0(q_\theta, T_\theta)$.

This PCG measurement can be described by the measurement operators

$$\hat{\Omega}_k^{(\theta)} = \int_{-\infty}^{\infty} dq_\theta M_k(q_\theta - q_\theta^{\text{cen}}, T_\theta) |q_\theta\rangle\langle q_\theta|, \quad (3.5)$$

where the mask function describes the detectors and is regarded as the periodic square waves

$$M_k(q_\theta, T_\theta) = \begin{cases} 1 & k \frac{T_\theta}{d} \leq q_\theta \pmod{d} < (k+1) \frac{T_\theta}{d} \\ 0 & \text{otherwise,} \end{cases} \quad (3.6)$$

such that $\hat{\Omega}_k^{(\theta)}$ projects a state on the subspace of \hat{q}_θ -eigenstates corresponding to all bins periodically labeled by k . The displacement parameter q_θ^{cen} is included to allow for freedom to define the origin and will be taken to be zero for simplicity. The Fourier series of the mask function is written as

$$M_k(q_\theta, T_\theta) = \frac{1}{d} + \sum_{n \in \mathbb{Z}/\{0\}} \frac{1 - e^{-i \frac{2\pi n}{d}}}{i 2\pi n} e^{-i \frac{2\pi n k}{d}} e^{-i \frac{2\pi n}{T_\theta} q_\theta}. \quad (3.7)$$

Let us now consider two PCG measurements $\{\hat{\Omega}_k^{(\theta)}\}_k$ and $\{\hat{\Omega}_k^{(\theta')}\}_k$ as the one described. They are defined in two nonparallel directions characterized by angles θ and θ' in phase space, with periods T_θ and $T_{\theta'}$, respectively. Without any loss of generality we can consider a pure state satisfying

$$p_k^{(\theta)} = \langle \psi | \hat{\Omega}_k^{(\theta)} | \psi \rangle = \delta_{kl} \quad \forall k = 0, \dots, d-1. \quad (3.8)$$

The q_θ and $q_{\theta'}$ representations of this state are denoted as $\langle q_\theta | \psi \rangle = \psi(q_\theta)$ and $\langle q_{\theta'} | \psi \rangle = \bar{\psi}(q_{\theta'})$. In order to determine the condition for MU of the two PCG measurements, the probability of detection in direction θ' must be calculated. By using Eq. (3.5) with the Fourier series (3.7) and the FrFT connection between the two phase space representations [Eq. (1.21)], one obtains

$$p_j^{(\theta')} = \langle \psi | \hat{\Omega}_j^{(\theta')} | \psi \rangle = \frac{1}{d} + \sum_{n \in \mathbb{Z} \setminus \{0\}} \frac{1 - e^{-i \frac{2\pi n}{d}}}{i 2\pi n} \int dq_\theta e^{i \phi_j^{(n)}(q_\theta)} \psi^*(q_\theta) \psi\left(q_\theta - n \frac{2\pi \sin \Delta\theta}{T_{\theta'}}\right), \quad (3.9)$$

where $\Delta\theta = \theta - \theta'$ and $\phi_j^{(n)}(q_\theta) = n \frac{2\pi \cos \Delta\theta}{T_{\theta'}} q_\theta - \left(n \frac{2\pi}{T_{\theta'}}\right)^2 \frac{\sin(2\Delta\theta)}{4} - \frac{2\pi j}{d}$. For the two measurements to be unbiased, $p_j^{(\theta')}$ must be equal to $1/d$ because we started from a localized state relative to the measurement in q_θ . Thus, the sum in the right hand side shall be forced to vanish. The terms in the sum with n multiple of d are already null because in this cases $e^{-i \frac{2\pi n}{d}} = 1$. Because of Eq. (3.8), $\psi(q_\theta)$ has nonnull values only inside the mask $M_l(q_\theta, T_\theta)$. Hence, if q_θ is any value for which $\psi(q_\theta) \neq 0$, then $\psi(q_\theta + \Delta q_\theta) = 0$, and so is $\psi^*(q_\theta) \psi(q_\theta + \Delta q_\theta)$, provided that $\frac{T_\theta}{d} \leq \Delta q_\theta \pmod{T_\theta} \leq (d-1) \frac{T_\theta}{d}$. Particularly, if the absolute value of the increment $\frac{2\pi \sin \Delta\theta}{T_{\theta'}}$ for $n = 1$ in Eq. (3.9) is equal to $m \frac{T_\theta}{d}$, with m an integer number non-multiple of d , the corresponding term in the summation vanishes for any $|\psi\rangle$ satisfying (3.8). For the other values of n non-multiple of d , we then have that $n \frac{2\pi \sin \Delta\theta}{T_{\theta'}} = nm \frac{T_\theta}{d}$ must be non-multiple of the period in order to all the integrals to vanish. This arguments yield the MUM condition for the PCG measurements

$$T_\theta T_{\theta'} = \frac{2\pi d |\sin \Delta\theta|}{m}, \quad \frac{nm}{d} \notin \mathbb{N} \quad \forall n = 1, \dots, d-1, \quad (3.10)$$

which is a relation between periods dependent on the dimensionality parameter chosen as well as on the angle between the two phase space directions. This relation was first shown in Ref. [30] for position and momentum only ($\Delta\theta = \frac{\pi}{2}$) and then extended to any two phase space observables in Ref. [82]. In the last reference, the authors also show that is it possible to build a triple (and no more than three) of PCG measurements pairwise MU when all the m numbers present in the period relations are equal to one. The cases above [30, 82] are interesting, but even in the ideal continuous case, we can have MU measurements for two or three phase space directions. A natural question is, using this periodic coarse graining, can we go beyond the CV case, obtaining more than three MU observables? To answer the question about the possibility of having a set with more MUMs and how many MUMs compose the maximal set for a given

dimension, one might try to find a set of periods and angles for which the relation (3.10) is satisfied for all pairs of measurements for some m . In the next section, it is presented a way to construct such set of measurements in which the angles are fixed and the equations are solved for the periods. The dimensions possible for a given number of measurement directions come as part of the solution.

3.4. Construction of several MUMs

Following Refs. [30, 82], let us consider R phase space operators \hat{q}_j as in Eq. (3.3), related to each other via phase space rotations, and each characterized by an angle θ_j , for $j = 0, \dots, R - 1$, illustrated in Fig. 3.4 a). We can then define R coarse-grained projective measurement operators:

$$\hat{\Omega}_j^{(m)} = \int dq_j M_r^{(j)}(q_j - q_j^{\text{cen}}; T_j) |q_j\rangle \langle q_j|, \quad (3.11)$$

with detector apertures encoded in “mask functions” $M_r^{(j)}$, such that $\sum_{m=0}^{d-1} M_r^{(j)} = 1$. The parameter T_j is the period of the mask function. The outcome probabilities produced by the set of projectors (3.11) then define the PCG of the probability distribution associated with the phase-space variable q_j . Since we work with dimensionless variables, the mask parameter T_j is also dimensionless.

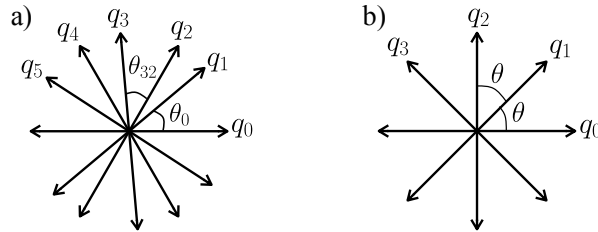


Figure 3.4.: Examples of phase space variables for a) $R = 6$ and b) the $R = 4$ case implemented experimentally.

We assume that $\theta_0 = 0$, without loss of generality, and $\theta_j > \theta_k$ if $j > k$. The condition (3.10) for mutual unbiasedness of PCG operators of the sort (3.11) is written as

$$T_j T_k m_{jk} = 2\pi d |\sin \theta_{jk}|, \quad (3.12)$$

where $\theta_{jk} \equiv \theta_j - \theta_k$ and m_{jk} is a positive integer. The MU condition (3.12) also requires that

$$\frac{m_{jk} n}{d} \notin \mathbb{N} \quad \forall n = 1, \dots, d - 1. \quad (3.13)$$

To construct a general recipe to obtain an arbitrary number of PCG MUMs, let us

consider that $\sin \theta_j \geq 0$, which defines variables q_j in the upper semi-plane of phase space. This is not a restriction, as variables in the lower half-plane can be taken to the upper half-plane by a reflection through the origin: $q_j \rightarrow -q_j$. Using the fact that $\theta_0 = 0$, we then have $R - 1$ conditions of the form:

$$T_j = \frac{2\pi d \sin \theta_j}{m_{j0} T_0}. \quad (3.14)$$

Plugging the above equations for the periods into condition (3.12) with $j, k \neq 0$, we have

$$T_j T_k m_{jk} = 2\pi d |\sin \theta_{jk}| = \frac{(2\pi d)^2 \sin \theta_j \sin \theta_k m_{jk}}{T_0^2 m_{j0} m_{k0}}. \quad (3.15)$$

Considering $j > k$, this can be rewritten as

$$\frac{m_{jk}}{m_{j0} m_{k0}} = \frac{T_0^2}{2\pi d} (\cot \theta_k - \cot \theta_j). \quad (3.16)$$

Since the left-hand side is composed of all natural numbers, it is a rational number, which results in a general restraint for the right-hand side (RHS). Condition (3.16) is enough to prove several important results concerning periodic discretization.

There is quite a bit of freedom in constraint (3.16) concerning the period T_0 , as well as the angles θ_j, θ_k (for $j, k \neq 0$). With some specification, we can construct a useful recipe for finding a general mutually unbiased set. As a step in this direction, let us choose angles that are distributed at integer multiples of an angle θ , such that $\theta \leq \pi/2$ and $\theta_j = j\theta$. Moreover, we will choose $T_0^2 = \pi d \tan \theta$, so that we can write

$$\frac{m_{jk}}{m_{j0} m_{k0}} = \frac{\tan \theta}{2} (\cot k\theta - \cot j\theta). \quad (3.17)$$

Choosing then

$$\tan \theta = \sqrt{N/N'}, \quad (3.18)$$

where $N, N' \in \mathbb{N}$, we can prove that the RHS of Eq. (3.17) is always a rational number for all $j, k = 1, \dots, M - 1$. The proof is provided in the next subsection. This allows one to find suitable numbers m_{j0}, m_{k0} and m_{jk} that satisfy Eq. (3.17). Eqs. (3.13), (3.17) and (3.18) then define the conditions for a set of mutually unbiased PCG observables.

3.4.1. Solution to equation (3.16)

The RHS of Eq. (3.16) must be a rational number for all allowed values of j and k . Thus, all elements in the sequence $\{a_k = \frac{T_0^2}{2\pi d} \cot \theta_k\}_k$ should be rational. There are two possibilities to assure this: requiring the product of $\frac{T_0^2}{2\pi d}$ and $\cot \theta_k$ to be rational, what implies a relation between the period and the angle, or requiring each term in the product to be indepen-

dently rational. In both cases, mathematical induction can be used to figure out the solutions. According to this method, we need to ensure the validity of the statement for the first element in the sequence ($k = 1$ in our case). The statement is valid for all k if it can be demonstrated that the assumption of validity for any value $k - 1$ implies its validity for k .

In what follows, we use the recurrence relation

$$\cot(k\theta) = \frac{\cot \theta \cot(k-1)\theta - 1}{\cot \theta + \cot(k-1)\theta}, \quad (3.19)$$

and all n_i are natural numbers.

First solution

We want to show what are the conditions that make all elements of the sequence a_k to be rational numbers. A relation between the period T_0 and the angle θ comes from the assertion that the first element of this sequence is a rational:

$$a_1 = \frac{T_0^2}{2\pi d} \frac{1}{\tan \theta} = \frac{n_1}{n_2} \Rightarrow T_0 = \sqrt{2\pi d \tan \theta \frac{n_1}{n_2}}. \quad (3.20)$$

Now suppose that for an arbitrary k the $(k-1)$ -th element is rational, that is

$$a_{k-1} = \frac{T_0^2}{2\pi d} \cot(k-1)\theta = \frac{n_3}{n_4}, \quad (3.21)$$

this should imply the k -th element to also be a rational number. Using the relations (3.19), (3.20), and (3.21) we have

$$a_k = \frac{n_1}{n_2} \frac{n_2 n_3 - n_1 n_4 \tan^2 \theta}{n_2 n_3 + n_1 n_4}, \quad (3.22)$$

which is not rational unless

$$\tan \theta = \sqrt{\frac{n_5}{n_6}}. \quad (3.23)$$

Therefore, if conditions (3.20) and (3.23) are satisfied, the inductive proof is concluded. The solution presented before for the period and angle are particular cases with $n_1 = 1$, $n_2 = 2$.

Second solution

We define a new sequence $\{b_k = \cot(k\theta)\}_k$ and $a_k = \frac{T_0^2}{2\pi d} b_k$. One possibility for the elements of $\{a_k\}$ to be rational is that the elements of $\{b_k\}$ are rational and

$$\frac{T_0^2}{2\pi d} = \frac{n_1}{n_2} \Rightarrow T_0 = \sqrt{2\pi d \frac{n_1}{n_2}}. \quad (3.24)$$

A condition for the angle comes from the requirement that b_1 is a rational number:

$$b_1 = \frac{n_3}{n_4} \Rightarrow \tan \theta = \frac{n_4}{n_3}. \quad (3.25)$$

It comes directly from relation (3.19) that, if b_{k-1} is rational, then it follows that b_k is also a rational number. This solution allows for choosing T_0 and θ independently.

3.4.2. Even dimensionality parameter

There are some interesting conditions that can be derived about the dimension parameter d . As a first result, we show that, *for d even, there are at most $R = 3$ mutually unbiased PCG operators.* To prove this, let us analyze once more the conditions (3.17) for $k = 1$ and $j = 2$, which gives

$$\frac{m_{20}m_{10}}{m_{21}} = 4 \cos^2 \theta. \quad (3.26)$$

For $R = 3$ this is the only condition that must be satisfied, and it alone is not prohibitive for any $d \geq 2$. For any number of bases $R > 3$, an additional condition for $k = 1$ and $j = 3$ is also present. The two conditions are related, since, using (3.17) and (3.26) we can write

$$\frac{m_{30}m_{10}}{m_{31}} = 4 \cos^2 \theta - 1 = \frac{m_{20}m_{10} - m_{21}}{m_{21}}. \quad (3.27)$$

Consider d even. Then, using $n = d/2$ in (3.13) determines that all m_{jk} must be odd. From (3.27) we can write $m_{30} = (m_{31}m_{20}m_{10} - m_{31}m_{21}) / (m_{21}m_{10})$, and assuming that all m_{jk} appearing in the RHS of this expression are odd, then the numerator turns out to be even and thus m_{30} must be even, which violates condition (3.13). Thus, there is no valid solution for even dimension if the number of phase space operators $R > 3$.

3.4.3. Examples for d odd

θ	$\tan \theta$	R	m values	allowable d
$\frac{\pi}{4}$	1	4	$m_{20} = 2$, all other $m_{jk} = 1$	$d \geq 3$, odd
$\frac{\pi}{6}$	$\frac{1}{\sqrt{3}}$	6	$m_{20} = m_{40} = m_{42} = 3$, $m_{30} = m_{41} = m_{52} = 2$, all other $m_{jk} = 1$	$d = 5, 7, 11, 13, 17, 19, 23, 25, 29$
0.35 rad	$\sqrt{\frac{2}{15}}$	8	many values	$d = 7, 11, 19, 23, 29$
≈ 0.3 rad	$\frac{1}{\sqrt{9}}$	9	many values	$d = 11, 17, 19, 23, 29$

Table 3.1.: Some results for $R = 4, 6, 8, 9$.

Let us now consider some particular cases. One can see that previous results [82] for $R = 3$ are retrieved when $\tan \theta = \sqrt{3}$ (here in present notation we have $q_0 = x$, $q_1 = -s$ and

$q_2 = r$, in terms of previous variables [82]) which from Eq. (3.12) gives all $m_{jk} = 1$.

In table 3.1 we show results for $R = 4, 6, 8$ and 9. The allowable dimensions d were tested up to $d = 30$. $R = 3, 4, 6$ are the only values that allow division of the first half-plane into equal “slices”, while still maintaining $\tan^2 \theta$ rational. For other values, this is not possible. For example, to divide the semi-plane into 7 equal slices, we need $\theta = \pi/7$, but this does not result in $\tan \theta = \sqrt{N/N'}$. Thus, we must choose an N and N' which results in a $\theta < \pi/7$. To take advantage of the entire phase space, in some sense, it seems logical to choose the angles so that θ is as large as possible, though this is not necessary. The results were obtained choosing the value of θ and fixing $m_{10} = 1$ from what is possible to obtain the values of the other m_{jk} as numerators and denominators of the RHS of Eq. 3.17. With the values of all m_{jk} we could check which are the allowed values of d satisfying 3.12.

Looking at our results for $R = 4, 6$ and 8 one might be tempted to assume that there are at most $R = d + 1$ MUMs for odd d , as is known to be true for some cases in discrete quantum mechanics. In fact, this is the case if d is a prime number, as we shall show in Sec. 3.5.

3.4.4. Experimental realization

To confirm and explore our results we performed a classical optics experiment, similar to those of Refs. [30, 82]. Optical fractional Fourier transforms (FrFT) and amplitude masks were used to prepare and measure the transverse spatial profile of a laser beam, as shown schematically in Fig. 3.5. Both the optical FrFTs as well as the amplitude masks were implemented using spatial light modulators (SLMs), as shown in Fig. 3.5 and described in detail in Chapter 1. The vertical transverse coordinate is used as the system CV while the horizontal coordinate is used for the amplitude masks diffraction. In each reflection by an SLM, only the first order diffraction in the horizontal plane is taken for the following operations. It is well known that when proper scaling is chosen, the FrFT of order α is equivalent to a rotation in phase space by the angle α . Using the three-lens FrFT scheme introduces a scaling factor such that the adimensional (T_j) and physical (T'_j) periods are related by $T'_j = \sqrt{\frac{\lambda z}{\pi}} T_j$, where $z = 0.29$ m is the distance between the lenses (quadratic phases implemented by the SLMs) and $\lambda = 632.9$ nm is the laser wavelength produced by the HeNe laser used. Moreover, for practical reasons the physical periods are given in number of SLM pixels. The pixel size of the Holographic SLMs used here is $8 \mu\text{m}$. The initial state is fixed and is prepared as a colimated Gaussian beam with width (2.54 ± 0.06) mm at the plane of the first SLM. It is considered as the state in the position-eigenstates representation. In the preparation stage, a FrFT of order $j\theta$ was implemented on the transverse profile, followed by the application of an amplitude mask $M_r^{(j)}$ of period T'_j . This maps the position representation in the first SLM plane to the $q_{j\theta}$ -representation in the third SLM plane, where the amplitude mask is also applied to prepare a localized state

in respect to PCG $q_{j\theta}$ measurement. The measurement stage consisted of an FrFT of order $(k - j)\theta$, mapping the $q_{j\theta}$ -representation in the third SLM plane to the $q_{k\theta}$ -representation in the third SLM plane, and an amplitude mask $M_s^{(k)}$. The full field of the resulting output beam was then attenuated and detected with a single photon detector.

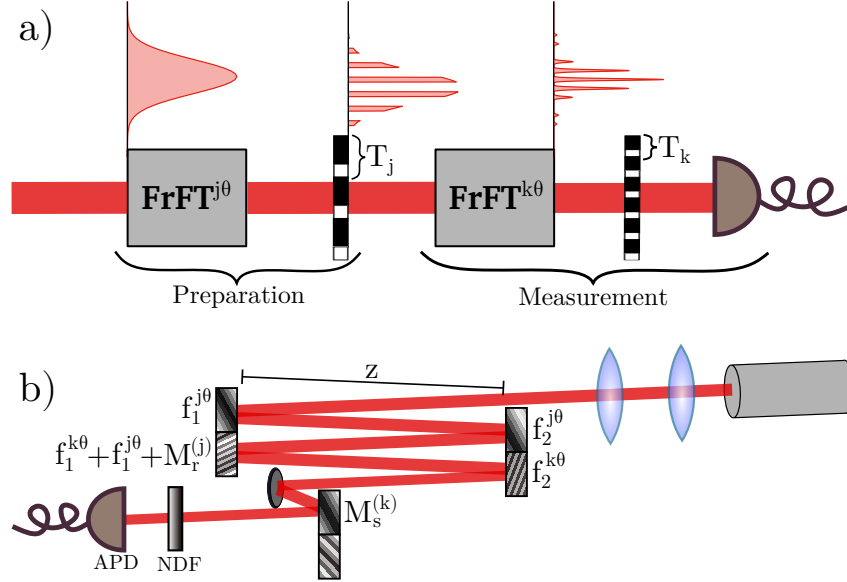


Figure 3.5.: a) Schematic of the experiment. Fractional Fourier Transforms (FrFT) and periodic amplitude masks (M) are used to prepare and measure the transverse spatial profile of the laser beam. All output light is incident on full-field single-photon detector. The scheme used to implement FrFT is composed by three lenses with separation distance z . If the focal distances satisfy $f_1^\theta = z \left(1 - \frac{\cot(\theta/2)}{2}\right)^{-1}$ and $f_2^\theta = z(1 - \sin \theta)^{-1}$ then the transverse profile of the optical field in the plane p_2 is the FrFT of order θ of the field in the plane p_1 up to a scaling factor that is independent of the FrFT order. b) Experimental setup using spatial light modulators (SLM) for preparation and measurement. The output of a 632.8nm He-Ne laser is enlarged and collimated using two lenses. The FrFTs are performed modulating the phase accordingly to the quadratic phase of lenses with the right focal distances. The use of SLMs allows us to make any order FrFT, which would be challenging with actual lenses. The amplitude masks are also implemented using phase-only modulators applying diffraction gratings and collecting only the first diffraction order. Finally, the beam is attenuated with a neutral density filter (NDF) and detected by a single photon detector. More details provided in main text.

We tested the case of $R = 4$ MUMs with dimension parameter $d = 3$ and $\theta = \pi/4$ for all nine combinations of preparation and measurement phase space directions. We chose the period of mask 0 to be $T'_0 = 93$ pixels, since this value is the closest integer number to the exact value (92.7476 pixels) satisfying condition (3.18) with $N = 1$ and $N' = 4$. Using (3.14), and choosing $m_{10} = m_{30} = 1$ we have $T'_1 = T'_3 = 131.165$ pixels that was approximated by 132 pixels so the bin width is an integer. Using these values, we tested MUM conditions between

		Measurement			
		0	1	2	3
Preparation	0	0.161(3)	1.5846(2)	1.579(1)	1.5847(2)
	1	1.5841(8)	0.143(3)	1.583(3)	1.584(4)
	2	1.5846(1)	1.5848(1)	0.140(5)	1.5838(1)
	3	1.5844(2)	1.5847(1)	1.5844(5)	0.162(3)

Table 3.2.: Entropy value for different preparation and measurement direction in the case $R = 4$ and $d = 3$.

preparations $j = 0, 1, 3$ and measurement $k = 2$, giving results shown in Fig. 3.6. For each measurement, the detection mask was scanned in all three positions ($d = 3$), and the number of photon counts registered. We then calculated the detection probabilities p_i , where $i = 0, 1, 2$ refers to the three amplitude masks, as well as the Shannon entropy $E = -\sum_i p_i \log_2 p_i$ of the probability distributions, plotted in Fig. 3.6 as a function of the period T'_2 of the mask used in the measurement stage. Vertical lines show values at which the period T'_2 corresponds to allowable m_{2j} values. We can see that at several places the entropy reaches its maximum value of $\log_2 3 \approx 1.5849$, which indicates the probability distribution is uniform, corresponding to a MUM result. In order to have a set of MUMs, the entropy must have its maximum value for all preparation directions with the same value of T'_2 , which only happens for the periods corresponding to some set of m_{2j} that satisfies (3.12) and (3.13) for all j simultaneously². The period parameter $T'_2 = 93$ pixels satisfies the MUM condition in all plots. Moreover, it corresponds to $m_{21} = m_{23} = 1$ and $m_{20} = 2$, as predicted by our theoretical results in Table 3.1. The entropy values obtained for these mask periods are given in table 3.2. We obtained results very close to the maximum value of $\log_2 3$ in all cases, indicating MUM results for $R = 4$ PCG measurements. To test the operation of our setup, we also made measurements with equal preparation and measurement phase space direction. The entropy ideally would vanish in this case, but it has non-zero experimental values as can be seen in Table 3.2. This is due to the existence of some background noise that makes the probability of preparing and measuring the system in the same mask to be slightly smaller than 1 (≈ 0.98), which is enhanced by the structure of Shannon entropy. Similar results were obtained for all combinations of preparation and measurement and are shown in App. B. Furthermore, in all plots we can observe that the entropy decreases greatly when $m_{2j} = 3$, which is not allowed by Eq. (3.13) when $d = 3$.

²This is visually observed for periods $T'_2 > 25\text{px}$ approximately. For periods smaller than that value, the entropy is too close to its maximum value and it is not possible to tell by the plot which periods give exactly the maximum entropy.

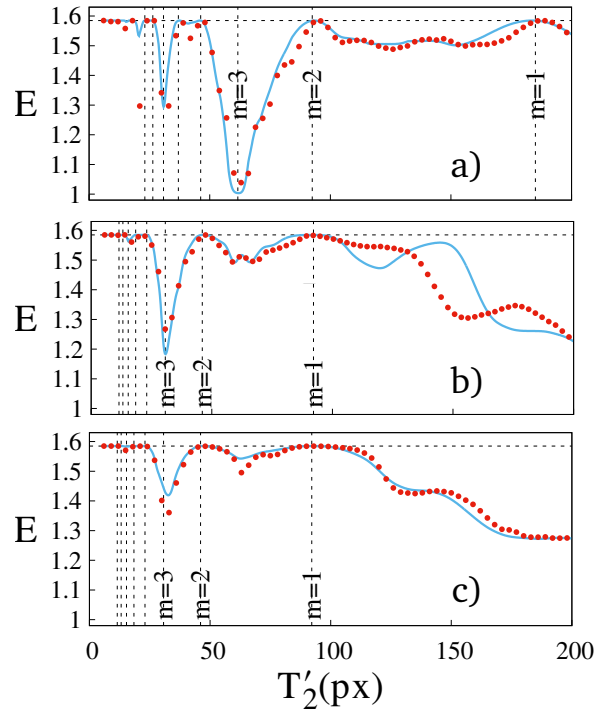


Figure 3.6.: Example of results for $R = 4$ MUMs, using angle $\theta = \pi/4$ and preparation directions with a) $j = 0$, b) $j = 1$ and c) $j = 3$. In all graphs the measurement used is $k = 2$. Entropy is plotted as a function of the period T'_2 of the measurement mask, with preparation mask $M_0^{(j)}$ fixed with the period that satisfies the MUM condition. The blue curves correspond to theoretical predictions with the same initial state as the measured one.

3.5. Maximum number of MUMs: general case

Our main results concern the maximum number of MUMs: First, let us consider d even. Using $n = d/2$ in (3.13) determines that all m_{jk} must be odd. Now, for $R \geq 4$ measurements we have conditions (3.16) for $jk = 12, 13, 23$. Combining these three constraints leads to $m_{23}m_{10} + m_{12}m_{30} = m_{13}m_{20}$, which requires one m to be even and violates Eq. (3.13). Thus, there are at most $R = 3$ MUMs for even d in the general case, showing that it is not a particularity of our construction.

Now, for odd d the PCG given in (3.11) and satisfying constraints (3.12) and (3.13), we can show that the maximum number of MUMs is given by $R_{max} = \varphi(d) + 2$, where $\varphi(d) = d \prod_{p|d} \left(1 - \frac{1}{p}\right)$ is Euler's totient function counting the positive integers less than d that are relatively prime to d , and $p|d$ denotes all prime divisors of d . Since $\varphi(d) = d - 1$ when d is prime we have $R_{max} = d + 1$ for prime d . The proof is provided below.

Proof for d odd

Consider again the MUM condition in the form of Eq. (3.16). This condition is particularly valid for $k = 1$ and $j \geq 2$ giving

$$\frac{m_{j1}}{m_{j0}m_{20}} = \frac{T_0^2}{2\pi d}(\cot \theta_1 - \cot \theta_j). \quad (3.28)$$

The previous equation can be substituted into the more general relation for $j > k$ and $j, k \geq 2$ yielding a relation involving only the m_{jk} 's

$$m_{j1}m_{k0} - m_{j0}m_{k1} = m_{jk}m_{10}. \quad (3.29)$$

Let us introduce an expansion of all m_{jk} as

$$m_{jk} = l_{jk}d + n_{jk}, \quad (3.30)$$

where l_{ij} the integer quotient of the division of m_{ij} by d and $n_{jk} = m_{jk} \bmod d$ is the integer remainder. By plugging this parametrization into (3.29), one can see that

$$n_{10}m_{jk} = Z_{jk}d + n_{j1}n_{k0} - n_{j0}n_{k1}, \quad (3.31)$$

with

$$Z_{jk} = -l_{10}m_{jk} + n_{j1}l_{k0} + n_{k0}l_{j1} + l_{j1}l_{k0}d - (n_{k1}l_{j0} + n_{j0}l_{k1} + l_{k1}l_{j0}d)$$

an integer. Notice that $n_{10} = 1, 2, \dots, d - 1$, thus one instance of condition (3.13) reads

$$\frac{n_{10}m_{jk}}{d} \notin \mathbb{N} \Leftrightarrow Z_{jk} + \frac{n_{j1}n_{k0} - n_{j0}n_{k1}}{d} \notin \mathbb{N}. \quad (3.32)$$

Hence, as Z_{jk} is integer, a necessary condition for the set of MUMs with R measurements to exist is that

$$(n_{j1}n_{k0} - n_{j0}n_{k1}) \bmod d \neq 0 \quad \forall j, k \in \{2, 3, \dots, R - 1\}. \quad (3.33)$$

It follows from the fact that $n_{j1}n_{k0} \neq n_{k1}n_{j0}$ must be satisfied for all pairs i, j that

$$n_{j1} = n_{j'1} \Rightarrow n_{j0} \neq n_{j'0} \quad (3.34a)$$

$$n_{j0} = n_{j'0} \Rightarrow n_{j1} \neq n_{j'1} \quad (3.34b)$$

$$n_{j1} = n_{j0} \Rightarrow n_{j'0} \neq n_{j'1} \quad \forall j' \neq j. \quad (3.34c)$$

Let us define the $2 \times (R - 2)$ -dimensional matrix

$$\Omega = \begin{pmatrix} n_{20} & n_{30} & \dots & n_{R-1,0} \\ n_{21} & n_{31} & \dots & n_{R-1,1} \end{pmatrix}. \quad (3.35)$$

The conditions (3.33) are thus equivalent to say that the determinant of all submatrices 2×2 of Ω must be congruent to zero modulo d , that is

$$\begin{vmatrix} n_{j0} & n_{k0} \\ n_{j1} & n_{k1} \end{vmatrix} \bmod d \neq 0. \quad (3.36)$$

Besides being more elegant, it is also helpful in having a more clear view of the problem.

The problem of finding the maximum number of MUMs is now equivalent to the problem of finding the maximum number of columns of matrix (3.35) such that condition (3.36) is obeyed. Now, let us look for the cases when condition (3.36) is not satisfied, i.e. the cases for which

$$(n_{j0}n_{k1} - n_{k0}n_{j1}) \equiv 0 \pmod{d}. \quad (3.37)$$

From Euclides Algorithm we know that for any $k \in \mathbb{Z}$, $k < d \exists \alpha, \beta \in \mathbb{Z}$ s.t. $\alpha k + \beta d = \text{gdc}(k, d)$. If d is prime, then $\text{gdc}(k, d) = 1$ since k is smaller than d . In this case, we can conclude that k has a modular inverse

$$[\alpha k + \beta d] \bmod d = 1 \quad \Rightarrow \quad [\alpha k] \bmod d = 1, \quad (3.38)$$

what leads to $[\alpha k i] \bmod d = i$ for any $i \in \mathbb{Z}$. Thus, all elements of matrix (3.35) have a modular inverse with respect to d for d prime, which we denote by \bar{n}_{ij}^{-1} , such that $n_{ij} \bar{n}_{ij}^{-1} \equiv 1 \pmod{d}$. Multiplying (3.37) by $\bar{n}_{1j}^{-1} \bar{n}_{1k}^{-1}$ we are left with

$$(\bar{n}_{k0}^{-1} n_{k1} - \bar{n}_{j0}^{-1} n_{j1}) \equiv 0 \pmod{d} \quad (3.39)$$

or

$$\bar{n}_{k0}^{-1} n_{k1} \equiv \bar{n}_{j0}^{-1} n_{j1} \pmod{d}. \quad (3.40)$$

Thus each column of Ω is characterized by a number $\chi_k = \bar{n}_{k0}^{-1} n_{k1} \pmod{d}$. Accordingly, to satisfy (3.36), each column must have a different value of χ_k . As $1 \leq \chi_k \leq d - 1$, only $d - 1$ columns are allowed, therefore it is not possible to have more than $d + 1$ MUMs.

If d is not a prime number, then the general MUM condition (3.13) implies that all elements of Ω are still coprime with d . The same argument can be used to show that only $\varphi(d)$ columns are allowed, $\varphi(d)$ being Euler's totient function of d , i.e. the number of all coprimes with d smaller than d calculated by $\varphi(d) = d \prod_{p|d} \left(1 - \frac{1}{p}\right)$, where $p|d$ denotes all prime divisors

of d . Therefore $\varphi(d) + 2$ is the maximum number of MUMs in this case.

A particular form of the matrix Ω that satisfies (3.36) is

$$N = \begin{pmatrix} 1 & \dots & 1 & \dots & 1 \\ n_{21} & \dots & n_{j1} & \dots & n_{R-1,1} \end{pmatrix}, \quad (3.41)$$

where $R = \varphi(d) + 2$. Note that for Ω of this form, the maximum value of R is easily determined. We can see that no two n_{j1} 's can be equal, since in this case condition (3.36) would not be satisfied. This, together with the constraints on n_{ij} , determine that the maximum number K_{max} of n_{2j} 's is then given by the number of non-factors of d , as shown above.

We have shown the maximum number of MUMs allowed, but not necessarily one can build a set containing the maximum number of measurements since condition (3.33) are only necessary but not sufficient. The possibility of having the maximum number of MUMs will depend on the particular choice of phase space directions. For example, as shown in Table 3.1, if $\theta = \tan^{-1} \left(\sqrt{\frac{2}{15}} \right)$ with eight MUMs, dimension $d = 7$ is allowed, but if $\theta = \tan^{-1} \left(\sqrt{\frac{1}{15}} \right) \approx 0.25\text{rad}$ the dimensions allowed up to 30 are $\{13,17,19,23,29\}$, which does not include $d = R - 1$.

3.6. Concluding remarks

MU is an essential concept in quantum mechanics and quantum information, about which there are still some basic open questions, such as the existence of a maximal set of such basis for a general dimension. For the current known cases, continuous and discrete systems differ in the number of bases or measurements contained in the maximal MU set. In this chapter we extended the recently proposed PCG measurements for CV systems that satisfy MU conditions [30]. This kind of measurement, although performed on CV variables systems, has a finite discrete number of outcomes resembling a discrete variable system in some aspects. Here we showed how to construct an arbitrary number of such PCG MUMs satisfying the MU conditions pairwise. In our construction, the measurements are determined by the choice of one angle and one period, for which we found MU conditions. For a given number of measurements, we could find the allowed dimensions. For the inverse question, given a dimension d , we showed that, if d is even, the maximum number of measurements is equal to three, as is the case of the original CV system. On the other hand, if d is odd then the maximum number of MUMs is determined by the number of prime factors of d and reproduces the discrete case for d prime. It was not expected that the PCG MUMs would follow the discrete or continuous behavior. Actually it is surprising that it does resemble both for particular dimensions. These results seems merely mathematical and reconnect them with physics, we also showed here an experimental realization of the constructed measurements in which the continuous variable is taken to be the

transverse position of an attenuated light beam. In our scheme, the FrFT connecting different phase space representations is performed in a programmable way, allowing for preparation and measurement in any phase space directions without changing the setup. It is shown for the case of $d = 3$ and $R = 4$ that the measurements only present MU if all the periods are chosen in accordance to the solutions we found.

An interesting future direction for this work is to identify a utility for these results in quantum information. For example, can these MU observables assist in a task such as tomography, cryptography, or random number generation?

Part II.

Discrete degrees of freedom

EXPERIMENTAL TECHNIQUES

In this Chapter we provide some experimental techniques used in the discrete degrees of freedom experiments. At the single photon level the methods used in our experiments are often equivalent to those used in classical optics. Thus they are partly presented in a classical manner. This Chapter does not intend neither to be complete nor rigorous, but its intention is to present the main concepts necessary to understand the experiments and the experimental issues.

4.1. Generating polarization entangled pairs of photons

Entangled pairs of photons can be generated through the process called spontaneous parametric down conversion (SPDC). In this process, the passage through a transparent second-order nonlinear medium can sometimes cause a photon of a pump beam of frequency ω_p to split in two photons of lower frequencies ω_s and ω_i , historically called signal and idler photons. Because they are generated together, conservation laws are responsible for the two photons to be correlated in many degrees of freedom such as frequency, momentum, orbital angular momentum and polarization [93]¹.

To conserve energy, the frequencies of signal and idler must sum up to that of their parent photon (Fig. (4.1)-c)), that is

$$\omega_i + \omega_s = \omega_p. \quad (4.1)$$

Momentum conservation implies

$$\mathbf{k}_s + \mathbf{k}_i = \mathbf{k}_p, \quad (4.2)$$

where the \mathbf{k} s are the wave vectors of each mode (Fig. (4.1)-b)). Relations (4.1) and (4.2) are called frequency and phase matching conditions, respectively.

¹The term parametric refer to the fact that no energy and momentum is transferred to the medium, so the conservation laws apply only to the three photons system.

As the pump and the generated fields have quite different frequencies, the dispersion of the medium causes them to travel at different velocities because they experience different indices of refraction. Moreover, isotropic media have null second order susceptibility (the electric polarization must be an odd function of the electric field such that the inversion of the last causes an inversion of the polarization without any alteration). Thus this conversion process requires anisotropy to take place. In anisotropic media the index of refraction depends not only on the frequency, but also on the direction of propagation and the polarization of the propagating field (See Appendix A). Actually, this dependence is beneficial, since, together with other properties like crystal thickness, the manipulation of the direction of the optical axis of the crystal permits one to control the phase matching and choose the type of SPDC allowed, as is described in the sequence.

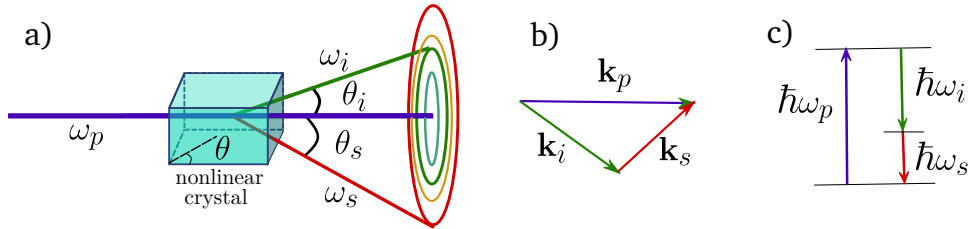


Figure 4.1: a) A collimated pump beam with frequency ω_p crosses a slab of second-order nonlinear crystal generating a continuum of lower frequency pairs of modes spatially distributed according to the phase matching conditions. Here the example of the so-called type-I phase matching: the generated beams have the same polarization and form a cone centered around the incident beam. The exit angles of the converted pairs is controlled by the optic axis angle θ . Two beams generated together, non-collinear with the pump beam propagation, are represented by the red and green rays. Each pair of beams conserve b) momentum and c) energy.

In a uniaxial crystal, as is the case of the β -barium-borate (BBO) crystal used in our experiments, for each propagation direction there are two orthogonally polarized modes with different indices of refraction. The ordinary wave (ϑ) with index of refraction independent of the propagation direction, and the extraordinary wave (e), whose refractive index depends on the angle θ that the propagation direction makes with the optic axis of the crystal. The phase-matching condition (4.2) can be separated into components giving

$$\begin{aligned} \omega_s n_{\vartheta,e}(\omega_s, \theta) \sin \theta_s &= \omega_i n_{\vartheta,e}(\omega_i, \theta) \sin \theta_i \\ \omega_s n_{\vartheta,e}(\omega_s, \theta) \cos \theta_s + \omega_i n_{\vartheta,e}(\omega_i, \theta) \cos \theta_i &= \omega_p n_{\vartheta,e}(\omega_p, \theta) \cos \theta_p, \end{aligned} \quad (4.3)$$

where the first equation is for the component perpendicular to the pump beam direction and the second is the parallel component. The norm of the wave vector is $|\mathbf{k}| = n\omega/c$. The index of refraction of each mode must take into account if its polarization is ordinary or extraordinary. These equations can be solved, together with the frequency matching, for the angle of the optic axis θ of the crystal fixing any combinations of ordinary and extraordinary polarization for the

three waves. If the polarization of the two converted beams is the same, the phase-matching is said to be of type-I and if they are orthogonal it is said to be of type-II. In type-I SPDC, the generated modes form coaxial cones and two corresponding modes are diametrically opposite because of momentum conservation, as shown in Fig. (4.1)-a). In type-II SPDC, two cones for the two different polarizations are generated. If the crystal orientation satisfies the phase-matching for a input polarization of the pump, the orthogonal polarization will not be able to give rise to SPDC.

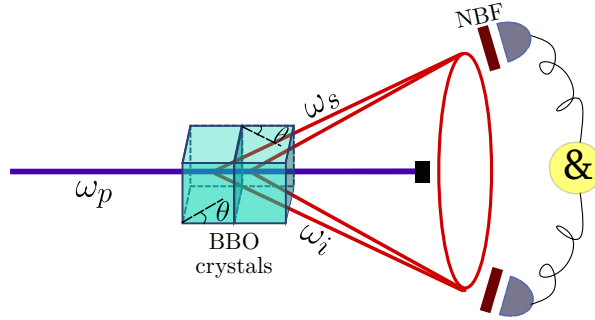


Figure 4.2.: SPDC scheme used in our experiments: two adjacent type-I BBO crystals cut as to attain the same phase-matching, one is rotated of $\pi/2$ relative to the other, such that the phase-matching is obeyed in each crystal by orthogonal polarizations. The crystals are thin enough to generate indistinguishable down-converted photons. The signal and idler detectors are placed symmetrically relative to the pump beam direction and collect the photon pairs with $\omega_s = \omega_i = \omega_p/2$. Only detections in coincidence are considered. Narrow band spectral filters (NBF) are placed in front of each detector.

In our experiments, we use a two-type-I-crystals source of entangled photons [94]. In this source, two thin type-I crystals are put adjacent, such that the pump beam passes through both. The two crystals are identically cut and form the same angle θ with the normal incidence direction, but they are rotated by an angle $\pi/2$ relative to each other such that, for the same propagation direction, the ordinary polarization of the first crystal is in the same direction as the extraordinary polarization of the second one. The phase matching is such that a photon with horizontal polarization (state $|H\rangle_p$) arriving at the first crystal produces two vertically polarized ones $|V\rangle_s|V\rangle_i$, while a vertically polarized pump photon (state $|V\rangle_p$) generates a pair of horizontally polarized photons $|H\rangle_s|H\rangle_i$ in the second crystal. If the two crystals are thin enough, then their cones of down-converted light coincide and the photons generated in one or in the other crystal are indistinguishable. The result is that each pair of photons is generated in a coherent superposition of being created in the first or in the second crystal. If the pump photons are in the superposition $(|H\rangle_p + e^{i\varphi}|V\rangle_p) / \sqrt{2}$, thus for a given pair of corresponding down-converted modes, the polarization state is (up to an irrelevant global phase)

$$\frac{|H\rangle_s|H\rangle_i + e^{i\varphi}|V\rangle_s|V\rangle_i}{\sqrt{2}}.$$

The phase difference φ is due to the thickness of the crystals and can be changed by controlling the phase difference φ_p of the input laser. The desired entangled state can be obtained by placing a QWP at 0° in the pump beam, tilting this wave plate around the vertical axis slightly changes the optical path length inside it, allowing for tuning of the phase φ .

The above described source of pairs of entangled photons can also be used as a single photon source as one of the photons may be used only to herald the presence of the other.

4.1.1. Coherence length

The phase-matching conditions are satisfied by a continuum of pairs of modes. In fact, the SPDC for a single mode pump beam can be effectively described by the interaction Hamiltonian

$$H_I = \sum_{\sigma_s, \sigma_i} \int d\mathbf{k}_s \int d\mathbf{k}_i g_{\mathbf{k}_s, \sigma_s} g_{\mathbf{k}_i, \sigma_i} \delta(\mathbf{k}_s + \mathbf{k}_i - \mathbf{k}_p) \delta(\omega_s(\mathbf{k}_s) + \omega_i(\mathbf{k}_i) - \omega_p(\mathbf{k}_p)) a_{\mathbf{k}_s, \sigma_s}^\dagger a_{\mathbf{k}_i, \sigma_i}^\dagger a_p + H.c., \quad (4.4)$$

where $g_{\mathbf{k}, \sigma}$ depends on the second-order nonlinear coefficient of the media, on the volume of the crystal and on the index of refraction for the mode with wave vector \mathbf{k} and polarization σ . The summation is over the two polarization directions of the converted photons. Operator $a_{\mathbf{k}, \sigma}^\dagger$ creates a photon with wave vector \mathbf{k} and polarization σ , while operator a_p annihilates a photon in the pump mode. *H.c.* stands for Hermitian conjugate. This effective description of the SPDC process is valid under several assumptions, among which are the assumptions of weak power of the pump laser such that the time between two down conversions is relatively large, and that the crystal is large as compared to the wavelength of the three beams [93]. Since the coupling is weak, such that a pump photon passes through the crystal without being absorbed with high probability, there is only a small probability that it can generate a pair of photons and a negligible probability of generating a higher number of photons. Thus, the time evolution operator in the interaction picture can then be approximated by its first order Taylor expansion

$$U(t) = e^{-itH_I} \approx \mathbb{1} - itH_I. \quad (4.5)$$

As a spontaneous process the initial state can be regarded as vacuum in the down converted modes and a strong classical field with amplitude E_p in the pump mode. The non-linearity of the material then produces the two photon state

$$|\psi\rangle = C \left(|vac\rangle - itE_p \sum_{\sigma_s, \sigma_i} \int d\mathbf{k}_s \int d\mathbf{k}_i g_{\mathbf{k}_s, \sigma_s} g_{\mathbf{k}_i, \sigma_i} \delta(\mathbf{k}_s + \mathbf{k}_i - \mathbf{k}_p) \delta(\omega_s(\mathbf{k}_s) + \omega_i(\mathbf{k}_i) - \omega_p(\mathbf{k}_p)) |1_{\mathbf{k}_s, \sigma_s}\rangle |1_{\mathbf{k}_i, \sigma_i}\rangle \right) \quad (4.6)$$

where $|vac\rangle$ is the vacuum state in the down converted modes and $|1_{k,\sigma}\rangle$ is the state with one photon in mode k, σ , C is a normalization constant. The interaction time t is the time for crossing the crystal. As was mentioned before, the photons produced by SPDC are non-monochromatic, rather it is quite the opposite: they are broadband photons. In the experiments, however, the photons are postselected by the position of the detectors whose narrow aperture selects only a narrow range of momenta, thus reducing the spatial and spectral bandwidths considered. Moreover, narrow bandwidth filters are placed in front of the detectors. Also, the vacuum contribution is neglected, since we consider only detections in coincidence between the signal and idler detectors. In particular, we use a pump laser centered at 325 nm and collect the degenerated pairs of photons at 650 nm with a single mode fiber.

The large bandwidth causes the photons to have a quite small coherence length. Roughly speaking, the coherence length is the maximum path difference between two parts of a split beam such that their recombination still gives rise to interference. It is expressed as $l_c \equiv \lambda^2/\Delta\lambda$ and is $\approx 40 \mu\text{m}$ for a 10 nm filter centered around 650 nm. This means that, for example, a diagonal state $|D\rangle = (|H\rangle + |V\rangle)/\sqrt{2}$ separated into horizontal and vertical polarization components and recombined with a path difference much larger than the coherent length will become the mixed state $(|H\rangle\langle H| + |V\rangle\langle V|)/2$.

The finite bandwidth of the converted photons also leads to a time duration of the order of femtoseconds for the converted photons. This also means that they are considered to be detected in coincidence within a time interval of the order of femtoseconds. In the experiment, though, we use a time window of 4 ns. It does not cause photons of different pairs to be considered coincident because of the big interval between down-conversions and it allows for path differences of the order of one meter between photons belonging to the same down-conversion.

4.1.2. Obtaining error bars: Poisson distribution

There are many methods to estimate the error of a measurement. For example, the same measurement can be repeated ideally an infinite number of times at the same conditions and the standard deviation can be regarded as the error associated to the measurement. Another common approach is to theoretically estimate the error from the previous knowledge of the probability distribution behind stochastic results. This last method, called Monte Carlo estimation, is quite useful when the experimentalist does not have access to many repetitions of the measurement. In this case, the mean value over the few measurements realized is used as the mean value of the distribution and a large number of random results is generated artificially from this distribution. The quantities of interest and their standard deviation are then calculated from this artificial experimental data.

SPDC is a very inefficient process and the probability of production of one pair of photons from the coherent state of the pump laser is very small, meaning that $|C|^2$ in Eq. (4.6)

is close to one. The probability of detection in coincidence of a pair of twin photons is further diminished because of the narrow aperture of the detectors and also their efficiency, as well as because of the frequency filters. In this way, the time between two consecutive down-conversions is large enough so that they can be regarded as independent events, as well as two consecutive coincidence detections. Let us consider that in a certain time interval δt there is a probability q of one pair detection and that the probability of detecting two or more pairs in this time interval is negligible. Then, the probability of having n detections in a time interval $T = N\delta t$, with $N > n$, is given by the binomial distribution

$$p(n; T) = \binom{N}{n} q^n (1 - q)^{N-n}, \quad (4.7)$$

where $q^n (1 - q)^{N-n}$ is the probability that the n first time intervals δt are going to register a coincidence count while in the last $N - n$ subintervals the detectors will not click, $\binom{N}{n} = \frac{N!}{n!(N-n)!}$ accounts for all the possible sequences of intervals with clicks and without clicks. Provided that δt is small enough to have at most one detection in this interval, it can be chosen arbitrarily. Thus, one can make it as small as desired while keeping the mean number of detections in the finite time interval T , $\langle n \rangle = Nq$, constant. When this limit is applied to Eq. (4.7), the binomial distribution becomes the Poisson distribution [95]

$$p(n; T) = \frac{e^{-\langle n \rangle} \langle n \rangle^n}{n!}, \quad (4.8)$$

which is a one-parameter distribution that only depends on the mean number of occurrences in the interval T . Knowing that the down-conversion events behave according to a Poisson distribution, Monte Carlo can be applied to produce artificial experimental results. This is done by randomly picking values of n according to the distribution (4.8), with $\langle n \rangle$ being the number of coincidence counts averaged over the few real measurements realized. To get rid of unlikely events coming from the tail of the distribution, which could spoil the mean value, we also eliminate measurements far from the median of the measured values before calculating their mean.

4.2. Generating path entanglement

In the works presented in the following chapters, we use discrete path degrees of freedom generated by beam displacers. A beam displacer (BD) is a birefringent crystal cut as to separate an input beam with arbitrary polarization into two orthogonally-polarized parallel beams as shown in Fig. 4.3.

The device is a parallelepipedic piece of a uniaxial crystal with optical axis (AB direction in the Figure) orthogonal to one of the input-face edges and making a $\pi/2 - \theta$ angle with the other edge. Let us define horizontal the polarization in the \hat{y} direction and vertical the one in the \hat{x} direction. A beam propagating in air in the \hat{z} direction reaches the BD perpendicularly to the input face. Snell's law guarantees that the two refracted beams will have wave vectors also in the \hat{z} direction as the incidence angle is 0° . If the BD is oriented in the way shown in Fig. 4.3-a), the horizontal polarization is perpendicular to the optical axis and will be the ordinary wave, which has energy propagation in the same direction of the wave vector (see Appendix (A)). The vertical polarization, on the other hand, is the extraordinary wave (only the electric displacement remains vertical inside the material) and the energy propagates with angle α with respect to the wave vector given by Eq. (A.6) (Appendix (A)). After leaving the crystal the two beams keep having wave vectors in the \hat{z} direction, therefore propagating parallel to each other, but now their centers are vertically separated, with separation d determined by the angle θ and the length ℓ of the crystal. For example, the BDs used in our experiments are made of calcite ($n_o = 1.658$, $n_e = 1.486$ [96]) cut at $\theta = 45^\circ$ and length of 2.5 cm, what gives separation angle $\alpha = 6.25^\circ$ and final separation of 2.7 mm. If the crystal is oriented as in Fig. 4.3-b), then the horizontal polarization turns out to be the extraordinary wave and the two beams come out the BD horizontally separated. If the BD is tilted around \hat{z} by an angle ϕ , then combinations of horizontal and vertical polarizations will come out displaced along a line also rotated by ϕ .

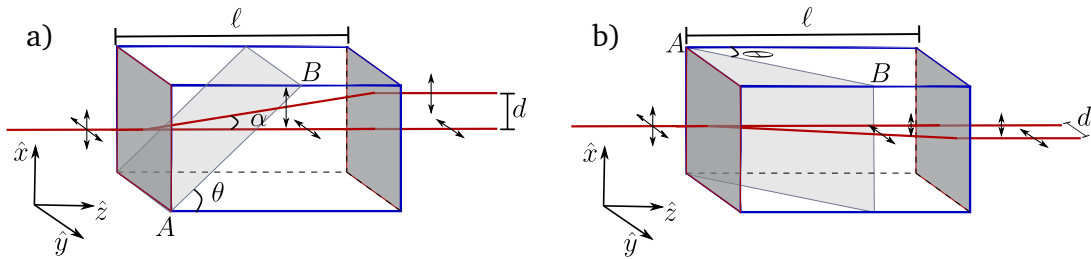


Figure 4.3.: Beam displacer operating in the **a)** vertical and **b)** horizontal polarizations.

Given that the input beam is collimated and narrow compared to the final separation, then the two diffracted beams define two independent non-overlapping path modes we label simply by 0 and 1. For a photon, these two spatial modes are two orthogonal states we represent by $|0\rangle$ and $|1\rangle$, reducing the continuous momentum degree of freedom to a discrete two level one. Moreover, if a photon pass through a BD starting in a state $(\alpha|H\rangle + \beta|V\rangle) \otimes |0\rangle$, after the BD it will become $\alpha|H\rangle|1\rangle + \beta|V\rangle|0\rangle$, considering the BD as in Fig. 4.3-b), creating entanglement between the polarization and path degrees of freedom. Actually, this description is only effective. The index of refraction for each beam is different causing an optical path difference of $\ell(n_o - n_e)$ that in our case is larger than the coherence length of the down-converted photons we use. As one path is delayed relatively to the other, this generates a temporal degree of freedom and the state after the BD would be better described as $\alpha|H\rangle|1\rangle|t_0\rangle + \beta|V\rangle|0\rangle|t_1\rangle$, where $|t_0\rangle$

and $|t_1\rangle$ not necessarily are orthogonal but have a small overlap. Thus, as we access only the polarization and momentum degrees of freedom and trace out the temporal one, the photons do not leave the BD in a pure state, but in a convex combination of $|H\rangle|1\rangle$ and $|V\rangle|0\rangle$. The pure state is recovered if one retrieves the possibility of interfering the two paths, i.e., coherently recombine them, recovering the out-of-diagonal terms of the density matrix. This is done by using a second BD exactly equal the first one generating the same delay to the previously non-displaced path. To recombine the paths it is necessary to use a HWP to interchange the beams polarization such that different beams are deviated in each BD and both acquire the same total phase (see Fig. 4.4-a). Now, using a second HWP we can measure the polarization in diagonal basis for example and check for interference while changing the phase difference ϕ .

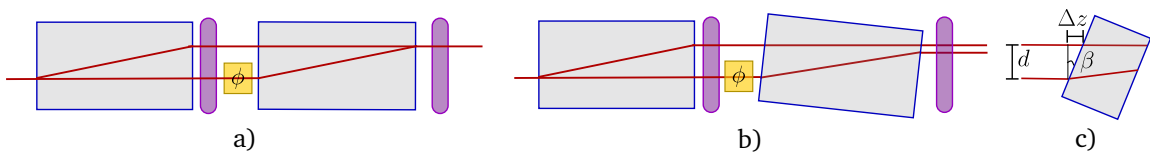


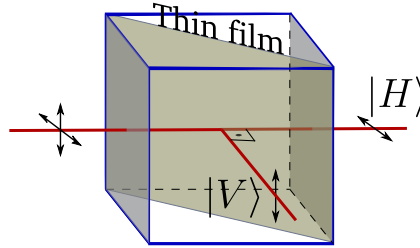
Figure 4.4.: Representation of an interferometer constructed with two BDs. **a)** shows a perfectly aligned scenario, **b)** shows an extreme case when a tilt of the second BD causes the two beams to not overlap and **c)** shows in detail the path difference caused by the tilt.

If the two BDs are not well aligned as shown in Fig. 4.4-b), the angle between the wave vector and the optical axis will be different affecting the relative angle between the two beams and possibly causing them to not overlap and consequently not interfere at the output. This absence of overlap or a partial overlap happens only in extreme cases when the angle of tilt is considerably large. In a case of slight misalignment, the angle of deviation is pretty much not affected [97], and what influences the most in the attainment of the expected state at the output of the second BD is the phase difference caused by the path difference Δz , exaggerated in Fig. 4.4-c). The phase difference, given by $\Delta\phi = \frac{2\pi}{\lambda}\Delta z = \frac{2\pi}{\lambda}d \tan \beta$, varies from zero to 2π with a small variation of approximately 2.5×10^{-4} rad in the tilt angle β when $d = 2.7$ mm and $\lambda = 650$ nm. This example shows the sensitivity of the two BD interference with the relative tilt between them. In an experiment, after a naked eye alignment, the second beam displacer is tilted until a region of maximal visibility of interference is found, this means that the beams are completely overlapping. Inside this region, the second BD is placed in a position for which we have a maximal or minimal power, depending on the projection we are realizing at the output.

4.3. Projective measurements

Ideally one would like to be able to perform any projective measurement in both degrees of freedom available. A projective measurement in polarization is realized by means of a polarizing beam splitter (PBS). A PBS (see Fig. 4.5) is composed by two triangular prisms

made of the same transparent glass and glued together in their hypotenuses. In the interface between the two prisms there is a thin film layer designed such that the polarization component parallel to the interface is completely reflected and the other is completely transmitted [98]. In this way this device separates the horizontal and vertical polarization components of the input beam in two orthogonal beams, horizontal polarization being transmitted and vertical polarization being reflected. Then, a PBS naturally provides a projective measurement in the basis $\{|H\rangle, |V\rangle\}$.



?figurename? 4.5.: Polarizing beam splitter.

It is possible to use a PBS also to project a polarization state into any basis of the polarization Hilbert space if wave plates are used to transform this basis into $\{|H\rangle, |V\rangle\}$. Indeed, it is possible using the minimum set of a QWP followed by a HWP. In order to understand this protocol easily, let us visualize the effect of a HWP and a QWP in the Poincaré sphere representation. In this representation, a general polarization state $\mathbf{E} = E_0 (\cos(\theta/2), e^{i\phi} \sin(\theta/2))$ becomes the normalized 3D vector

$$\hat{\mathbf{r}}_{\mathbf{E}} = (\cos \theta, \sin \theta \cos \phi, \sin \theta \sin \phi), \quad (4.9)$$

whose components are the mean values of the Pauli matrices $(\langle \sigma_z \rangle, \langle \sigma_x \rangle, \langle \sigma_y \rangle)$ normalized by the total intensity [99]. It turns out that the angle between this vector and the x axis is θ and the angle between the vector projection in the yz plane and the y axis is ϕ , as illustrated in Fig. 4.6-a). All the linear polarization states lie in the equator of the sphere, while the circularly polarized ones are situated in the poles. By calculating the Poincaré vector after the action of a half wave plate with optical axis forming angle γ with the vertical [Eq. (1.4)], it is easy to show that it is equivalent to apply the operator

$$R_{\lambda/2}(\gamma) = \begin{pmatrix} \cos(4\gamma) & \sin(4\gamma) & 0 \\ \sin(4\gamma) & -\cos(4\gamma) & 0 \\ 0 & 0 & -1 \end{pmatrix} \quad (4.10)$$

to the initial Poincaré vector (4.9). This matrix is a reflection with respect to the x axis of the Poincaré space along with a rotation of 4γ about the z axis. Analogously, the action of a QWP at angle α [Eq. (1.5)] in Poincaré space is obtained as the operator

$$R_{\lambda/4}(\alpha) = \begin{pmatrix} \cos^2(2\alpha) & \sin(2\alpha)\cos(2\alpha) & \sin(2\alpha) \\ \sin(2\alpha)\cos(2\alpha) & \sin^2(2\alpha) & \cos(2\alpha) \\ -\sin(2\alpha) & \cos(2\alpha) & 0 \end{pmatrix}, \quad (4.11)$$

which represents a $\pi/2$ rotation around the equator vector $(\cos(2\alpha), \sin(\alpha), 0)$.

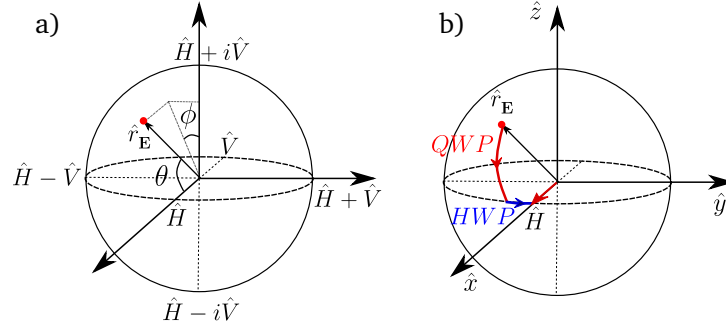


Figure 4.6.: **a)** Polarization state representation in the Poincaré sphere. **b)** Geometric representation of the transformation of an arbitrary state into horizontal polarization: first a QWP rotates the state to the equator and then a HWP rotates it to the horizontal state.

The transformation of any polarization state (4.9) into the horizontally polarized state $(1, 0, 0)$ can be made in two steps represented in Fig. 4.6-b):

1. Apply a QWP to the state with an angle such that the final state has null z -component, lying in the equator of the Poincaré sphere. It is achieved if the wave plate angle is chosen as to satisfy $\tan(2\alpha) = \tan \theta \cos \phi$. The resulting state is

$$\begin{pmatrix} \cos \theta' \\ \sin \theta' \\ 0 \end{pmatrix} = \begin{pmatrix} \cos^2(2\alpha) \cos \theta + \sin(2\alpha) \sin \theta [\cos(2\alpha) \cos \phi + \sin \phi] \\ \sin^2(2\alpha) \sin \theta \cos \phi + \cos(2\alpha) [\sin(2\alpha) \cos \theta + \sin \theta \sin \phi] \\ 0 \end{pmatrix}$$

2. Apply a HWP to the resulting state rotating it about the z axis and vanishing the second component. It is attained if the angle is $\gamma = \theta'/4$.

Thus for a photon, after the combination of waveplates just described, the original state $|\theta, \phi\rangle = \cos(\theta/2)|H\rangle + e^{i\phi} \sin(\theta/2)|V\rangle$ becomes $|H\rangle$ and is transmitted by a PBS, as well as its orthogonal state is transformed in $|V\rangle$ being reflected. If it is desirable to really make a projection, producing state $|\theta, \phi\rangle$ after the measurement, one can reprepare the state using the inverted sequence HWP+QWP at angles $-\gamma$ and $-\alpha$.

The procedure was presented with this order of wave-plates to facilitate its geometrical visualization. Nevertheless, it could be made in the changing the order of HWP and QWP. For some states it is direct to see this possibility. For example, to project over any state in the equator, only a rotation around z is required. The HWP can be used for this purpose and the

QWP may come after it if set to $\alpha = 0$. Another example, projecting over the right and left polarized states in the poles require a $\pm\pi/2$ rotation about y axis, which is achieved by a QWP with $\alpha = \pm 45^\circ$. Placing a HWP at 0° before this QWP only changes the sign of the angle α since it causes a minus sign in the vertical component.

4.3.1. Path degree of freedom

One could directly have access to the intensity of each path, however it is necessary to project over arbitrary path states to have access to quantum superpositions of the momentum. It is possible by mapping the path state into a polarization state. As discussed in Sec. 4.2, careful alignment of two BDs enables the coherent recombination of the two path modes. Consider the particular case where the incoming photons in the measurement stage in Fig. 4.7 are in a separable state $(a|0\rangle + b|1\rangle)(c|H\rangle + d|V\rangle)$ ². Then the lower path ($|0\rangle$) path passes through a HWP set at 45° , which converts $|H\rangle$ into $|V\rangle$ and vice-versa. A HWP at 0° is placed in the upper path ($|1\rangle$) to guarantee the coherence between the two paths by ensuring no optical-path-length difference. When the photons pass through the BD, a new path is created and the state becomes $ac|0\rangle|V\rangle + d|1\rangle(a|H\rangle + b|V\rangle) + bc|2\rangle|H\rangle$ (assuming perfect coherent combination of paths). Thus, the initial path state is transferred to the polarization state of mode $|1\rangle$ and measurements on polarization as explained before give access to the path state.

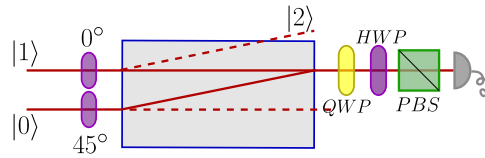


Figure 4.7.: Path state measurement: the path state is mapped to polarization and a projective measurement of polarization is performed.

4.4. Unitary transformations

A unitary transformation of a qubit is equivalent to a rotation in the Bloch sphere. As such, it can be specified by the rotation axis, determined by the unit vector $\mathbf{n} = (n_1, n_2, n_3)$, and by the rotation angle ξ . It is expressed as

$$U = e^{-i\frac{\xi\mathbf{n}\cdot\boldsymbol{\sigma}}{2}} = \cos\frac{\xi}{2}\mathbb{1} - i\sin\frac{\xi}{2}(\mathbf{n}\cdot\boldsymbol{\sigma}) \quad (4.12)$$

²This is the only case we consider here since it is what we have in all the experiments.

or in matrix form

$$U = \begin{pmatrix} \cos \frac{\xi}{2} - in_3 \sin \frac{\xi}{2} & -\sin \frac{\xi}{2}(in_1 + n_2) \\ -\sin \frac{\xi}{2}(in_1 - n_2) & \cos \frac{\xi}{2} + i \sin \frac{\xi}{2} \end{pmatrix}. \quad (4.13)$$

As a unit vector, \mathbf{n} is specified by two spherical-coordinates angles. Thus, any unitary operator for a qubit is completely characterized by three parameters. A configuration of optical elements devised to implement any unitary transformation over a photon polarization qubit should provide also this number of parameters to be changed as to produce any values for ξ and \mathbf{n} . In fact, the combination (QWP@ α_1)-(HWP@ γ)-(QWP@ α_2), represented in Fig. 4.8, is able to realize the unitary transformation given that the waveplate angles are chosen to satisfy

$$\cos \frac{\xi}{2} = \cos \Theta \cos \Delta \quad n_1 = \frac{\sin \Theta \cos \Delta}{\sqrt{\Omega}} \quad (4.14)$$

$$n_2 = \frac{\cos \Theta \sin \Delta}{\sqrt{\Omega}} \quad n_3 = \frac{\sin \Theta \sin \Delta}{\sqrt{\Omega}} \quad (4.15)$$

with $\Theta = \alpha_1 - \alpha_2$, $\Delta = 2\gamma - (\alpha_1 + \alpha_2)$, and $\Omega = 1 - \cos^2 \Theta \cos^2 \Delta$. This can be verified directly calculating the product of the waveplate operators.

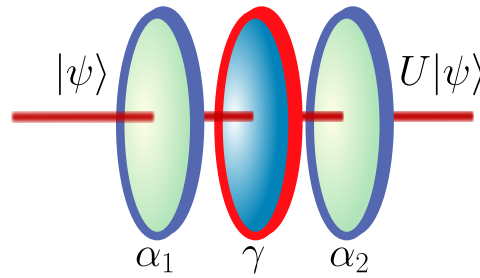


Figure 4.8.: Unitary operator implementation on a polarization qubit: a light beam with initial polarization state $|\psi\rangle$ passes through a sequence of a QWP, a HWP and finally another QWP with angles chosen to implement the unitary transformation U .

EXPOSURE OF SUBTLE MULTIPARTITE QUANTUM NONLOCALITY

Quantum systems can exhibit correlations that are stronger than the ones allowed by classical physics, which can be classified as entanglement, steering or Bell nonlocality depending on the level of characterization of the parties involved. The definition of such quantum correlations relies on the violation of a classical model. In this work, we show an inconsistency on the current multipartite definition of steering and Bell nonlocality. Namely, we show an apparent creation of such correlations by applying a local operation on a system that is initially believed to be uncorrelated. The inconsistency comes from the fact that local operations are not able to increase or create nonlocal correlations. This leads to a redefinition of these correlations, according to which the conflicting models are allocated a subtle form of correlation, which is exposed – as opposed to created – by the local operations. Finally, we provide the first experimental demonstration of both steering and Bell nonlocality exposure with three photonic qubits.

This work was done in collaboration with professors Leandro Aolita, Gabriel Aguilar and Stephen Walborn, and with postdocs Márcio Taddei and Ranieri Nery, all at UFRJ at the time the research was developed. I contributed to the design of the experiment, and I was the main experimentalist in the execution of the experiment and analysis of data. The paper was submitted to *Physical Review X* and a preprint can be found in [100].

5.1. Introduction

Three forms of quantum correlations occur in nature — entanglement, Bell nonlocality and steering. The distinction between them is given by the level of trust and control that one has on the systems involved, as depicted in Fig. 5.1. Entanglement (Fig. 5.1-c)), for instance, is naturally formulated in the so-called device-dependent (DD) scenario [101]. There, one as-

sumes that the system can be completely characterized by the measurement apparatus, at least in principle. Thus, in this scenario, the quantum state of the system is known and entanglement is defined as the impossibility of finding a separable model for the global state. Bell nonlocality (Fig. 5.1-d)), in contrast, takes place in the device-independent (DI) description [102]. There, measurement devices are treated as untrusted black boxes whose actual measurement process is uncharacterized or ignored, relying only on classical measurement settings (inputs) and results (outputs). Here the description is given by the probability distribution of the outcome results given the measurement choice. Quantum steering (Fig. 5.1-e)), on the other hand, is a hybrid type of correlation – intermediate between entanglement and Bell nonlocality – that arises in semi-DI settings [31, 103, 104]. The latter involves both DD and DI parties. In this case, the total system is described by a hybrid mathematical object involving probability distributions and quantum states, the so called assemblage which is presented in the next section.

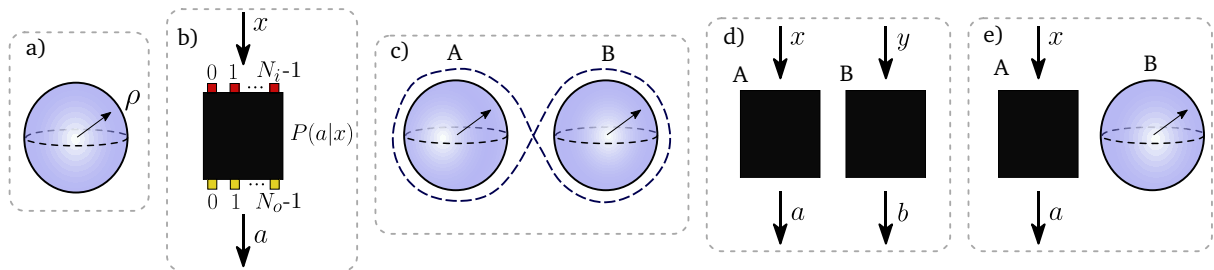


Figure 5.1.: *The different levels of characterization of a quantum system: a) the device-dependent scenario in which the system is completely characterized and its quantum state ρ is known, here represented by a point inside a qubit Bloch sphere (obviously the system could have any dimension); and b) the device-independent scenario in which only the labels of measurement settings $x \in \{0, 1, \dots, N_o - 1\}$ and the labels of measurement outcomes $a \in \{0, 1, \dots, N_i - 1\}$ are known, the underpinning mechanism being ignored, in this case the conditional probabilities $P(a|x)$ are the only accessible information about the system. The scenarios of the three forms of quantum correlations for a bipartite system: c) entanglement, d) Bell nonlocality, e) quantum steering.*

Whereas entanglement is a resource for DD applications in quantum information, Bell nonlocality is the key resource for DI applications such as DI quantum key distribution [105–108] and DI certified randomness [109–112], which are typically much more experimentally demanding than the corresponding DD protocols. Steering is known to be the crucial resource for key technological applications in the semi-DI scenario, which are generally less technically difficult than their DI counterparts, while requiring less assumptions than the corresponding DD protocols. These include semi-DI entanglement certification [31, 104, 113, 114], quantum key distribution [115, 116], certified-randomness generation [117], quantum secret sharing [118, 119], as well as other useful protocols in multipartite quantum networks [120]. Moreover, there are tasks for which the presence of steering, i. e. the capability of a entangled state to present steering, gives the minimum amount of entanglement necessary for that task to be successful.

An example of this is the subchannel identification task using a probe and an ancilla which are entangled, if only local measurements and classical communication are allowed, then only steerable states are useful [121].

These applications, as well as fundamental interest, motivated the development of a resource theory of steering [122, 123]. Resource theories constitute formal treatments of a physical property as a resource, providing a complete toolbox for its quantification, classification, and operational manipulation (see, e.g., [124–126]). They have been formulated for entanglement [101] and Bell nonlocality [127–130], as well as for other interesting quantum properties [130–135]. The cornerstone of any resource theory is the set of its *free operations*. These are unable to create the resource: they transform every resourceless state into a resourceless state.

Interestingly, their study in fully-DI multipartite scenarios has revealed an operational inconsistency at the very heart of the theory [127, 136]. A fully DI description is cast in terms of a *Bell behavior*, given by a conditional probability distribution of the outputs given the inputs. The inconsistency is that, in a tripartite DI scenario, operations that are local in AB can map tripartite Bell behaviors that are local in the $AB|C$ bipartition into bipartite Bell behaviors that violate a Bell inequality across $AB|C$. Bell locality implies that there exists a local-hidden-variable (LHV) model, in which correlations are explained by a (hypothetical) classical common cause (the hidden variable) within the common past light-cone of the measurement events [4]. Any Bell-inequality violation implies incompatibility with LHV models, i.e. Bell nonlocality. The observation above thus seems contradictory, as local wirings within AB are free operations of Bell nonlocality in $AB|C$ and therefore unable to increase Bell-inequality violations. The problem, however, lied in the definition of Bell nonlocality in multipartite scenarios used previously [137].

According to the traditional definition [137], Bell nonlocality across a system bipartition is incompatible with any LHV model with respect to it. This includes so-called “fine-tuned” models [138] with hidden signaling. These are LHV models where, for each value of the hidden variable, the subsystems on each side of the bipartition communicate, but for which the statistical mixture over all values of the hidden variable renders the observable correlations non-signaling. The problem is that the bilocal wiring (taking the output of one black-box as the input of the other) can conflict with the hidden communication in such models, giving rise to a causal loop. For instance, to physically implement the wiring, Bob must be in the causal future of Alice, which is inconsistent with hidden communication from Bob to Alice. This explains why apparently bilocal behaviors can lead to Bell violations after a bilocal wiring. A redefinition of multipartite Bell nonlocality was then proposed [127, 136]. This considers the correlations from conflicting bilocal models already nonlocal across the bipartition, so that the wiring simply exposes an already-existing subtle form of Bell nonlocality. We refer to the latter

form and effect as *subtle Bell nonlocality* and *Bell-nonlocality exposure*, respectively.

The redefinition fixed the inconsistency, but also opened several intriguing questions. First, no experimental observation of Bell-nonlocality exposure has been reported. Second, even though steering theory is relatively mature [116, 139–142], little is known about *steering exposure*. Operational consistency relative to steering exposure was considered, in particular, in a definition of multipartite steering [116], but based on models where each party is probabilistically either trusted or untrusted. On the other hand, a definition based on multipartite entanglement detection in semi-DI setups with fixed trusted-versus-untrusted divisions was proposed in Ref. [143]. There, bilocal hidden-variable models (for multipartite assemblages) with an explicit quantum realization are considered, which automatically rules out potentially-conflicting fine-tuned models. Nevertheless, this has the side-effect of over-restricting the set of unsteerable assemblages, thus potentially over-estimating steering. Third, exposure as a resource-theoretic transformation is yet unexplored territory. For instance, is it possible to obtain every bipartite assemblage via exposure from some multipartite one? What about Bell behaviors? Moreover, is there a single N -partite assemblage from which all bipartite ones are obtained via exposure?

These are the questions we answer. To begin with, we show that, remarkably, exposure of quantum nonlocality is a universal effect, in the sense that every bipartite Bell behavior (assemblage) can be the result of Bell-nonlocality (steering) exposure starting from some tripartite one. This highlights the power of exposure as a resource-theoretic transformation. However, we also delimit such power: we prove a no-go theorem for multi-black-box universal steering bits: there exists no single N -partite assemblage (with $N - 1$ untrusted and 1 trusted devices) from which all bipartite ones can be obtained through free operations of steering. Interestingly, in the universal steering exposure protocol, the starting behavior is not guaranteed to admit a physical realization, i.e. it may be supra-quantum [144–146]. Therefore, we also derive an example that is manifestly within quantum theory. Moreover, we show that the output assemblage of such protocol is not only steerable but also Bell nonlocal (in the sense of producing a nonlocal behavior upon measurements by Charlie). This is notable as Bell nonlocality is a stronger form of quantum correlation than steering. We refer to this effect as *super-exposure of Bell nonlocality*. In turn, we provide a redefinition of (both multipartite and genuinely multipartite) steering to re-establish operational consistency. Finally, we experimentally demonstrate exposure as well as super-exposure. This is done using three degrees of freedom of two entangled photons generated by spontaneous parametric down conversion, in a deterministic protocol.

This chapter is organized as follows: in Section 5.2 the basic concepts related to quantum steering are presented, including the current definition of multipartite steering, postquantum steering, resource theory of steering and the methods we use to detect and quantify steering in the following sections. In the sequence, the general steering and Bell nonlocality exposure

protocols are presented together with a quantum realizable example in Section 5.3. In Section 5.4 the experimental implementation and experimental results are shown. Lastly, the proposed redefinition of multipartite quantum steering is given in Section 5.5, this redefinition removes any inconsistency with the resource theory of steering.

5.2. Steering and the semi-DI setting

The concept of quantum steering originates with the beginning of the quantum theory. The name "steering" is attributed to Schrödinger who was studying the possibility of producing different ensembles of quantum states at a distance [147] by performing local measurements. The formal treatment of steering though was given only recently for a bipartite system [113, 114].

The scenario in which quantum steering is defined for a bipartite system is as follows. A two-party system is shared between Alice and Bob. Alice cannot characterize her measurement device such that all the information she has is the classical input x she gives to the device and the classical output a . That is, Alice holds a black box with N_o possible choices of untrusted measurements she can perform, and for each input N_i different results can come out with probability $P_{a|x}$ conditioned to the input. On the other hand, Bob can realize tomographic measurements upon his particle to figure out what is the quantum state he holds. If he performs quantum state tomography conditioned to Alice's input and output, then what he gets is a conditional state $\rho_{a|x}$, a state that has been prepared by Alice at a distance while performing her local measurements.

In this setting, the global system is completely characterized by a mathematical object called an assemblage $\sigma = \{\sigma_{a|x}\}_{a,x}$ defined as the set of sub-normalized states such that $\text{Tr}[\sigma_{a|x}] = P_{a|x}$ and $\sigma_{a|x}/\text{Tr}[\sigma_{a|x}] = \rho_{a|x}$ containing all the combinations of inputs and outputs. If the joint system is in a quantum state ρ^{AB} then the assemblage elements are obtained as $\sigma_{a|x} = \text{Tr}_B[(M_{a|x} \otimes \mathbb{1})\rho^{AB}]$ considering that Alice's action is described by the measurement operators $M_{a|x}$. However, because of the semi-device independence, the global state is unknown. We assume that σ satisfies the no-signaling (NS) principle, by virtue of which measurement-outcome correlations alone do not allow for communication. This physical situation imposes the non-signaling condition to the assemblage

$$\sum_a \sigma_{a|x} = \sum_a \sigma_{a|x'} = \varrho^{(B)}, \quad (5.1)$$

which means that if Bob does not know Alice's output (and he does not without explicit communication) he cannot infer anything about her input. Moreover, the normalization of Alice's

probabilities require

$$\mathrm{Tr} \left[\sum_a \sigma_{a|x} \right] = 1 \quad \forall x. \quad (5.2)$$

The correlation between Alice's measurement and Bob's states is classified as quantum steering if it cannot be explained by a classical model. On the other hand, the assemblage σ is said to be unsteerable if its elements admit a classical explanation in terms of a classical hidden stochastic variable

$$\sigma_{a|x} = \sum_{\lambda} P_{\lambda} P_{a|x,\lambda} \varrho_{\lambda}, \quad (5.3)$$

i.e., a classical stochastic variable λ is distributed to Alice and Bob with probability P_{λ} , this variable is the local common cause for Alice's probability distribution and for Bob's state. They do not have access to this hidden variable and after unavoidably averaging their assemblage over it, it seems that the quantum states are nonlocally correlated to the measurements. The description (5.3) is called local hidden state (LHS) model.

5.2.1. Multipartite steering

The multipartite scenario is considerably richer than the bipartite one. For the simplest case of three parties, the semi-device independent setting allows for two configurations, either 1DD-2DI or 2DD-1DI, as shown in Fig. 5.2. In this work we focus in the former since it is enough to show the inconsistency in the current definition of steering. Such systems are fully described by a Bell behavior $\mathbf{P}^{(AB)} := \{P_{a,b|x,y}\}_{a,b,x,y}$, with $P_{a,b|x,y}$ the conditional probability of outputs a, b given inputs x, y , for Alice and Bob, and an ensemble of conditional quantum states $\varrho_{a,b|x,y}$ for Charlie. These can be encapsulated in the assemblage $\sigma := \{\sigma_{a,b|x,y}\}_{a,b,x,y}$, of sub-normalized conditional states $\sigma_{a,b|x,y} := P_{a,b|x,y} \varrho_{a,b|x,y}$. The NS-principle implies that the statistics observed by any subset of users should be independent of the input(s) of the remaining user(s). Mathematically, this condition reads

$$\sum_a \sigma_{a,b|x,y} = \sigma_{b|y}^{(BC)}, \quad \forall b, x, y, \quad (5.4a)$$

$$\sum_b \sigma_{a,b|x,y} = \sigma_{a|x}^{(AC)}, \quad \forall a, x, y, \quad (5.4b)$$

$$\sum_a \sigma_{a|x}^{(AC)} = \sum_b \sigma_{b|y}^{(BC)} = \varrho^{(C)}, \quad \forall x, y, \quad (5.4c)$$

where $\sigma^{(AC)} := \{\sigma_{a|x}^{(AC)}\}_{a,x}$ and $\sigma^{(BC)} := \{\sigma_{b|y}^{(BC)}\}_{b,y}$ are respectively the reduced assemblages on the AC and BC subsystems, and $\varrho^{(C)}$ is the reduced state on C .

Unlike in Bell nonlocality or entanglement, semi-DI systems have a natural bipartition: the one separating the trusted devices from the untrusted ones. This is the bipartition with respect to which we define steering throughout, unless otherwise explicitly stated. According

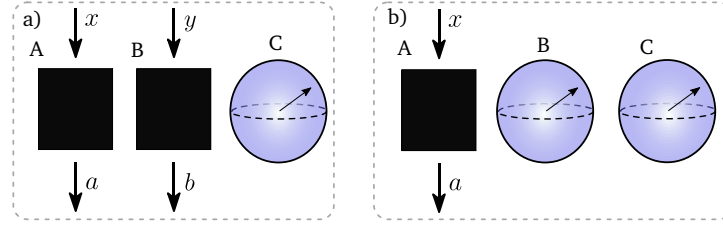


Figure 5.2.: Possible semi-device independent settings: a) Two black boxes (A and B) and a trustful device (C), i.e. 1DD-2DI, and b) one black box (A) and two quantum systems (B and C), i.e. 2DD-1DI.

to the standard definition [104], σ is unsteerable if it admits a local hidden-state (LHS) model, namely, if it can be decomposed as

$$\sigma_{a,b|x,y} = \sum_{\lambda} P_{\lambda} P_{a,b|x,y,\lambda} \varrho_{\lambda}. \quad (5.5)$$

Otherwise σ is steerable. Here, P_{λ} is the probability of the hidden variable Λ taking the value λ , each $P_{\lambda}^{(AB)} := \{P_{a,b|x,y,\lambda}\}_{a,b,x,y}$ is a λ -dependent behavior, and ϱ_{λ} is the λ -th hidden state for C (locally correlated with AB only via Λ). Importantly, that σ is non-signaling does not imply that so is each $P_{\lambda}^{(AB)}$. In fact, LHS models can exploit hidden communication between Alice and Bob as long as actual communication at the observable level (i.e. upon averaging Λ out) is impossible. This effect is known as fine-tuning [138]; the standard definition of steering imposes no restriction on fine-tuned LHS models. This turns out to be critical. Indeed, we will see that unrestricted hidden signaling is responsible for a stark conflict with the reasonable expectation that local operations should not increase inter-party correlations.

The definition of steering as the violation of Eq. (5.5) is concerned only with the joint capability of Alice and Bob to steer Charlie's state, without making any reference to the mechanism responsible for it. If a violation of that model occurs, it could be the case that only Alice is correlated to Charlie or only Bob or both. Also, although they do not have the ability to steer Charlie, the joint probability of Alice and Bob $P_{a,b|x,y,\lambda}$ can in principle be non factorizable. In the particular case of a fully separable quantum state $\rho_{sep}^{ABC} = \sum_{\lambda} P_{\lambda} \varrho_{\lambda}^A \otimes \varrho_{\lambda}^B \otimes \varrho_{\lambda}^C$ with the realization of the local measurements $\{M_{a|x}^A\}_{a,x}$ and $\{M_{b|y}^B\}_{b,y}$ in the parties A and B , respectively, the assemblage obtained is always unsteerable and moreover the Bell behavior is separable

$$\sigma_{a,b|xy} = \text{Tr}_{AB} \left[\left(M_{a|x}^A \otimes M_{b|y}^B \otimes \mathbb{1} \right) \rho_{sep}^{ABC} \right] = \sum_{\lambda} P_{\lambda} P_{a|x,\lambda} P_{b|y,\lambda} \otimes \varrho_{\lambda}^C. \quad (5.6)$$

Another extreme case is that of a biseparable state $\rho_{bisep}^{ABC} = \sum_{\nu} P_{\nu} \varrho_{\nu}^A \otimes \varrho_{\nu}^{BC} + \sum_{\mu} P_{\mu} \varrho_{\mu}^{AB} \otimes \varrho_{\mu}^C + \sum_{\lambda} P_{\lambda} \varrho_{\lambda}^B \otimes \varrho_{\lambda}^{AC}$, i. e. a state that is the mixture of states that are separable in at least one bipartition. The violation of a biseparable state model defines genuine tripartite entanglement.

Analogously, a biseparable assemblage model

$$\begin{aligned}\sigma_{a,b|xy} &= \text{Tr}_{AB} \left[\left(M_{a|x}^A \otimes M_{b|y}^B \otimes \mathbb{1} \right) \rho_{\text{bisep}}^{ABC} \right] \\ &= \sum_{\nu} P_{\nu} P_{a|x,\nu} \sigma_{b|y,\nu}^{BC} + \sum_{\lambda} P_{\lambda} P_{b|y,\lambda} \sigma_{a|x,\lambda}^{AC} + \sum_{\mu} P_{\mu} P_{a,b|x,y,\lambda} \varrho_{\mu}^C\end{aligned}\quad (5.7)$$

is when either Alice or Bob can steer Charlie's state (first and second terms in the equation), but not collectively. The violation of such a model defines genuine multipartite steering [143].

5.2.2. Post-quantum steering

In obtaining Eqs. (5.6) and (5.7) we used the fact that the assemblage comes from a quantum state by performing local quantum measurements, but by definition, steering occurs in a semi-device independent scenario in which one does not have trustful information about what measurements are being realized in the black-box parties nor have access to the global quantum state. Possessing only the Bell-behavior $P_{a,b|x,y}$ and the conditional states $\varrho_{a,b|x,y}$ satisfying the positivity condition $\sigma_{a,b|x,y} = P_{a,b|x,y} \varrho_{a,b|x,y} \geq 0$, the normalization condition $\text{Tr} \left[\sum_{a,b} \sigma_{a,b|x,y} \right] = 1$ for all x, y and the no-signaling conditions (5.4), one may ask whether it is possible to find a quantum realization for such assemblage. In other words, given a no-signaling assemblage $\sigma_{a,b|x,y}$, is it always possible to find a tripartite state ρ^{ABC} and local measurement operators $\{M_{a|x}^A\}_{a,x}$ and $\{M_{b|y}^B\}_{b,y}$ such that $\sigma_{a,b|x,y} = \text{Tr}_{AB} \left[\left(M_{a|x}^A \otimes M_{b|y}^B \otimes \mathbb{1} \right) \rho^{ABC} \right]$?

In the bipartite case, the answer to this question is negative as it is always possible to construct the bipartite state and measurement operators yielding to any no-signaling assemblage. This is not true for multipartite assemblages as is shown in [144]. A assemblage for which there is no quantum realization is called postquantum. A trivial example comes when one considers that the Bell-behavior $\{P_{a,b|x,y}\}_{a,b,x,y}$ alone has correlations stronger than the allowed by quantum theory, as is the case of the Popescu-Rohrlich (PR) box where $P_{a,b|x,y} = 1/2$ if $a \oplus b = xy$ and zero otherwise, \oplus is sum modulo 2 [148]. The authors of [144] also show cases for which there is no postquantumness in the Bell-behavior, but still the assemblage is postquantum, showing that it is an intrinsic feature of the assemblage as a whole.

5.2.3. Resource theory of steering

Quantum steering is a resource for quantum information and can be used for many tasks as mentioned before. Accordingly, a resource theory for steering was built a few years ago [122]. For any resource theory it is necessary to define the objects that do not possess the resource, known as free states, and the operations that take any free state into a free state, called free operations. In the case of steering, the free states are those which admit a LHS model. A useful set of free operations is the 1W-LOCCs (one way local operations and classical

communication). Consider a bipartition according to the characterization of the parties, that is, all the DI parties are grouped together in one partition as well as all the DD ones are grouped in another partition. The initial assemblage $\sigma_{A|X}$ is transformed into the final assemblage $\sigma_{A_f|X_f}$. The allowed operations that do not create steering are the following: the quantum partition can perform stochastic generalized measurements over her quantum system and communicate the result to the black-box partition, which can realize the black box measurements and process the classical information at disposal. The classical information processing is called wiring.

Two examples of free operations are shown in Fig. 5.3. In these examples, no quantum operation is realized in the quantum partition and there is no classical communication from this partition to the black boxes. In the black-box partition, classical information, namely the classical inputs and outputs, is processed. It is intuitive that these operations do not create the quantum correlation as they are local in the black-box partition. In the first example in Fig. 5.3-a), Alice and Bob are no longer space-like separated: she communicates her output to him and he uses this to choose his input. This is an example of a bilocal *wiring* (local with respect to the bipartition $AB|C$). The tripartite assemblage becomes equivalent to a bipartite one in the sense that Alice and Bob work as only one black box with input x and output b . In the rest of this work we focus on this simple example and show that, although such operations cannot create any correlations across the bipartition, they can *expose* a subtle form of multipartite quantum nonlocality that otherwise does not violate any Bell or steering inequality across the bipartition. In the second example in Fig. 5.3-b), a 4DI+1DD assemblage is mapped onto a 2DI+1DD one by a bilocal wiring [$x_2 = a_3$, $x_3 = x_4$, and $a'_1 = a_1 \oplus a_2$ (sum modulo 2)], such that the final assemblage has only two classical inputs (x_1 and x_3) and two outputs (a'_1 and a_4).

Such wirings can implement non-trivial resource-theoretic transformations. One could ask whether there exists an N -partite assemblage with $N - 1$ black boxes and one quantum party from which all bipartite ones can be produced, e.g., can be reached by means of reductions on the number of inputs and outputs using classical information processing. Below we this question in the negative. Although powerful, these wiring operations are not enough to enable a multi-black-box universal *steering bit* even allowing for quantum operations and classical communication from the DD party to the DI ones. This is formalized in the theorem below whose demonstration is left to Appendix C.1.

Theorem 1. [No pure steering bit with higher number of parties] *There does not exist any pure $(N - 1)$ -DI qubit assemblage $\sigma_{\mathbf{a}|\mathbf{x}}^{bit}$, where $\mathbf{a} = \{a_1, \dots, a_{N-1}\}$, $\mathbf{x} = \{x_1, \dots, x_{N-1}\}$ (with finite sets of input and output values), that can be transformed via IW-LOCCs into all qubit assemblages of minimal dimension $\sigma_{\mathbf{a}|\mathbf{x}}^{(target)}$.*

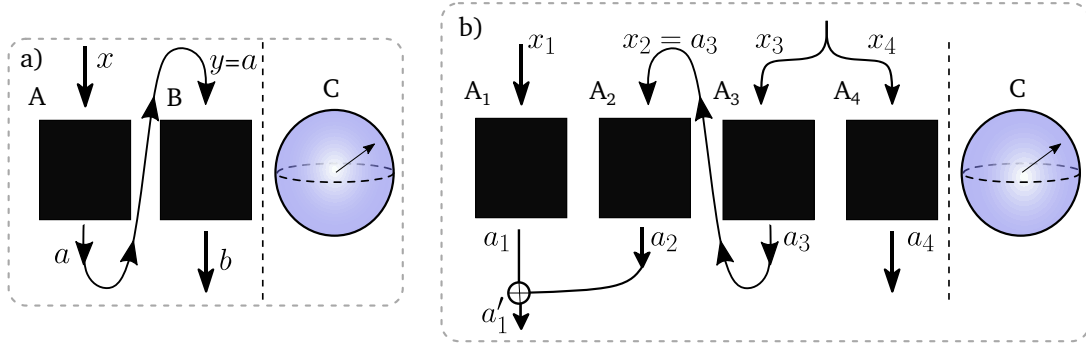


Figure 5.3.: Examples of free operations of steering in scenarios with only one trusted party.

5.2.4. Steering detection, witnesses and quantifiers

In order to detect whether a known assemblage is steerable or not, one can directly use the definition of a non-steerable assemblage as given by Eq. (5.3) for bipartite assemblages or by Eq. (5.5) for a tripartite case. In this way, the problem of steering detection amounts to search for states ϱ_λ and probability distributions P_λ and $P_{a|x,\lambda}$ (we consider here the bipartite case for simplicity) such that the given assemblage can be described by a LHS model, if there do not exist such mathematical objects, then the assemblage is steerable. In principle, this is a hard problem since the sum in Eq. (5.3) has infinitely many terms. However, this problem can be stated in a way that fits the semi-definite programming (SDP) paradigm, a class of linear optimization problems over a convex set of positive semi-definite operators known to be efficiently solvable with developed algorithms.

To begin with, let us consider the deterministic behaviors with one input and one output, that is, the probability distributions such that, given an input, it does not vanish for only one output. Given that the black box has N_i possible inputs and N_o possible outputs, the number of deterministic behaviors is $n = N_o^{N_i}$ and they are written as $D(a|x, \lambda') = \delta_{a,\lambda'(x)}$, where λ' is defined as a string $\lambda' = a_{x=0}, \dots, a_{x=N_i-1}$ with the deterministic outputs related to each input. Any probability distribution $P_{a|x,\lambda}$ can be written as a convex combination of this extreme deterministic behavior with a weight that depends on λ

$$P_{a|x,\lambda} = \sum_{\lambda'=1}^n P_{\lambda'|\lambda} D(a|x, \lambda'). \quad (5.8)$$

Substituting Eq. (5.8) into Eq. (5.3) we get

$$\sigma_{a|x} = \sum_{\lambda'=1}^n D(a|x, \lambda') \sigma_{\lambda'}, \quad (5.9)$$

a finite sum with only a finite number of positive semidefinite objects $\sigma_{\lambda'} = \sum_\lambda P_{\lambda'|\lambda} P_\lambda \varrho_\lambda$ to be determined. In order to transform the problem of trying to find the set $\{\sigma_{\lambda'}\}_{\lambda'}$ into an

optimization, one can define a number μ such that $\sigma_{\lambda'} \geq \mu \mathbb{1}$. Now the question of whether the known assemblage $\{\sigma_{a|x}\}_{a,x}$ is LHS can be written as the SDP

$$\begin{aligned}
 & \text{given } \{\sigma_{a|x}\}_{a,x}, \{D(a|x, \lambda')\}_{a,x,\lambda'} \\
 & \max_{\{\sigma_{\lambda'}\}} \mu \\
 & \text{s.t. } \sum_{\lambda'=1}^n D(a|x, \lambda') \sigma_{\lambda'} = \sigma_{a|x} \quad \forall a, x \\
 & \sigma_{\lambda'} \geq \mu \mathbb{1} \quad \forall \lambda'
 \end{aligned} \tag{5.10}$$

Put in this way, μ is allowed to be a negative number. The program searches for the set $\{\sigma_{\lambda'}\}_{\lambda'}$ which maximizes μ keeping the LHS decomposition for the given assemblage $\{\sigma_{a|x}\}_{a,x}$ valid. Because $\sigma_{\lambda'} \geq 0$ should be valid by definition, if the maximum value of μ is negative, it means that there is no valid LHS decomposition for the assemblage and therefore it is steerable. Otherwise, if the solution for μ is positive, then the assemblage is unsteerable and the program returns its LHS decomposition. Here the problem is written for a bipartite assemblage, but the same statement can be put forward for any number of parties.

The SDP also has a so called dual program obtained by using Lagrange multipliers for each of the constraints. The Lagrangian of the problem is written as

$$\mathcal{L} = \mu + \sum_{a,x} \text{Tr} \left[w_{a|x} \left(\sigma_{a|x} - \sum_{\lambda} D(a|x, \lambda) \sigma_{\lambda} \right) \right] + \sum_{\lambda} \text{Tr} [z_{\lambda} (\sigma_{\lambda} - \mu \mathbb{1})], \tag{5.11}$$

where the first term on the right hand side is the function to be maximized, the second one is related to the first set of constraints in (5.10) and vanishes in the optimal point, the third term represents the second set of constraints in (5.10) and is always bigger than zero if we impose that $z_{\lambda} \geq 0$ for all λ . Thus, the Lagrangian \mathcal{L} is always bigger than μ and its minimum value serves as a good upper bound for μ , in most problems the minimum value of \mathcal{L} is actually equal to the maximum value of μ . Before writing the dual problem as a minimization, some further simplification is possible. Let us rewrite the Lagrangian grouping the terms related to each optimization variable of the primal SDP

$$\mathcal{L} = \sum_{a,x} \text{Tr} [w_{a|x} \sigma_{a|x}] - \sum_{\lambda} \text{Tr} \left[\left(\sum_{a,x} w_{a|x} D(a|x, \lambda) - z_{\lambda} \right) \sigma_{\lambda} \right] + \left(1 - \text{Tr} \left[\sum_{\lambda} z_{\lambda} \right] \right) \mu. \tag{5.12}$$

In the minimum point, the gradient of \mathcal{L} vanishes, thus the partial derivatives relative to each σ_{λ} and also relative to μ are also zero. It means that the coefficients accompanying each of these variables must vanish due to the linearity of the Lagrangian and the independence of the

variables. Explicitly, the optimal point satisfies

$$\mathrm{Tr} \left[\sum_{a,x} w_{a|x} D(a|x, \lambda) - z_\lambda \right] = 0 \quad (5.13)$$

$$1 - \mathrm{Tr} \left[\sum_\lambda z_\lambda \right] = 0. \quad (5.14)$$

By substituting (5.14) in (5.13) and using the restriction that $z_\lambda \geq 0$ for all λ , we get the conditions for the dual minimization problem that eliminate the variables of primal problem: $\mathrm{Tr} \left[\sum_{a,x,\lambda} w_{a|x} D(a|x, \lambda) \right] = 1$ and $\sum_{a,x} w_{a|x} D(a|x, \lambda) \geq 0$. We can finally write down the dual problem as the minimization of the remaining term of the Lagrangian

$$\begin{aligned} & \text{given } \{ \sigma_{a|x} \}_{a,x}, \{ D(a|x, \lambda) \}_{a,x,\lambda} \\ & \min_{\{w_{a|x}\}} \sum_{a,x} \mathrm{Tr} \left[w_{a|x} \sigma_{a|x} \right] \\ & \text{s.t. } \mathrm{Tr} \left[\sum_{a,x,\lambda} w_{a|x} D(a|x, \lambda) \right] = 1 \\ & \sum_{a,x} w_{a|x} D(a|x, \lambda) \geq 0 \quad \forall \lambda. \end{aligned} \quad (5.15)$$

As the minimum of \mathcal{L} coincides with the maximum of μ , only if the assemblage is steerable, the optimal value of the dual program is negative. Moreover, in this case, the solutions $\{w_{a|x}\}_{a,x}$ define a steering witness, i.e., an inequality that, if violated, guarantees that the assemblage is steerable. To see that, let us consider again the decomposition of an LHS assemblage $\sigma'_{a|x} = \sum_\lambda D(a|x, \lambda) \sigma_\lambda$, multiply the second condition in the SDP (5.15) by σ_λ and sum over λ . This results in $\sum_{a,x} w_{a|x} \sum_\lambda D(a|x, \lambda) \sigma_\lambda \geq 0$ or

$$\mathrm{Tr} \left[\sum_{a,x} w_{a|x} \sigma'_{a|x} \right] \geq 0$$

for all LHS assemblages. In particular, this inequality is violated by the steerable assemblage that generated $\{w_{a|x}\}_{a,x}$ since the left hand side is precisely the negative minimized Lagrangian. The inequality can still be manipulated to change the bound or the direction of it.

Although the above methods serve to detect steering they do not quantify it. A good quantifier of steering must vanish for any LHS assemblage and must not increase under 1W-LOCC operations. One such quantifier is the steering robustness which can also be written as an SDP [121]. The steering robustness is defined as the minimum amount of an LHS assemblage or, in other words, the minimum amount of noise that must be mixed to the assemblage under

question such that it becomes LHS, that is

$$\begin{aligned}
 R(\sigma_{a|x}) = & \min_{\{\xi_\lambda\}, \{\sigma_\lambda\}} r \\
 \text{s.t.} & \frac{\sigma_{a|x} + r \sum_\lambda D(a|x, \lambda) \xi_\lambda}{1 + r} = \sum_\lambda D(a|x, \lambda) \sigma_\lambda \quad \forall a, x \\
 & \sigma_\lambda, \xi_\lambda \geq 0 \quad \forall \lambda,
 \end{aligned} \tag{5.16}$$

which is clearly zero if the assemblage $\sigma_{a|x}$ already has an LHS decomposition. Finding the robustness of an assemblage is an optimization problem but it is not a SDP because it is not even linear. In order to linearize it, we define $\xi'_\lambda = r\xi_\lambda$ and $\sigma'_\lambda = (1 + r)\sigma_\lambda$ such that we have $\sigma_{a|x} = \sum_\lambda D(a|x, \lambda) (\sigma'_\lambda - \xi'_\lambda)$ and $r = \text{Tr} [\sum_\lambda \xi'_\lambda]$ due to the normalization $\sum_\lambda \text{Tr} [\xi_\lambda] = 1$. The robustness now can be found by solving the SDP

$$\begin{aligned}
 R(\sigma_{a|x}) = & \min_{\{\xi'_\lambda\}, \{\sigma'_\lambda\}} \text{Tr} \left[\sum_\lambda \xi'_\lambda \right] \\
 \text{s.t.} & \sigma_{a|x} = \sum_\lambda D(a|x, \lambda) (\sigma'_\lambda - \xi'_\lambda) \quad \forall a, x \\
 & \sigma'_\lambda, \xi'_\lambda \geq 0 \quad \forall \lambda.
 \end{aligned} \tag{5.17}$$

Here we choose an LHS noise, but in fact the robustness can be defined relatively to any subset or even to the whole convex set of assemblages [149], for this reason it is better to call (5.17) LHS-robustness. The motive for the name of this quantifier is obvious: the larger the noise that must be added to extinguish the steering, the more robust is the steering present in the assemblage.

All the methods and quantities discussed in this section can be extended to more party assemblages. Although this quantities are well defined, applying them to experimentally recovered assemblages to determine if it is LHS or not may be challenging since this assemblages are not even non-signaling in general. We discuss this issue later in this chapter.

5.2.5. Assemblage Fidelity

To quantify the similarity between two assemblages $\sigma_1 = \{P_1(\mathbf{a}|\mathbf{x})\varrho_1(\mathbf{a}|\mathbf{x})\}$ and $\sigma_2 = \{P_2(\mathbf{a}|\mathbf{x})\varrho_2(\mathbf{a}|\mathbf{x})\}$, we use a mean assemblage fidelity defined by

$$F(\sigma_1, \sigma_2) = \frac{1}{N_x} \sum_{\mathbf{x}, \mathbf{a}} \sqrt{P_1(\mathbf{a}|\mathbf{x})P_2(\mathbf{a}|\mathbf{x})\mathcal{F}(\varrho_1(\mathbf{a}|\mathbf{x}), \varrho_2(\mathbf{a}|\mathbf{x}))}, \tag{5.18}$$

where \mathbf{x} (\mathbf{a}) is a list of inputs (outputs) of all black boxes, N_x is the number of different measurement choices, and

$$\mathcal{F}(\varrho_1, \varrho_2) = \text{Tr} \sqrt{\sqrt{\varrho_1} \varrho_2 \sqrt{\varrho_1}} \quad (5.19)$$

is the usual fidelity between two quantum states. The above defined fidelity can be seen as a mean of the fidelities of the quantum parts weighted by the square root of blackbox probabilities. It has the property of being 1 if all elements of the two assemblages are equal and vanishes if all quantum states are orthogonal.

5.3. Steering exposure and super exposure of Bell-nonlocality

The main result of this work is to show that the current definition of multipartite quantum steering as the violation of model (5.5) is deficient since it presents inconsistencies with the resource theory of steering. We begin by an exposure protocol for steering (Bell nonlocality) that is universal in the sense of being capable of producing any bipartite assemblage (behavior) whatsoever from an appropriate tripartite assemblage (behavior) originally admitting an LHS (LHV) model. As in Ref. [127], we exploit bilocal wirings as that of Fig. 5.3-a), which makes Bob's input y equal to Alice's output a . This requires that Bob's measurement is in the causal future of Alice's. Indeed, after the wiring, systems A and B now behave as a single black box with input x and output b . In other words, exposure is a form of conversion from tripartite correlations into bipartite ones. Here, we restrict to the case of binary inputs and outputs (each one can take only two values) for simplicity, where we prove the following surprising result.

Universal exposure of quantum nonlocality: *Any bipartite assemblage $\sigma^{(target)}$ or Bell behavior $\mathbf{P}^{(target)}$ can be obtained via the wiring $y = a$ on the tripartite assemblage $\sigma^{(initial)}$ or behavior $\mathbf{P}^{(initial)}$, respectively, of elements*

$$\sigma_{a,b|x,y}^{(initial)} := \frac{1}{2} \sigma_{b|x \oplus a \oplus y}^{(target)} \quad (5.20a)$$

or

$$P^{(initial)}(a, b, c|x, y, z) = \frac{1}{2} P^{(target)}(b, c|x \oplus a \oplus y, z), \quad (5.20b)$$

where \oplus stands for addition modulo 2. Moreover, $\sigma^{(initial)}$ and $\mathbf{P}^{(initial)}$ admit respectively an LHS and an LHV models across the $AB|C$ bipartition, for all $\sigma^{(target)}$ and $\mathbf{P}^{(target)}$.

Proof. It is straightforward to check that applying the wiring $y = a$ to Eqs. (5.20a) and (5.20b), the target assemblage and behavior are obtained, i.e., $\sum_a \sigma_{a,b|x,y=a}^{(initial)} = \sigma_{b|x}^{(target)}$ and $\sum_a P^{(initial)}(a, b, c|x, y = a, z) = P^{(target)}(b, c|x, z)$.

It is certainly not evident that the initial correlations are bilocal. To prove this, we construct an explicit LHS model for the source assemblage $\sigma^{(\text{initial})}$. It is given by

$$P_\lambda = \frac{1}{2} \text{Tr} \left(\sigma_{\lambda_0|\lambda_1}^{(\text{target})} \right), \quad \varrho_\lambda = \frac{\sigma_{\lambda_0|\lambda_1}^{(\text{target})}}{\text{Tr} \left(\sigma_{\lambda_0|\lambda_1}^{(\text{target})} \right)}, \quad (5.21)$$

$$P_{a,b|x,y,\lambda} = \delta_{\lambda_0,b} \delta_{\lambda_1,x \oplus a \oplus y}, \quad (5.22)$$

where $\lambda = (\lambda_0, \lambda_1)$ is a two-bit hidden variable.

For the Bell behavior, this expression readily lends itself for a local hidden-variable decomposition of $\mathbf{P}^{(\text{initial})}$ on $AB|C$, $P^{(\text{initial})}(a, b, c|x, y, z) = \sum_\lambda P_\lambda P_{a,b|x,y,\lambda} P(c|z; \lambda)$ with

$$P_\lambda = \frac{1}{2}; \quad P(c|z; \lambda) = P^{(\text{target})}(\lambda_0, c|\lambda_1, z); \quad (5.23)$$

and the same bipartite distribution from Eq. (5.22). \square

When the target assemblage (behavior) is steerable (Bell nonlocal), exposure of steering (Bell nonlocality) is achieved. Furthermore, apart from steerable, assemblages can also be Bell nonlocal in the sense of giving rise to nonlocal behaviors under local measurements [141]. Hence, when $\sigma^{(\text{target})}$ is Bell nonlocal, a seemingly unsteerable system is mapped onto a Bell nonlocal one, which is outstanding in view of the fact that unsteerable assemblages form a strict subset of Bell-local ones.

The protocol above highlights the power of bilocal wirings as resource-theoretic transformations. Remarkably, such wirings compose a strict subset of well-known classes of free operations of quantum nonlocality (across $AB|C$): local operations with classical communication (LOCCs) [101] for entanglement, one-way (1W) LOCCs from the trusted to the untrusted parts [122] for steering, and local operations with shared randomness [127–129] for Bell nonlocality. However, there are also limitations to the power of these wirings. In particular, in Supplementary Section VI we prove a no-go theorem for universal steering bits in the $NDI+1DD$ scenario [exemplified in Fig. 5.3-b) for $N = 4$]. That is, we show there that there is no N -partite assemblage, for all N , from which all bipartite ones can be obtained via arbitrary 1W-LOCCs.

Although the protocol above is universal, it is unclear whether it can actually be physically implemented in general. This is due to the fact that the tripartite initial correlations may be supra-quantum, i.e. well-defined non-signaling correlations that can however not be obtained from local measurements on any quantum state [144–146, 148]. Physical protocols for Bell-nonlocality exposure were devised in Refs. [127, 136], but no such protocols have been reported for steering. Hence, we next show an example for both steering exposure and Bell-nonlocality super-exposure that is manifestly within quantum theory. This also exploits the bilocal wirings of Fig. 5.3-a), but starting from a different initial assemblage. We describe the latter directly in

terms of its quantum realization.

Consider a tripartite Greenberg-Horne-Zeilinger (GHZ) state $(|000\rangle + |111\rangle)/\sqrt{2}$, with $|0\rangle$ and $|1\rangle$ the eigenvectors of the third Pauli matrix Z . Bob makes von Neumann measurements on his share of the state for both his inputs, for $y = 0$ in the $Z + X$ basis and for $y = 1$ in the $Z - X$ basis, with X the first Pauli matrix. Alice, however, makes either a trivial measurement, given by the positive operator-valued measure $\{\mathbb{1}/2, \mathbb{1}/2\}$, for $x = 0$, or a von Neumann X -basis measurement, for $x = 1$. For the resulting initial assemblage, $\sigma^{(\text{GHZ})}$, the following holds.

Physically-realizable exposure and super-exposure: *The quantum assemblage $\sigma^{(\text{GHZ})}$, of elements*

$$\sigma_{a,b|x,y}^{(\text{GHZ})} = \frac{1}{8} \left\{ \mathbb{1} + \frac{(-1)^b}{\sqrt{2}} [Z + x(-1)^{a+y} X] \right\} \quad (5.24)$$

admits an LHS model and, under the wiring $y = a$, is mapped to the assemblage of elements

$$\sigma_{b|x} = \frac{1}{4} \left[\mathbb{1} + \frac{(-1)^b}{\sqrt{2}} (Z + xX) \right], \quad (5.25)$$

which is both steerable and Bell-nonlocal.

Equation (5.24) can be obtained in the same way as in Eq. (5.6), but substituting ρ_{sep}^{ABC} by the GHZ state. It is also straightforward to show that the resulting wired assemblage is that of Eq. (5.25). Now, we proceed to prove that the physically-realizable source assemblage $\sigma^{(\text{GHZ})}$ in Eq. (5.24) admits an LHS model across the bipartition $AB|C$, and that the latter is both steerable and Bell nonlocal.

Proof. The LHS decomposition for Eq. (5.24) is found via solving the SDP (5.10). The numerical results in this case allow one to find analytic formulas for the decomposition, namely

$$P_\lambda = \frac{1}{4}; \quad \varrho_\lambda = \frac{\mathbb{1}}{2} + \frac{(-1)^{\lambda_0}}{2\sqrt{2}} [Z + (-1)^{\lambda_1} X]; \quad (5.26)$$

$$P_{a,b|x,y,\lambda} = \delta_{\lambda_0,b} \frac{1 + x(-1)^{a+y+\lambda_1}}{2}, \quad (5.27)$$

where again $\lambda = (\lambda_0, \lambda_1)$ is a two-bit hidden variable.

Let us now prove the steerability and Bell-nonlocality of assemblage (5.25). Steerability: with the SDP (5.15), we have obtained an assemblage-like object $W = \{w_{a|x}\}_{a,x}$ that serves as a steering witness, i.e. it establishes the inequality $\sum_{a,x} \text{Tr} [w_{a|x} \sigma_{a|x}] \leq 1$, which can only be violated if assemblage $\sigma = \{\sigma_{a|x}\}_{a,x}$ is steerable. Optimized for assemblage (5.25), the witness returns a value of 1.0721 and can be cast as

$$w_{0|0} = \begin{bmatrix} p & -c \\ -c & 1-p \end{bmatrix}, \quad w_{0|1} = \begin{bmatrix} q & p/2 \\ p/2 & -q \end{bmatrix}, \quad (5.28)$$

with $p = \frac{1}{2}(1 + \frac{1}{\sqrt{5}})$, $c \approx 0.1382$, $q \approx 0.2236$, and $w_{1|x} = Y w_{0|x} Y$, $x = 0, 1$. Bell-nonlocality: The necessary and sufficient criterion from [141] yields an optimal violation of the Clauser-Horne-Shimony-Holt (CHSH) inequality of $|\frac{\sqrt{5}+1}{\sqrt{2}}| \approx 2.29 \not\leq 2$, attained when Charlie makes von Neumann measurements in the eigenbases of $2Z + X$ and X . \square

5.4. Experimental implementation

Because of experimental imperfections and even the finite statistics inherent to the experimental data, it could be the case that, although we have a quantum realizable example of steering exposure, we would be unable to determine that the exposure has happened. In this section, we present an implementation of that example and show that the exposure of steering and Bell-nonlocality is a detectable phenomenon.

The exposure procedure was experimentally implemented using entangled photons produced via spontaneous parametric down conversion. The experimental setup is shown in Fig. 5.4. A photon pair is generated in the Bell state $|\Phi^+\rangle = (|00\rangle + |11\rangle) / \sqrt{2}$, where $|0\rangle$ ($|1\rangle$) stands for horizontal (vertical) polarization of the photons [94]. The photons in the signal mode (s) pass through a calcite beam displacer (BD), which creates two momentum modes (paths) depending on the polarization. This results in a tripartite GHZ state, where the extra qubit is the path degree of freedom of the photons in s . Alice's and Bob's qubits are the polarization and path of the photons in mode s , respectively, while Charlie's qubit is the polarization of the photon in mode i . The measurements onto all the degrees of freedom required for the assemblage production and tomography are performed as described below.

To implement the wiring from Fig. 5.3-a), Alice's polarization measurements are realized before Bob's measurements onto the path degree of freedom. Alice's results are read from the output of PBS_A , which determines whether D_2 ($a = 0$) or D_3 ($a = 1$) clicks. For Alice's trivial measurement ($x = 0$), crucial for the original assemblage to be LHS-decomposable, both her wave plates located before the imbalanced interferometer (represented by Δ) are kept at 0° , and $H_{@0}$ is adjusted to 22.5° . The role of Δ is to remove the coherence between horizontal and vertical polarization components, ensuring that the photon exits PBS_A randomly, independent of the input polarization state. To see that it is indeed implementing the desired measurement, consider an arbitrary pure polarization state $a|H\rangle + b|V\rangle$ entering Δ . We can associate orthogonal states $|s\rangle$ and $|l\rangle$ for the photon going through the short and long paths of the interferometer, respectively. As horizontally (vertically) polarized photons take the short (long) path, the state of the photons is $a|H\rangle|s\rangle + b|V\rangle|l\rangle$ inside the interferometer. After exiting the interferometer, the paths recombine, but because of the incoherence introduced between the two paths, the effect is equal to tracing out the path degree of freedom obtaining the mixed state $|a|^2|H\rangle\langle H| + |b|^2|V\rangle\langle V|$. Lastly, the photons pass through the HWP after

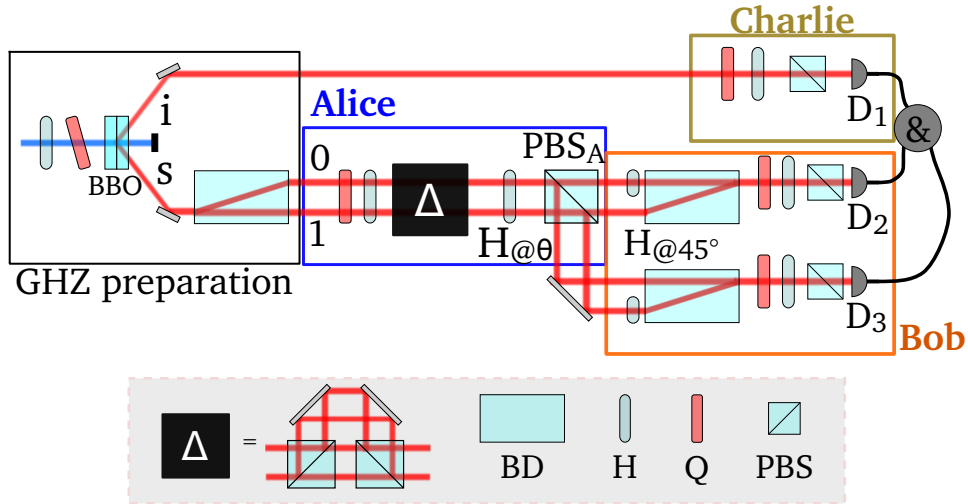


Figure 5.4.: Experimental setup. Two crossed-axis BBO crystals are pumped by a He-Cd laser centered at 325 nm, producing pairs of photons at 650 nm entangled in the polarization degree of freedom [94]. The signal (s) photon is sent through a BD which deviates only the horizontal-polarization component, producing a tripartite GHZ state on two photons using polarization and path degrees of freedom. Idler (i) photons are sent directly to Charlie’s polarization measurements. Signal photons are first measured in polarization by Alice, then Bob maps his path qubit onto a polarization qubit for his measurements. H stands for half-wave plate, Q for quarter-wave plate and PBS for polarizing beam splitter.

Δ which transforms horizontal (vertical) into diagonal (anti-diagonal) polarization delivering the state $\frac{1}{2} [|H\rangle\langle H| + |V\rangle\langle V| + (|a|^2 - |b|^2) (|H\rangle\langle V| + |V\rangle\langle H|)]$ which, regardless of a and b , gives probability $1/2$ for detecting the photon in horizontal or vertical polarization, going randomly to D_2 or D_3 .

For $x = 1$, Alice’s wave plates before Δ are set to project the polarization on the X eigenstates, such that the interferometer and $H_{@}\theta$ ($\theta = 0^\circ$) play no role. Bob performs his projective measurements by first mapping the path degrees of freedom onto polarization using BDs and then projecting the polarization state using his set of wave plates and PBSs, as was realized in Ref. [150] and described in Section 4.3.1. To reconstruct the assemblage in Eq. (5.24), measurements for $y = 0$ and $y = 1$ are made in both detectors D_2 and D_3 , by varying the angle of the wave plates in Bob’s box. To collect the data corresponding to the wired assemblage (5.25) only the $y = 0$ measurement is made in D_2 ($a = 0$) and only $y = 1$ is made in D_3 ($a = 1$), enforcing that Bob’s input equals Alice’s output ($y = a$).

Although we treat two of the qubits as black boxes, in order to ensure that the resulting assemblage is generated by quantum measurements performed onto a GHZ, we first performed state tomography to determine the tripartite quantum state. This can be done without adding any optical element to the setup. By varying the angles on Alice’s quarter-wave plate and half-wave plate before the unbalanced interferometer, we set her apparatus to make any tomographic

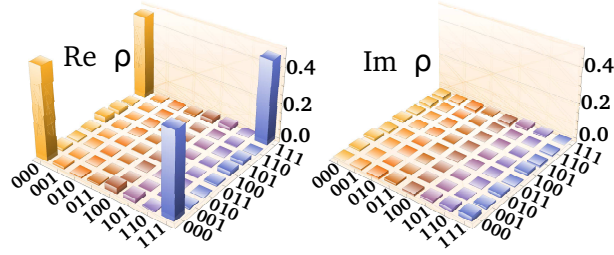


Figure 5.5.: Real and imaginary parts of the experimental reconstructed GHZ state.

measurement in polarization if we set $H_{@θ}$ to 0° . The tomographic projections for the path degree of freedom of photons in s and polarization of photons in i is done using the set of wave plates just before detectors D_1 and D_2 , respectively. Using the collected coincidence counts we reconstructed the tripartite quantum state by maximum likelihood. The reconstructed density matrix is shown in Fig. 5.5. The experimental state presents fidelity (Eq. (5.19)) with GHZ state equals to 0.981 ± 0.004 .

The assemblage $\sigma^{(\text{GHZ})}$ was obtained experimentally by performing state tomography on Charlie’s system for each measurement setting and outcome of Alice and Bob. Sixteen density matrices are obtained through maximum likelihood. Each element of the tripartite assemblage is composed of Charlie’s conditional quantum state and the conditional probability $P_{a,b|x,y}$ for the black boxes. All sixteen experimental density matrices of Charlie are shown in Fig. 5.6 in comparison with the corresponding theoretical ones. The associated conditional probabilities are also shown. The assemblage presents a fidelity-like measure of $98.2 \pm 0.2\%$ compared to the theoretical one.

The experimental wired assemblage is shown in Fig. 5.7 a). For the wired assemblage, the expected conditional probability of each outcome is $\frac{1}{2}$; the experimental values are 0.46 ± 0.01 , 0.54 ± 0.01 , 0.49 ± 0.01 , 0.51 ± 0.01 (following the order in Fig.5.7a). The imaginary components of the density matrix average to 0.05 ± 0.02 (theoretical: zero). and returns a fidelity of $98.1 \pm 0.6\%$ with respect to the theoretical wired assemblage given in (5.25).

An exact LHS decomposition of the experimental assemblage is not feasible due to imperfections and finite statistics — in fact, assemblages reproducing raw experimental data exactly are not even physical, since they disobey the NS principle [143]. To show that the experimental tripartite assemblage is statistically compatible with an LHS decomposition, we proceed as follows: First, we assume the photocounts obtained for each measured projector are averages of Poisson distributions; with a Monte Carlo simulation, we sample many times each of these distributions and reconstruct the corresponding assemblages. Second, for each reconstructed assemblage, we find the physical (NS) assemblage that best approximates it through maximum-likelihood estimation, as well as the best LHS approximation for comparison. As an initial indication of LHS-compatibility, the log-likelihood error of both approximations is extremely

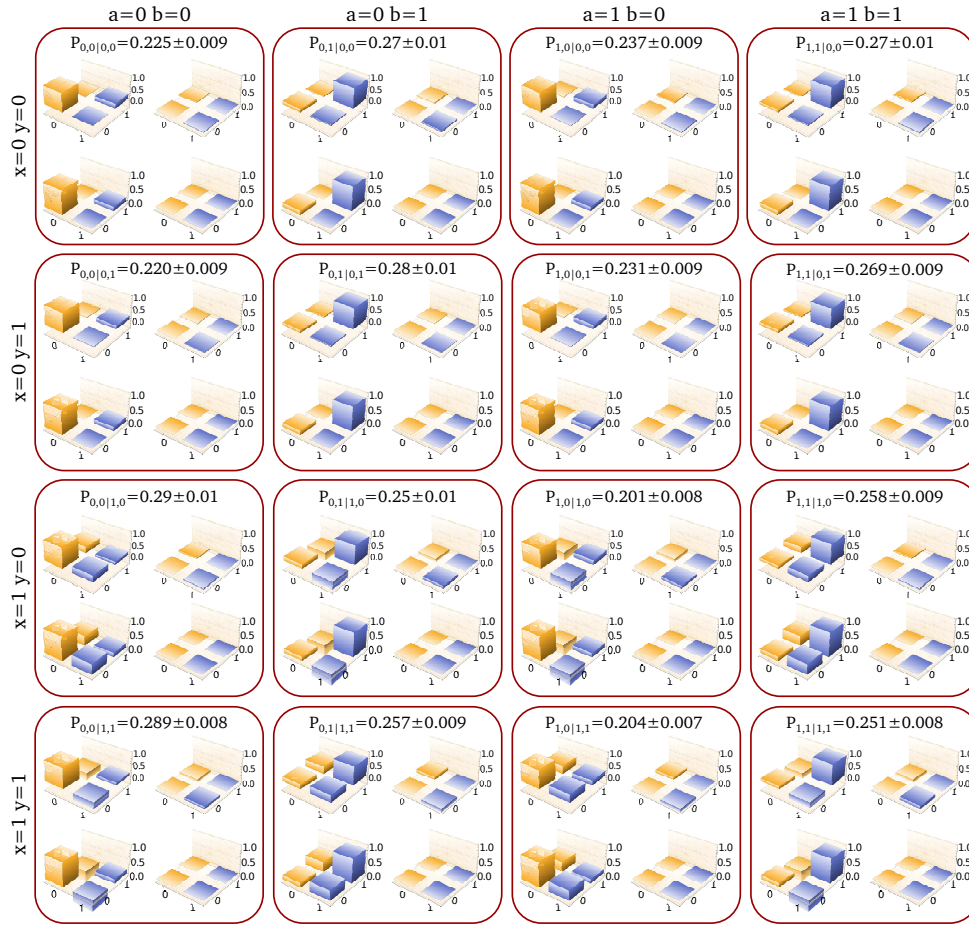


Figure 5.6.: Theoretical and experimental reconstructed assemblages for different values of inputs x, y and outputs a, b . Each box shows the joint probability of measurement for the black boxes, real (top left) and imaginary (top right) parts of the experimental density matrix of Charlie's partition, and real (bottom left) and imaginary (bottom right) parts of theoretical Charlie's density matrix. The theoretical probability is 0.25 for all measurement choices and measurement outputs.

similar, see Fig.5.7c). Third, for the NS approximations we calculate the LHS-robustness. For comparison, we repeat the procedure starting with simulated finite-photocount statistics from the theoretical LHS assemblage from Eq. (5.24). In Fig.5.7d) we see that the experimental robustness has a sizable zero component and a distribution fully compatible with that of an LHS assemblage under finite measurement statistics. To show that the experimental wired assemblage is steerable, we tested it on the optimal steering witness W with respect to assemblage (5.25) (Eq. (5.28)). This returned a value $1.015 \pm 0.009 \not\leq 1$ (theoretical: $1.0721 \not\leq 1$), where the inequality violation implies steering, see Fig.5.7b). This allows us to conclude that the bipartite wired assemblage is indeed steerable. The experimental error was calculated using 500 assemblages also from a Monte Carlo simulation of measurement results with Poisson photocount statistics.

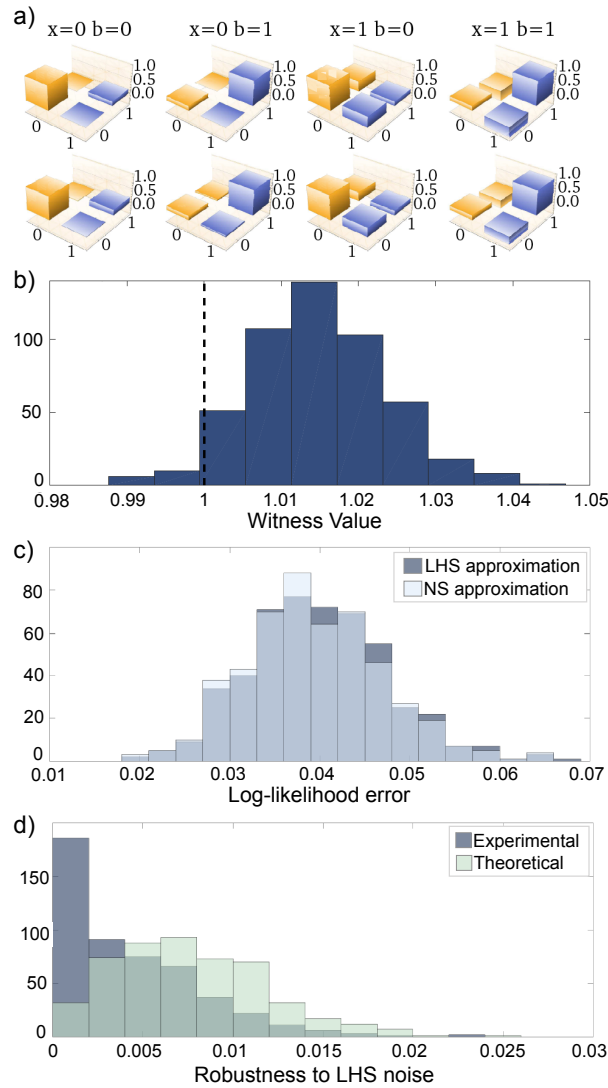


Figure 5.7.: a), b) Experimental assemblages after $y = a$ wiring. a) Real part of Charlie’s conditional density matrices, theoretical (top) and experimental (bottom). b) Steering-witness histogram. The witness value is 1.015 ± 0.009 , meaning that the experimental assemblage is more than one standard deviation above the steering threshold (dashed line). c), d) Compatibility of the tripartite experimental assemblage with the naive (LHS) definition of unsteerability [Eq. (5.5)]. c) Histogram of the error of approximating the tripartite assemblage by an NS and an LHS assemblage, showing that the error of assuming the LHS decomposition is as small as that of the physically necessary NS assumption. d) From the best NS approximation to the experimental data, histogram of the LHS-robustness, a measure of deviations from the set LHS. Even with all experimental error, there is only a residual amount of robustness, fully compatible with that of the theoretical LHS assemblage solely under finite-statistics error. All histograms come from Monte Carlo simulation assuming solely Poisson distributions.

Using the same experimental setup, we can also experimentally demonstrate super-exposure of Bell nonlocality. As argued above, the initial experimental assemblage is compatible with an LHS model. Therefore, no matter what measurement Charlie makes, the corre-

sponding Bell behavior will be compatible with an LHV model. Hence, we must only show that the experimental wired assemblage is Bell nonlocal. In Ref. [141], a necessary and sufficient criterion for Bell nonlocality of assemblages was derived: Given Alice and Bob's wired measurements ($y = a$) with input bit x and output bit b , to maximally violate a Bell inequality, Charlie performs von Neumann measurements in the $2Z + X$ and X bases, labeled by input bit z , obtaining binary output result c . They thus obtain sixteen probabilities $P(b, c|x, z)$, which are used to calculate the Clauser-Horne-Shimony-Holt (CHSH) inequality [151]. We obtained an experimental violation of $2.21 \pm 0.04 \not\leq 2$ (theoretical prediction: $2.29 \not\leq 2$), showing Bell nonlocality in a DI fashion.

Thus, we have experimentally demonstrated both exposure of steering and super-exposure of Bell nonlocality.

5.5. Redefinition of steering

The results of the previous sections suggest the necessity of a redefinition of steering in the multipartite scenario, since, analogously to [127], an assemblage can belong to LHS and still be steerable. The existence of subtle steering implies a stark inconsistency between the naive definition of steering from LHS decomposability, Eq. (5.5), and the formulation of its resource theory. Since the free operations that cause exposure are classical and strictly local (fully contained in the AB partition), it is reasonable that they are unable to create not only steering but also any form of correlations (even classical ones) across $AB|C$. The alternative left is to redefine bipartite steering in multipartite scenarios such that, e.g., the assemblages in Eqs. (5.20a) and (5.24) are already steerable. Formally, we need to exclude a subclass of LHS decompositions from the set of unsteerable assemblages. In principle, no restriction must be imposed over the probability distribution $P_{a,b|x,y,\lambda}$ in Eq. (5.5), once the NS conditions are satisfied for the visible assemblage. A suitable choice is to restrict all signaling between Alice and Bob also at the level of each λ in Eq.(5.5); this defines the set NS-LHS (non-signaling local hidden states). This restriction, however, can be consistently relaxed to allow signaling between the two as long as, for each λ , Alice and Bob's distribution is compatible with both orders (A before B and B before A); this defines TO-LHS (time-ordered local hidden states), a strict superset of NS-LHS; see Fig.5.9. This has consequences for genuine multipartite correlations, including the possibility of certifying genuine multipartite entanglement in a semi-DI scenario without steering.

To identify that subclass, let us apply the wiring $y = a$ to a general σ fulfilling Eq. (5.5). This gives $\sigma^{(\text{wired})}$, of elements

$$\sigma_{b|x}^{(\text{wired})} := \sum_a \sigma_{a,b|x,a} = \sum_{\lambda} P_{\lambda} \left(\sum_a P_{a,b|x,a,\lambda} \right) \varrho_{\lambda}. \quad (5.29)$$

This is a valid LHS decomposition as long as the term within brackets yields a valid (normalized) conditional probability distribution (of B given X and Λ). This is the case if every $P_\lambda^{(AB)}$ in Eq. (5.5) is non-signaling. In that case, by summing over b and applying the NS condition, one gets

$$\sum_{a,b} P_{a,b|x,a,\lambda} = \sum_a P_{a|x,a,\lambda} \stackrel{\text{NS}}{=} \sum_a P_{a|x,\lambda} = 1, \quad (5.30)$$

which renders $\sigma^{(\text{wired})}$ indeed unsteerable. However, this reasoning can in general not be applied if any $P_\lambda^{(AB)}$ is signaling from Bob to Alice, i.e. if Alice's marginal distribution for a depends on y (apart from x and λ). In fact, it can be checked that this is the case of the probability distributions (5.22) and (5.27) of the general exposure protocol and of the quantum exposure example, respectively.

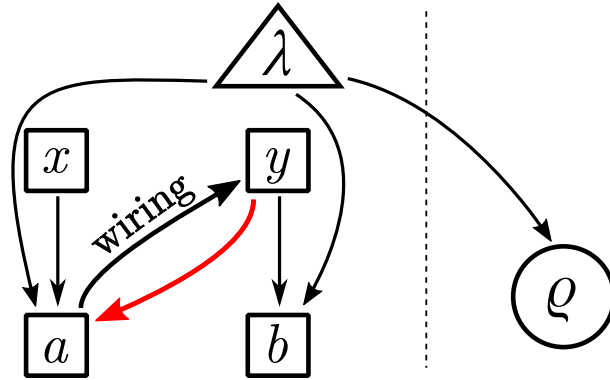


Figure 5.8.: Steering exposure as a causal loop. In the causal network underlying LHS models, given by Eq. (5.5), the hidden variable λ directly influences Charlie's quantum state ρ as well as the Alice and Bob's outputs a and b , which are in turn also influenced by the inputs x and y , respectively. Even though the observed assemblage (after averaging λ out) is non-signaling, the model can still exploit hidden communication (i.e. at the level of λ). For instance, for each λ , Alice's output may depend (red arrow) on Bob's input in a different fine-tuned way such that the dependence vanishes at the observable level. The wiring of Fig. 5.3a) forces $y = a$, closing a causal loop that will in general conflict with the latter dependence for some λ . As a consequence, the final assemblage resulting from the wiring may not admit a valid LHS decomposition, exposing steering. Hence, the exposure can in a sense be thought of as an operational benchmark for hidden signaling in the LHS model describing the initial assemblage.

Therefore, we see that the inconsistency is rooted in hidden signaling. In fact, at the level of the underlying causal model, the phenomenon of exposure can be understood as a causal loop between such signaling and the applied wiring (see Fig. 5.8).

To restore consistency, hidden signaling must be restricted. An obvious possibility would be to allow only for non-signaling $P_\lambda^{(AB)}$'s in Eq. (5.5). Interestingly, however, this turns out to be over-restrictive. Following the redefinition of multipartite Bell nonlocality [127, 136], we propose the following for bipartite steering in multipartite scenarios.

Redefinition of steering: An assemblage σ is unsteerable if it admits time-ordered LHS (TO-LHS) decompositions both from A to B and from B to A simultaneously, i.e. if

$$\sigma_{a,b|x,y} = \sum_{\lambda} P_{\lambda} P_{a,b|x,y,\lambda}^{(A \rightarrow B)} \varrho_{\lambda} \quad (5.31)$$

$$= \sum_{\lambda} P'_{\lambda} P_{a,b|x,y,\lambda}^{(B \rightarrow A)} \varrho'_{\lambda}, \quad (5.32)$$

where each $P_{\lambda}^{(A \rightarrow B)}$ is non-signaling from Bob to Alice and each $P'_{\lambda}^{(B \rightarrow A)}$ from Alice to Bob. Otherwise σ is steerable.

The validity of both time orderings simultaneously prevents conflicting causal loops. More precisely, if a wiring from Alice to Bob is applied on σ , one uses decomposition (5.31) to argue with the $P_{\lambda}^{(A \rightarrow B)}$'s [as in Eq. (5.30)] that the wired assemblage is unsteerable. Analogously, if a wiring from Bob to Alice is performed, one argues using the $P'_{\lambda}^{(B \rightarrow A)}$'s from decomposition (5.32). Hence, no exposure is possible for TO-LHS assemblages, guaranteeing consistency with bilocal wirings (as well as generic 1W-LOCCs from trusted to untrusted parts) as free operations of steering. On the other hand, when all λ -dependent behaviors in Eqs. (5.5) are fully non-signaling, then the assemblage is called *non-signaling LHS* (NS-LHS). There exists TO-LHS assemblages that are not NS-LHS, which proves that the latter is a strict subset of the former. One could criticize our results by arguing that it is a mere mathematical statement and no physical realization of a TO-LHS assemblage outside NS-LHS set is possible. To show the importance of this redefinition, in App. C.3 we provide a quantum and a supra-quantum example of TO-LHS assemblages that are not NS-LHS. In Fig. 5.9 a pictorial representation of the structure of the set of NS assemblages is shown.

In either case, the redefinition above automatically implies also a redefinition of genuinely multipartite steering (GMS). We present this explicitly in App. C.2. There, we follow the approach of Ref. [143] in that a fixed trusted-versus-untrusted partition is kept. However, instead of defining GMS as incompatibility with quantum-LHS assemblages (i.e. with λ -dependent behaviors with explicit quantum realizations) as in [143], we use the more general TO-LHS ones. This reduces the set of genuinely multipartite steerable assemblages safely, i.e. without introducing room for exposure. Interestingly, this enables genuine multipartite entanglement to be certified in the semi-DI scenario without steering (App. C.2).

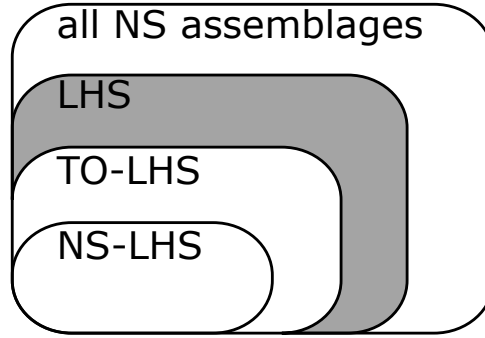


Figure 5.9.: Pictorial representation of inner structure of the set of all non-signaling assemblages in the tripartite scenario. The subset of generic local-hidden-state (LHS) assemblages strictly contains the subset TO-LHS of time-ordered LHS ones, which in turn strictly contains the subset NS-LHS of non-signaling LHS ones. The shaded region represents the set of assemblages with subtle steering. Bilocal wirings can expose such steering by mapping that region to the set of (bipartite) steerable assemblages.

5.6. Concluding remarks

We have demonstrated that the traditional definition of multipartite steering for more than one untrusted party based on decomposability in terms of generic bilocal hidden-state models presents inconsistencies with a widely accepted, basic operational framework for the resource. We have also shown how, according to such a definition, a broad set of steerable (exposure) and even Bell-nonlocal (super-exposure) assemblages would be created seemingly from scratch, e.g. by bilocal wirings acting on an unsteerable assemblage. A surprising discovery that we have made is the fact that exposure of quantum nonlocality is a universal effect, in the sense that all steering assemblages as well as Bell behaviors can be obtained as the result of an exposure protocol starting from bilocal correlations in a scenario with one more untrusted party. This highlights the power of exposure as a resource-theoretic transformation. However, we also delimit such power: we prove a no-go theorem for multi-black-box universal steering bits: there exists no single assemblage with many untrusted and one trusted party from which all assemblages with one untrusted and one trusted party can be obtained through generic free operations of steering. To restore operational consistency, we offer a redefinition of both bipartite steering in multipartite scenarios and genuinely multipartite steering that does not leave room for exposure. Finally, both steering exposure and Bell nonlocality super-exposure have been demonstrated experimentally using an optical implementation. This is to our knowledge the first experimental observation of exposure of quantum nonlocality reported, not only in semi device-independent scenarios but also in fully device-independent ones, as originally predicted in [127, 136].

DETECTION OF QUANTUM NON-MARKOVIANITY CLOSE TO THE BORN-MARKOV APPROXIMATION

In this chapter we explore memory effects in quantum systems. The presence of such memory is called non-Markovianity and appears when a quantum system is interacting with an environment. Under some approximations, however, this memory effects are so weak that they are not detected by the majority of memory indicators. Here we present a study of non-Markovianity for the decay dynamics of a two-level system in a bosonic bath. We use an operational indicator, the so-called conditional past-future (CPF) correlation, which relies on three measurement interventions on the system. This indicator is able to detect memory effects even close to the weak-interaction Born-Markov approximation. We also show an experimental realization of the measurement of the CPF correlation for a photonic qubit, showing the limitations of this approach in a realistic experimental scenario.

This work was realized in collaboration with Adrián Budini from Consejo Nacional de Investigaciones Científicas y Técnicas (CONICET - Argentina) and the UFRJ professors Gabriel Aguilar, Marcelo Santos and Stephen Walborn. My contribution to this work was in designing the experiment and realizing it, as well as the data analysis. A resulting paper is accepted for publication in Physical Review A and a preprint can be found in Ref. [152].

6.1. Introduction

Giving the time evolution of a quantum system's state as a unitary operation is an accurate description only if the system is completely isolated. Usually, the more general treatment of open quantum systems (OQS) is necessary, either because it is impossible to perfectly iso-

late a real system and spurious interactions with the surroundings remain or because desirable interactions with a large uncontrolled environment is present. In both cases one can only control and access a small system of interest within a larger one and the reduced time evolution of this portion is no longer unitary. The interaction with the environment gives rise to energy dissipation, irreversible dynamics and losses of quantum coherence and correlations.

A first approach to the OQS problem is the so called Born-Markov approximation (BMA) which considers that the coupling between system and environment is much smaller than the other energy values involved and that the environment is large enough such that its state is kept unchanged during the OQS evolution [153]. This approximation leads to a memoryless dynamics meaning that the future state of the reduced system only depends on its present state and not on its past story. The BMA has been used extensively, providing excellent agreement with many experiments in the context of quantum optics and magnetic resonance. However the actual time evolution of any real system departs to some extent from this idealized dynamics. For many situations it is also the case that one has only partial information about the microscopic details of the dynamics and it is necessary to quantify the degree of non-Markovianity present [154]. As we shall present in the next section, most of the typical non-Markovianity measures are based at least on the possibility of performing tomographic measurements over the OQS state for different times during the evolution or process tomography, or still on optimizations. From an experimental perspective, in many cases, this renders determining the non-Markovian character of the evolution almost impossible. The measure we employ here, the conditional past-future (CPF) correlation [35], relies only on three subsequent measurements for different times, being a useful and practical alternative to the other measurements capable of univocally determine the non-Markovianity of the dynamics.

To illustrate the CPF correlation capability of detecting non-Markovianity close to BMA, in this work we study the non-Markovian features of the spin-boson model which describes the decay of a two-level system in a Bosonic bath. In contrast to previous memory indicators, we show that the system propagator by itself is unable to detect quantum non-Markovianity close to the BMA. Instead, a self-convolution of the system propagator weighted by the environment correlation becomes the proper memory indicator. A photonic experiment that allows to measure the CPF correlation for this system is also implemented, providing experimental support to our main findings.

Before presenting our results, the concept of classical Markovianity is introduced in Section 6.2. In order to extend this concept to quantum physics, some basic elements on quantum open systems dynamics are presented together with the Born-Markov approximation and the quantum memory indicator used here (Section 6.3). In sequence, it is presented the model of a two-level system in a bosonic bath with the CPF correlation for this model (Section 6.4). At last, the experiment and experimental results are presented (Section 6.5).

6.2. Markov processes in classical Physics

This kind of stochastic process was named after the Russian mathematician Andrei Andreevich Markov (1856-1922) whose contributions to number and probability theory were fundamental to solve many subsequent problems in science and technology [155]. Roughly speaking, Markov processes are those that do not possess memory, what means that a result in the future, given a certain present condition, will be the same regardless what happened in the past.

To get to a formal definition, consider the stochastic process $X(t)$ taking discrete values $\{x_i\}_{i \in \mathbb{N}}$ on a finite set χ for discrete time instants $\{t_i\}_{i \in \mathbb{N}}$. It can be characterized by the hierarchy of joint probabilities $P_n(x_n, t_n; x_{n-1}, t_{n-1}; \dots; x_1, t_1)$ that values x_k occur at time t_k for a given initial condition $\{x_0, t_0\}$, with $n \in \mathbb{N}$ and $t_n > t_{n-1} > \dots > t_1 > t_0$. This process is said to be Markovian if the conditional probability of the random variable at time t_{n+1}

$$P_{1|n}(x_{n+1}, t_{n+1} | x_n, t_n, \dots, x_1, t_1) = \frac{P_{n+1}(x_{n+1}, t_{n+1}; x_n, t_n; \dots; x_1, t_1)}{P_n(x_n, t_n; x_{n-1}, t_{n-1}; \dots; x_1, t_1)} \quad (6.1)$$

does not depend on the previous values of $X(t)$ but x_n , i.e.

$$P_{1|n}(x_{n+1}, t_{n+1} | x_n, t_n, \dots, x_1, t_1) = P_{1|1}(x_{n+1}, t_{n+1} | x_n, t_n) \quad \forall n \in \mathbb{N}, \quad (6.2)$$

where $P_{j|k}$ is the probability distribution of j events given k precedent events [33].

Although by its definition, one would need to ensure the validity of Eq. (6.2) for an infinity hierarchy of probability distributions in order to characterize the Markovianity of a process, there are a plethora of methods used to determine the non-Markovianity of it which require much less information. This is the case of the conditional past-future correlations presented in Section (6.3.3).

An interesting property that comes directly from (6.2) is the Chapman-Kolmogorov equation

$$P_{1|1}(x_3, t_3 | x_1, t_1) = \sum_{x_2 \in \chi} P_{1|1}(x_3, t_3 | x_2, t_2) P_{1|1}(x_2, t_2 | x_1, t_1), \quad \forall t_3 > t_2 > t_1 \geq 0 \quad (6.3)$$

which can be interpreted as the possibility of writing the evolution from the initial time t_1 to the final time t_3 as the composition of the evolution from t_1 to an intermediate time t_2 and then from t_2 to t_3 . This property is called divisibility [34].

6.3. Open quantum system dynamics and Markovianity

The quantum mechanical description of nature is intrinsically stochastic. Thus it is natural to translate the concept of Markovianity to processes described by quantum mechanics. The mathematical object used to calculate probability distributions of a quantum system is its density matrix denoted by ρ . In this section we give the basic concepts of dynamics of OQS density matrices.

The time evolution of a OQS is given by a dynamical map $\Lambda_t : S(\mathcal{H}) \rightarrow S(\mathcal{H})$ acting on the convex set of physical states belonging to the Hilbert space \mathcal{H} of the system. If the system is initially prepared in the state ρ_0 then its state in a posterior time $t \geq 0$ is given as

$$\rho_t = \Lambda_t[\rho_0]. \quad (6.4)$$

To be regarded as a physical map, Λ_t must take physical density matrices into physical density matrices. In other words, the map must be trace preserving (TP) and positive, and also preserve Hermiticity. A map is positive if $\Lambda[\rho] \geq 0$ for all $\rho \geq 0$. The first property ensures the conservation of the probability and the second one guarantees that all probabilities remain positive numbers as they must be. A further requirement may be imposed, namely complete positivity (CP). If one considers that the system may be correlated to another quantum system that is not under the action of the map, still the map should take the composite-system initial state into a physical state, no matter what dimension the additional Hilbert space has. Mathematically this is expressed as $(\Lambda_t \otimes \mathbb{1}_A)[\rho_{sa}] > 0$ for all composite states $\rho_{sa} \in S(\mathcal{H} \otimes \mathcal{H}_a)$ of OQS and ancilla, $\mathbb{1}_a$ is the identity operator in the ancilla Hilbert space \mathcal{H}_a . For finite dimensional Hilbert space \mathcal{H} complete positivity is equivalent to positivity in a $[\dim(\mathcal{H})]^2$ space, i. e., in the case when the ancilla Hilbert space has the same dimension as the OQS [156].

A microscopic description of system and environment is usually used to obtain the dynamical map for the OQS. The total system Hilbert space is the tensor product of the Hilbert spaces of the OQS and the environment $\mathcal{H} \otimes \mathcal{H}_e$. The reduced state of the OQS (environment) is obtained by partial trace of the total state over \mathcal{H}_e (\mathcal{H}). The composed system is closed and its time evolution is given by the von Neumann equation

$$i \frac{d}{dt} \rho_{se}(t) = [H_{se}, \rho_{se}(t)] \quad (6.5)$$

with Hamiltonian

$$H_{se} = H \otimes \mathbb{1}_e + \mathbb{1}_s \otimes H_e + H_I, \quad (6.6)$$

where H (H_e) is the free Hamiltonian of the OQS (environment) and H_I is the interaction between system and environment. The solution is a unitary evolution of the total initial state

ρ_{se} . Accordingly, the system reduced state in time t is obtained as

$$\rho(t) = \text{Tr}_e[U(t)\rho_{se}U^\dagger(t)], \quad (6.7)$$

being $U(t)$ the unitary operator associated with the Hamiltonian H_{se} and $\text{Tr}_e[\cdot]$ denotes the partial trace over the environment degrees of freedom.

Equation (6.7) provides the dynamical map Λ_t once we can write the right hand side as the transformation of the initial OQS state ρ_0 . In the case of initially separable state¹ $\rho_{se} = \rho_0 \otimes \rho_e$ it is easy to obtain a physical CPTP map as follows. First let us write the bath state in its spectral decomposition $\rho_e = \sum_q p_q |q\rangle\langle q|$ with $p_q > 0$ and $\sum_q p_q = 1$. Now, it is easy to identify the Kraus decomposition of the dynamical map directly from (6.7) as

$$\rho_t = \Lambda_t[\rho_0] = \sum_l E_l(t)\rho_0 E_l^\dagger(t), \quad (6.8)$$

with the Kraus operators $E_l(t) = \sqrt{p_{q'}}\langle q|U(t)|q'\rangle$, $l = \{q, q'\}$. Because of the unitarity of the total evolution the Kraus operators fulfill the property $\sum_l E_l(t)E_l^\dagger(t) = \mathbb{1}$. The existence of a Kraus form for the map already ensures the complete positivity of it [157].

On the other hand, if the initial state of system and environment has quantum correlations, then the dynamical map is not necessarily CP [158]. In fact, in this case it is not possible to define such a dynamical map consistently defined for any initial system state because the environment state is different for different system states and the dynamics is changed. Even starting with a separable total state, entanglement between OQS and its environment is typically created along the evolution not allowing for the definition of dynamical maps from intermediate times. As we are going to see in the next section, this is behind the non-Markovianity feature of the dynamics.

6.3.1. Born-Markov approximation

Instead of directly obtaining the dynamical map, a typical approach to OQS problems is to build a model yielding to a dynamical equation for the OQS density matrix, the so called master equation, in which the environment is part only by means of characteristic parameters. It is usually a very hard problem to exactly obtain a master equation from the unitary dynamics of the composite system and many approximations are made necessary. Among these approximations, the most celebrated is the Born-Markov approximation (BMA) that is presented in this section, more details can be found in [153] or any other book on the subject of OQS.

In the interaction picture the time evolution for the total system is given by

¹This is a common case, since usually the system is prepared in a initial state through a measurement, destroying any previous existing correlation between system and environment.

$$i \frac{d}{dt} \rho_{se}^I(t) = [H_I(t), \rho_{se}^I(t)], \quad (6.9)$$

where $\rho_{se}^I(t) = e^{iH_0 t} \rho_{se}(t) e^{-iH_0 t}$, $H_I(t) = e^{iH_0 t} H_I e^{-iH_0 t}$, and $H_0 = H \otimes \mathbb{1}_e + \mathbb{1}_s \otimes H_e$. The formal solution come by integration as

$$\rho_{se}^I(t) = \rho_{se}^I(0) - i \int_0^t d\tau [H_I(\tau), \rho_{se}^I(\tau)], \quad (6.10)$$

and after the first iteration

$$\rho_{se}^I(t) = \rho_{se}^I(0) - i \int_0^t d\tau [H_I(\tau), \rho_{se}^I(0)] - \int_0^t d\tau \int_0^\tau d\tau' [H_I(\tau), [H_I(\tau'), \rho_{se}^I(\tau')]]. \quad (6.11)$$

The reduced system state is obtained from (6.11) by partial trace over the environment degrees of freedom. Moreover, a differential equation satisfied by the reduced state is obtained by taking the time derivative after the partial trace. Now come a series of considerations. First of all, let us suppose that the initial state commutes with the interaction Hamiltonian, such that the second term in the right hand side of (6.11) vanishes. After this consideration and performing also a change of variables, one is left with the following integro-differential equation

$$\frac{d}{dt} \rho(t) = - \int_0^t d\tau \text{Tr}_e [H_I(t), [H_I(t - \tau), \rho_{se}^I(t - \tau)]], \quad (6.12)$$

where the superscript I was suppressed only for simplicity. The global state can be written as $\rho_{se}(t) = \rho(t) \otimes \rho_e(t) + \chi_{se}(t)$, the sum of a separable part with a traceless part which contains the correlations. Assuming that the correlations vanish in a time that is small compared to the relaxation time of the OQS and also that the environment is large enough such that its state is hardly affected by the presence of the system we can approximate $\rho_{se}(t) \approx \rho(t) \otimes \rho_e$. Moreover, the kernel inside the integral in Eq. (6.12), which contains the correlation functions of the bath $\text{Tr}_e [H_I(t) H_I(t - \tau) \rho_e]$, vanish for τ larger than τ_c the correlation time of the bath. If this correlation time is again small as compared with the relaxation time of the OQS, for the values of τ that the integrand does not vanish, we can approximate $\rho(t - \tau) \approx \rho(t)$ and extend the integral superior limit. The final master equation that gives the OQS state time evolution is read

$$\frac{d}{dt} \rho(t) = - \int_0^\infty d\tau \text{Tr}_e [H_I(t), [H_I(t - \tau), \rho(t) \otimes \rho_e]]. \quad (6.13)$$

The set of approximations performed above is called the *Born-Markov approximation* and it is widely used since it allows for writing a pure differential equation for the OQS state. In the very limit of BMA, the correlation function can be regarded as a Dirac delta function. As can be noticed, in general this approximation can be valid only for large enough time, such that all the correlation have been destroyed. Increasing the time resolution to which one has access

demands treating the OQS beyond this approximation.

Under general assumptions, the BMA equation (6.13) can be put in the form $\frac{d}{dt}\rho(t) = \mathcal{L}\rho(t)$, whose solutions have the semigroup expression $\rho(t) = e^{\mathcal{L}t}\rho_0$, being \mathcal{L} a Lindblad superoperator.

6.3.2. Quantum Markovianity

The direct translation of the classical Markovianity to quantum theory leads to issues related to the disturbance caused by measurement on quantum systems [159]. Because of it, many different definitions of Markovianity in this context have arisen in the past few years [34].

In the quantum realm the joint probability distributions analogous to those that define classical Markovianity are calculated from the quantum state of the system and measurement operators \mathcal{M}_x . Given that we chose to measure a non-degenerate observable $X = \sum_x x|x\rangle\langle x|$, the measurement operators can be the projectors over the eigenstates of it: $\mathcal{M}_x = |x\rangle\langle x|$. Not only does the joint probability distribution obtained not satisfy basic conditions valid for the classical counterparts [33], but also the measurement of the system alters the total system-environment state, completely destroying its correlations and consequently strongly altering the subsequent dynamics. One can easily be convinced of that from the construction of the dynamical map shown in the previous section and from the fact that, if the total state is $\rho_{se}(t_i)$ in time t_i and at this time the eigenvalue x_i is measured, then the total state immediately after the intervention becomes

$$\rho'(t_i) = \frac{\mathcal{M}_{x_i}\rho_{se}(t_i)\mathcal{M}_{x_i}}{\text{Tr}[\mathcal{M}_{x_i}\rho_{se}(t_i)\mathcal{M}_{x_i}]} = |x\rangle\langle x| \otimes \rho_e^{x_i}(t_i), \quad (6.14)$$

where $\rho_e^{x_i}(t_i)$ is the altered bath state possibly dependent on the measurement result.

In order to define a notion of quantum Markovianity that resembles the classical one and rely only on the dynamics itself and not on a particular measurement scheme, it must be related to the dynamical map itself. One of the most used definitions of Markovianity uses the concept of divisibility (6.3), valid for the classical Markovian probability distributions. A map Λ_t is divisible if it is possible to define a two parameter trace preserving map Λ_{t_2,t_1} such that $\Lambda_{t,0} = \Lambda_t$, $\Lambda_{t,t} = \mathbb{1}$ and

$$\Lambda_{t_2,0} = \Lambda_{t_2,t_1}\Lambda_{t_1,0}, \quad t_2 > t_1 > 0. \quad (6.15)$$

A Markovian dynamics is defined as that given by a CP-divisible time evolution map, i.e., a divisible map for which Λ_{t_2,t_1} is completely positive for all $t_2, t_1 \geq 0$ [154]. If this is the case, then roughly speaking there is a valid CP time evolution from any t_1 to any t_2 independent of the history of the system or the environment, thus no memory is entailed in this process. Clearly the solutions of the BMA master equation (6.13) are Markovian because of the

semigroup property with $\Lambda_{t_2, t_1} = e^{\mathcal{L}(t_2 - t_1)}$.

The definition of Markovianity directly gives rise to a measure of non-Markovianity. A divisible map is CP-divisible if and only if $[\Lambda_{t_2, t_1} \otimes \mathbb{1}] |\Phi\rangle\langle\Phi| \geq 0$, with $|\Phi\rangle = \frac{1}{\sqrt{\dim\mathcal{H}}} \sum_{i=1}^{\dim\mathcal{H}} |n_i\rangle\langle n_i|$ the maximally entangled state in $\mathcal{H} \otimes \mathcal{H}$ [156]. Consider the trace norm defined as $\|A\| = \text{Tr} \sqrt{A^\dagger A}$ that is equal to $\sum_i |a_i|$, the sum of the modulus of the eigenvalues of A if the operator is selfadjoint. Then, because of the trace preservation property, it is true that $\|[\Lambda_{t_2, t_1} \otimes \mathbb{1}] |\Phi\rangle\langle\Phi|\|$ is equal to 1 if the map is CP and larger than 1 otherwise. Then the function

$$g(t) = \lim_{\epsilon \rightarrow 0^+} \frac{\|[\Lambda_{t+\epsilon, t} \otimes \mathbb{1}] |\Phi\rangle\langle\Phi|\| - 1}{\epsilon} \quad (6.16)$$

is positive only if the dynamics is non-Markovian and the quantity $\Gamma = \int_I g(t) dt$ is a measure of the non-Markovianity of the evolution in the time interval I [154]. This is the commonly called RHP measure.

Another possible definition of quantum Markovianity that is in some cases nonequivalent to the previous one can be given in terms of the trace distance of states for different time instants [160]. The interaction between system and environment tends to diminish the distinguishability between any two system states, which can be interpreted as a loss of information from the system to the environment. Non-Markovian dynamics would be mainly characterized by a reversed flow of information from the environment to the system causing an increase in the distinguishability of states during some interval of time [161]. The distinguishability between any two states ρ_1 and ρ_2 can be measured by the trace distance $D(\rho_1, \rho_2) = \frac{1}{2} \|\rho_1 - \rho_2\|$ between them. A non-Markovian dynamics is then characterized by

$$\sigma(t) = \frac{d}{dt} D(\rho_1(t), \rho_2(t)) > 0, \quad (6.17)$$

for any value of time and for any pair of possible initial states ρ_1 and ρ_2 , with $\rho_i(t) = \Lambda_t \rho_i$. This definition also leads to a measure of non-Markovianity, the BLP measure, defined as $\Gamma = \max_{\rho_{1,2}(0)} \int_{\sigma > 0} dt \sigma(t)$, the maximization is over all possible pairs of initial states of the OQS.

It is possible to show that correlations between system and environment play a central role in non-Markovianity. As mentioned before, if the initial total state is entangled, then the dynamical map may not be CP. The time evolution ususally produces entanglement between system and environment, that is why the map linking two intermediate states in Eq. (6.15) is in general not CP characterizing non-Markovianity. It is also possible to show that the trace distance always decreases monotonically in the absence of correlations [162].

6.3.3. Conditional past future correlation

The previous mathematical definitions of classical and quantum Markovianity are not practical in the sense that they require absolute knowledge on infinity hierarchies of conditional probabilities (classical case) or on the whole dynamical map (quantum case). An operational definition or witness of non-Markovianity, on the other hand, should be obtained from the mathematical definitions and would ideally rely on the minimum number of measurements possible.

Lets consider a classical or quantum system on which three sequential measurements are performed at time instants $t_x < t_y < t_z$. This is the minimum number of measurements one can think of when trying to determine memory effects. A lack of memory is characterized by a complete independence of the future measurement outcome O_z on the past measurement outcome O_x for a given present outcome O_y , i.e. the future result is completely determined by the present state. Mathematically, it means that the conditional-past-future (CPF) correlation, conditioned to a fixed present outcome, defined as

$$C_{pf|y} = \langle O_x O_z \rangle_y - \langle O_x \rangle_y \langle O_z \rangle_y = \sum_{x,y} [P(x, z|y) - P(x|y)P(z|y)] O_x O_z, \quad (6.18)$$

vanishes for Markov (memoryless) processes. Here $\langle \cdot \rangle_y$ denotes the mean value conditioned to the intermediate outcome labeled by y and the sum runs over all possible outcomes. In order to verify that this statement is consistent with the classical definition of a Markovian process, lets write Bayes rules for the various conditional and joint probabilities of this triple measurement procedure. First, one can write the triple joint probability in terms of different conditionals as

$$P(x, y, z) = P(z|x, y)P(y|x)P(x), \quad (6.19a)$$

$$P(x, y, z) = P(x, z|y)P(y). \quad (6.19b)$$

Bayes rule can be applied again to invert the present-past dependence since it gives $P(x, y) = P(y|x)P(x) = P(x|y)P(y)$. Therefore, in general Eqs. (6.19) yield $P(x, z|y) = P(z|x, y)P(x|y)$ and the CPF correlation (6.18) is not null. For Markovian processes, on the other hand, Eq. (6.2) tells that $P(z|x, y) = P(z|y)$ and hence the correlation is zero regardless the value of the present outcome and also the time instants at which the system is measured.

The CPF correlation can also be calculated for a quantum system. In this case, a measurement is represented by a set of operators $\{\Omega_x\}$ satisfying $\sum_x \Omega_x \Omega_x^\dagger = \mathbb{1}$, x running over all possible measurement outcomes. The probability of a result x of a measurement performed on a system in a state ρ is calculated as $P(x) = \text{Tr} [\Omega_x \rho \Omega_x^\dagger]$ and, after the measurement, the state of the system is $\rho^{(x)} = \Omega_x \rho \Omega_x^\dagger / \text{Tr} [\Omega_x \rho \Omega_x^\dagger]$. For the CPF correlation protocol, three sequential measurements represented by the possibly different sets of operators $\{\Omega_x\}$, $\{\Omega_y\}$ and $\{\Omega_z\}$ are realized. Between the measurements the system evolves in contact with

its environment according to Eq. (6.5) as illustrated in Fig. 6.1. The initial state $\rho_{se}^{(0)}$ goes to the state $\rho_{se}^{(x)} = \Omega_x \rho_{se}^{(0)} \Omega_x^\dagger / \text{Tr} [\Omega_x \rho_{se}^{(0)} \Omega_x^\dagger]$ after the first (past) measurement with probability $P(x|0) = \text{Tr} [\Omega_x \rho_{se}^{(0)} \Omega_x^\dagger]$, where Ω_x must be understood as $\Omega_x \otimes \mathbb{1}_e$. After a period $t = t_y - t_x$ of interaction between OQS and bath, the second (present) measurement delivers the result y with probability $P(y|x) = \text{Tr} [\Omega_y U_t \rho_{se}^{(x)} U_t^\dagger \Omega_y^\dagger]$, letting the composite system in the state

$$\rho_{se}^{(y)}(t) = \frac{\Omega_y U_t \rho_{se}^{(x)} U_t^\dagger \Omega_y^\dagger}{\text{Tr} [\Omega_y U_t \rho_{se}^{(x)} U_t^\dagger \Omega_y^\dagger]}. \quad (6.20)$$

The retrodicted probability of past given present can then be calculated as $P(x|y) = P(x, y)/P(y)$, where $P(y) = \sum_x P(x, y)$ and the joint probability is obtained from the predictive probabilities as $P(x, y) = P(y|x)P(x|0)$. The last stage is a time evolution for period $\tau = t_z - t_y$ followed by a last (future) measurement on the OQS, the probability of an outcome z being $P(z|x, y) = \text{Tr} [\Omega_z U_\tau \rho_{se}^{(y)}(t) U_\tau^\dagger \Omega_z^\dagger]$. Provided that the state $\rho_{se}^{(y)}(t)$ after the present intervention does not depend on the past measurement, $P(z|x, y) = P(z|y)$, the independence between past and future is attained, and the CPF correlation given by Eq. (6.18) vanishes. Usually, this is not the case. If the intermediate measurement is projective over the eigenstates of an observable $O = \sum_y O_y |y\rangle\langle y|$, the resulting composite state is

$$\rho_{se}^{(y)}(t) = |y\rangle\langle y| \otimes \rho_e^{(y|x)}(t) = |y\rangle\langle y| \otimes \text{Tr}_s \left[\frac{\Omega_y U_t \rho_{se}^{(x)} U_t^\dagger \Omega_y^\dagger}{\text{Tr} [\Omega_y U_t \rho_{se}^{(x)} U_t^\dagger \Omega_y^\dagger]} \right]. \quad (6.21)$$

The interaction between system and environment creates entanglement between the two parts causing the reduced state of the environment $\rho_e^{(y|x)}(t)$ to depend on the measurement result of the system in the past intervention, although the state of the system itself does not depend on the past.

If the system is not interacting with the environment ($H_I = 0$), then $\rho_e^{(y|x)}(t)$ does not depend on x and $C_{pf}|_y = 0$ for any measurement choice. It means that the measurement process itself does not violate the past-future independence, any violation comes from the memory effects induced by the environment, the characteristic of non-Markovian dynamics.

Another remarkable particular case is when the Born-Markov approximation is valid. In this case, the state of the bath is approximately constant, and $\rho_e^{(y|x)}(t) = \rho_e$ equals the initial state leading to a null CPF correlation. Thus, the CPF correlation can also be seen as a measure of departure from the BMA.

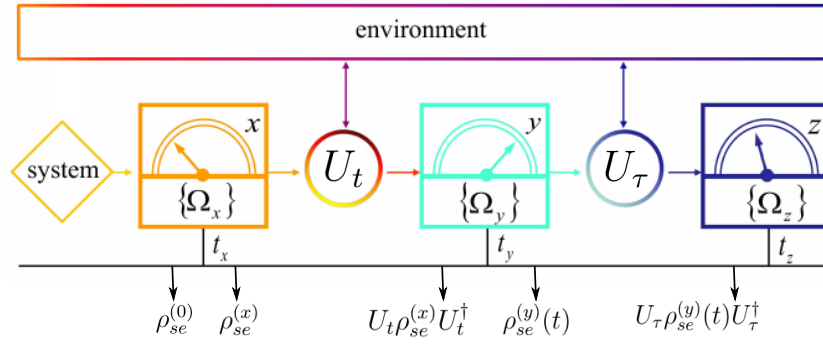


Figure 6.1.: Representation of the CPF correlation protocol. Here we consider that system and environment do not interact at the before t_x , but this is not mandatory for the protocol. Three measurements are performed on the OQS without any intervention in the environment, between two measurements system and environment are let to interact and unitarily evolve. The composite state before and after each measurement is represented bellow the time line. Adapted from [35].

6.4. The spin-boson model

The spin-boson model describes a two-level system (spin) interacting with a quantum environment composed of a continuum of bosonic modes [153]. This is a paradigmatic model in quantum optics used to describe the dipole interaction of a two-level atom with the electromagnetic field [163], as well as in condensed matter physics where it is used to describe defects in a solid interacting with the phononic environment [164], only to give two examples.

The total Hamiltonian is given by

$$H_{\text{tot}} = \frac{\omega_0}{2} \sigma_z + \sum_k \omega_k b_k^\dagger b_k + \sum_k \sigma_x (g_k b_k + g_k^* b_k^\dagger), \quad (6.22)$$

where σ_z is the z -Pauli matrix, ω_0 is the energy difference between the two levels of the qubit. The index k labels the reservoir mode with frequency ω_k which couples to the qubit with coupling constant g_k . The bosonic operators satisfy the relations $[b_k, b_k^\dagger] = 1$. The first two terms on the right hand side are the free energies of system and environment, respectively, while the last term gives the interaction between the two sub-parts.

Here the rotating wave approximation is considered, the terms of the Hamiltonian that do not conserve energy are dropped off and it becomes

$$H_{\text{tot}} = \frac{\omega_0}{2} \sigma_z + \sum_k \omega_k b_k^\dagger b_k + \sum_k (g_k \sigma_+ b_k + g_k^* \sigma_- b_k^\dagger), \quad (6.23)$$

where $\sigma_+ = |\uparrow\rangle\langle\downarrow|$ and $\sigma_- = |\downarrow\rangle\langle\uparrow|$ are the raising and lowering operators of the qubit in the natural base $\{|\uparrow\rangle, |\downarrow\rangle\}$.

As usual, we assume that the total initial state is the pure separable wave vector

$|\Psi_0\rangle = (a|\uparrow\rangle + b|\downarrow\rangle) \otimes |0\rangle$, where the environment vacuum state is $|0\rangle \equiv \prod_k |0\rangle_k$. As the commutator of the total number of excitations $N = \sigma_+\sigma_- + \sum_k b_k^\dagger b_k$ with the total Hamiltonian vanishes ($[H_{tot}, N] = 0$), this quantity is conserved and a good ansatz for the evolved state in the interaction picture is

$$|\Psi_t\rangle = \left[a(t)|\uparrow\rangle + b(t)|\downarrow\rangle + |\downarrow\rangle \sum_k c_k(t)b_k^\dagger \right] |0\rangle, \quad (6.24)$$

as it has only terms with at most one excitation. The time evolution in this representation is given by

$$i \frac{d|\Psi_t\rangle}{dt} = H_I(t)|\Psi_t\rangle, \quad (6.25)$$

with $H_I(t) = \sum_k (g_k e^{i\omega_0 t} \sigma_+ e^{i\omega_k b_k^\dagger b_k} b_k e^{-i\omega_k b_k^\dagger b_k} + h.c.)$. After solving the Schrödinger equation (6.25) (the details are left for Appendix), the system density matrix $\rho_t = \text{Tr}_e[|\Psi_t\rangle\langle\Psi_t|]$ in the interaction representation can be found as

$$\rho_t = \begin{pmatrix} |a|^2 |G(t)|^2 & ab^* G(t) \\ a^* b G^*(t) & 1 - |a|^2 |G(t)|^2 \end{pmatrix}, \quad (6.26)$$

which fulfills the non-Markovian master equation $(d\rho_t/dt) = \frac{-i}{2}\omega(t)[\sigma_z, \rho_t] + \gamma(t)([\sigma_-\rho_t, \sigma_+] + [\sigma_-, \rho_t\sigma_+])$ [153]. The time-dependent decay rate and frequency are defined as $\gamma(t) + i\omega(t) = -(d/dt) \ln[G(t)]$. The ‘‘wave vector propagator’’ $G(t)$ is defined by

$$\frac{d}{dt}G(t) = - \int_0^t f(t-t')G(t')dt', \quad (6.27)$$

where the memory kernel is defined by the bath correlation $f(t) \equiv \sum_k |g_k|^2 \exp[+i(\omega_0 - \omega_k)t]^2$. For a continuous of modes with isotropic interaction the bath correlation becomes $f(t) = \int d\omega J(\omega) \exp[+i(\omega_0 - \omega)t]$, $J(\omega)$ is called spectral function.

In the Born-Markov limit, the bath correlation remains for a very short time and the bath correlation function can be approximated by a Dirac delta function. In this limit the Green function that satisfies Eq. (6.27) represents a pure exponential decay and the dynamics is Markovian. The usual measures as the ones described in Section (6.3.2) are able to detect non-Markovianity only if the decay rate $\gamma(t)$ is negative in some time interval [165]. For the model (6.23), standard memory witness, such as the ones presented in Section 6.3.2, coincide [166]. In fact, these measures are able to detect non-Markovianity only if the decay rate $\gamma(t)$ is negative in some time interval [165]. Equivalently, this means that if $|G(t)|^2$ decays monotonically, giving place to a monotonous decay from the upper level $|\uparrow\rangle$ to the lower state $|\downarrow\rangle$, then the

²This function is called bath correlation because it can be written as $f(t-t') = \text{Tr}_e (B(t)B^\dagger(t')\rho_e) e^{i\omega(t-t')}$, where $B = \sum_k g_k b_k$ is the bath operator which participate in the interaction, and $\rho_e = |0\rangle\langle 0|$ is the environment initial state.

dynamics is considered Markovian. Nevertheless, in this regime it is not necessarily within the BMA. Non-Markovianity close to the BMA can be detected with a CPF correlation [35, 36].

6.4.1. CPF correlation

For different measurement schemes, the CPF correlation associated to the dynamics Eq. (6.22) can be calculated in an exact way. Considering the initial condition $|\Psi_0\rangle = (a|\uparrow\rangle + b|\downarrow\rangle) \otimes |0\rangle$ and performing three projective measurements in the σ_z direction of the Bloch sphere ($\sigma_z - \sigma_z - \sigma_z$), which implies $x = \pm 1, y = \pm 1, z = \pm 1$, the exact CPF correlation reads (see Appendixes) $C_{pf}(t, \tau)|_{y=+1}^{\sigma_z \sigma_z \sigma_z} = 0$, while for the conditional $y = -1$, it reads

$$C_{pf}(t, \tau)|_{y=-1}^{\sigma_z \sigma_z \sigma_z} = \left\{ \frac{4|a|^2|b|^2}{[(1 - |G(t)|^2)|a|^2 + |b|^2]^2} \right\} |G(t, \tau)|^2. \quad (6.28)$$

Alternatively, by performing the successive measurement in the $\sigma_x - \sigma_z - \sigma_x$ directions, we get $C_{pf}(t, \tau)|_{y=+1}^{\sigma_x \sigma_z \sigma_x} = 0$, while for the conditional $y = -1$, it reads

$$C_{pf}(t, \tau)|_{y=-1}^{\sigma_x \sigma_z \sigma_x} = \left\{ \frac{1 - [2\text{Re}(ab^*)]^2}{1 - |G(t)|^2/2} \right\} \text{Re}[G(t, \tau)]. \quad (6.29)$$

In the previous two expressions, the function $G(t, \tau)$ is

$$G(t, \tau) \equiv \int_0^t dt' \int_0^\tau d\tau' f(\tau' + t') G(t - t') G(\tau - \tau'). \quad (6.30)$$

The exact result $C_{pf}(t, \tau)|_{y=+1}^{\sigma_z \sigma_z \sigma_z} = 0$ jointly with $C_{pf}(t, \tau)|_{y=+1}^{\sigma_x \sigma_z \sigma_x} = 0$, follow from the symmetry of the problem. In fact, the conditional $y = +1$ implies that the system evolution during the first two measurements (interval t) is exactly the same than in the interval between the second and third measurements (interval τ). Thus, the CPF correlation vanishes [35, 36]. This accidental symmetry does not appear for the conditional $y = -1$.

Besides normalization factors proportional to the initial system condition and the propagator $G(t)$, Both Eq. (6.28) and (6.29) are determined by $G(t, \tau)$ [Eq. (6.30)]. Thus, in contrast to previous approaches, where $G(t)$ takes the main role, here $G(t, \tau)$ is the main mathematical object capturing the memory effects. It consist in a convolution involving two system propagators mediated by the environment correlation. It is simple to check that $G(t, \tau) \rightarrow 0$ when $f(t)$ approaches a delta function. Consequently, $G(t, \tau)$ measures departures with respect to the BMA, even close to its validity.

Backflow of information: Given that the underlying dynamics admits an exact treatment, a simple relation between a non-operational backflow of information [166] and an operational one can be established as follows: Let us consider that the system is at the initial time in

the upper state, a non-monotonous decay of the conditional probability $P(\uparrow, t | \uparrow, 0) = |G(t)|^2$ determines the presence of an environment-to-system backflow of information (non-operational way). In contrast, under the same initial condition, an operational backflow of information can be defined by the probability $P(\uparrow, t + \tau | \downarrow, t; \uparrow, 0) = |G(t, \tau)|^2 / [1 - |G(t)|^2]$, which measures the capacity of the environment of reexciting the system after it has been found in the lower state at an intermediate time. This probability only vanishes in the Markovian limit. These two clearly different physical scenarios determine the possibility of detecting departure from the BMA or not, which in turn may be read as different notions of environment-to-system backflow of information.

6.5. Experiment

In order to demonstrate the experimental feasibility of measuring memory effects close to the BMA, we developed a photonic platform that simulates the non-Markovian system dynamics. The CPF correlation is measured through the sequence $X \rightarrow U(t) \rightarrow Y \rightarrow U(\tau) \rightarrow Z$, where X , Y , and Z are the measurement processes while $U(t)$ and $U(\tau)$ are the unitary transformation maps associated to the total Hamiltonian (6.23). These maps represent the system-environment total changes between consecutive measurement processes. Although the real environment is composed of an infinite number of modes, the system reduced dynamical map can be obtained if the environment is regarded also as a two-level system [167]. The map $U(t)$ is defined by the transformations

$$|\downarrow\rangle \otimes |0\rangle \rightarrow |\downarrow\rangle \otimes |0\rangle, \quad (6.31a)$$

$$|\uparrow\rangle \otimes |0\rangle \rightarrow \cos(2\theta) |\uparrow\rangle \otimes |0\rangle + \sin(2\theta) |\downarrow\rangle \otimes |1\rangle. \quad (6.31b)$$

Here, $|0\rangle$ and $|1\rangle$ represent the bath in its ground state and (first) excited state respectively. The angle θ is such that $\cos(2\theta) = G(t)$. Given that the intermediate (second) measurement may leave the system in its ground state and the bath in an excited state, the map associated to $U(\tau)$ involves one extra initial state,

$$|\downarrow\rangle \otimes |0\rangle \rightarrow |\downarrow\rangle \otimes |0\rangle, \quad (6.32a)$$

$$|\uparrow\rangle \otimes |0\rangle \rightarrow \cos(2\tilde{\theta}) |\uparrow\rangle \otimes |0\rangle + \sin(2\tilde{\theta}) |\downarrow\rangle \otimes |1\rangle, \quad (6.32b)$$

$$|\downarrow\rangle \otimes |1\rangle \rightarrow \sin(2\tilde{\theta}') |\uparrow\rangle \otimes |0\rangle + \cos(2\tilde{\theta}') |\downarrow\rangle \otimes |1\rangle. \quad (6.32c)$$

The angles are given by the relations $\cos(2\tilde{\theta}) = G(\tau)$, and $\sin(2\tilde{\theta}') = G(t, \tau) / \sqrt{1 - |G(t)|^2}$. This last term measures the capacity of the environment of reexciting the system. It involves a normalization proportional to the decay probability in the interval $(0, t)$ (see Appendix D).

The previous maps can be experimentally simulated by encoding the system states $\{|\downarrow\rangle, |\uparrow\rangle\}$ into polarization of a photon $\{|H\rangle, |V\rangle\}$, while the bath states are encoded into the path degree of freedom of the same photons. Angles $\{\theta, \tilde{\theta}, \tilde{\theta}'\}$ are chosen as a function of the simulated bath properties [168, 169]. We approach the spectral density by a Lorentzian $J(\omega) = (1/2\pi)\gamma\tau_c^{-2}/[(\omega - \omega_0)^2 + \tau_c^{-2}]$, which implies the exponential correlation $f(t) = (\gamma/2\tau_c)\exp[-|t|/\tau_c]$, γ is the strength of the coupling between system and environment and τ_c is correlation time of the bath. In this case, the propagator (6.27) reads

$$G(t) = e^{-t/2\tau_c} \left[\cosh\left(\frac{t\chi}{2\tau_c}\right) + \frac{1}{\chi} \sinh\left(\frac{t\chi}{2\tau_c}\right) \right], \quad (6.33)$$

where $\chi \equiv \sqrt{1 - 2\gamma\tau_c}$. Furthermore, Eq. (6.30) becomes

$$G(t, \tau) = \frac{2\gamma\tau_c}{\chi^2} e^{-(t+\tau)/2\tau_c} \sinh\left(\frac{t\chi}{2\tau_c}\right) \sinh\left(\frac{\tau\chi}{2\tau_c}\right). \quad (6.34)$$

As $\omega(t) = 0$ ($G(t)$ real), in the considered case there is no time-dependent energy shift. In the weak coupling limit $\gamma \ll 1/\tau_c$, where the correlation time τ_c of the bath is the minor time scale of the problem, it follows that $G(t) \simeq \exp[-\gamma t/2]$, $G(t, \tau) \simeq 0$, which in turn implies that, independently of the measurement scheme, a Markovian limit is approached $C_{pf}(t, \tau)|_y \simeq 0$.

The specific experimental setup is illustrated in Fig. 6.2. A continuous-wave (CW) laser, centered at 325 nm, is sent to a beta-barium-borate (BBO) crystal. Degenerated pairs of photons (wavelength centered at 650 nm), are produced in the modes signal ‘‘s’’ and idler ‘‘i’’ via spontaneous-parametric-down-conversion [94]. The photons in mode i are sent directly to detection as they only herald the presence of photons in mode s, while the photons in mode s pass through nested interferometers, which emulate the maps $U(t)$ and $U(\tau)$ [169]. Projective measurements are introduced in modules X, Y, Z . The CPF correlation is extracted by using coincidence counts for all the different combinations of past, present and future outcomes.

Given that the photons created in the BBO crystal are horizontally polarized, we prepare any initial linear polarization state $(a|H\rangle + b|V\rangle)$, $a, b \in \mathbb{R}$ using a half-wave plate (HWP₁). The past measurement X is performed using a set of two HWPs and a polarizing beam-splitter (PBS), which transmits the horizontal polarization and reflects the vertical one. In this measurement, the angle set in HWP₂ selects the linear polarization state mapped to H and hence transmitted by the PBS, while HWP₃ prepares the projected state from the transmitted horizontal polarization. After this module, the map $U(t)$ [Eq. (6.31)] is implemented by coupling the polarization with the path degrees of freedom. For this, we use an interferometer composed of two beam-displacers (BD), each one transmitting (deviating) the vertical (horizontal) polarization, and two HWPs, one at each path mode. HWP _{θ} rotates the polarization such that part of the light exits the interferometer in (spatial) mode $|0\rangle$ (upper path) and part in mode $|1\rangle$ (lower path), depending on θ . HWP_{45°} simply rotates the photons from H to V , such that all

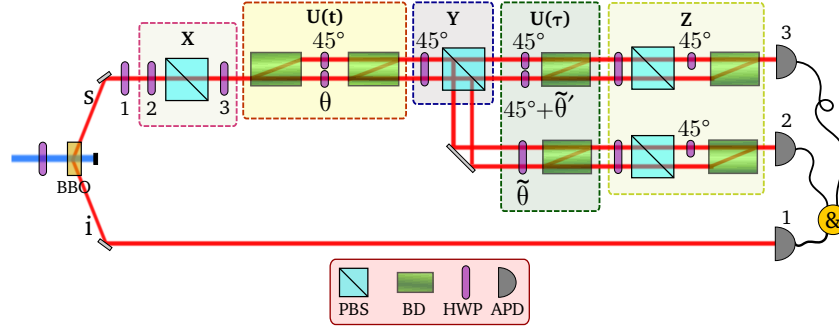


Figure 6.2.: Experimental Setup. Modules X , Y , and Z perform the projective measurements. Modules $U(t)$ and $U(\tau)$ implement the unitary system-environment maps. From coincidence counting, the avalanche photon detectors (APD) allow measuring the CPF correlation for photon signal (“s”), while photon idler (“i”) only heralds its presence (see text). Spatial mode 0 (1) corresponds to the upper (lower) path after the first beam displacer (BD). PBS - polarizing beam splitter; HWP - half wave plate.

photons of this mode are mapped to mode $|0\rangle$ at the output of the interferometer. Posteriorly, measurement Y is performed using a HWP and a PBS. We restrict ourselves to perform projections onto the σ_z basis. This is done by fixing a HWP at 45° to correct the polarization state such that the H -polarized photons are transmitted and V -polarized ones are reflected. The map $U(\tau)$ [Eq. (6.32)], characterized by angles $\tilde{\theta}$ and $\tilde{\theta}'$, is implemented in a similar way, noticing that slightly different dynamics take place depending on the result of the Y measurement ($|\downarrow\rangle$ or $|\uparrow\rangle$, equivalent here to transmitted or reflected). The photons on both path are coherently combined at the two BDs. The final Z measurement is also implemented by two sets of HWP and PBS, one set for the transmitted light and the other to the reflected light. The last two BDs, which are just before the detectors Det_2 and Det_3 , are used to trace out the path degrees of freedom.

An example of angle values used in the experiment is shown in Fig. 6.3. Specially for the $\text{HWP}_{\tilde{\theta}'}$ the angle changes must be performed very carefully and for this purpose the half-wave plates responsible for the three dynamical angles $\{\theta, \tilde{\theta}, \tilde{\theta}'\}$ are motorized and moved with precision of 0.001° .

From an experimental viewpoint, to condition the probabilities on the result y of the intermediate measurement means to consider only the coincidence counts between Det_1 and Det_3 (Det_1 and Det_2) for $y = -1$ ($y = +1$). Let $N_{z,x}^{(j)}$ denotes the number of coincidences registered between Det_1 and Det_j when the past and future projective measurements are set to x and z correspondent eigenvectors, respectively. Let also $y^{(j)}$ be the value of the intermediate outcome corresponding to Det_j . The probabilities used to calculate the CPF correlation (6.18) can be obtained as $P(z, x|y^{(j)}) = N_{z,x}^{(j)} / (\sum_{x',z'} N_{z',x'}^{(j)})$, while $P(z|y^{(j)}) = \sum_x P(z, x|y^{(j)})$ and $P(x|y^{(j)}) = \sum_z P(z, x|y^{(j)})$.

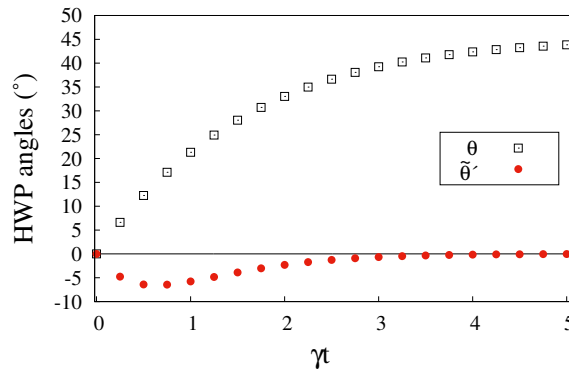


Figure 6.3.: Calculated angle values as functions of time for the case of $\gamma\tau_c = 0.5$.

6.5.1. Results

In Fig. 6.4 we plot both the theoretical results (full lines) as well as the experimental ones (symbols) for the CPF correlation at equal times, $C_{pf}(t, t)|_{y=-1}$. Both the \hat{z} - \hat{z} - \hat{z} [Eq. (6.28)] and \hat{x} - \hat{z} - \hat{x} [Eq. (6.29)] measurement schemes were implemented (upper and lower curves respectively). While for the chosen bath correlation parameters the propagator $G(t)$ decays in a monotonous way, detection of memory close to the BMA is confirmed for different bath correlation times τ_c . An excellent agreement between theory and experiment is observed. In particular, at time $t = 0$, null values of the CPF correlation are experimentally observed, meaning that correlation between the system and environment are negligible at the preparation stage [170]. While the modulus of $C_{pf}(t, t)|_{y=-1}$ depends on the initial system state, we note that it is smaller in the \hat{z} - \hat{z} - \hat{z} scheme when compared with the \hat{x} - \hat{z} - \hat{x} measurement scheme. In fact, $|G(t, \tau)|^2 \leq |\text{Re}[G(t, \tau)]|$ [see Eqs. (6.28) and Eq. (6.29)]. This feature also reflects that in the former case, in contrast to the last one, the dynamics between measurements is incoherent.

We also used the experimental setup for measuring memory effects even closer to the BMA, that is, for smaller bath correlation times. Experimental limitations emerge due to different aspects, as explained in the next section. For instance, reduced visibility in the interferometers degrades the quality of our operations, weakening agreement between theory and experiment. The finite count statistics also become more relevant when approaching the Markovian limit, as it becomes unclear if a nonnull CPF comes from memory or fluctuation effects. In spite of these limitations, our experiment demonstrates the total feasibility of measuring quantum non-Markovian effects close and beyond the BMA.

The CPF correlation was also measured for different time intervals for the two unitary evolution steps $t \neq \tau$ and the result is shown in Fig. 6.5 together with the expected theoretical correlation. For $t = 0$ the correlation vanishes meaning that the initial state presents no correlation between system and environment. For $t, \tau > 0$ the correlation is as big as the time intervals are close to the correlation time of the bath τ_c . As the dynamics goes to the Born-Markov

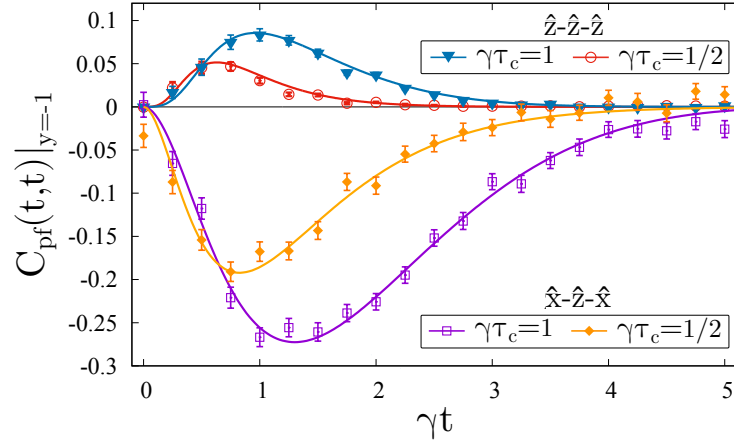


Figure 6.4.: CPF correlation for different projective measurements and bath correlation times. Theoretical results (full lines), experimental results (symbols). The two upper curves correspond to the \hat{z} - \hat{z} - \hat{z} measurements and the lower ones to \hat{x} - \hat{z} - \hat{x} measurements. The initial system state is $(\sqrt{p}|\uparrow\rangle + \sqrt{1-p}|\downarrow\rangle)$ with $p = 0.8$ (upper curves) and $p = 1$ (lower curves). From top to bottom, the bath parameters are $\gamma\tau_c = 1, 1/2, 1/2, 1$.

limit ($t \gg \tau_c$) the correlation vanishes. This experimental results suffer even more from the aforementioned finite statistics fluctuations as we have used approximately one fifth of the total counts we used in the $t = \tau$ case to build each experimental point.

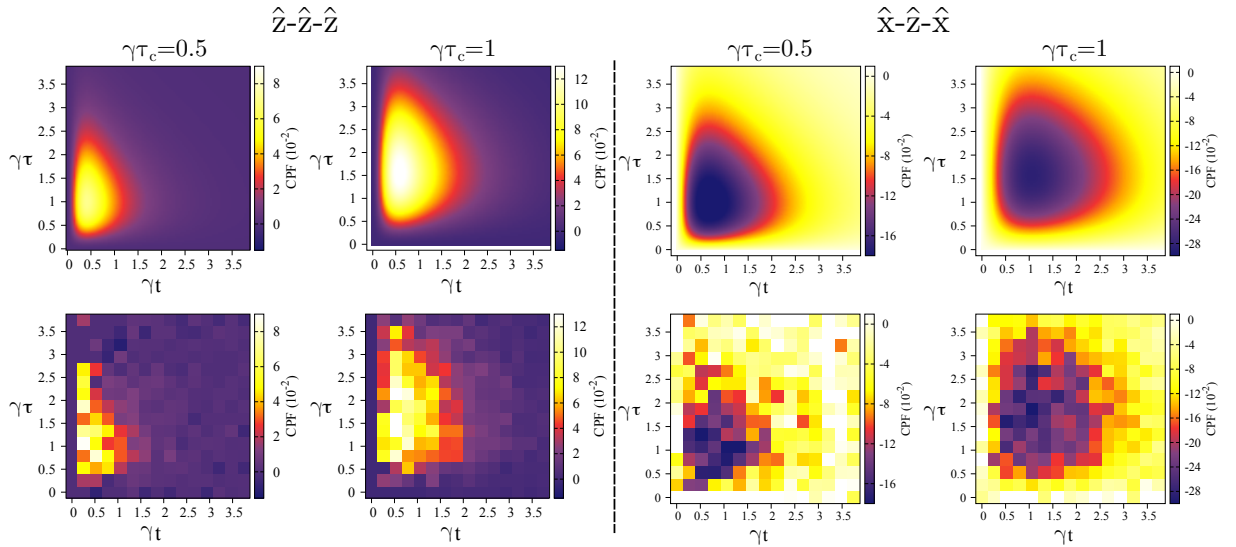


Figure 6.5.: CPF correlation as a function of the time intervals t and τ of the two unitary system-environment evolutions. The upper row shows the theoretical result and in the line below, the experimental data is shown. The initial system state is $(\sqrt{p}|\uparrow\rangle + \sqrt{1-p}|\downarrow\rangle)$ with $p = 0.8$ (\hat{z} - \hat{z} - \hat{z} scheme) and $p = 1$ (\hat{x} - \hat{z} - \hat{x} scheme).

6.5.2. Robustness of the experimental setup

In this section we study the behavior of the CPF correlation in real world implementations. In particular, we consider two limitations of our experimental setup, namely the finite counts statistics and the non-unit visibility of the interferometers. The last one is an issue only for the \hat{x} - \hat{z} - \hat{x} scheme, since the evolution in the \hat{z} - \hat{z} - \hat{z} scheme is incoherent and no interference take place in this case. In Fig. 6.6 we show results of simulations when these issues are considered. In Fig. 6.6-a) we show in black hollow squares the results for the ideal case of visibility V equals to one and infinite counts. In red circles, we also show results for $V=1$ but considering finite counts such as the ones we have in the experiment (around 10000 events in total). One can see that the circles are dispersed around the theoretical prediction, giving rise to values of the CPF correlation up to 15% greater than what is expected theoretically. This shows that the CPF correlation is quite sensitive to statistical fluctuations. In Fig. 6.6-b) we show results of simulations for $V=0.9$. The results do not coincide with the theoretical prediction even in the case of infinite counts (blue hollow squares). Moreover, when non perfect visibility and finite counts are considered together, experimental values could differ from theory for more than 25%. When $V=0.8$, results in Fig. 6.6-c), the dispersion of the simulated values is even larger, obtaining high discrepancy between theory and data. As consequence, to restore the agreement between theory and experiment it would be necessary to introduce dephasing in the theoretical description.

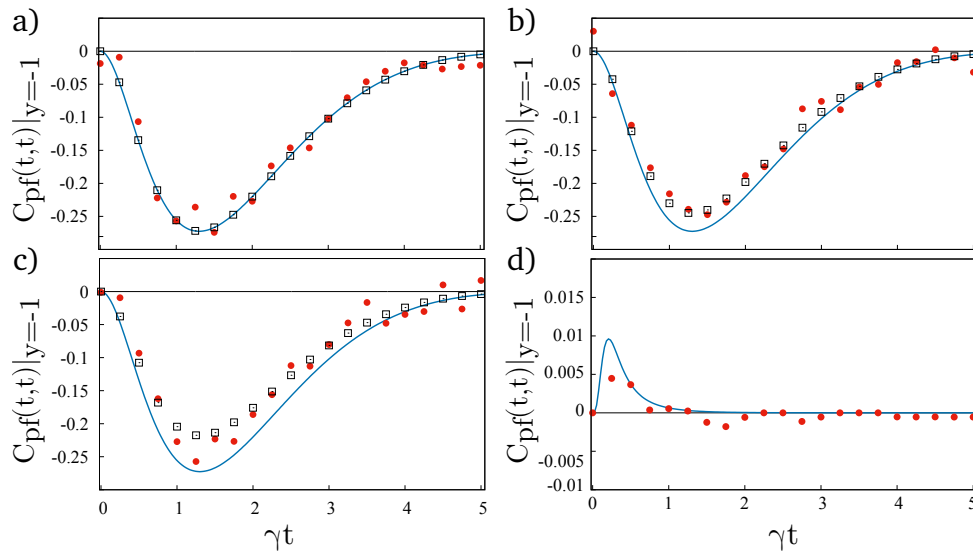


Figure 6.6.: CPF correlation as a function of time for simulated data taking into account experimental issues. a), b) and c): \hat{x} - \hat{z} - \hat{x} scheme of measurement with $\gamma\tau_c = 1$, and initial state $|\uparrow\rangle$. In d) the \hat{z} - \hat{z} - \hat{z} scheme of measurement is used with initial state $\sqrt{p}|\uparrow\rangle + \sqrt{1-p}|\downarrow\rangle$, $p = 0.8$. More details in the text.

As mentioned above, we find further experimental issues closer to BMA limit ($\tau_c \rightarrow 0$). In Fig. 6.6-d) we show the exact value of the CPF correlation (blue solid curve) and a

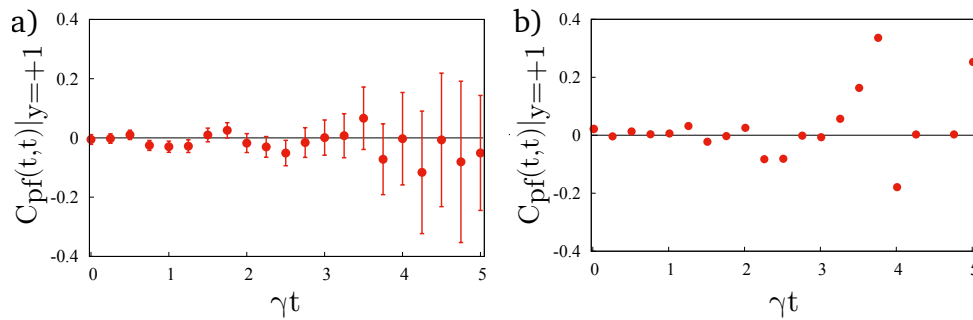


Figure 6.7.: CPF correlation when $y = +1$ in the $\hat{x}-\hat{z}-\hat{x}$. $\gamma\tau_c = 1$, and $p = 1$ are used in this case. a) Experimental data and b) simulation assuming Poissonian fluctuations.

theoretical simulation including finite statistic effects (red circles) for $\tau_c\gamma = 0.1$ in the $\hat{z}-\hat{z}-\hat{z}$ scheme of measurement. In this case, the values of CPF correlation and its experimental variations due to fluctuations in the number of counts are comparable. This alone prevents us to assign a non vanishing correlation to memory effects instead of fluctuations, without considering any other experimental issue.

In Fig. 6.7-a), we plot the experimental values of CPF correlation when the measurement outcome in the present is $y = +1$. In this case, the correlation is null within the error bars, in agreement with what is predicted theoretically. One can see that the error bars increase substantially while time passes. This is related with the fact that the system excitation tends to decay to the reservoir, making the probabilities to find it in an excited state ($y = +1$) almost null for values of γt larger than 3. In our setup, this is translated as a reduction of the number of coincidence counts, causing the probabilities to be much more sensitive to statistical fluctuations. The fluctuations observed experimentally are compatible with finite count statistics as shown in Fig. 6.7-b), where we plot the result of a simulation assuming Poissonian fluctuations around the ideal theoretical value of the counts.

6.6. Conclusions

Detection of quantum non-Markovianity close to the Born-Markov approximation was characterized through an operational-based memory witness. The CPF correlation was calculated for the decay dynamics of a two-level system coupled to a bosonic environment. Instead of the propagator, here the relevant object associated to memory effects consists in the convolution of two system propagators weighted by the environment correlation. This structure can be related to an alternative formulation of the phenomenon of environment-to-system backflow of information, where an intermediate condition on the system state allows to detect memory effects even close to the validity of the BMA. A photonic experiment corroborates the feasibility of detecting quantum memory effects close to the BMA with excellent agreement with the

theory.

These results provide a relevant contribution to the understanding of operational-based quantum memory witnesses. In particular, our study elucidates which structure replaces the system propagator when studying these alternative approaches. The validity of the present conclusions to arbitrary system-environment dynamics can be established by using perturbation techniques [171].

EXPERIMENTAL REALIZATION OF AN ARBITRARY QUBIT CHANNEL: A PROPOSAL

In Section 6.3 we briefly discussed the general evolution of open quantum systems and how it is given by maps that can be regarded as unitary evolutions for larger systems. In that chapter however, the focus was to use this treatment to present the concept of quantum non-Markovianity. In this chapter, we are concerned only about the completely positive maps themselves, also called quantum channels. Here we show how to use the experimental platform presented in chapters 5 and 6 to implement a large class of quantum channels for a photonic qubit using the path degrees of freedom of the photon itself as ancillary systems, which allows us to introduce decoherence in a controllable way in the qubit evolution (the polarization degree of freedom of the photon). This is still only a proposal for an experiment that we hope will be implemented soon.

Aiming to be self-contained, the chapter starts with a brief review of quantum channels already presented in Chapter 6, followed by the particular case of qubit transformations. Before presenting the most general protocol, we motivate it in Section 7.3 by showing how to implement a particular channel called “generalized amplitude damping”. The general protocol is presented in Section 7.4, together with many examples of how to set the experimental parameters to implement some particular channels. The chapter ends with a brief description of quantum process tomography, that should be used to verify what channel is indeed being realized by the setup.

This work is being developed in collaboration with Gabriel Aguilar (UFRJ), Gabriel Landi (USP), and the students of the Quantum Optics Lab Rodrigo Piera and Thiago Guimarães. I contributed to the theoretical part and design of the experiment. At this moment the experiment is being set up.

7.1. Quantum maps

In Chapter 6, we have introduced the concept of quantum maps: the mathematical transformations leading from an initial to a final state. Although there we presented this by tracing out the environmental degrees of freedom from the global time-evolved state, once defined, the map does not need to make reference to the passage of time.

Let us consider a system of interest whose Hilbert space is \mathcal{H} and $S(\mathcal{H})$ denotes the set of positive self-adjoint operators acting on \mathcal{H} with trace 1, i.e. $S(\mathcal{H})$ is the set of all possible density matrices of the system. A quantum map $\Lambda : S(\mathcal{H}) \rightarrow S(\mathcal{H})$ describes mathematically the state transformation from a initial state $\rho \in S(\mathcal{H})$ to a final state $\Lambda[\rho] \in S(\mathcal{H})$, without necessarily mentioning the underlying physical process or the time it takes. To be a proper quantum map, Λ must keep the basic features which define a density matrix:

- It must be trace preserving such that the total probability is conserved;
- It must be positive such that the transformed state is a positive semidefinite operator, which means that all the probabilities are always positive numbers;
- As the system can be a part in a bigger system, it should maintain the positivity also of a global state in a joint Hilbert space $\mathcal{H} \otimes \mathcal{H}_e$, regardless the dimension of the environment Hilbert space \mathcal{H}_e . This feature is called complete positivity¹.

An operation obeying all this requirements is called a completely-positive and trace-preserving (CPTP) map. If the nonunitary dynamics is the result of a partial trace of a unitarily evolved global state, then all these requirements are fulfilled. However, it is not always mathematically friendly to solve or even to enunciate the global evolution problem. Therefore it is often convenient to heuristically find the map and to deal only with the smaller system problem, ignoring the source of dissipation and decoherence.

Every completely positive map has a operator-sum decomposition

$$\Lambda[\rho] = \sum_k E_k \rho E_k^\dagger, \quad (7.1)$$

which is not unique [157]. The E_k s are called Kraus operators. The trace preservation condition $\text{Tr} \Lambda[\rho] = \sum_k \text{Tr} E_k E_k^\dagger \rho = \text{Tr} \rho$, valid for all $\rho \in S(\mathcal{H})$, is attained if $\sum_k E_k E_k^\dagger = \mathbb{1}$. The number of Kraus operators required to represent a map is not fixed, but there is a minimal number of operators which is at most equal to d^2 (the Hilbert space dimension squared) [172]. If the initial state of the environment and the global Hamiltonian evolution are known, the operator-sum

¹In Section 6.3, it was mentioned that it is not always possible to define a complete positive map if the initial state has entanglement between system and environment. Here we disregard these cases when we considered maps defined in the whole set of states $S(\mathcal{H})$.

representation can be obtained as shown in Eq. (6.8). It is possible to see that the maximum number of Kraus operators depends on the Hilbert space dimension of the environment and that the Kraus decomposition is not unique since it depends on the environmental Hilbert space basis being used.

There is an interpretation for the operator-sum representation in terms of measurements of the environment. Consider that the total system is initially in the separable state $\rho \otimes |e_0\rangle\langle e_0|$, which evolves under the unitary U . If the environment is measured and its state after the intervention is $|e_k\rangle$, then the system state becomes proportional to

$$\text{Tr}_e\{|e_k\rangle\langle e_k|U(\rho \otimes |e_0\rangle\langle e_0|)|e_k\rangle\langle e_k|\}. \quad (7.2)$$

It is easy to see from Eq. (6.8) that the normalized state is given by

$$\rho_k = \frac{E_k \rho E_k^\dagger}{\text{Tr}[E_k \rho E_k^\dagger]}.$$

Now, the probability of getting the outcome k is given by

$$p(k) = \text{Tr}[|e_k\rangle\langle e_k|U(\rho \otimes |e_0\rangle\langle e_0|)|e_k\rangle\langle e_k|] = \text{Tr}[E_k \rho E_k^\dagger]. \quad (7.3)$$

Thus, if the measurement outcome is kept unrevealed, the state of the system is

$$\rho' = \sum_k p(k) \rho_k \quad (7.4)$$

which is exactly the operator-sum decomposition (7.1). Thus the effect of the quantum channel is equivalent to taking the initial state and randomly replacing it by the states ρ_k , the inherent randomness coming from the unknown measurement of the reservoir.

Once pursuing a Kraus decomposition, it is possible to solve the converse problem and obtain a unitary transformation in a larger Hilbert space that gives rise to the reduced transformation given by the map. Many environmental dimensions and interactions may give rise to the same dynamics for the main system. Considering that the environment is initially in a pure state, the minimal dimension of the environment Hilbert space is given by the minimal number of Kraus operators in the map decomposition. In this case, the unitary evolution operator U can be obtained as to satisfy

$$U|\psi\rangle|e_0\rangle = \sum_k E_k |\psi\rangle |e_k\rangle, \quad (7.5)$$

where $|\psi\rangle$ is an arbitrary pure state of the main system, the sum runs over the orthogonal basis states $\{|e_k\rangle\}$ of the environment, and the environment is initially in the state $|e_0\rangle$ of the basis [173]. In this construction, U is not uniquely defined because its action is not prescribed for the

basis states but $|e_0\rangle$.

In what follows we restrict ourselves to the case of a bi-dimensional Hilbert space. It is tempting to think that in this case it is possible to build any map from the unitary evolution with a qubit environment initially prepared in a mixed state [174]. Although there are many quantum channels for which it is indeed possible, there are indeed a few well-known and relevant counterexamples [175].

7.2. Quantum maps of qubits

The simplest but also one of the most interesting systems for quantum computation consists of a two level system or a qubit. As well as the qubit is the basic unit for unitary quantum computation, it can be thought of as the primitive for open quantum system protocols as well [176].

The identity and the Pauli matrices form a basis for 2×2 matrices with complex coefficients. In particular, any density matrix, i.e., any positive Hermitian operator with trace equals to one can be decomposed in this basis as $\rho = \frac{1}{2} [\mathbb{1} + \mathbf{r} \cdot \boldsymbol{\sigma}]$ with $\mathbf{r} \in \mathbb{R}^3$ and $|\mathbf{r}| \leq 1$ to ensure positivity, $\boldsymbol{\sigma}$ denotes a vector with the three Pauli matrices σ_x, σ_y and σ_z as components. It defines the so called Bloch sphere, a 3-dimensional sphere with radius equals to unity, inside which all the qubit states are uniquely represented through their vector \mathbf{r} , with the pure states all lying on the surface. As a positive trace preserving transformation takes states into states, it must change only the 3-dimensional vector \mathbf{r} , thus it consists of rotations, reflections, contractions and translations provided that the vector stays inside the Bloch sphere. The map can thus be represented as

$$\Lambda[\rho] = \Lambda \left[\frac{1}{2} [\mathbb{1} + \mathbf{r} \cdot \boldsymbol{\sigma}] \right] = \frac{1}{2} [\mathbb{1} + (\mathbf{t} + T\mathbf{r}) \cdot \boldsymbol{\sigma}], \quad (7.6)$$

where \mathbf{t} is a real 3D vector and T is a real 3×3 matrix [177]. It must be pointed that not all maps (7.6) admit a Kraus form or are completely positive. In this parameterization it is clear that any map is characterized by at most 12 independent parameters (the 9 elements of T plus the 3 components of \mathbf{t}) which is of course the same number of parameters of a Kraus decomposition as it has at most four 2×2 matrices with a 2×2 completeness conditions.

Before moving to the simulation of a more general channel, let us present a particular case, the generalized amplitude damping channel, as a motivation for the more general protocol.

7.3. Generalized amplitude damping channel

The generalized amplitude damping (GAD) channel for one qubit is defined by its action over a qubit state ρ

$$\Lambda_{GAD}[\rho] = \sum_{j=1}^4 E_j \rho E_j^\dagger \quad (7.7)$$

with the four Kraus operators [173]

$$\begin{aligned} E_1 &= \sqrt{p} \begin{bmatrix} 1 & 0 \\ 0 & \sqrt{\eta} \end{bmatrix} & E_2 &= \sqrt{p} \begin{bmatrix} 0 & \sqrt{1-\eta} \\ 0 & 0 \end{bmatrix} \\ E_3 &= \sqrt{1-p} \begin{bmatrix} \sqrt{\eta} & 0 \\ 0 & 1 \end{bmatrix} & E_4 &= \sqrt{1-p} \begin{bmatrix} 0 & 0 \\ \sqrt{1-\eta} & 0 \end{bmatrix}, \end{aligned} \quad (7.8)$$

where the channel parameters η and p are positive numbers in the interval $[0, 1]$. When $p = 1$ it becomes the so-called amplitude damping channel, which characterizes the interaction of the qubit with a bath initially with no excitation, i.e. at zero temperature. If the system is prepared in the excited state $|1\rangle$, then it can decay and emit one excitation to the bath with probability $1 - \eta$. This channel was presented before as the map (6.31). Many works exploring the effects of the amplitude damping channel over entanglement with a third party and system-environment entanglement dynamics as well as quantum Markovianity have been published using as basic tool for photonic simulations [150, 168, 178–182]. Although this particular case channel has been widely studied experimentally, the more general GAD is lacking a proper implementation as far as we know.

When applied to a pure state $|\psi\rangle = a|0\rangle + b|1\rangle$, the map (7.7) leads to the mixed state

$$\begin{aligned} \Lambda_{GAD}[|\psi\rangle\langle\psi|] &= |a|^2 \{p\rho_0 + (1-p)[\eta\rho_0 + (1-\eta)\rho_1]\} \\ &+ |b|^2 \{(1-p)\rho_1 + p[\eta\rho_1 + (1-\eta)\rho_0]\} + \sqrt{\eta}(ab^*|0\rangle\langle 1| + a^*b|1\rangle\langle 0|), \end{aligned} \quad (7.9)$$

where $\rho_0 = |0\rangle\langle 0|$ and $\rho_1 = |1\rangle\langle 1|$. Thus a qubit originally in state $|1\rangle$ ($a = 0$) has probability $1 - p$ to remain in this state and probability p of passing through a simple amplitude damping with coupling $1 - \eta$ between system and environment. A similar statement is valid for initial state $|0\rangle$, but in this case the system can absorb one excitation from the bath. If the original state is a coherent combination of the two states of the basis, then the channel reduces its coherence by a factor $\sqrt{\eta}$.

Let us encode the qubit in the polarization degree of freedom of photons

$$|0\rangle \longrightarrow |H\rangle \quad |1\rangle \longrightarrow |V\rangle.$$

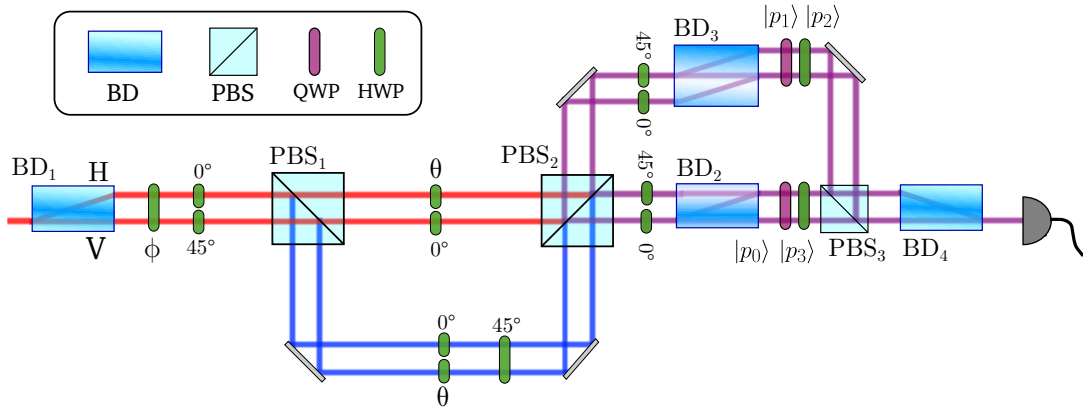


Figure 7.1.: Implementation of GAD channel for a qubit encoded in the polarization of single photons.

A setup implementing the GAD channel is shown in Fig.7.1. Consider a pure initial state $|\psi\rangle = \alpha|H\rangle + \beta|V\rangle$. In the sequence that follows, the state of the photon is written after each optical element:

- Beam displacer BD_1 : creates a path qubit by displacing only the horizontal polarization. Two parallel paths, up and down, come out of this element.

$$a|H\rangle + b|V\rangle \longrightarrow a|H\rangle|u\rangle + b|V\rangle|d\rangle \quad (7.10)$$

- Half wave plate set to an angle $\phi/2$ (the angle is chosen such that $\sin \phi^2 = p$) followed by half wave plates at 45° (down path) and 0° (up path, only compensates the optical path difference caused by the other plate).

$$a|H\rangle|u\rangle + b|V\rangle|d\rangle \longrightarrow a(\cos \phi|H\rangle - \sin \phi|V\rangle)|u\rangle + b(-\cos \phi|H\rangle + \sin \phi|V\rangle)|d\rangle \quad (7.11)$$

- Polarizing beam splitter (PBS_1): it creates two new paths, which we call short (s) and long (l), by transmitting horizontally polarized photons while reflecting the vertically polarized ones. Because of the short coherence length of the heralded photons, the optical path difference is enough to cause decoherence between the two paths. This decoherence is already being considered when we attribute orthogonal states to each path, which are traced out at the end of the unbalanced interferometer.

$$\longrightarrow a(\cos \phi|H\rangle|s\rangle - \sin \phi|V\rangle|l\rangle)|u\rangle + b(-\cos \phi|H\rangle|s\rangle + \sin \phi|V\rangle|l\rangle)|d\rangle \quad (7.12)$$

- Half wave plates at angle $\theta/2$ such that $\cos^2 \theta = \eta$

$$\begin{aligned} &\longrightarrow a [\cos \phi (\cos \theta |H\rangle + \sin \theta |V\rangle) |s\rangle + \sin \phi |V\rangle |l\rangle] |u\rangle \\ &\quad + b [-\cos \phi |H\rangle |s\rangle + \sin \phi (\sin \theta |H\rangle - \cos \theta |V\rangle) |l\rangle] |d\rangle \end{aligned} \quad (7.13)$$

- Half wave plate at 45° only in the long path

$$\begin{aligned} &\longrightarrow a [\cos \phi (\cos \theta |H\rangle + \sin \theta |V\rangle) |s\rangle + \sin \phi |H\rangle |l\rangle] |u\rangle \\ &\quad + b [-\cos \phi |H\rangle |s\rangle + \sin \phi (\sin \theta |V\rangle - \cos \theta |H\rangle) |l\rangle] |d\rangle \end{aligned} \quad (7.14)$$

- Polarizing beam splitter (PBS_2): although there are only two output ports after the PBS, we add two extra outputs to take into account the path difference decoherence. Let us make the following associations $|H\rangle |s\rangle \rightarrow |H\rangle |p0\rangle$, $|V\rangle |s\rangle \rightarrow |V\rangle |p1\rangle$, $|H\rangle |l\rangle \rightarrow |H\rangle |p2\rangle$ and $|V\rangle |l\rangle \rightarrow |V\rangle |p3\rangle$. The real paths are indicated in Fig.7.1.

$$\begin{aligned} &\longrightarrow a [\cos \phi (\cos \theta |H\rangle |p0\rangle + \sin \theta |V\rangle |p1\rangle) + \sin \phi |H\rangle |p2\rangle] |u\rangle \\ &\quad + b [-\cos \phi |H\rangle |p0\rangle + \sin \phi (\sin \theta |V\rangle |p3\rangle - \cos \theta |H\rangle |p2\rangle)] |d\rangle \end{aligned} \quad (7.15)$$

$$\begin{aligned} &= [a \cos \phi \cos \theta |H\rangle |u\rangle - b \cos \phi |H\rangle |d\rangle] |p0\rangle + a \cos \phi \sin \theta |V\rangle |u\rangle |p1\rangle \\ &\quad + [a \sin \phi |H\rangle |u\rangle - b \sin \phi \cos \theta |H\rangle |d\rangle] |p2\rangle + b \sin \phi \sin \theta |V\rangle |d\rangle |p3\rangle \end{aligned} \quad (7.16)$$

- Half wave plates at 45° and beam displacers: in order to assure the right reduction on the final coherence we coherently recombine the polarization components on paths 0 and 2 by using the wave plates and beam displacers BD_2 and BD_3 . To compensate the optical path difference created by BD_1 only the down path is displaced.

$$\begin{aligned} &\longrightarrow [a \cos \phi \cos \theta |V\rangle |u\rangle - b \cos \phi |H\rangle |u\rangle] |p0\rangle + a \cos \phi \sin \theta |H\rangle |u\rangle |p1\rangle \\ &\quad + [a \sin \phi |V\rangle |d\rangle - b \sin \phi \cos \theta |H\rangle |d\rangle] |p2\rangle - b \sin \phi \sin \theta |V\rangle |d\rangle |p3\rangle \end{aligned} \quad (7.17)$$

- Recombining the paths all together incoherently is equivalent to tracing out the path degrees of freedom, what leads to

$$\begin{aligned} &|a|^2 [\sin^2 \phi |V\rangle \langle V| + \cos^2 \phi (\cos^2 \theta |V\rangle \langle V| + \sin^2 \theta |H\rangle \langle H|)] \\ &\quad + |b|^2 [\cos^2 \phi |H\rangle \langle H| + \sin^2 \phi (\cos^2 \theta |H\rangle \langle H| + \sin^2 \theta |V\rangle \langle V|)] \\ &\quad - \cos \theta (ab^* |V\rangle \langle H| + a^* b |H\rangle \langle V|). \end{aligned} \quad (7.18)$$

The last expression is equivalent to (7.9) with the given relations for the wave plate angles if we invert the polarization. Instead of adding more HWP to correct this, we can take it into consideration when setting the angles of the pair of HWP and QWP we use before PBS_3 to make measurements on polarization. In this scheme, the last PBS serves not only to trace out some of the path information but also to perform the measurement. The remaining path information is erased by BD_4 .

7.3.1. Accessing the environment state

First of all, it is necessary to identify what the environment is. If the combination system plus environment is considered as a closed system, then its evolution must be given by a unitary transformation. We can consider a separable initial state ρ_{se} that evolves through the global unitary U :

$$\rho_{se} = \rho_s \otimes \rho_e \longrightarrow U \rho_s \otimes \rho_e U^\dagger. \quad (7.19)$$

The transformation over the system state is recovered by tracing out the environment:

$$\rho_s \longrightarrow \sum_k \langle k | U \rho_s \otimes \rho_e U^\dagger | k \rangle, \quad (7.20)$$

where $\{|k\rangle\}$ is a orthonormal basis of the environment Hilbert space.

If ρ_e is a pure state, say $\rho_e = |0\rangle\langle 0|$, then we identify the Kraus operators with $E_k = \langle e_k | U | 0 \rangle$ and the allowed number of independent Kraus operators is equal to the environment Hilbert space dimension. For example, a GAD channel would require a four-dimensional environment. Instead of using this, let us recall the existence of an isomorphism between CPTP maps for qudit states and density matrices of two qudits [174]. This isomorphism does not exist for all qubit channels [175], but particularly for the GAD it does. For this isomorphism to hold we need to allow the second qudit to be in a mixed initial state.

Thinking about the physical interpretation of the GAD channel, it makes sense to consider the environment in a mixed initial state, it is actually desired to be in a thermal state whose temperature determines the channel parameter p . Since a thermal state includes an infinite number of states for the reservoir, we can identify a qubit whose state $|0\rangle$ corresponds to the ground state of the bath and all excited states are encoded in qubit state $|1\rangle$

$$\rho_e = \frac{e^{-\beta \mathcal{H}_e}}{\sum_k e^{-\beta \mathcal{E}_k}} = \frac{e^{-\beta \mathcal{E}_0} |0\rangle\langle 0|}{\sum_k e^{-\beta \mathcal{E}_k}} + \frac{\sum_j e^{-\beta \mathcal{E}_j} |j\rangle\langle j|}{\sum_k e^{-\beta \mathcal{E}_k}} \longrightarrow p |0\rangle\langle 0| + (1-p) |1\rangle\langle 1|, \quad (7.21)$$

with $p = e^{-\beta \mathcal{E}_0} / \sum_k e^{-\beta \mathcal{E}_k}$. The energy values \mathcal{E}_k are the eigenvalues of the environment free Hamiltonian \mathcal{H}_e and β^{-1} is its temperature.

Thus we can consider the reservoir as being a qubit and the initial state of larger system

(system and reservoir) as $\rho_{se} = \rho_s \otimes [p|0\rangle\langle 0| + (1-p)|1\rangle\langle 1|]$. Plugging this state into equation (7.20) leads to

$$\rho_S \longrightarrow \sum_{k=0,1} [\sqrt{p}\langle k|U|0\rangle] \rho_S [\sqrt{p}\langle 0|U^\dagger|k\rangle] + [\sqrt{1-p}\langle k|U|1\rangle] \rho_S [\sqrt{1-p}\langle 1|U^\dagger|k\rangle]. \quad (7.22)$$

This is a CPTP map with Kraus operators

$$E_1 = \sqrt{p}\langle 0|U|0\rangle \quad E_2 = \sqrt{p}\langle 1|U|0\rangle \quad E_3 = \sqrt{1-p}\langle 1|U|1\rangle \quad E_4 = \sqrt{1-p}\langle 0|U|1\rangle. \quad (7.23)$$

Let us consider the following map (the first entry is the system and the second one is the reservoir)

$$\begin{aligned} |00\rangle &\longrightarrow |00\rangle \\ |01\rangle &\longrightarrow \sqrt{\eta}|01\rangle + \sqrt{1-\eta}|10\rangle \\ |10\rangle &\longrightarrow -\sqrt{1-\eta}|01\rangle + \sqrt{\eta}|10\rangle \\ |11\rangle &\longrightarrow |11\rangle \end{aligned} \quad (7.24)$$

associated to the two-qubit unitary transformation

$$U = \begin{bmatrix} 1 & 0 & 0 & 0 \\ 0 & \sqrt{\eta} & -\sqrt{1-\eta} & 0 \\ 0 & \sqrt{1-\eta} & \sqrt{\eta} & 0 \\ 0 & 0 & 0 & 1 \end{bmatrix}. \quad (7.25)$$

Using (7.23) we see that this map produces the GAD channel.

In our experiment, we would like to be able to monitor also the environment, tracing out the system. In order to do so, first we need to identify what are the optical states representing each state of the environment in our description above. It cannot be the up and down paths since they were inserted only as ancillaries allowing the amplitude damping to be realized for the two polarization components. It remains to consider the output ports of the PBS's. If we recombined the up and down paths after PBS_1 we would find (remember that short and long paths do not recombine coherently)

$$(\alpha|V\rangle - \beta|H\rangle)(\alpha^*\langle V| - \beta^*\langle H|) \otimes (\cos^2\phi|s\rangle\langle s| + \sin^2\phi|l\rangle\langle l|), \quad (7.26)$$

which is the initial state we want (after half wave plate transformations) and path $|l\rangle$ ($|s\rangle$) is the state $|0\rangle$ ($|1\rangle$) of the environment. Now we can analyze the output ports of PBS_2 . For that aim we consider the extreme cases $p = 0$ ($\phi = 0$ and reservoir initially in excited state) and $p = 1$

($\phi = 90^\circ$ and reservoir initially in ground state). Each joint basis vector evolves as follows:

$$\begin{aligned}
 |H\rangle|l\rangle &\longrightarrow |H\rangle|p2\rangle \\
 |H\rangle|s\rangle &\longrightarrow \sqrt{\eta}|H\rangle|p0\rangle + \sqrt{1-\eta}|V\rangle|p1\rangle \\
 |V\rangle|l\rangle &\longrightarrow -\sqrt{1-\eta}|V\rangle|p3\rangle + \sqrt{\eta}|H\rangle|p2\rangle \\
 |V\rangle|s\rangle &\longrightarrow |H\rangle|p0\rangle
 \end{aligned} \tag{7.27}$$

Notice that the final polarization generated from the initial states that are vertically polarized is inverted, it is corrected by the wave plates before the beam displacers. Comparing (7.24) with (7.27) leads to the conclusion that the paths coming out from the up port of PBS_2 are related to reservoir state $|0\rangle$. In the same way, the right paths represent reservoir state $|1\rangle$. Measuring the populations on each reservoir states can be realized by projecting the photons in each output of PBS_2 regardless of the polarization. To obtain the coherence between environment states $|0\rangle$ and $|1\rangle$, we first notice that the only terms which can produce coherence are those coming from the same initial reservoir state (because they start in an incoherent superposition) and with the same final polarization state (because we are tracing out the polarization in this case). This can be done by correcting the polarization of the initially vertical state (down path) before PBS_2 . This makes the final polarization components associated with different reservoir states coming from the same path (short or long) to recombine in one of the beam displacers BD_2 and BD_3 .

7.4. General protocol

The setup proposed for the GAD channel can be extended to implement a more general class of maps. It is clear that if one observes that the same angle θ is set in the HWP unitaries in up short and down long paths, also no transformation is carried out for down-short and up-long paths (Fig. 7.1). In fact, slightly changing this setup it is possible to implement any qubit channel of a large class as we argue in this section.

Recall the parameterization for qubit maps given by Eq. (7.6). It would be more convenient if the matrix T were diagonal. In fact, it can be diagonalized through its singular value decomposition (SVD) which asserts that any real $n \times n$ matrix T can be written as the product

$$T = R_1 D R_2^T \tag{7.28}$$

of two rotation matrices R_1 and R_2^T and a diagonal matrix D ², ^T denotes transposition. More-

²Actually the SVD is more general and applies for any rectangular matrix. Also, it states that any matrix can be written as the product of two orthogonal matrices and a diagonal positive semidefinite matrix, but as any orthogonal matrices are either a rotation or a product of a rotation by a inversion, our statement is correct if we

over, a rotation of the Bloch sphere vector is the effect of a unitary operation over the density matrix. That said, the map can be rewritten as

$$\Lambda[\rho] = U_1 \left(\Lambda_{\mathbf{t}', D} \left[U_2 \rho U_2^\dagger \right] \right) U_1^\dagger, \quad (7.29)$$

where U_1 and U_2 are the unitary operators associated with the rotations R_1 and R_2 , respectively, and $\Lambda_{\mathbf{t}', D}$ is the map parameterized by

$$\mathbf{t}' = R_1^T \mathbf{t} \quad T' = D = \begin{pmatrix} \lambda_1 & 0 & 0 \\ 0 & \lambda_2 & 0 \\ 0 & 0 & \lambda_3 \end{pmatrix}. \quad (7.30)$$

The unitary transformations do not alter complete positivity, consequently, any analysis made over $\Lambda_{\mathbf{t}', D}$ can be automatically extended to Λ . The image of such a channel when applied to the Bloch sphere vectors is the ellipsoid

$$\left(\frac{x'_1 - t'_1}{\lambda_1} \right)^2 + \left(\frac{x'_2 - t'_2}{\lambda_2} \right)^2 + \left(\frac{x'_3 - t'_3}{\lambda_3} \right)^2 \leq 1, \quad (7.31)$$

which must be contained inside the Bloch sphere for positivity preservation, a necessary condition for this is $|t'_k| + |\lambda_k| \leq 1$, $k = 1, 2, 3$. An example of the image of a qubit map is shown in Fig. 7.2, this map takes all points inside the Bloch sphere to points inside the ellipsoid. Being contained inside the Bloch sphere does not guarantees complete positivity.

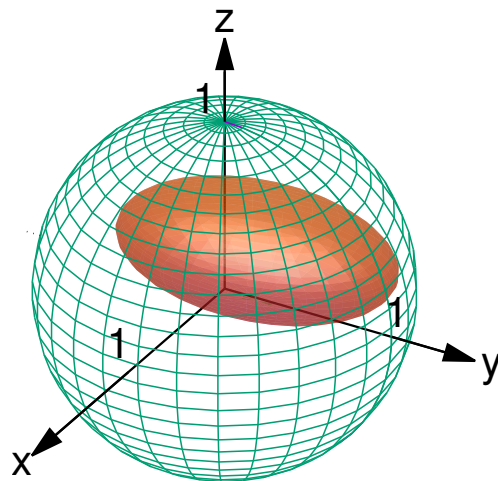


Figure 7.2.: The Bloch sphere is represented in green. Inside of it, an example of ellipsoid containing all the image points of a map as given by Eq. (7.31).

disregard the positivity of D .

To find what is the condition on the channel's parameters in order to assure complete positivity, one may recall the result of Choi [172] that a qubit map is CP if and only if the matrix

$$\beta(\Lambda) = (\mathbb{1}_2 \otimes \Lambda) [|\psi^+\rangle\langle\psi^+|] \quad (7.32)$$

is positive semidefinite, where $|\psi^+\rangle = \frac{|00\rangle+|11\rangle}{\sqrt{2}}$ is one of the Bell states of two qubits. This matrix is a density matrix in a Hilbert space of dimension 4 and as such can be put in the block form

$$\beta(\Lambda) = \begin{pmatrix} A & C \\ C^\dagger & B \end{pmatrix} \quad (7.33)$$

with the 2×2 matrices A , B and C . The positivity condition requires that $A \geq 0$, $B \geq 0$ and $C = A^{\frac{1}{2}} R B^{\frac{1}{2}}$ for some contraction R [167]. By definition a contraction satisfies $\mathbb{1} - RR^\dagger \geq 0$. The extreme points of the set of CPTP maps are those for which the equality is attained, which means that for these maps the contraction is actually a unitary matrix. Now, using the SVD for a contraction, one gets

$$R = V \begin{pmatrix} \cos \theta_1 & 0 \\ 0 & \cos \theta_2 \end{pmatrix} W^\dagger = \frac{1}{2} V \begin{pmatrix} e^{i\theta_1} & 0 \\ 0 & e^{i\theta_2} \end{pmatrix} W^\dagger + \frac{1}{2} V \begin{pmatrix} e^{-i\theta_1} & 0 \\ 0 & e^{-i\theta_2} \end{pmatrix} W^\dagger. \quad (7.34)$$

Once V and W are unitary, Eq. (7.34) states that any contraction is the sum of two unitary matrices, each one corresponding to one extreme channel. Thus, because of the linearity of the map and the one-to-one association between map and $\beta(\Lambda)$, it implies on the **Theorem 14** of [167]: *Any CPTP map of a qubit can be written as the convex combination of two extreme points of the set of all CPTP maps.* Mathematically, this means that

$$\Lambda[\rho] = p\mathcal{E}_1[\rho] + (1-p)\mathcal{E}_2[\rho], \quad (7.35)$$

where \mathcal{E}_1 and \mathcal{E}_2 are extreme maps and $0 \leq p \leq 1$.

The above decomposition is quite useful and has been widely used in qubit channel simulation [176, 183, 184]. What makes it suitable for practical purposes is that any extreme channel has its diagonal form (7.30) with only one t_k component nonnull, which can always be chosen as the third one. Moreover these channels admit the parameterization

$$\mathbf{t} = (0, 0, \sin u \sin v) \quad T = \begin{pmatrix} \cos u & 0 & 0 \\ 0 & \cos v & 0 \\ 0 & 0 & \cos u \cos v \end{pmatrix}, \quad (7.36)$$

which gives the two Kraus operators

$$E_1 = \begin{pmatrix} \cos \alpha & 0 \\ 0 & \cos \beta \end{pmatrix} \quad E_2 = \begin{pmatrix} 0 & \sin \beta \\ \sin \alpha & 0 \end{pmatrix}, \quad (7.37)$$

with $\alpha = u - v$, $\beta = u + v$, $u \in [0, 2\pi)$ and $v \in [0, \pi)$. Thus an extreme channel resembles a generalized amplitude damping in which the probability of exciting the ground state ($|\sin \alpha|^2$) is different from the probability of decay of the excited state ($|\sin \beta|^2$), and these two processes occur in a coherent way.

All the aforementioned works using the extreme-channel decomposition for a channel simulation use it directly to try to find the parameters of the decomposition that fits the simulated channel. The problem in doing this is that the decomposition (7.35) has 17 free parameters: the convex parameter p , the four parameters of the extreme maps in their diagonal form, plus the 6 parameters of the unitaries used to diagonalize each of the extreme maps. Thus the problem is over complicated, since the solution must be done before the quantum simulation in a classical computer which requires computational power that grows with the number of parameters. Obviously, the two extreme channels in the decomposition are related somehow as can be seen from Eq. (7.34). It is left for a future work to simplify this decomposition in order to reach the number of 12 parameters, as is required for characterizing any qubit channel. Furthermore, in the already mentioned implementations of qubit quantum channels the convex combination is carried out classically by selecting which extreme channel is going to be realized in each round. Contrary, our initial goal was to realize any qubit channel in one shot. It is still work in progress, so far we can already do this for a particular set of quantum maps.

Let us consider a restricted class of maps for which the two extreme points participating on its decomposition (7.35) are diagonal in the sense of (7.30) in the same basis or that their SVD differs by at most one rotation. Mathematically, we are considering maps of the form

$$\Lambda[\rho] = U_3 \left(p \mathcal{E}'_1 [U_1 \rho U_1^\dagger] + (1 - p) U_2 \mathcal{E}'_2 [U_1 \rho U_1^\dagger] U_2^\dagger \right) U_3^\dagger, \quad (7.38)$$

the \mathcal{E}_i are extreme maps whose diagonal form is denoted by \mathcal{E}'_i , and U_i are unitary operators. Although it possibly does not contain the entire set of qubit maps, many interesting examples can be represented in this way, as is shown in the next section.

The proposed setup for the implementation of maps of kind (7.38) is shown in Fig. 7.3. A realization of such a map starts with the unitary transformation U_1 and ends also with a unitary transformation U_3 . Regarding the qubit as the polarization of single photons, these operations are performed in the manner described in Sec. 4.4. In order to have all four Kraus operators implemented in each shot of the experiment, one can proceed as for the GAD channel, transferring the polarization state to a path degree of freedom using a BD and resetting the

polarization to state $|H\rangle$ (pink box in Fig.7.3). The path works as a qubit ancilla with possible states $|d\rangle, |u\rangle$, for down and up paths, respectively. The qubit state at this stage becomes

$$(a|H\rangle + b|V\rangle)|d\rangle \rightarrow |H\rangle(a|u\rangle + b|d\rangle), \quad (7.39)$$

where a and b are the coefficients of the polarization state after the unitary U_1 . We are assuming the initial state to be pure without any loss of generality. The polarization now becomes free to be used as a control for which extreme channel is going to be applied with the right probability. The probability is controlled by the angle ϕ of a HWP set such that $\cos^2 2\phi = p$. When the photon passes through a PBS, two new paths are created, one for each extreme channel (yellow box in Fig.7.3). Again this new path degree of freedom works as a qubit ancilla with the two states $|s\rangle, |l\rangle$, for short and long paths. The coherence between the two extreme-maps action is removed by the optical path difference between long and short paths which is greater than the coherence length of the photons.

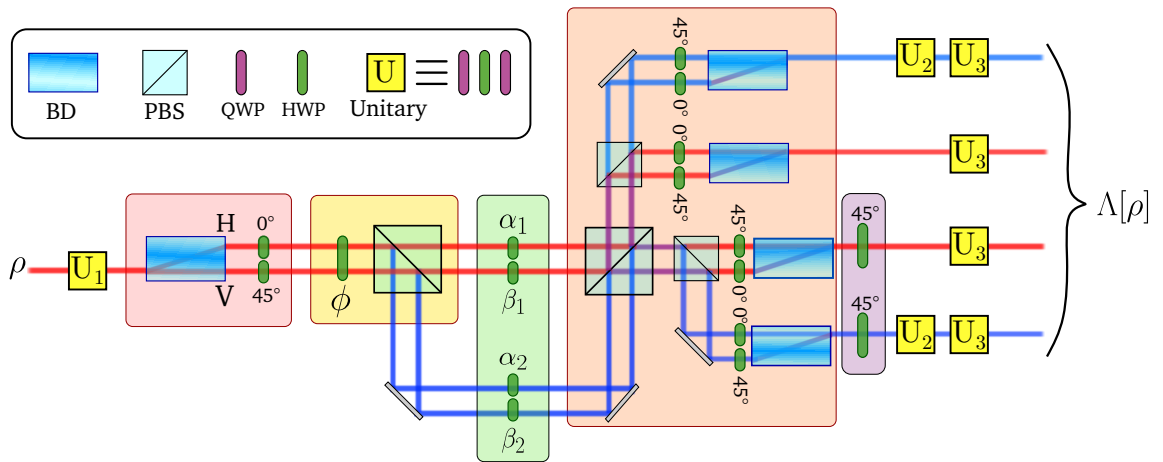


Figure 7.3.: Setup for the channel simulation. A photon in a polarization state ρ ends up in a polarization state $\Lambda[\rho]$ after passing through the setup if the final path information is erased. The beam colors are different only to indicate which beam is coming from the short and long paths in the unbalanced interferometer.

Now let us consider the action of an extreme map in its diagonal basis in Bloch sphere, when its Kraus operators are given by Eq. (7.37) with angles α_1 and β_1 . The Kraus operators E_1 and E_2 transform a pure state, respectively, as

$$\begin{aligned} a|0\rangle + b|1\rangle &\rightarrow a \cos \alpha_1|0\rangle + b \cos \beta_1|1\rangle \\ a|0\rangle + b|1\rangle &\rightarrow b \sin \beta_1|0\rangle + a \sin \alpha_1|1\rangle, \end{aligned} \quad (7.40)$$

the map itself being the convex sum of this two non-normalized states. Each Kraus operator alone keeps the coherence between the two basis states. To implement this map over the photon

qubit, we use two HWPs set to $\alpha_1/2$ and $\beta_1/2$, positioned in the up and down paths, respectively, in the short arm of the interferometer. The resulting transformation is given by

$$|H\rangle (a|u\rangle + b|d\rangle) \rightarrow a (\cos \alpha_1 |H\rangle + \sin \alpha_1 |V\rangle) |u\rangle + b (\cos \beta_1 |H\rangle + \sin \beta_1 |V\rangle) |d\rangle. \quad (7.41)$$

Notice that the terms that should be coherently recombined to recover (7.40) are those in orthogonal path states but with the same polarization. The orthogonal polarizations are separated in a PBS and then the up and down paths are recombined in BDs. This recombination is coherent if there is no optical-path difference between the two path states which is ensured by the waveplates before the BD which shifts the down path up, equaling the optical-path of the up state. Analogously, the second extreme map of the composition is realized in the long arm of the interferometer with HWPs set to $\alpha_2/2$ and $\beta_2/2$.

After the BDs recombination the unitary transformation U_2 is applied to the long arm photons and the unitary transformation U_3 is applied to all path states. If the four out-coming paths are traced out, the polarization state is exactly the one given by the action of map (7.38). To trace them out it is enough to detect the photons with a large aperture detector, such that all photons are detected regardless their path states. Although, if the photons are intended to be used for a further purpose, then one should be able to gather all the output paths together in a single spatial mode. A realistic experimental design for this is left for a future work, possibly using devices that are reflective on one side and transmissive when light is incident on the other side, as the one proposed in [185]. Another option for our setup would be to use fiber couplers, which acts as a beam splitter for two input fiber paths, taking them to two output paths, each of them being the 50:50 combination of the inputs. Without tracing out the paths, according to the interpretation of Eq. (7.4), what we have is one unrevealed measurement result of the environment in each output path, since each path results from one Kraus operator application.

The circuit representation of the process just described is shown in Fig. 7.4. The protocol is not the most efficient possible, as it is not intended to be. It requires two ancilla qubits and many two and even three-qubits operations. Still, because of the features of our system it is feasible, since the ancillary qubits are degrees of freedom of the same system that provides the main qubit of the computation, so controlled multi-qubit operations can be implemented deterministically with common optical elements.

7.4.1. Examples

In this section some examples of channels are shown together with the proper parameter applicable for their simulation. This examples are interesting since they represent much of the intuitive effects one can think of taking place over a qubit state. Also, via change of basis, infinitely many other channels can be obtained from these textbook examples [173].

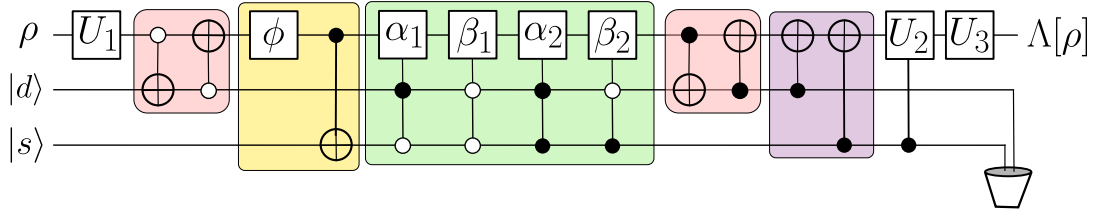


Figure 7.4.: Circuit representation of the channel simulation protocol. The colors match the ones used in the setup (Fig. 7.3) to indicate equivalent steps. The two ancillary qubits are initialized in their ground states. \oplus is a “NOT” operation. Single qubit operations can be controlled by the excited (\bullet) or ground (\circ) state of another qubit. A sequence of two C-NOTs, like the ones in the pink boxes, are equivalent to a SWAP operation. The white boxes are either arbitrary unitary operators or the transformation of a HWP. In the end the two ancillas are discarded.

Bit flip channel

The bit-flip channel is given as the action of the two Kraus operators

$$E_1 = \sqrt{p} \begin{pmatrix} 1 & 0 \\ 0 & 1 \end{pmatrix} \quad E_2 = \sqrt{1-p} \begin{pmatrix} 0 & 1 \\ 1 & 0 \end{pmatrix}, \quad (7.42)$$

with $0 \leq p \leq 1$. Thus, a qubit passing through a bit-flip channel has probability p of remaining in the same state and with probability $1 - p$ it will flip from $|0\rangle$ to $|1\rangle$ and vice-versa. There are at least two ways of implementing this channel writing it as combination of extreme maps (Eq.(7.38)), both of them without the necessity of unitary transformations. One could either chose $\phi = 0^\circ$ and $\alpha_1 = \beta_1 = \cos^{-1} \sqrt{p}$, or $2\phi = \cos^{-1} p$ and $\alpha_1 = \beta_1 = 0^\circ$ and $\alpha_2 = \beta_2 = 90^\circ$.

Phase flip channel

The phase-flip channel has the two Kraus operators

$$E_1 = \sqrt{p} \begin{pmatrix} 1 & 0 \\ 0 & 1 \end{pmatrix} \quad E_2 = \sqrt{1-p} \begin{pmatrix} 1 & 0 \\ 0 & -1 \end{pmatrix}, \quad (7.43)$$

and corresponds to a π phase shift between the two computational basis vectors with probability $1 - p$. This channel can be realized by setting $2\phi = \cos^{-1} p$, $\alpha_1 = \beta_1 = \alpha_2 = 0^\circ$ and $\beta_2 = 180^\circ$.

Depolarizing channel

The effect of a depolarizing channel is to let the qubit state untouched with probability $1 - p$ and turn it into a complete mixture with probability p . Its transformation is given as

$$\Lambda[\rho] = \frac{p}{2} \mathbb{1} + (1 - p)\rho, \quad (7.44)$$

or in terms of Pauli matrices

$$\Lambda[\rho] = \left(1 - \frac{3p}{4}\right) \rho + \frac{p}{4} (\sigma_x \rho \sigma_x + \sigma_y \rho \sigma_y + \sigma_z \rho \sigma_z). \quad (7.45)$$

The last expression is useful for our purposes because it explicit the operator-sum decomposition of the depolarizing channel. Before proceeding to the simulation parameters, let us consider a slightly more general channel

$$\Lambda[\rho] = p_0 \rho + p_1 \sigma_x \rho \sigma_x + p_2 \sigma_y \rho \sigma_y + p_3 \sigma_z \rho \sigma_z, \quad (7.46)$$

with $\sum_{i=0}^3 p_i = 1$. This channel class actually comprises all the previous cases presented. It is possible to represent this transformation in the form of Eq. (7.38) with two extreme channels diagonalized in the same basis. In such a convex combination, the identity and σ_x compose the first extreme map, while σ_y and σ_z are the Kraus operators of the second one. For the equality between Eqs. (7.38) and (7.46) to hold, the parameters must obey

$$\begin{aligned} p &= p_0 + p_1 & \alpha_1 &= \beta_1 = \tan^{-1} \sqrt{\frac{p_1}{p_0}} \\ \alpha_2 &= \beta_2 - 180^\circ & &= \tan^{-1} \sqrt{\frac{p_2}{p_3}} \end{aligned} \quad (7.47)$$

Generalized amplitude damping channel

Finally, the largely discussed GAD channel whose Kraus operators are given in Eq. (7.8) can also be seen as a combination of extreme channels with the parameters choice

$$\alpha_1 = \beta_2 = 0 \quad \beta_1 = \alpha_2 = \cos^{-1} \sqrt{\eta}. \quad (7.48)$$

7.5. Quantum process tomography

We would like to certify that indeed our setup is performing the desired operation we designed it to do. If we have access to a trustful source of input states and we are also able to faithfully determine the output state after the channel, then we can find out what map produced that resulting transformation and know if it is the desired one. This method is named quantum process tomography (QPT) [186].

Consider a set of pure states $\{|\psi_i\rangle\}_{i=1}^N$ such that the associated density matrices set $\{\rho_i\}_{i=1}^N$ forms a basis for the $d \times d$ matrices, d being the dimension of the Hilbert space of the system. This implies that the set has $N = d^2$ linearly independent elements. If we prepare each state of the set, sending them through the channel and for each one a quantum state tomography

is realized, so the set of states $\{\rho'_i = \Lambda[\rho_i]\}_{i=1}^N$ is obtained, then the channel is determined since for any other state we can write

$$\rho = \sum_{i=1}^N \lambda_i \rho_i \rightarrow \Lambda[\rho] = \sum_{i=1}^N \lambda_i \rho'_i. \quad (7.49)$$

In order to determine the Kraus operators of the channel, one needs also to set a basis for these operators, let us say $\{\tilde{E}_n\}$. Any Kraus operator can be expressed as a sum $E_k = \sum_n e_{kn} \tilde{E}_n$. In this operator basis the map becomes

$$\Lambda[\rho] = \sum_{n,m} \chi_{nm} \tilde{E}_n \rho \tilde{E}_m^\dagger, \quad (7.50)$$

being completely described by the numbers $\chi_{nm} = \sum_k e_{kn} e_{km}^*$. Now one can look at the action of this channel upon the basis matrices

$$\Lambda[\rho_j] = \sum_k \lambda_{jk} \rho_k, \quad (7.51)$$

the λ_{jk} 's are numbers experimentally determined from the quantum state tomography. On the other hand, one can also write it using (7.50) as

$$\Lambda[\rho_j] = \sum_{m,n,k} \chi_{nm} \beta_{jk}^{nm} \rho_k, \quad (7.52)$$

where we have defined β_{jk}^{nm} from $\tilde{E}_n \rho_j \tilde{E}_m^\dagger = \sum_{m,n,k} \beta_{jk}^{nm} \rho_k$. The numbers β_{jk}^{nm} are known since they are calculated using only the states and operators bases. By comparing (7.51) and (7.52) we get

$$\sum_{m,n} \chi_{nm} \beta_{jk}^{nm} = \lambda_{jk}, \quad (7.53)$$

which determines operator-sum representation for the channel from the experimental data λ_{jk} .

For the case of a qubit, the standard choice of pure states prepared and measured in an experiment is $\{|0\rangle, |+\rangle = \frac{|0\rangle+|1\rangle}{\sqrt{2}}, |L\rangle = \frac{|0\rangle-i|1\rangle}{\sqrt{2}}, |1\rangle\}$. A possible operator basis is the set $\{\tilde{E}_1 = \mathbb{1}, \tilde{E}_2 = \sigma_x, \tilde{E}_3 = -i\sigma_y, \tilde{E}_4 = \sigma_z\}$. In this basis, Eq. (7.53) gives

$$\chi = \Omega \begin{pmatrix} \rho'_1 & \rho'_2 \\ \rho'_3 & \rho'_4 \end{pmatrix} \Omega, \quad (7.54)$$

χ is a 4×4 matrix with elements χ_{nm} ,

$$\Omega = \frac{1}{2} \begin{pmatrix} \mathbb{1} & \sigma_x \\ \sigma_x & -\mathbb{1} \end{pmatrix}, \quad (7.55)$$

and

$$\begin{aligned}\rho'_1 &= \Lambda[\rho_1] \\ \rho'_2 &= \Lambda[\rho_2] - i\Lambda[\rho_3] - (1 - i)\frac{\Lambda[\rho_1] + \Lambda[\rho_4]}{2} \\ \rho'_3 &= \Lambda[\rho_2] + i\Lambda[\rho_3] - (1 + i)\frac{\Lambda[\rho_1] + \Lambda[\rho_4]}{2} \\ \rho'_4 &= \Lambda[\rho_4],\end{aligned}$$

ρ_i are the states being prepared and $\Lambda[\rho_i]$ is an experimentally tomographed state.

7.6. Conclusion

In this chapter a proposal for quantum channel simulation for a qubit was presented. The same way as qubit unitary transformations are the basis for closed-system quantum computation, qubit quantum channels can become the basic entity for open-system quantum computation [187]. Thus it would be interesting to design a platform to implement an arbitrary qubit channel. Our attempt to do so is based on the decomposition of a qubit map in a convex combination of the extremes of the set of maps. As a work in progress, some details are missing. For example, the setup devised so far is able to simulate only a particular class of channels. At the same time, what we call a particular class may still be the whole set, since it offers even more free parameters than is necessary to describe an arbitrary channel. However, up to now we could not show that this is the case. An interesting feature of our proposal in comparison to other works is that we are able to implement the entire channel for each photon, without the necessity to realize the convex sum in a classical probabilistic way. Moreover, the interpretation of the operator-sum representation as unrevealed measurements of the environment occurs exactly in our setup, since each Kraus operator leads to a different output path and is associated with a different states of the environment (ancillas). Our proposal also represents an experimental problem, since it would be desirable to gather the outputs of all Kraus operators in a single resulting path as to have the complete transformed state.

FINAL REMARKS

During my PhD the goal was to explore as many techniques and thus as many degrees of freedom of light as available in the Quantum Optics Laboratory of Federal University of Rio de Janeiro. It was possible by also exploring many different aspects of the quantum theory itself. The result is the series of experiments presented in this thesis. It contained two experiments using the transverse degrees of freedom of classical light beams (which could equivalently be performed using single photons with the same spatial profile), one of them uses also the polarization degree of freedom. The SLM, one of the crucial devices used, is applied in two different ways: as a phase modulator or as an amplitude mask. These two experiments also differ in their detection method which is an intensity profile captured by a CCD camera in one case, and the detection of the number of photons in the attenuated beam using a free space avalanche detector in the other case. The thesis also contains one experiment using the entanglement in polarization and path degrees of freedom between two photons produced in a nonlinear crystal by spontaneous parametric down conversion. At last, two experiments (one of them only proposed but not realized yet) using the SPDC process as a source of single photons are also presented. In these experiments, the polarization of single photons represent the computational qubit while the path degrees of freedom are used as the qubit environment or simply as ancillary systems.

As the results of the individual works were summarized at the end of each chapter, here I would like to just point some clear open questions and further investigations regarding some of the works realized. Relative to the content of Chapter 2, it is still open if a slight change in our simulation protocol would enable us to simulate an interacting particle. Maybe more interesting and direct is to investigate if it is possible to observe the Hegerfeldt paradox in our simulation. This paradox is related to the superluminal propagation of relativistic wavefunctions that were initially localized in a finite region of space [188, 189]. Using our experiment, we can check its occurrence or not in both Dirac and FW representations. The two major open questions about the content presented in Chapter 3 are: is there any practical application of the nice construction we showed? And as done in Ref. [190], is it possible to relate the PCG MUMs to angular momentum for quantum information processing? At last, about the subject of Chapter 7 it is left to prove or disprove that the parameterization we simulate is able to describe a general qubit channel. Also, as was mentioned, one must solve the experimental issue of

grouping all the output paths, transforming them in a single output which state is the result of the map application to the initial state. Moreover, we are now seeking for applications of the experimental platform in the investigation of correlation dynamics, since the photon used can be entangled with the herald photon, or quantum thermodynamics phenomena.

BIREFRINGENT MATERIALS

Most of the linear optical devices for manipulating polarization available are made of birefringent materials. This birefringence or double refraction property is present in many crystals and liquid crystals where a preferred direction is naturally defined by the internal symmetry of the material. In the experiments presented in this thesis many are the examples of birefringence-based devices: wave plates, polarizing beam splitters, beam displacers and spatial light modulators. In many cases, it makes necessary to understand the physical principles behind the desired final effect such to correct imperfections and obtain the best performance of the devices. This Section is devoted to present the general principles valid for propagation and incidence in any birefringent media. As it is valid for all dispositives used in the experiments, it is considered a non-magnetic and lossless crystal. The treatment presented is completely classical but it extends to the modes of quantum electromagnetic field.

In a homogeneous linear medium, an electric field \mathbf{E} produces a linearly dependent polarization \mathbf{P} and thus a linear electric displacement $\mathbf{D} = \epsilon_0 \mathbf{E} + \mathbf{P} = \epsilon \mathbf{E}$. ϵ_0 is the permittivity of vacuum and ϵ is the permittivity of the medium. If the medium is in addition isotropic, then its permittivity is just a scalar. If it is not the case and the medium presents anisotropy, as is the common case in crystals, then the polarization direction and strength depends on the electric field direction and is no longer co-linear with it. In this case, the electric permittivity is an order 2 tensor and, because of energy conservation considerations, it can be represented by a 3×3 Hermitian matrix [191]. Thus its eigenvectors are all orthogonal and in this eigenbasis, called the principal directions of the material, the permittivity tensor reads

$$\epsilon = \begin{pmatrix} \epsilon_1 & 0 & 0 \\ 0 & \epsilon_2 & 0 \\ 0 & 0 & \epsilon_3 \end{pmatrix}. \quad (\text{A.1})$$

In terms of electromagnetic waves, if the polarization of the wave is an eigenvector of the

electric permittivity , then the polarization is not altered during propagation inside the medium.

For the so called uniaxial crystals like calcite and quartzo, because of the symmetry present, the electric responses in two of the principal directions are equal $\epsilon_1 = \epsilon_2 = \epsilon_\vartheta$. The direction with different value of permittivity $\epsilon_3 = \epsilon_e$ define the optical axis of the crystal.

Let us consider a plane wave with frequency ω propagating through the crystal, such that all the fields vary in space and time as $e^{i\omega t - i\mathbf{k}\cdot\mathbf{r}}$, $\mathbf{k} = n\frac{\omega}{c}\mathbf{s}$ is the wave vector in the direction of the unity vector \mathbf{s} , n is the index of refraction and c is the light velocity. The Maxwell equations impose the following relations for the amplitudes of the fields

$$\begin{aligned} \mathbf{k} \times \mathbf{E} &= \omega\mu\mathbf{H} & \mathbf{k} \times \mathbf{H} &= -\omega\mathbf{D} \\ \mathbf{k} \cdot \mathbf{D} &= 0 & \mathbf{k} \cdot \mathbf{H} &= 0, \end{aligned} \quad (\text{A.2})$$

μ is the scalar magnetic permeability. The relation between the field vectors and wave vector is shown in Fig. A.1-a). The first two equations imply that \mathbf{k} is perpendicular to the electric displacement \mathbf{D} and to the magnetic fields \mathbf{B} , \mathbf{H} . Also \mathbf{E} and \mathbf{D} are both perpendicular to \mathbf{B} , \mathbf{H} . Thus the vectors \mathbf{k} , \mathbf{E} and \mathbf{D} lie in the same plane, but as \mathbf{E} and \mathbf{D} are not colinear, the electric field is not , in general, perpendicular to the direction of propagation in this material. Moreover, as the energy flow is given by the Poynting vector $\mathbf{E} \times \mathbf{H}$, surprisingly the wave vector is not in the energy flow direction generally.

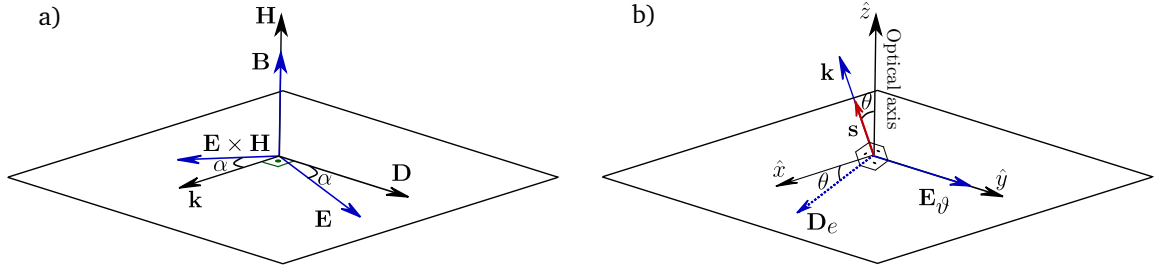


Figure A.1.: Representation of the field vectors for an anisotropic material. **a)** All the field vectors for an arbitrary material and an arbitrary mode of propagation. Vectors with the same color are orthogonal. **b)** The ordinary and extraordinary modes of propagation in a uniaxial crystal. The plane perpendicular to the optical axis contains all the directions for which $\epsilon = \epsilon_\vartheta$.

By eliminating \mathbf{H} in Eqs. (A.2) gives for the electric field $\mathbf{k} \times (\mathbf{k} \times \mathbf{E}) + \omega^2\mu\epsilon\mathbf{E} = 0$ or explicitly in the principal direction basis

$$\begin{pmatrix} \frac{\epsilon_\vartheta}{\epsilon_0} - n^2(s_y^2 + s_z^2) & n^2s_x s_y & n^2s_x s_z \\ n^2s_x s_y & \frac{\epsilon_\vartheta}{\epsilon_0} - n^2(s_x^2 + s_z^2) & n^2s_z s_y \\ n^2s_x s_z & n^2s_z s_y & \frac{\epsilon_e}{\epsilon_0} - n^2(s_x^2 + s_y^2) \end{pmatrix} \begin{pmatrix} E_x \\ E_y \\ E_z \end{pmatrix} = N\mathbf{E} = 0, \quad (\text{A.3})$$

where the substitution $\mathbf{k} = n\frac{\omega}{c}\mathbf{s}$ was made. The nontrivial solutions for \mathbf{E} come when the determinant of N vanishes. It implies that the index of refraction n must satisfy the equation

[96]

$$\left[\frac{n^2}{n_o^2} - 1 \right] \left[\frac{n^2}{n_e^2} (s_x^2 + s_y^2) + \frac{n^2}{n_o^2} s_z^2 - 1 \right] = 0, \quad (\text{A.4})$$

the principal indexes of refraction being defined as $n_o^2 \equiv \frac{\epsilon_o}{\epsilon_0}$ and $n_e^2 \equiv \frac{\epsilon_e}{\epsilon_0}$. The above equation has two solutions, what means that, for each propagation direction, there are two propagating modes with different indexes of refraction. The first one is independent of the direction of propagation and has index of refraction $n = n_o$. This mode is called the ordinary wave. It is possible to show that the electric field of the ordinary mode is perpendicular to the wave vector, causing all the optical phenomena to have the same behavior as for isotropic materials. The other solution is called extraordinary wave. Lets choose the x and y axis such that \mathbf{k} is contained in the xz plane, as shown in Fig. A.1-b). This arbitrary choice is possible because ϵ_o is degenerate. According to Eq. (A.4), the index of refraction of the extraordinary wave depends on the angle θ between the wave vector and the optical axis as

$$\frac{1}{n^2} = \frac{\cos^2 \theta}{n_o^2} + \frac{\sin^2 \theta}{n_e^2}. \quad (\text{A.5})$$

From the fact that the two modes are known to be orthogonal, the electric displacement \mathbf{D}_e lies in the xz plane, being written as $\mathbf{D}_e = \epsilon_o E_x \hat{x} + \epsilon_e E_z \hat{z}$. Using the orthogonality of \mathbf{k} and \mathbf{D}_e and the scalar product $\mathbf{D}_e \cdot \mathbf{E}_e$ give the angle α between the electric field and the electric displacement as

$$\cos \alpha = \cos \theta \left(1 + \frac{n_o^2}{n_e^2} \tan^2 \theta \right)^{-\frac{1}{2}}, \quad (\text{A.6})$$

this is also the angle between the wave vector and the direction of energy flow. As particular cases: if the two principal indexes of refraction are equal then $\cos \alpha = 1$ and $\alpha = 0$ and the two modes are perpendicular to the wave vector as expected for a isotropic material; if $\theta = 0$ then $\alpha = 0$ and the two modes are ordinary waves; if $\theta = \frac{\pi}{2}$ the above equation is actually not valid, in this case the ordinary electric field and electric displacement are parallel and in the direction of the optical axis, the index of refraction being $n = n_e$.

When a electromagnetic wave is propagating in a isotropic medium and reach an interface with an anisotropic material, the same boundary conditions as if both media are isotropic are still valid. As the index of refraction depends on the direction of propagation and on the polarization of the wave, two different waves are refracted. In particular, all the wave vectors are contained in the incidence plane and the phase of the wave at the interface must be continuous leading to a Snell's law for each refracted wave

$$n_i \sin \theta_i = n_o \sin \theta_o = n(\theta_e) \sin \theta_e, \quad (\text{A.7})$$

n_i is the index of refraction of the incident medium, θ_i is the angle of incidence, θ_o and θ_e are the angles of refraction of the ordinary and extraordinary waves, respectively. Again, the ordinary wave behaves like if it was a isotropic medium while to find the angle of refraction for the extraordinary wave it is necessary to solve a quartic equation because of the dependence of the index of refraction on the direction of propagation.

FURTHER EXPERIMENTAL RESULTS OF SEVERAL PCG MUM

In this appendix, the measurements for all combinations of preparation and measurement phase space directions are shown. All plots show the Shannon entropy as a function of the period of the measurement mask (T_j should be changed by T_k). The preparation mask is fixed in $M_0^{(j)}(q_j, T_j)$ with T_j satisfying the MUM condition for the m_{jk} values shown in Table 3.1. In this way, it was expected that for the same measurement direction, all three preparations would give the maximum entropy for the same measurement period values. This can be verified in the plots and particularly this happens for the periods corresponding to the right m_{jk} values.

Measurement $k = 0$

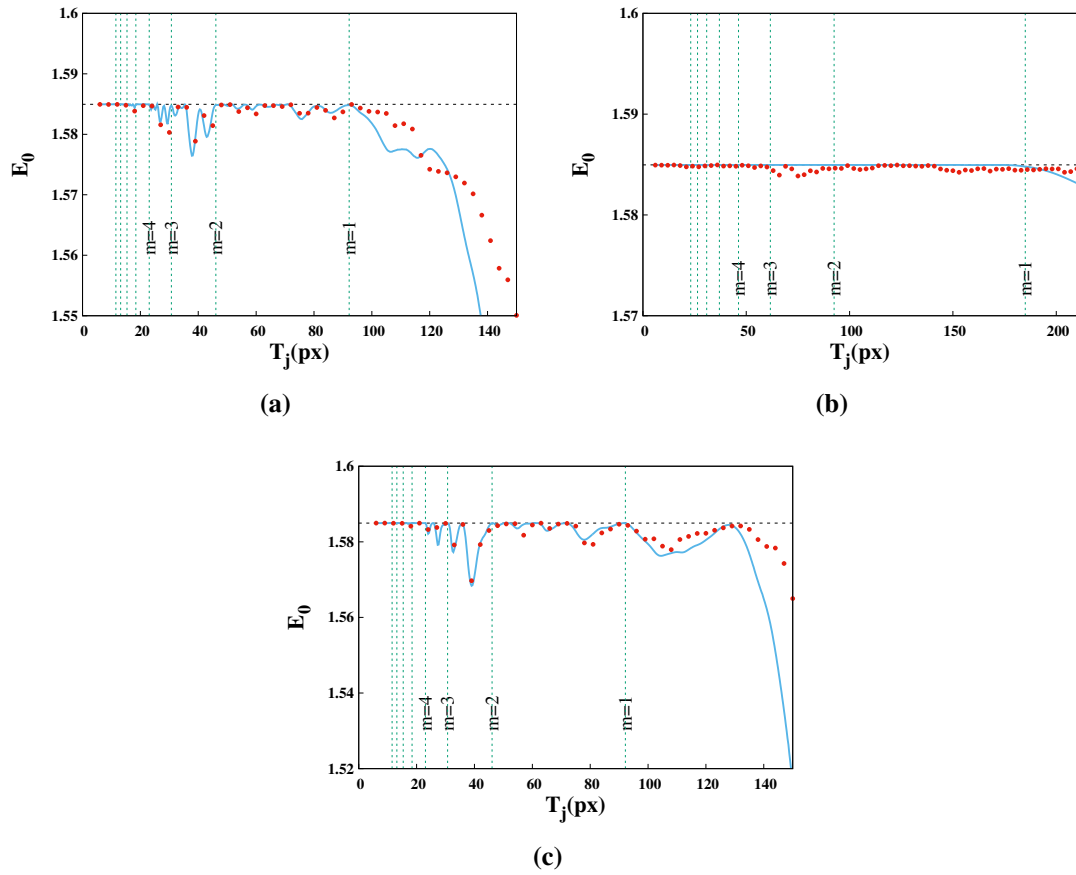


Figure B.1.: Measurements on $k = 0$ direction for preparation a) $j = 1$, b) $j = 2$ and c) $j = 3$.

Measurement $k = 1$

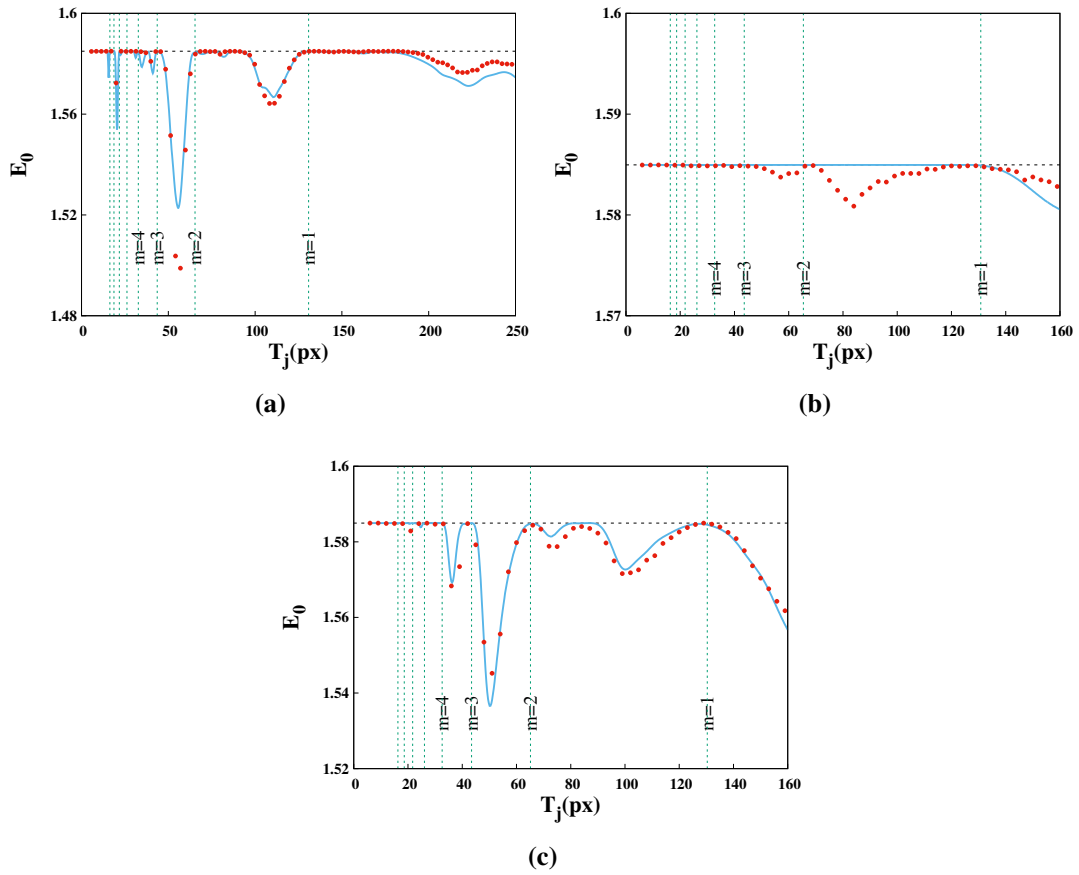


Figure B.2.: Measurements on $k = 1$ direction for preparation a) $j = 0$, b) $j = 2$ and c) $j = 3$.

Measurement $k = 2$

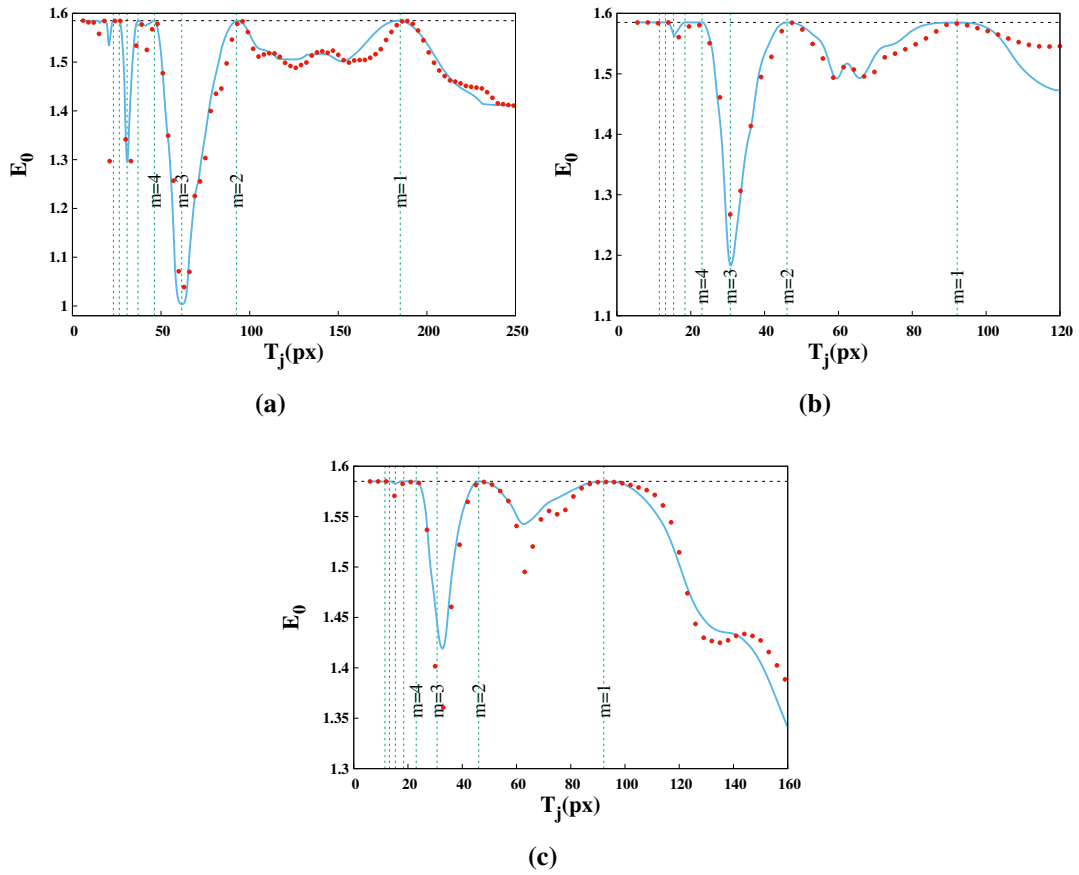


Figure B.3.: Measurements on $k = 2$ direction for preparation a) $j = 0$, b) $j = 1$ and c) $j = 3$.

Measurement $k = 3$

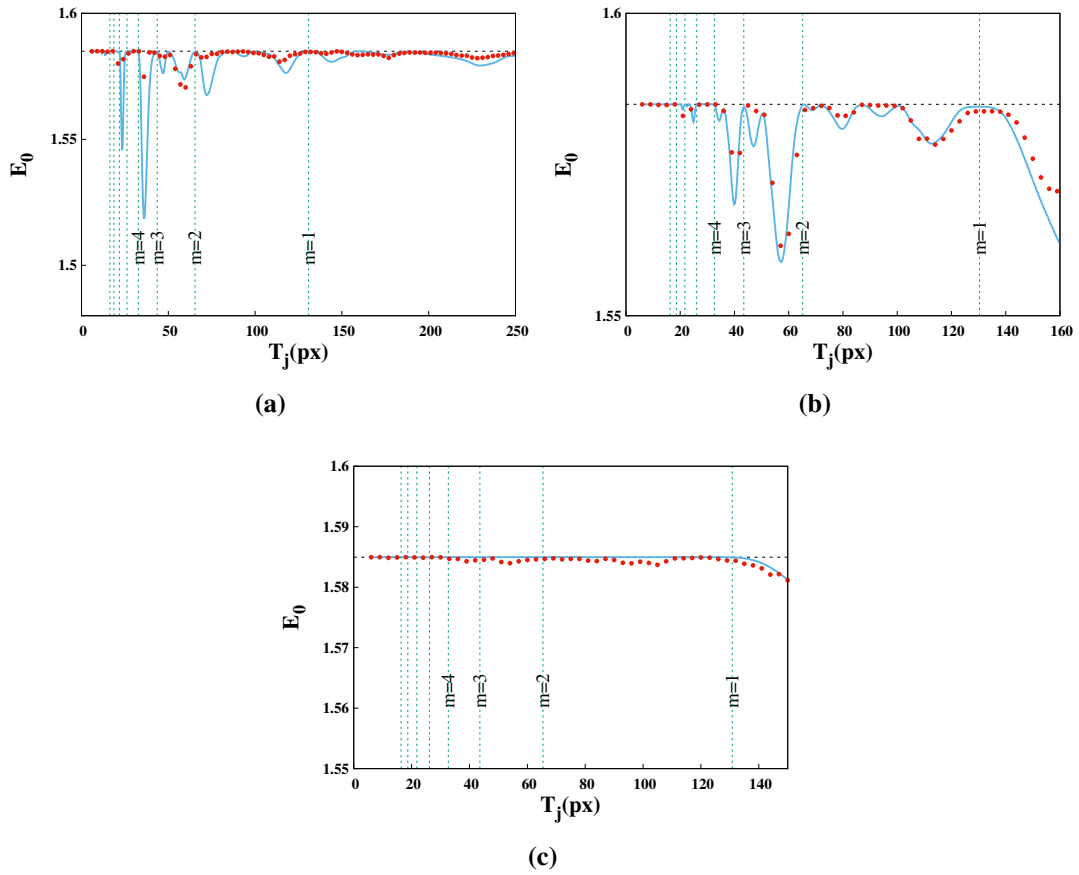


Figure B.4.: Measurements on $k = 3$ direction for preparation a) $j = 0$, b) $j = 1$ and c) $j = 2$.

SUPPLEMENT TO STEERING EXPOSURE

C.1. No-go theorem for multi-black-box universal steering bits

In contrast to the protocols exploring the capabilities of wirings within the AB partition, in this section we present a no-go theorem limiting their transformation power. Since it is known [122] that in minimal dimension there is no steering bit — i.e. no “universal” minimal-dimension assemblage that can be transformed into any other under 1W-LOCCs — one can ask whether reduction from a higher number of inputs, outputs or parties allows such a steering bit to be established. We answer in the negative even in minimal dimension.

Theorem 2. *[No pure steering bit with higher number of parties] There does not exist any pure $(N - 1)$ -DI qubit assemblage $\sigma_{\mathbf{a}|\mathbf{x}}^{\text{bit}}$, where $\mathbf{a} = \{a_1, \dots, a_{N-1}\}$, $\mathbf{x} = \{x_1, \dots, x_{N-1}\}$ (with finite sets of input and output values), that can be transformed via 1W-LOCCs into all qubit assemblages of minimal dimension $\sigma_{\mathbf{a}|\mathbf{x}}^{(\text{target})}$.*

Proof. The proof is similar in spirit to that of Theorem 5 of [122]. We consider a pure $(N - 1)$ -DI qubit assemblage as a candidate for higher-dimensional “bit” assemblage. With the more detailed notation of [122], it reads

$$\sigma_{\mathbf{a}|\mathbf{x}}^{\text{bit}} = P_{A|X}(\mathbf{a}|\mathbf{x}) |\psi(\mathbf{a}, \mathbf{x})\rangle\langle\psi(\mathbf{a}, \mathbf{x})|. \quad (\text{C.1})$$

We assume the NS principle only between the DD party and all others, the $N - 1$ DI parties may signal to each other at will. We will show that no single choice of $\sigma_{\mathbf{a}|\mathbf{x}}^{\text{bit}}$ can be freely transformed into members of a family of minimal-dimension assemblages $\sigma_{\mathbf{a}_f|\mathbf{x}_f}^\theta =$

$\frac{1}{2}|\psi^\theta(a_f, x_f)\rangle\langle\psi^\theta(a_f, x_f)|$ for all $\theta \in]0, \pi/2[$, where

$$|\psi^\theta(0, 0)\rangle = |0\rangle \quad (\text{C.2a})$$

$$|\psi^\theta(1, 0)\rangle = |1\rangle \quad (\text{C.2b})$$

$$|\psi^\theta(0, 1)\rangle = \cos\theta|0\rangle + \sin\theta|1\rangle \quad (\text{C.2c})$$

$$|\psi^\theta(1, 1)\rangle = -\sin\theta|0\rangle + \cos\theta|1\rangle. \quad (\text{C.2d})$$

The most general form of a 1W-LOCC applied to $\sigma_{a|x}^{\text{bit}}$ is

$$\sum_{\mathbf{a}, \mathbf{x}, \omega} P_{X|X_f, \Omega}^\theta(\mathbf{x}|x_f, \omega) P_{A_f|A, X, \Omega, X_f}^\theta(a_f|\mathbf{a}, \mathbf{x}, \omega, x_f) P_{A|X}(\mathbf{a}|\mathbf{x}) K_\omega^\theta |\psi(\mathbf{a}, \mathbf{x})\rangle \langle\psi(\mathbf{a}, \mathbf{x})| K_\omega^{\theta\dagger}, \quad (\text{C.3})$$

where Ω is a variable (with values ω) representing information sent by the quantum party to the classical ones, $P_{X|X_f, \Omega}^\theta$ and $P_{A_f|A, X, \Omega, X_f}^\theta$ are conditional probability distributions, and K_ω^θ is a Kraus operator [122]; the three may depend on θ . Since this transformed assemblage is intended to equal the rank-1 assemblage $\sigma_{a_f|x_f}^\theta$, we can conclude that $\forall a_f, x_f$

$$\begin{aligned} \sum_{\mathbf{a}, \mathbf{x}} P_{X|X_f, \Omega}^\theta(\mathbf{x}|x_f, \omega) P_{A_f|A, X, \Omega, X_f}^\theta(a_f|\mathbf{a}, \mathbf{x}, \omega, x_f) P_{A|X}(\mathbf{a}|\mathbf{x}) K_\omega^\theta |\psi(\mathbf{a}, \mathbf{x})\rangle \langle\psi(\mathbf{a}, \mathbf{x})| K_\omega^{\theta\dagger} \\ \sim |\psi^\theta(a_f, x_f)\rangle \langle\psi^\theta(a_f, x_f)|, \quad (\text{C.4}) \end{aligned}$$

where \sim signifies ‘‘is either null or proportional to’’ and we have used the fact that the relation, valid for the sum in ω , is also valid for each ω term.

We will assume for now that $\sigma_{a|x}^{\text{bit}}$ is not a single-state assemblage, i.e., there is no state $|\psi_{\text{single}}\rangle$ such that $|\psi(\mathbf{a}, \mathbf{x})\rangle = |\psi_{\text{single}}\rangle$ for all \mathbf{a}, \mathbf{x} (for our purposes throughout this proof, states are equal if they differ only by an global phase).

We now notice that, due to normalization, $\forall x_f, \omega, \exists \tilde{\mathbf{x}}, \tilde{\mathbf{a}}, \tilde{a}_f$ such that $P_{X|X_f, \Omega}^\theta(\tilde{\mathbf{x}}|x_f, \omega) \times P_{A_f|A, X, \Omega, X_f}^\theta(\tilde{a}_f|\tilde{\mathbf{a}}, \tilde{\mathbf{x}}, \omega, x_f) \times P_{A|X}(\tilde{\mathbf{a}}|\tilde{\mathbf{x}}) \neq 0$. For these values, then,

$$K_\omega^\theta |\psi(\tilde{\mathbf{a}}, \tilde{\mathbf{x}})\rangle \sim |\psi^\theta(\tilde{a}_f, x_f)\rangle. \quad (\text{C.5})$$

In fact, there must be at least two different values $\tilde{\mathbf{a}}$ for each $\tilde{\mathbf{x}}$ for which Eq. (C.5) is true, with the corresponding pure states $|\psi(\tilde{\mathbf{a}}, \tilde{\mathbf{x}})\rangle$ being not all equal: if, for some $\tilde{\mathbf{x}}$ there is a single $\tilde{\mathbf{a}}$ with $P_{A|X}(\tilde{\mathbf{a}}|\tilde{\mathbf{x}}) \neq 0$, then by purity and the NS property between the DD and DI partitions, $\sigma_{a|x}^{\text{bit}}$ would be a single-state assemblage; if for all values $\tilde{\mathbf{a}}$, $|\psi(\tilde{\mathbf{a}}, \tilde{\mathbf{x}})\rangle$ is the same, it would also be a single-state assemblage due to NS and purity.

Let us now exclude the possibility of $K_\omega^\theta |\psi(\mathbf{a}, \mathbf{x})\rangle = 0$ with $K_\omega^\theta \neq 0$. If that were the case, K_ω^θ would have a rank-1 support, hence a rank-1 span: $K_\omega^\theta |\psi(\mathbf{a}, \mathbf{x})\rangle \sim |k_\omega^\theta\rangle \forall \mathbf{a}, \mathbf{x}$.

From (C.4) and the independence of x_f from ω , this would require either $|\psi^\theta(a_f, 0)\rangle \propto |k_\omega^\theta\rangle \propto |\psi^\theta(\tilde{a}_f, 1)\rangle$ [contradiction with Eq. (C.2)] or that, for some value of x_f , for the corresponding $\tilde{\mathbf{x}}$, $K_\omega^\theta |\psi(\tilde{\mathbf{a}}, \tilde{\mathbf{x}})\rangle = 0$ for all $\tilde{\mathbf{a}}$ with $P_{A|X}(\tilde{\mathbf{a}}|\tilde{\mathbf{x}}) \neq 0$ [contradiction with there existing two different states $|\psi(\tilde{\mathbf{a}}, \tilde{\mathbf{x}})\rangle$].

Finally, we can conclude from the dependencies of the three probabilities $P_{X|X_f, \Omega}^\theta$, $P_{A_f|A, X, \Omega, X_f}^\theta$, $P_{A|X}$ on $x_f, \omega, \mathbf{x}, \mathbf{a}, \tilde{a}_f$, that

$$K_\omega^\theta |\psi(\tilde{\mathbf{a}}, \tilde{\mathbf{x}})\rangle \propto |\psi^\theta(\tilde{a}_f, x_f)\rangle . \quad (\text{C.6})$$

The validity conditions of this equation are as follows: for all (x_f, ω) , there exists some value $\tilde{\mathbf{x}}$ for which (C.6) holds; for each $\tilde{\mathbf{x}}$, there are at least two values $\tilde{\mathbf{a}}$ for which (C.6) holds; and for each choice of $(x_f, \omega, \tilde{\mathbf{x}}, \tilde{\mathbf{a}})$ there is some value \tilde{a}_f for which (C.6) holds. Moreover, for given $\tilde{\mathbf{x}}$, the corresponding $|\psi(\tilde{\mathbf{a}}, \tilde{\mathbf{x}})\rangle$ (for varying $\tilde{\mathbf{a}}$) are not all equal.

Let us explore the possible ways of satisfying Eq. (C.6) by case analysis. A first possibility is that, for the two different values $x_f = 0, 1$, the values of $\tilde{\mathbf{x}}$ for which (C.6) holds intersect at some value $\tilde{\mathbf{x}}_{\text{int}}$. Then $\exists \tilde{\mathbf{a}}, \tilde{a}_{f0}, \tilde{a}_{f1}$ such that

$$\begin{aligned} K_\omega^\theta |\psi(\tilde{\mathbf{a}}, \tilde{\mathbf{x}}_{\text{int}})\rangle &\propto |\psi^\theta(\tilde{a}_{f0}, x_f = 0)\rangle , \\ K_\omega^\theta |\psi(\tilde{\mathbf{a}}, \tilde{\mathbf{x}}_{\text{int}})\rangle &\propto |\psi^\theta(\tilde{a}_{f1}, x_f = 1)\rangle , \end{aligned} \quad (\text{C.7})$$

which is incompatible with Eq. (C.2). We are then left with the values $\tilde{\mathbf{x}}$ for $x_f = 0$ and $x_f = 1$ being all different. Taking the liberty to relabel our variables, let us consider a value $\tilde{\mathbf{x}} = \mathbf{0}$ for $x_f = 0$ and a value $\tilde{\mathbf{x}} = \mathbf{1}$ for $x_f = 1$, ignoring the other possible values of $\tilde{\mathbf{x}}$ for which Eq. (C.6) holds. Let us call $\tilde{\mathbf{a}} = \mathbf{0}$ and $\tilde{\mathbf{a}} = \mathbf{1}$ the two values of $\tilde{\mathbf{a}}$ for which, given $\tilde{\mathbf{x}}$, Eq. (C.6) holds. We see that \tilde{a}_f could take any value for each $\tilde{\mathbf{a}}$. However, if \tilde{a}_f is the same for the same $(x_f, \tilde{\mathbf{x}})$ and two different $\tilde{\mathbf{a}}$, e.g.,

$$\begin{aligned} K_\omega |\psi(\mathbf{0}, \mathbf{1})\rangle &\propto |\psi^\theta(0, 1)\rangle \\ K_\omega |\psi(\mathbf{1}, \mathbf{1})\rangle &\propto |\psi^\theta(0, 1)\rangle , \end{aligned} \quad (\text{C.8})$$

then Eq. (C.6) cannot be satisfied for all x_f . This is because $\{|\psi(\mathbf{0}, \mathbf{1})\rangle, |\psi(\mathbf{1}, \mathbf{1})\rangle\}$ form a basis of the qubit Hilbert space, hence K_ω has a 1-rank span given by $|\psi^\theta(0, 1)\rangle$, which does not span $|\psi^\theta(\tilde{a}_f, 0)\rangle$ as needed. Hence \tilde{a}_f is different for each $\tilde{\mathbf{a}}$ value.

We can then conclude that, up to relabeling, there must be states $|\psi(\tilde{\mathbf{a}}, \tilde{\mathbf{x}})\rangle$ belonging

to σ^{bit} which obey

$$K_\omega |\psi(\mathbf{0}, \mathbf{0})\rangle \propto |\psi^\theta(0, 0)\rangle \quad (\text{C.9a})$$

$$K_\omega |\psi(\mathbf{1}, \mathbf{0})\rangle \propto |\psi^\theta(1, 0)\rangle \quad (\text{C.9b})$$

$$K_\omega |\psi(\mathbf{0}, \mathbf{1})\rangle \propto |\psi^\theta(0, 1)\rangle \quad (\text{C.9c})$$

$$K_\omega |\psi(\mathbf{1}, \mathbf{1})\rangle \propto |\psi^\theta(1, 1)\rangle \quad (\text{C.9d})$$

to obtain the family of assemblages $\{\sigma^\theta\}_{\theta \in [0, \pi/2]}$. We will choose the following parametrization:

$$|\psi(\tilde{\mathbf{a}}, \tilde{\mathbf{x}})\rangle = \cos(\varphi_{\tilde{\mathbf{a}}, \tilde{\mathbf{x}}})|0\rangle + e^{i\alpha_{\tilde{\mathbf{a}}, \tilde{\mathbf{x}}}} \sin(\varphi_{\tilde{\mathbf{a}}, \tilde{\mathbf{x}}})|1\rangle, \quad (\text{C.10})$$

where $\varphi_{\tilde{\mathbf{a}}, \tilde{\mathbf{x}}} \in [0, \pi/2]$. It should be noted that $(\varphi_{\tilde{\mathbf{a}}, \tilde{\mathbf{x}}}, \alpha_{\tilde{\mathbf{a}}, \tilde{\mathbf{x}}})$ may depend on θ through $\tilde{\mathbf{a}}, \tilde{\mathbf{x}}$: because $P_{X|X_f, \Omega}^\theta$ may depend on θ , the values $\tilde{\mathbf{a}}, \tilde{\mathbf{x}}$ for which Eq. (C.6) holds may vary for different values of θ . However, for finitely many values of \mathbf{a}, \mathbf{x} , there are only finitely many states and finitely many $(\varphi_{\mathbf{a}, \mathbf{x}}, \alpha_{\mathbf{a}, \mathbf{x}})$ to pick from, so some choice of states as in Eq. (C.10) must still be able to satisfy Eq. (C.9) for a continuous set of values θ .

Substituting Eqs. (C.2) and (C.10) in (C.9a,C.9b), respectively, we see that

$$\frac{K_{\omega 00}^\theta}{K_{\omega 01}^\theta} = -e^{i\alpha_{10}} \tan \varphi_{10}; \quad \frac{K_{\omega 10}^\theta}{K_{\omega 11}^\theta} = -e^{i\alpha_{00}} \tan \varphi_{00}; \quad (\text{C.11})$$

where $K_{\omega ij}^\theta := \langle i | K_\omega^\theta | j \rangle$. Doing the same in (C.9c,C.9d) and substituting (C.11), we find, respectively,

$$\frac{K_{\omega 11}^\theta}{K_{\omega 01}^\theta} = \tan \theta \frac{\tan \varphi_{01} e^{i\alpha_{01}} - \tan \varphi_{10} e^{i\alpha_{10}}}{\tan \varphi_{01} e^{i\alpha_{01}} + \tan \varphi_{00} e^{i\alpha_{00}}} \quad (\text{C.12})$$

$$\frac{K_{\omega 11}^\theta}{K_{\omega 01}^\theta} = \frac{-1 \tan \varphi_{11} e^{i\alpha_{11}} - \tan \varphi_{10} e^{i\alpha_{10}}}{\tan \theta \tan \varphi_{11} e^{i\alpha_{11}} - \tan \varphi_{00} e^{i\alpha_{00}}}. \quad (\text{C.13})$$

Equating the two, we have

$$\tan^2 \theta \left(\frac{\tan \varphi_{01} e^{i\alpha_{01}} - \tan \varphi_{10} e^{i\alpha_{10}}}{\tan \varphi_{01} e^{i\alpha_{01}} + \tan \varphi_{00} e^{i\alpha_{00}}} \right) + \left(\frac{\tan \varphi_{11} e^{i\alpha_{11}} - \tan \varphi_{10} e^{i\alpha_{10}}}{\tan \varphi_{11} e^{i\alpha_{11}} - \tan \varphi_{00} e^{i\alpha_{00}}} \right) = 0, \quad (\text{C.14})$$

which, for fixed $\varphi_{\tilde{\mathbf{a}}, \tilde{\mathbf{x}}}, \alpha_{\tilde{\mathbf{a}}, \tilde{\mathbf{x}}}$, must hold for a continuous set of values θ . This is only possible if both parentheses are zero, which in turn implies $(\varphi_{0,1}, \alpha_{0,1}) = (\varphi_{1,0}, \alpha_{1,0}) = (\varphi_{1,1}, \alpha_{1,1})$, or $|\psi(\mathbf{0}, \mathbf{1})\rangle = |\psi(\mathbf{1}, \mathbf{0})\rangle = |\psi(\mathbf{1}, \mathbf{1})\rangle$, contradicting the established relation $|\psi(\mathbf{0}, \mathbf{1})\rangle \neq |\psi(\mathbf{1}, \mathbf{1})\rangle$. This concludes the demonstration for non-single-state assemblages.

Finally, let us show that a single-state assemblage is unable to do the task. From (C.3),

$$\begin{aligned} \sum_{\mathbf{a}, \mathbf{x}} P_{\mathbf{X}|X_f, \Omega}^\theta(\mathbf{x}|x_f, \omega) P_{A_f|A, \mathbf{X}, \Omega, X_f}^\theta(a_f|\mathbf{a}, \mathbf{x}, \omega, x_f) P_{A|\mathbf{X}}(\mathbf{a}|\mathbf{x}) \times \\ \times K_\omega^\theta |\psi_{\text{single}}\rangle \langle \psi_{\text{single}}| K_\omega^{\theta\dagger} \sim |\psi^\theta(a_f, x_f)\rangle \langle \psi^\theta(a_f, x_f)|. \end{aligned} \quad (\text{C.15})$$

The sum on the left-hand side is not zero for at least two pairs (a_f, x_f) , hence $K_\omega^\theta |\psi_{\text{single}}\rangle$ must be proportional to $|\psi^\theta(a_f, x_f)\rangle$ for both these pairs. This is incompatible with Eq. (C.2), since none of the $|\psi^\theta(a_f, x_f)\rangle$ are proportional to one another. \square

C.2. Redefinition of genuinely multipartite steering

Although our discussion has focused on steering along a fixed bipartition, it has a bearing on genuine multipartite steering as well. This concept hinges on bi-separability over all possible bipartitions, as used by D. Cavalcanti *et al* to define genuine multipartite steering in [143]. Interestingly, however, our results can be used to generalize that definition.

Redefinition of genuinely multipartite steering: *An assemblage σ is genuinely multipartite steerable if it does not admit a decomposition of the form*

$$\sigma_{a,b|x,y} = \sum_{\mu} p_{\mu}^{A|BC} P_{a|x;\mu} \sigma_{b|y}^C(\mu) \quad (\text{C.16a})$$

$$+ \sum_{\nu} p_{\nu}^{B|AC} P_{b|y;\nu} \sigma_{a|x}^C(\nu) \quad (\text{C.16b})$$

$$+ \sum_{\lambda} p_{\lambda}^{AB|C} P_{a,b|x,y,\lambda} \varrho^C(\lambda) \quad (\text{C.16c})$$

where the last sum can be any TO-LHS assemblage.

The difference from D. Cavalcanti *et al*'s definition is that they consider assemblages obtained from a quantum realization with bi-separable states. Reproducing Eqs. (4,5,6) of [143], a tripartite state ϱ^{ABC} is bi-separable when decomposable as

$$\varrho^{ABC} = \sum_{\mu} p_{\mu}^{A|BC} \varrho_{\mu}^A \otimes \varrho_{\mu}^{BC} \quad (\text{C.17a})$$

$$+ \sum_{\nu} p_{\nu}^{B|AC} \varrho_{\nu}^B \otimes \varrho_{\nu}^{AC} \quad (\text{C.17b})$$

$$+ \sum_{\lambda} p_{\lambda}^{AB|C} \varrho_{\lambda}^{AB} \otimes \varrho_{\lambda}^C. \quad (\text{C.17c})$$

Under local measurements on the A and B partitions, this yields a 2DI+1DD assemblage of the form (C.16) (akin to Eqs. (7,8,9) of [143]), but with a distribution $P_{a,b|x,y,\lambda}$ in Eq. (C.16c) necessarily quantum-realizable (a subset of NS distributions). In other words, they only allow the sum in Eq. (C.16c) to be quantum-realizable NS-LHS assemblages. Our redefinition, then,

reduces the set of genuinely multipartite steerable assemblages.

Moreover, we show in Section C.3 that there are, in fact, quantum-realizable assemblages affected by this change. These assemblages are decomposable as in Eq. (C.16) only with a TO-LHS (not NS-LHS) term in Eq. (C.16c), and hence their quantum realization requires genuinely multipartite entangled states [i.e. not decomposable as Eq. (C.17)]. Interestingly, in this case genuine multipartite entanglement is certified in the semi-DI scenario without steering: the need for a TO-LHS term in Eq. (C.16c) implies the inexistence of a bi-separable decomposition (C.17) for the underlying quantum state, and also implies unsteerability.

C.3. On the sets of LHS assemblages, TO-LHS assemblages, and NS-LHS assemblages

We now state a theorem that sustains Fig.5.9 b), concerning the inclusion relations between the sets NS-LHS, TO-LHS, and LHS.

Theorem 3. *NS-LHS \subset TO-LHS \subset LHS, and these relations also hold strictly if we restrict to quantum-realizable assemblages.*

Proof. From the definitions in Eqs. (5.5,5.5), it is clear that NS-LHS \subseteq TO-LHS \subseteq LHS. The phenomenon of exposure implies that the assemblages in Eqs. (5.20a,5.24) belong to LHS, but not to TO-LHS, so the inclusion of one in the other is strict (notice that assemblage (??) is quantum realizable). To prove that NS-LHS is a strict subset of TO-LHS, we need an example of a TO-LHS assemblage that does not belong to NS-LHS. One way to do so is to follow the reasoning of [127]: take the time-ordered decomposition of the distribution \mathbf{P} from [192] that violates the guess-your-neighbor's-input (GYNI) inequality and find the ϱ_λ that best mimic the marginal $P_{a|x,\lambda}$ — this effectively amounts to a one-time program [193]. The resulting TO-LHS assemblage violates GYNI, hence is not NS-LHS, but it is also supra-quantum, since no quantum state can violate the GYNI inequality.

To find a quantum-realizable assemblage that belongs to TO-LHS, but not to NS-LHS, we take inspiration from Bancal *et al* [136], who have found Bell behaviors obtainable from noisy W states with the analogous DI-scenario property (TO-LHV, but not NS-LHV). A pure W state is given by $|W\rangle := (|001\rangle + |010\rangle + |100\rangle)/\sqrt{3}$, its noisy version with visibility v , by

$$\rho_W = v |W\rangle\langle W| + (1 - v) \mathbb{1}^{(ABC)}/8. \quad (\text{C.18})$$

Alice and Bob make von Neumann measurements on the bases $\eta X + \sqrt{1 - \eta^2} Z$ (x or $y = 0$) and $\sqrt{1 - \eta^2} X - \eta Z$ (x or $y = 1$), with $\eta \approx 0.97177$, which yields the assemblage

$$\sigma_{a,b|x,y}^{\text{noisy } W} = v \sigma_{a,b|x,y}^W + (1 - v) \mathbb{1}^C/8, \quad (\text{C.19})$$

a	b	x	y	$\sigma_{a,b x,y}^W$
0	0	0	0	$\frac{1}{6} \left[2\eta^2 0\rangle\langle 0 + (1 + \sqrt{1-\eta^2} - \eta^2/2) 1\rangle\langle 1 + \eta(1 + \sqrt{1-\eta^2})X \right]$
0	1	0	0	$\frac{1}{6} \left[2(1-\eta^2) 0\rangle\langle 0 + \eta^2/2 1\rangle\langle 1 - \eta\sqrt{1-\eta^2}X \right]$
1	0	0	0	$\frac{1}{6} \left[2(1-\eta^2) 0\rangle\langle 0 + \eta^2/2 1\rangle\langle 1 - \eta\sqrt{1-\eta^2}X \right]$
1	1	0	0	$\frac{1}{6} \left[2\eta^2 0\rangle\langle 0 + (1 - \sqrt{1-\eta^2} - \eta^2/2) 1\rangle\langle 1 - \eta(1 - \sqrt{1-\eta^2})X \right]$
0	0	0	1	$\frac{1}{12} \left[2(1 + 2\eta\sqrt{1-\eta^2}) 0\rangle\langle 0 + (1 - \eta + \sqrt{1-\eta^2} - \eta\sqrt{1-\eta^2}) 1\rangle\langle 1 + (1 + \eta + \sqrt{1-\eta^2} - 2\eta^2)X \right]$
0	1	0	1	$\frac{1}{12} \left[2(1 - 2\eta\sqrt{1-\eta^2}) 0\rangle\langle 0 + (1 + \eta + \sqrt{1-\eta^2} + \eta\sqrt{1-\eta^2}) 1\rangle\langle 1 - (1 - \eta + \sqrt{1-\eta^2} - 2\eta^2)X \right]$
1	0	0	1	$\frac{1}{12} \left[2(1 - 2\eta\sqrt{1-\eta^2}) 0\rangle\langle 0 + (1 - \eta - \sqrt{1-\eta^2} + \eta\sqrt{1-\eta^2}) 1\rangle\langle 1 - (1 + \eta - \sqrt{1-\eta^2} - 2\eta^2)X \right]$
1	1	0	1	$\frac{1}{12} \left[2(1 + 2\eta\sqrt{1-\eta^2}) 0\rangle\langle 0 + (1 + \eta - \sqrt{1-\eta^2} - \eta\sqrt{1-\eta^2}) 1\rangle\langle 1 + (1 - \eta - \sqrt{1-\eta^2} - 2\eta^2)X \right]$
a	b	1	0	$\sigma_{a,b 1,0}^W = \sigma_{b,a 0,1}^W$
0	0	1	1	$\frac{1}{6} \left[2(1-\eta^2) 0\rangle\langle 0 + (1 - \eta - (1-\eta^2)/2) 1\rangle\langle 1 + \sqrt{1-\eta^2}(1-\eta)X \right]$
0	1	1	1	$\frac{1}{6} \left[2\eta^2 0\rangle\langle 0 + (1-\eta^2)/2 1\rangle\langle 1 + \eta\sqrt{1-\eta^2}X \right]$
1	0	1	1	$\frac{1}{6} \left[2\eta^2 0\rangle\langle 0 + (1-\eta^2)/2 1\rangle\langle 1 + \eta\sqrt{1-\eta^2}X \right]$
1	1	1	1	$\frac{1}{6} \left[2(1-\eta^2) 0\rangle\langle 0 + (1 + \eta - (1-\eta^2)/2) 1\rangle\langle 1 - \sqrt{1-\eta^2}(1+\eta)X \right]$

Table C.1.: Example quantum assemblage to demonstrate strict inclusion of NS-LHS in TO-LHS.

where $\sigma_{a,b|x,y}^W$ is given in Table C.1. These measurements, together with an appropriate measurement by Charlie, yield in [136] a DI-inequality violation requiring minimal visibility.

We obtain the optimal NS-LHS witness $\mathbf{W} = \{W_{abxy}\}_{a,b,x,y}$ for $\sigma_{a,b|x,y}^{\text{noisy } W}$ for $v = 0.58$, i.e. \mathbf{W} satisfies the property

$$-1 \leq \sum_{a,b,x,y} \text{Tr}[W_{abxy} \sigma_{a,b|x,y}^{\text{NS-LHS}}] \leq 0 \quad (\text{C.20})$$

for every NS-LHS assemblage $\sigma^{\text{NS-LHS}}$. Its components W_{abxy} are given in Table C.2. This witness is violated by $\sigma_{a,b|x,y}^{\text{noisy } W}$ from $v \approx 0.58$ onwards; for $v = 0.64$, it returns 0.0301.

$x,y \backslash a,b$	00	01	10	11
00	$\begin{bmatrix} -0.0056 & 0.1194 \\ 0.1194 & -0.1205 \end{bmatrix}$	$\begin{bmatrix} -0.1394 & -0.0603 \\ -0.0603 & 0.0662 \end{bmatrix}$	$\begin{bmatrix} -0.1394 & -0.0603 \\ -0.0603 & 0.0662 \end{bmatrix}$	$\begin{bmatrix} 0.0239 & -0.0656 \\ -0.0656 & -0.1869 \end{bmatrix}$
01	$\begin{bmatrix} 0.0233 & -0.0324 \\ -0.0324 & -0.1706 \end{bmatrix}$	$\begin{bmatrix} -0.2194 & 0.1346 \\ 0.1346 & -0.0079 \end{bmatrix}$	$\begin{bmatrix} -0.0560 & 0.1109 \\ 0.1109 & 0.0114 \end{bmatrix}$	$\begin{bmatrix} -0.0417 & -0.1490 \\ -0.1490 & -0.1079 \end{bmatrix}$
10	$\begin{bmatrix} 0.0233 & -0.0324 \\ -0.0324 & -0.1706 \end{bmatrix}$	$\begin{bmatrix} -0.0560 & 0.1109 \\ 0.1109 & 0.0114 \end{bmatrix}$	$\begin{bmatrix} -0.2194 & 0.1346 \\ 0.1346 & -0.0079 \end{bmatrix}$	$\begin{bmatrix} -0.0417 & -0.1490 \\ -0.1490 & -0.1079 \end{bmatrix}$
11	$\begin{bmatrix} -0.0410 & -0.0560 \\ -0.0560 & 0.0863 \end{bmatrix}$	$\begin{bmatrix} 0.0665 & 0.0431 \\ 0.0431 & -0.2194 \end{bmatrix}$	$\begin{bmatrix} 0.0665 & 0.0431 \\ 0.0431 & -0.2194 \end{bmatrix}$	$\begin{bmatrix} -0.4431 & -0.0727 \\ -0.0727 & 0.0239 \end{bmatrix}$

Table C.2.: Elements of witness W_{abxy} used to demonstrate strict inclusion of NS-LHS in TO-LHS.

λ	σ_λ	λ	σ_λ	λ	σ_λ	λ	σ_λ
0	$\begin{bmatrix} 0.0045 & 0.0013 \\ 0.0013 & 0.0009 \end{bmatrix}$	1	$\begin{bmatrix} 0.0928 & 0.0246 \\ 0.0246 & 0.0070 \end{bmatrix}$	2	$\begin{bmatrix} 0.0036 & 0.0011 \\ 0.0011 & 0.0009 \end{bmatrix}$	3	$\begin{bmatrix} 0.0244 & 0.0068 \\ 0.0068 & 0.0024 \end{bmatrix}$
4	$\begin{bmatrix} 0.0055 & 0.0058 \\ 0.0058 & 0.0071 \end{bmatrix}$	5	$\begin{bmatrix} 0.0084 & 0.0071 \\ 0.0071 & 0.0067 \end{bmatrix}$	6	$\begin{bmatrix} 0.0066 & 0.0076 \\ 0.0076 & 0.0098 \end{bmatrix}$	7	$\begin{bmatrix} 0.0100 & 0.0090 \\ 0.0090 & 0.0089 \end{bmatrix}$
8	$\begin{bmatrix} 0.0048 & -0.0029 \\ -0.0029 & 0.0025 \end{bmatrix}$	9	$\begin{bmatrix} 0.0118 & -0.0052 \\ -0.0052 & 0.0029 \end{bmatrix}$	10	$\begin{bmatrix} 0.0040 & -0.0026 \\ -0.0026 & 0.0024 \end{bmatrix}$	11	$\begin{bmatrix} 0.0079 & -0.0037 \\ -0.0037 & 0.0024 \end{bmatrix}$
12	$\begin{bmatrix} 0.0007 & -0.0004 \\ -0.0004 & 0.0024 \end{bmatrix}$	13	$\begin{bmatrix} 0.0008 & -0.0002 \\ -0.0002 & 0.0014 \end{bmatrix}$	14	$\begin{bmatrix} 0.0006 & -0.0004 \\ -0.0004 & 0.0029 \end{bmatrix}$	15	$\begin{bmatrix} 0.0007 & -0.0002 \\ -0.0002 & 0.0015 \end{bmatrix}$
16	$\begin{bmatrix} 0.0219 & 0.0118 \\ 0.0118 & 0.0064 \end{bmatrix}$	17	$\begin{bmatrix} 0.0001 & 0.0002 \\ 0.0002 & 0.0010 \end{bmatrix}$	18	$\begin{bmatrix} 0.0028 & -0.0005 \\ -0.0005 & 0.0001 \end{bmatrix}$	19	$\begin{bmatrix} 0.0002 & -0.0002 \\ -0.0002 & 0.0004 \end{bmatrix}$
20	$\begin{bmatrix} 0.0612 & 0.0411 \\ 0.0411 & 0.0277 \end{bmatrix}$	21	$\begin{bmatrix} 0.0034 & 0.0126 \\ 0.0126 & 0.0467 \end{bmatrix}$	22	$\begin{bmatrix} 0.0007 & -0.0001 \\ -0.0001 & 0.0001 \end{bmatrix}$	23	$\begin{bmatrix} 0.0002 & -0.0002 \\ -0.0002 & 0.0004 \end{bmatrix}$
24	$\begin{bmatrix} 0.0007 & 0.0003 \\ 0.0003 & 0.0002 \end{bmatrix}$	25	$\begin{bmatrix} 0.0001 & 0.0001 \\ 0.0001 & 0.0010 \end{bmatrix}$	26	$\begin{bmatrix} 0.0135 & -0.0036 \\ -0.0036 & 0.0010 \end{bmatrix}$	27	$\begin{bmatrix} 0.0074 & -0.0106 \\ -0.0106 & 0.0153 \end{bmatrix}$
28	$\begin{bmatrix} 0.0006 & 0.0003 \\ 0.0003 & 0.0003 \end{bmatrix}$	29	$\begin{bmatrix} 0.0010 & 0.0073 \\ 0.0073 & 0.0545 \end{bmatrix}$	30	$\begin{bmatrix} 0.0008 & -0.0002 \\ -0.0002 & 0.0001 \end{bmatrix}$	31	$\begin{bmatrix} 0.0015 & -0.0025 \\ -0.0025 & 0.0045 \end{bmatrix}$
32	$\begin{bmatrix} 0.0020 & 0.0006 \\ 0.0006 & 0.0016 \end{bmatrix}$	33	$\begin{bmatrix} 0.0049 & 0.0013 \\ 0.0013 & 0.0013 \end{bmatrix}$	34	$\begin{bmatrix} 0.0017 & 0.0006 \\ 0.0006 & 0.0018 \end{bmatrix}$	35	$\begin{bmatrix} 0.0038 & 0.0011 \\ 0.0011 & 0.0014 \end{bmatrix}$
36	$\begin{bmatrix} 0.0020 & -0.0013 \\ -0.0013 & 0.0022 \end{bmatrix}$	37	$\begin{bmatrix} 0.0031 & -0.0012 \\ -0.0012 & 0.0014 \end{bmatrix}$	38	$\begin{bmatrix} 0.0018 & -0.0013 \\ -0.0013 & 0.0024 \end{bmatrix}$	39	$\begin{bmatrix} 0.0026 & -0.0011 \\ -0.0011 & 0.0015 \end{bmatrix}$
40	$\begin{bmatrix} 0.0037 & -0.0000 \\ -0.0000 & 0.0009 \end{bmatrix}$	41	$\begin{bmatrix} 0.0261 & 0.0009 \\ 0.0009 & 0.0007 \end{bmatrix}$	42	$\begin{bmatrix} 0.0029 & -0.0000 \\ -0.0000 & 0.0010 \end{bmatrix}$	43	$\begin{bmatrix} 0.0125 & 0.0005 \\ 0.0005 & 0.0008 \end{bmatrix}$
44	$\begin{bmatrix} 0.0069 & -0.0040 \\ -0.0040 & 0.0032 \end{bmatrix}$	45	$\begin{bmatrix} 0.0227 & -0.0094 \\ -0.0094 & 0.0045 \end{bmatrix}$	46	$\begin{bmatrix} 0.0055 & -0.0034 \\ -0.0034 & 0.0030 \end{bmatrix}$	47	$\begin{bmatrix} 0.0140 & -0.0060 \\ -0.0060 & 0.0033 \end{bmatrix}$
48	$\begin{bmatrix} 0.0062 & 0.0036 \\ 0.0036 & 0.0022 \end{bmatrix}$	49	$\begin{bmatrix} 0.0011 & 0.0051 \\ 0.0051 & 0.0258 \end{bmatrix}$	50	$\begin{bmatrix} 0.0031 & -0.0006 \\ -0.0006 & 0.0002 \end{bmatrix}$	51	$\begin{bmatrix} 0.0007 & -0.0011 \\ -0.0011 & 0.0018 \end{bmatrix}$
52	$\begin{bmatrix} 0.0009 & 0.0005 \\ 0.0005 & 0.0003 \end{bmatrix}$	53	$\begin{bmatrix} 0.0001 & 0.0005 \\ 0.0005 & 0.0034 \end{bmatrix}$	54	$\begin{bmatrix} 0.0035 & -0.0008 \\ -0.0008 & 0.0003 \end{bmatrix}$	55	$\begin{bmatrix} 0.0193 & -0.0303 \\ -0.0303 & 0.0479 \end{bmatrix}$
56	$\begin{bmatrix} 0.0044 & 0.0023 \\ 0.0023 & 0.0013 \end{bmatrix}$	57	$\begin{bmatrix} 0.0002 & 0.0004 \\ 0.0004 & 0.0024 \end{bmatrix}$	58	$\begin{bmatrix} 0.0287 & -0.0055 \\ -0.0055 & 0.0011 \end{bmatrix}$	59	$\begin{bmatrix} 0.0008 & -0.0011 \\ -0.0011 & 0.0018 \end{bmatrix}$
60	$\begin{bmatrix} 0.0008 & 0.0004 \\ 0.0004 & 0.0003 \end{bmatrix}$	61	$\begin{bmatrix} 0.0001 & 0.0002 \\ 0.0002 & 0.0015 \end{bmatrix}$	62	$\begin{bmatrix} 0.0967 & -0.0246 \\ -0.0246 & 0.0063 \end{bmatrix}$	63	$\begin{bmatrix} 0.0206 & -0.0300 \\ -0.0300 & 0.0440 \end{bmatrix}$

Table C.3.: Non-normalized states σ_λ needed in Eq. (C.21) for the TO-LHS decomposition of the assemblage (C.19).

However, there is a TO-LHS decomposition of $\sigma_{a,b|x,y}^{\text{noisy } W}$ for $v = 0.64$ (hence for $v < 0.64$), which, equivalently to Eq. (5.5), can be written as

$$\sigma_{a,b|x,y}^{\text{noisy } W} = \sum_{\lambda} D_{\lambda}(a|x) D_{\lambda}(b|x, y) \sigma_{\lambda} \quad (\text{C.21a})$$

$$= \sum_{\lambda} D_{\lambda}(a|x, y) D_{\lambda}(b|y) \sigma_{\lambda}, \quad (\text{C.21b})$$

where the D_{λ} are deterministic response functions and $\sigma_{\lambda} := p_{\lambda} \rho_{\lambda}$ are non-normalized states. Each $D_{\lambda}(a|x)$ is specified by a_x , the deterministic outcome a conditioned on x ; the notation follows analogously for $D_{\lambda}(b|x, y)$, $D_{\lambda}(a|x, y)$, and $D_{\lambda}(b|y)$ (b_{xy} , a_{xy} , and b_y , respectively).

These are given by

λ	a_0	a_1	b_{00}	b_{01}	b_{10}	b_{11}		λ	a_{00}	a_{01}	a_{10}	a_{11}	b_0	b_1	
0	0	0	0	0	0	0		0	0	0	0	0	0	0	
1	0	0	0	0	0	1		1	0	0	0	0	0	1	
2	0	0	0	0	1	0		2	0	0	0	0	1	0	
3	0	0	0	0	1	1		3	0	0	0	0	1	1	
			\vdots								\vdots				
62	1	1	1	1	1	0		62	1	1	1	1	1	0	
63	1	1	1	1	1	1		63	1	1	1	1	1	1	

where in each table, the six columns to the right are the binary expression of the leftmost column (λ). The states σ_λ are given in Table C.3. □

TIME EVOLUTION AND CPF CORRELATION FOR THE DECAY OF A TWO LEVEL SYSTEM IN A BOSONIC BATH

In this Appendix, it is shown the detailed calculation to get to the time evolved state (Eq. (6.26) in the main text) and to the expression of the CPF correlation for the different schemes (Eq. (6.28) and Eq. (6.29) in the main text). It is also shown in more details the relation between the experimental HWP angles and the theoretical time evolution.

D.1. Solution of Eq. (6.25) for initial separable states

The dynamics of the composite system (qubit + bosonic environment) is given by the total Hamiltonian (6.23) that can be regarded as the sum of a free evolution term $H_0 = \frac{\omega_0}{2}\sigma_z + \sum_k \omega_k b_k^\dagger b_k$ with an interaction term $H_I = \sum_k (g_k \sigma_+ b_k + g_k^* \sigma_- b_k^\dagger)$. In the interaction picture the total state satisfies the Schrödinger equation (6.25) with the time dependent interaction Hamiltonian $H_I(t) = e^{iH_0 t} H_I e^{-iH_0 t} = \sum_k (g_k e^{i\omega_0 t} \sigma_+ e^{i\omega_k b_k^\dagger b_k} b_k e^{-i\omega_k b_k^\dagger b_k} + h.c.)$. We assume that this composite system is closed and initially in a pure separable state¹. The commutator of the total number of excitations $N = \sigma_+ \sigma_- + \sum_k b_k^\dagger b_k$ with the total Hamiltonian vanishes ($[H_{tot}, N] = 0$), therefore this quantity is conserved. As in the initial instant we consider that the system has at most one excitation and the environment is in its vacuum state, then the state at time $t > 0$ must be the general state

$$|\Psi_t\rangle = \left[a(t)|\uparrow\rangle + b(t)|\downarrow\rangle + |\downarrow\rangle \sum_k c_k(t) b_k^\dagger \right] |0\rangle, \quad (\text{D.1})$$

¹This is the case for the very initial state because the environment starts to evolve from vacuum and the system is measured before each step of time evolution.

which is the superposition of all possible composite states with at most one excitation.

From Schrödinger equation, the coefficients evolves as

$$\frac{d}{dt}b(t) = 0. \quad (\text{D.2})$$

Therefore, $b(t) = b(0) = b$. In addition, it follows that

$$\frac{d}{dt}a(t) = -i \sum_k g_k \exp(+i\phi_k t) c_k(t), \quad (\text{D.3})$$

$$\frac{d}{dt}c_k(t) = -ig_k^* \exp(-i\phi_k t) a(t), \quad (\text{D.4})$$

where $\phi_k \equiv \omega_0 - \omega_k$. Integrating the last equation as

$$c_k(t) = c_k(0) - ig_k^* \int_0^t dt' \exp(-i\phi_k t') a(t'), \quad (\text{D.5})$$

the evolution for $a(t)$ becomes

$$\frac{d}{dt}a(t) = - \int_0^t f(t-t') a(t') dt' - ig(t). \quad (\text{D.6})$$

Here, $f(t)$ defines the bath correlation

$$f(t) \equiv \sum_k |g_k|^2 \exp(+i\phi_k t), \quad (\text{D.7})$$

while the inhomogeneous term is

$$g(t) \equiv \sum_k g_k \exp(+i\phi_k t) c_k(0). \quad (\text{D.8})$$

Defining the Green function $G(t)$ by the evolution

$$\frac{d}{dt}G(t) = - \int_0^t f(t-t') G(t') dt', \quad (\text{D.9})$$

with $G(0) = 1$, the coefficient $a(t)$ can be written as

$$a(t) = G(t)a(0) - i \int_0^t G(t-t') g(t') dt'. \quad (\text{D.10})$$

Evolution in the time interval $(0, t)$

The total system is prepared in the initial state $|\Psi_0\rangle = (a|\uparrow\rangle + b|\downarrow\rangle) \otimes |0\rangle$. Immediately after the preparation, the OQS is measured and the composite system's state becomes $|\Psi_0^x\rangle =$

$(a_x|\uparrow\rangle + b_x|\downarrow\rangle) \otimes |0\rangle$, with new coefficients dependent on the measurement outcome x .

Thus, the initial conditions are

$$a(0) = a_x, \quad b(0) = b_x, \quad c_k(0) = 0, \quad (\text{D.11})$$

implying $g(t) = 0$. The coefficients can be expressed as

$$a(t) = G(t)a_x, \quad c_k(t) = -ia_x g_k^* \int_0^t dt' \exp(-i\phi_k t') G(t'). \quad (\text{D.12})$$

Evolution in the time interval $(t, t + \tau)$

The measurement module Y is applied, projecting the OQS into one of its energy eigenstates $|\uparrow\rangle$ or $|\downarrow\rangle$. Different initial conditions must be used for this second step of time evolution, depending on this measurement result. The initial state for this step is the projection of Eq. (D.1) on $|\uparrow\rangle$ or $|\downarrow\rangle$ for $y = +1$ or $y = -1$, respectively.

First Initial conditions: when $y = +1$

$$\tilde{a}(0) = 1, \quad \tilde{b}(0) = 0, \quad \tilde{c}_k(0) = 0, \quad (\text{D.13})$$

which implies $\tilde{g}(\tau) = 0$, if follows the solution

$$\tilde{a}(\tau) = G(\tau), \quad (\text{D.14})$$

while from Eq. (D.5) we get

$$\tilde{c}_k(\tau) = -ig_k^* \int_0^\tau d\tau' \exp[-i\phi_k(\tau' + t)] G(\tau'). \quad (\text{D.15})$$

These solutions are equivalent to the previous ones [Eq. (D.12)] under the replacement $t \rightarrow \tau$.

Second initial conditions: If $y = -1$, the set of initial conditions for this second step is given by

$$\tilde{a}'(0) = 0, \quad \tilde{b}'(0) = b_x / \sqrt{1 - |G(t)|^2}, \quad \tilde{c}'_k(0) = c_k(t) / \sqrt{1 - |G(t)|^2}. \quad (\text{D.16})$$

From Eq. (D.5) we write $c_k(t) = -ig_k^* \int_0^t dt' \exp(-i\phi_k t') G(t')$. Thus, Eq. (D.8) becomes

$$\begin{aligned} \tilde{g}(\tau) &= -i \frac{\int_0^t dt' \sum_k |g_k|^2 \exp[+i\phi_k(\tau + t - t')] G(t')}{\sqrt{1 - |G(t)|^2}}, \\ &= \frac{-i}{\sqrt{1 - |G(t)|^2}} \int_0^t dt' f(\tau + t - t') G(t'). \end{aligned} \quad (\text{D.17})$$

From Eq. (D.10), $\tilde{a}'(\tau) = -i \int_0^\tau G(\tau - \tau') \tilde{g}(\tau') d\tau'$, delivering

$$\tilde{a}'(\tau) = \frac{-\int_0^\tau d\tau' \int_0^t dt' f(\tau' + t - t') G(\tau - \tau') G(t')}{\sqrt{1 - |G(t)|^2}}, \quad (\text{D.18})$$

which can be rewritten as

$$\tilde{a}'(\tau) = \frac{-G(t, \tau)}{\sqrt{1 - |G(t)|^2}}. \quad (\text{D.19a})$$

This equation defines the function $G(t, \tau)$. Moreover, from Eq. (D.5), the other coefficients read

$$\begin{aligned} \tilde{c}'_k(\tau) &= \frac{1}{\sqrt{1 - |G(t)|^2}} \left\{ c_k(t) + i g_k^* \right. \\ &\quad \left. \times \int_0^\tau d\tau' \exp[-i\phi_k(\tau' + t)] G(\tau', t) \right\}. \end{aligned} \quad (\text{D.19b})$$

The function $G(t, \tau)$, after a change of integration variables in Eq. (D.18), can be written as

$$G(t, \tau) = \int_0^t dt' \int_0^\tau d\tau' f(\tau' + t') G(t - t') G(\tau - \tau'). \quad (\text{D.20})$$

Eq. (D.19) shows that $G(t, \tau)$ measures the probability of finding the system in the upper state at time τ given that at the initial time t it was in the ground state [Eq. (D.16)].

D.2. Calculation of the CPF correlation

Here we explicitly calculate the CPF correlation defined as:

$$C_{pf}(t, \tau)|_y = \langle O_z O_x \rangle_y - \langle O_z \rangle_y \langle O_x \rangle_y. \quad (\text{D.21})$$

Equivalently, $C_{pf}(t, \tau)|_y = \sum_{zx} O_z O_x [P(z, x|y) - P(z|y)P(x|y)]$, for different possible measurement schemes. The conditional values explicitly read

$$\langle O_x \rangle_y = \sum_{x=\pm 1} x P(x|y), \quad \langle O_z \rangle_y = \sum_{z=\pm 1} z P(z|y), \quad (\text{D.22})$$

and

$$\langle O_z O_x \rangle_y = \sum_{z,x=\pm 1} zx P(z, x|y). \quad (\text{D.23})$$

Furthermore, $P(z|y) = \sum_{x=\pm 1} P(z, x|y)$, and $P(x|y) = \sum_{z=\pm 1} P(z, x|y)$. Measurement outcomes are indicated by x , y , and z , while directions in Bloch sphere are given by the eigenvectors of the Pauli matrices, σ_x , σ_y , and σ_z .

D.2.1. First scheme, measurements $\sigma_z - \sigma_z - \sigma_z$

The three measurements necessary to obtain the CPF correlations are performed in the same σ_z -direction, with corresponding measurement projectors $\Pi_{+1} = |\uparrow\rangle\langle\uparrow|$ and $\Pi_{-1} = |\downarrow\rangle\langle\downarrow|$. The initial condition is taken as

$$|\Psi_0\rangle = (a|\uparrow\rangle + b|\downarrow\rangle) \otimes |0\rangle. \quad (\text{D.24})$$

After the first x -measurement (measurement in the past), the total state suffers the transformation $|\Psi_0\rangle \rightarrow |\Psi_0^x\rangle = \Pi_{\hat{z}=x}|\Psi_0\rangle / \sqrt{\langle\Psi_0|\Pi_{\hat{z}=x}|\Psi_0\rangle}$ delivering ($x = \pm 1$)

$$|\Psi_0^x\rangle = |x\rangle \otimes |0\rangle, \quad (\text{D.25})$$

where we disregarded a global phase contribution. The probability of each option $P(x) = \langle\Psi_0|\Pi_{\hat{z}=x}|\Psi_0\rangle$, reads

$$P(x = +1) = |a|^2, \quad P(x = -1) = |b|^2. \quad (\text{D.26})$$

After the x -measurement, the system and environment evolve with the Hamiltonian dynamics during a time interval t , $|\Psi_0^x\rangle \rightarrow |\Psi_t^x\rangle$. We get,

$$\begin{array}{c|c} x & |\Psi_t^x\rangle \\ \hline + & [a(t)|\uparrow\rangle + |\downarrow\rangle \sum_k c_k(t) b_k^\dagger] |0\rangle \\ - & |\downarrow\rangle \otimes |0\rangle \end{array}, \quad (\text{D.27})$$

with $a(0) = 1$, $c_k(0) = 0$ and normalization $|a(t)|^2 + \sum_k |c_k(t)| = 1$. Thus, from Eq. (D.11), these coefficients are explicitly given by Eq. (D.12).

Posteriorly, the second y -measurement, correspondent to the present, is performed. The conditional probability of outcomes y , given the previous outcomes x , is given by $P(y|x) = \langle\Psi_t^x|\Pi_{\hat{z}=y}|\Psi_t^x\rangle$. The joint probability of both outcomes is $P(y, x) = P(y|x)P(x)$. The retrodicted probability of past outcomes given the present ones is $P(x|y) = P(y, x)/P(y)$, where $P(y) = \sum_x P(y, x)$. We get

$$\begin{array}{c|c|c|c|c} y & x & P(y|x) & P(y, x) & P(x|y) \\ \hline + & + & |a(t)|^2 & |G(t)|^2 |a|^2 & 1 \\ + & - & 0 & 0 & 0 \\ - & + & 1 - |a(t)|^2 & (1 - |G(t)|^2) |a|^2 & \frac{(1 - |G(t)|^2) |a|^2}{(1 - |G(t)|^2) |a|^2 + |b|^2} \\ - & - & 1 & |b|^2 & \frac{|b|^2}{(1 - |G(t)|^2) |a|^2 + |b|^2} \end{array}. \quad (\text{D.28})$$

After the second measurement, the total state suffer the transformation $|\Psi_t^x\rangle \rightarrow |\Psi_t^{yx}\rangle = \Pi_{\hat{z}=y}|\Psi_t^x\rangle / \sqrt{\langle\Psi_t^x|\Pi_{\hat{z}=y}|\Psi_t^x\rangle}$. Posteriorly, starting at time t , $|\Psi_t^{yx}\rangle$ evolves with the total unitary

dynamics during a time interval τ , leading to the transformation $|\Psi_t^{yx}\rangle \rightarrow |\Psi_{t+\tau}^{yx}\rangle$. From Eq. (D.27) the states conditioned to the output of each measurement are

$$\begin{array}{c|c|c}
 y & x & |\Psi_t^{yx}\rangle \\
 \hline
 + & + & |\uparrow\rangle \otimes |0\rangle \\
 + & - & \not\equiv \\
 - & + & |\downarrow\rangle \frac{\sum_k c_k(t) b_k^\dagger |0\rangle}{\sqrt{1-|a(t)|^2}} \\
 - & - & |\downarrow\rangle \otimes |0\rangle \\
 \hline
 y & x & |\Psi_{t+\tau}^{yx}\rangle \\
 \hline
 + & + & [\tilde{a}(\tau)|\uparrow\rangle + |\downarrow\rangle \sum_k \tilde{c}_k(\tau) b_k^\dagger] |0\rangle \\
 + & - & \not\equiv \\
 - & + & [\tilde{a}'(\tau)|\uparrow\rangle + |\downarrow\rangle \sum_k \tilde{c}'_k(\tau) b_k^\dagger] |0\rangle \\
 - & - & |\downarrow\rangle \otimes |0\rangle
 \end{array} . \quad (\text{D.29})$$

The solution form $(y, x) = (+, +)$ comes from Eq. (D.13) [solutions (??)], while for $(y, x) = (-, +)$ follows from Eq. (D.16) [solutions (D.19)].

Finally, the third z -measurement is performed (measurement in the future). The probability $P(z|yx)$ of outcome z given the previous outcomes y and x , is given by $P(z|yx) = \langle \Psi_{t+\tau}^{yx} | \Pi_{\hat{z}=z} | \Psi_{t+\tau}^{yx} \rangle$. The conditional probability of past and future event is $P(z, x|y) = P(z|y, x)P(x|y)$, where $P(x|y)$ follows from Eq. (D.28). We get

$$\begin{array}{c|c|c|c}
 z & y & x & P(z|y, x) \\
 \hline
 + & + & + & |\tilde{a}(\tau)|^2 \\
 + & + & - & 0 \\
 + & - & + & |\tilde{a}'(\tau)|^2 \\
 + & - & - & 0 \\
 - & + & + & 1 - |\tilde{a}(\tau)|^2 \\
 - & + & - & 0 \\
 - & - & + & 1 - |\tilde{a}'(\tau)|^2 \\
 - & - & - & 1 \\
 \hline
 z & y & x & P(z, x|y) \\
 \hline
 + & + & + & |G(\tau)|^2 \\
 + & + & - & 0 \\
 + & - & + & \frac{|G(t, \tau)|^2 |a|^2}{(1-|G(t)|^2)|a|^2 + |b|^2} \\
 + & - & - & 0 \\
 - & + & + & 1 - |G(\tau)|^2 \\
 - & + & - & 0 \\
 - & - & + & \frac{(1-|G(t, \tau)|^2 - |G(t)|^2) |a|^2}{(1-|G(t)|^2)|a|^2 + |b|^2} \\
 - & - & - & \frac{|b|^2}{(1-|G(t)|^2)|a|^2 + |b|^2}
 \end{array} . \quad (\text{D.30})$$

The conditional probability of the last measurement follows from $P(z|y) = \sum_x P(z, x|y)$, delivering

$$\begin{array}{c|c|c}
 z & y & P(z|y) \\
 \hline
 + & + & |G(\tau)|^2 \\
 + & - & \frac{|G(t, \tau)|^2 |a|^2}{(1-|G(t)|^2)|a|^2 + |b|^2} \\
 - & + & 1 - |G(\tau)|^2 \\
 - & - & \frac{(1-|G(t, \tau)|^2 - |G(t)|^2) |a|^2 + |b|^2}{(1-|G(t)|^2)|a|^2 + |b|^2} \\
 \hline
 z & y & P(z|y) \\
 \hline
 + & + & |G(\tau)|^2 \\
 + & - & \frac{|G(t, \tau)|^2 |a|^2}{(1-|G(t)|^2)|a|^2 + |b|^2} \\
 - & + & 1 - |G(\tau)|^2 \\
 - & - & \frac{(1-|G(t, \tau)|^2 - |G(t)|^2) |a|^2 + |b|^2}{(1-|G(t)|^2)|a|^2 + |b|^2}
 \end{array} . \quad (\text{D.31})$$

From Eqs. (D.28) and (D.31), the expectation values [Eqs. (D.22) and (D.23)] read

$$\langle O_x \rangle_{y=1} = 1, \quad \langle O_z \rangle_{y=1} = 2|G(\tau)|^2 - 1, \quad (\text{D.32})$$

while from Eq. (D.30) we get

$$\langle O_z O_x \rangle_{y=1} = 2|G(\tau)|^2 - 1. \quad (\text{D.33})$$

Thus, it follows

$$C_{pf}(t, \tau)|_{y=+1} = 0. \quad (\text{D.34})$$

On the other hand, for $y = -1$, the averages read

$$\langle O_x \rangle_{y=-1} = \frac{(1 - |G(t)|^2)|a|^2 - |b|^2}{(1 - |G(t)|^2)|a|^2 + |b|^2}, \quad (\text{D.35})$$

while

$$\langle O_z \rangle_{y=-1} = \frac{(2|G(t, \tau)|^2 + |G(t)|^2 - 1)|a|^2 - |b|^2}{(1 - |G(t)|^2)|a|^2 + |b|^2}, \quad (\text{D.36})$$

and

$$\langle O_z O_x \rangle_{y=-1} = \frac{(2|G(t, \tau)|^2 + |G(t)|^2 - 1)|a|^2 + |b|^2}{(1 - |G(t)|^2)|a|^2 + |b|^2}. \quad (\text{D.37})$$

The CPF correlation then is

$$C_{pf}(t, \tau)|_{y=-1} \stackrel{\hat{z}\hat{z}\hat{z}}{=} \left\{ \frac{4|a|^2|b|^2}{[(1 - |G(t)|^2)|a|^2 + |b|^2]^2} \right\} |G(t, \tau)|^2. \quad (\text{D.38})$$

D.2.2. Second scheme, \hat{x} - \hat{z} - \hat{x}

In this scheme, the first and last measurements are performed in \hat{x} -direction, with measurement projector $\Pi_{\hat{x}=+1} = |+\rangle\langle+|$, and $\Pi_{\hat{x}=-1} = |-\rangle\langle-|$, where $|\pm\rangle = (1/\sqrt{2})(|\uparrow\rangle \pm |\downarrow\rangle)$. The intermediate one is realized in \hat{z} -direction, with projector $\Pi_{\hat{z}=+1}$ and $\Pi_{\hat{z}=-1}$ defined above. The initial system-environment state is

$$|\Psi_0\rangle = (a|\uparrow\rangle + b|\downarrow\rangle) \otimes |0\rangle. \quad (\text{D.39})$$

After the first x -measurement $|\Psi_0\rangle \rightarrow |\Psi_0^x\rangle = \Pi_{\hat{x}=x}|\Psi_0\rangle / \sqrt{\langle\Psi_0|\Pi_{\hat{x}=x}|\Psi_0\rangle}$, the bipartite state is

$$|\Psi_0^x\rangle = \frac{|\uparrow\rangle + x|\downarrow\rangle}{\sqrt{2}} \otimes |0\rangle, \quad (\text{D.40})$$

where global phase contributions are disregarded. The probability of each option ($x = \pm 1$) $P(x) = \langle\Psi_0|\Pi_{\hat{x}=x}|\Psi_0\rangle$, reads

$$P(x) = \frac{1}{2}|a + xb|^2. \quad (\text{D.41})$$

After the previous step, $|\Psi_0^x\rangle$ evolves with the unitary evolution during a time interval

t , $|\Psi_0^x\rangle \rightarrow |\Psi_t^x\rangle$. Using the initial conditions (D.11) and their associated solution (D.12), we get

$$|\Psi_t^x\rangle = \frac{1}{\sqrt{2}} \left[a(t) |\uparrow\rangle + x |\downarrow\rangle + |\downarrow\rangle \sum_k c_k(t) b_k^\dagger \right] |0\rangle, \quad (\text{D.42})$$

where $a(0) = 1$ and $c_k(0) = 0$.

Posteriorly, the second y -measurement is performed. The conditional probability for the outcomes is $P(y|x) = \langle \Psi_t^x | \Pi_{\hat{z}=y} | \Psi_t^x \rangle$, which deliver

$$P(+|x) = \frac{|a(t)|^2}{2}, \quad P(-|x) = 1 - \frac{|a(t)|^2}{2}, \quad (\text{D.43})$$

where we used $|a(t)|^2 + \sum_k |c_k(t)|^2 = 1$. This result indicates that the random variable y is statistically independent of x , $P(y|x) = P(y)$. Thus, the joint probability for the first and second outcomes is $P(y, x) = P(y|x)P(x) = P(y)P(x)$. The retrodicted probability $P(x|y) = P(y, x)/P(y)$, where $P(y) = \sum_x P(y, x)$, becomes

$$P(x|y) = P(x). \quad (\text{D.44})$$

After the second measurement, the state suffers the transformation $|\Psi_t^x\rangle \rightarrow |\Psi_t^{yx}\rangle = \Pi_{\hat{z}=y} |\Psi_t^x\rangle / \sqrt{\langle \Psi_t^x | \Pi_{\hat{z}=y} | \Psi_t^x \rangle}$. From Eq. (D.42), for $y = +1$ we get

$$|\Psi_t^{+,x}\rangle = |\uparrow\rangle \otimes |0\rangle, \quad (\text{D.45})$$

while for $y = -1$,

$$|\Psi_t^{-,x}\rangle = \frac{1}{\sqrt{2 - |a(t)|^2}} |\downarrow\rangle \otimes \left[x + \sum_k c_k(t) b_k^\dagger \right] |0\rangle. \quad (\text{D.46})$$

Starting at time t , $|\Psi_t^{yx}\rangle$ evolves with the total unitary dynamics during a time interval τ , leading to the transformation $|\Psi_t^{yx}\rangle \rightarrow |\Psi_{t+\tau}^{yx}\rangle$. From Eq. (D.45) we get

$$|\Psi_{t+\tau}^{+,x}\rangle = \left[\tilde{a}(\tau) |\uparrow\rangle + |\downarrow\rangle \sum_k \tilde{c}_k(\tau) b_k^\dagger \right] |0\rangle, \quad (\text{D.47})$$

with $\tilde{a}(0) = 1$, $\tilde{c}_k(0) = 0$ [Eq. (D.13)], with $|\tilde{a}(\tau)|^2 + \sum_k |\tilde{c}_k(\tau)|^2 = 1$. Thus, $\tilde{a}(\tau)$ and $\tilde{c}_k(\tau)$ are given by Eq. (??). On the other hand, from Eq. (D.46), it follows

$$\begin{aligned} |\Psi_{t+\tau}^{-,x}\rangle &= \frac{x |\downarrow\rangle \otimes |0\rangle}{\sqrt{2 - |a(t)|^2}} + \sqrt{\frac{1 - |a(t)|^2}{2 - |a(t)|^2}} \\ &\times \left[\tilde{a}'(\tau) |\uparrow\rangle + |\downarrow\rangle \sum_k \tilde{c}'_k(\tau) b_k^\dagger \right] |0\rangle, \end{aligned} \quad (\text{D.48})$$

where $\tilde{a}'(0) = 0$ and $\tilde{c}'_k(0) = c_k(t)/\sqrt{1 - |a(t)|^2}$ [Eq. (D.16)] with $|\tilde{a}'(\tau)|^2 + \sum_k |\tilde{c}'_k(\tau)|^2 = 1$. In this case, $\tilde{a}'(\tau)$ and $\tilde{c}'_k(\tau)$ are then given by Eq. (D.19).

At the final stage, the third z -measurement is performed, where the corresponding conditional probability reads $P(z|yx) = \langle \Psi_{t+\tau}^{yx} | \Pi_{\hat{x}=z} | \Psi_{t+\tau}^{yx} \rangle$. From the previous expressions, we get

$$P(z|+, x) = \frac{1}{2}, \quad (\text{D.49})$$

while

$$P(z|-, x) = \frac{1}{2} \left[1 - zx \frac{G(t, \tau) + G^*(t, \tau)}{2 - |G(t)|^2} \right]. \quad (\text{D.50})$$

The CPF probability $P(z, x|y) = P(z|y, x)P(x|y)$, from the previous two expressions and Eq. (D.44), reads ($y = +1$)

$$P(z, x|+) = \frac{1}{2} P(x) = \frac{1}{4} |a + xb|^2, \quad (\text{D.51})$$

while ($y = -1$)

$$P(z, x|-) = \frac{|a + xb|^2}{4} \left[1 - zx \frac{G(t, \tau) + G^*(t, \tau)}{2 - |G(t)|^2} \right]. \quad (\text{D.52})$$

From Eqs. (D.51) and (D.52), the conditional expectation values [Eqs. (D.22) and (D.23)] for $y = +1$ read

$$\langle O_x \rangle_{y=+1} = 2\text{Re}(ab^*), \quad \langle O_z \rangle_{y=+1} = 0, \quad (\text{D.53})$$

and

$$\langle O_z O_x \rangle_{y=+1} = 0, \quad (\text{D.54})$$

which implies

$$C_{pf}(t, \tau)|_{y=+1} = 0. \quad (\text{D.55})$$

On the other hand, for $y = -1$, the averages read

$$\langle O_x \rangle_{y=-1} = 2\text{Re}(ab^*), \quad (\text{D.56})$$

while

$$\langle O_z \rangle_{y=-1} = -2\text{Re}(ab^*) \frac{G(t, \tau) + G^*(t, \tau)}{2 - |G(t)|^2}. \quad (\text{D.57})$$

Furthermore,

$$\langle O_z O_x \rangle_{y=-1} = -\frac{G(t, \tau) + G^*(t, \tau)}{2 - |G(t)|^2}. \quad (\text{D.58})$$

The CPF correlation then is

$$C_{pf}(t, \tau)|_{y=-1} \stackrel{\hat{x}\hat{z}\hat{x}}{=} - \left\{ \frac{1 - [2\text{Re}(ab^*)]^2}{1 - |G(t)|^2/2} \right\} \text{Re}[G(t, \tau)]. \quad (\text{D.59})$$

For a $\hat{y} - \hat{z} - \hat{y}$ measurements scheme, by performing a similar calculation, the CPF correlation reads

$$C_{pf}(t, \tau)|_{y=-1} \stackrel{\hat{y}\hat{z}\hat{y}}{=} - \left\{ \frac{1 - [2\text{Im}(ab^*)]^2}{1 - |G(t)|^2/2} \right\} \text{Re}[G(t, \tau)]. \quad (\text{D.60})$$

D.3. Map representation of the total unitary dynamics

For experimental implementation, the system is encoded in the light polarization states, while the bath is effectively implemented through different spatial light modes [168, 169].

The total unitary evolution in first interval $(0, t)$ can be written as the map

$$|\downarrow\rangle \otimes |0\rangle \rightarrow |\downarrow\rangle \otimes |0\rangle, \quad (\text{D.61a})$$

$$|\uparrow\rangle \otimes |0\rangle \rightarrow \cos(\theta)|\uparrow\rangle \otimes |0\rangle + \sin(\theta)|\downarrow\rangle \otimes |1\rangle, \quad (\text{D.61b})$$

where here $|0\rangle$ and $|1\rangle$ represent spatial modes that respectively take into account the absence or presence of one excitation in the environment Bosonic modes. Thus, the angle θ is given by the relation

$$\cos(\theta) = a(t) = G(t), \quad (\text{D.62})$$

where $a(t)$ follows from Eq. (D.12).

In the interval $(t, t + \tau)$ the total unitary dynamics realize the following mapping

$$|\downarrow\rangle \otimes |0\rangle \rightarrow |\downarrow\rangle \otimes |0\rangle, \quad (\text{D.63a})$$

$$|\uparrow\rangle \otimes |0\rangle \rightarrow \cos(\tilde{\theta})|\uparrow\rangle \otimes |0\rangle + \sin(\tilde{\theta})|\downarrow\rangle \otimes |1\rangle, \quad (\text{D.63b})$$

$$|\downarrow\rangle \otimes |1\rangle \rightarrow \sin(\tilde{\theta}')|\uparrow\rangle \otimes |0\rangle + \cos(\tilde{\theta}')|\downarrow\rangle \otimes |1\rangle. \quad (\text{D.63c})$$

The angles are given by the relations

$$\cos(\tilde{\theta}) = \tilde{a}(\tau) = G(\tau), \quad (\text{D.64})$$

and

$$\sin(\tilde{\theta}') = \tilde{a}'(\tau) = -\frac{G(t, \tau)}{\sqrt{1 - |G(t)|^2}}, \quad (\text{D.65})$$

where $\tilde{a}(\tau)$ and $\tilde{a}'(\tau)$ follows from Eqs. (D.12) and (D.19) respectively.

From the previous mapping, it is possible to rewrite the CPF correlation in terms of angle variables. From Eq. (D.38) we get

$$C_{pf}|_{y=-1} \stackrel{\hat{z}\hat{z}\hat{z}}{=} \left\{ \frac{4|a|^2|b|^2}{[\sin^2(\theta)|a|^2 + |b|^2]^2} \right\} \sin^2(\theta) \sin^2(\tilde{\theta}'), \quad (\text{D.66})$$

while from Eq. (D.60) it follows

$$C_{pf}|_{y=-1} \underset{\hat{x}\hat{z}\hat{x}}{=} \left\{ \frac{1 - [2\text{Re}(ab^*)]^2}{1 - \cos^2(\theta)/2} \right\} \sin(\theta) \sin(\tilde{\theta}). \quad (\text{D.67})$$

These two expressions do not depend on angle $\tilde{\theta}$. In fact, this angle is relevant when $y = +1$, where $C_{pf}|_{y=+1} \underset{\hat{z}\hat{z}\hat{z}}{=} 0$ and $C_{pf}|_{y=+1} \underset{\hat{x}\hat{z}\hat{x}}{=} 0$.

The previous expressions for the CPF correlation in terms of angle variables can also be derived from the measurement schemes and by using the dynamical maps Eqs. (D.61) and (D.63). For example, the CPF probability $P(z, x|y)$ for the $\hat{z} - \hat{z} - \hat{z}$ scheme [compare with Eq. (D.30)] reads

z	y	x	$P(z, x y)$	
+	+	+	$\cos^2(\tilde{\theta})$.
+	+	-	0	
+	-	+	$\frac{\sin^2(\theta) \sin^2(\tilde{\theta}) a ^2}{\sin^2(\theta) a ^2 + b ^2}$	
+	-	-	0	
-	+	+	$\sin^2(\tilde{\theta})$	
-	+	-	0	
-	-	+	$\frac{\sin^2(\theta) \cos^2(\tilde{\theta}) a ^2}{\sin^2(\theta) a ^2 + b ^2}$	
-	-	-	$\frac{ b ^2}{\sin^2(\theta) a ^2 + b ^2}$	

For the $\hat{x} - \hat{z} - \hat{x}$ scheme [compare with Eqs. (D.51) and (D.52)] it can be written as ($y = +1$)

$$P(z, x|+) = \frac{1}{4} |a + xb|^2, \quad (\text{D.69})$$

while ($y = -1$)

$$P(z, x|-) = \frac{1}{4} |a + xb|^2 \left[1 + 2zx \frac{\sin(\theta) \sin(\tilde{\theta})}{2 - \cos(\theta)} \right]. \quad (\text{D.70})$$

BIBLIOGRAPHY

- [1] MICHELSON, A.A. and MORLEY, E.W.: *On the relative motion of the earth and the luminiferous ether*. The Am. J. Sci. **203**: 883 (1887).
- [2] LENARD, P.: *Ueber die lichtelektrische wirkung*. Annalen der Physik **313**(5): 149 (1902).
- [3] EINSTEIN, A.: *On a heuristic point of view concerning the production and transformation of light*. Annalen der Physik **322**: 132 (1905).
- [4] BELL, J.S.: *On the Einstein Podolsky Rosen Paradox*. Phys. (N.Y) **1**(3): 195 (1964).
- [5] ASPECT, A.; GRANGIER, P.; and ROGER, G.: *Experimental tests of realistic local theories via bell's theorem*. Phys. Rev. Lett. **47**: 460 (1981).
- [6] ASPECT, A.; GRANGIER, P.; and ROGER, G.: *Experimental realization of einstein-podolsky-rosen-bohm gedankenexperiment: A new violation of bell's inequalities*. Phys. Rev. Lett. **49**: 91 (1982).
- [7] ASPECT, A.; DALIBARD, J.; and ROGER, G.: *Experimental Test of Bell's Inequalities Using Time- Varying Analyzers*. Phys. Rev. Lett. **49**(25): 1804 (1982).
- [8] OU, Z.Y. and MANDEL, L.: *Violation of bell's inequality and classical probability in a two-photon correlation experiment*. Phys. Rev. Lett. **61**: 50 (1988).
- [9] SHIH, Y.H. and ALLEY, C.O.: *New type of einstein-podolsky-rosen-bohm experiment using pairs of light quanta produced by optical parametric down conversion*. Phys. Rev. Lett. **61**: 2921 (1988).
- [10] KWIAT, P.G.; MATTLE, K.; WEINFURTER, H.; ZEILINGER, A.; SERGIENKO, A.V.; and SHIH, Y.: *New high-intensity source of polarization-entangled photon pairs*. Phys. Rev. Lett. **75**: 4337 (1995).

-
- [11] PAN, J.W.; BOUWMEESTER, D.; DANIELL, M.; WEINFURTER, H.; and ZEILINGER, A.: *Experimental test of quantum nonlocality in three-photon greenberger-horne-zeilinger entanglement*. Nat. **403**: 515 (2000).
- [12] BOUWMEESTER, D.; PAN, J.W.; MATTLE, K.; EIBL, M.; WEINFURTER, H.; and ZEILINGER, A.: *Experimental quantum teleportation*. Nat. **390**: 575 (1997).
- [13] MA, X.s.; KOFLER, J.; and ZEILINGER, A.: *Delayed-choice gedanken experiments and their realizations*. Rev. Mod. Phys. **88**: 015005 (2016).
- [14] HONG, C.K.; OU, Z.Y.; and MANDEL, L.: *Measurement of subpicosecond time intervals between twophotons by interference*. Phys. Rev. Lett. **59**: 2044 (1987).
- [15] ZEILINGER, A.; WEIHS, G.; JENNEWEIN, T.; and ASPELMEYER, M.: *Happy centenary, photon*. Nat. **433**: 230 (2005).
- [16] JENNEWEIN, T.; SIMON, C.; WEIHS, G.; WEINFURTER, H.; and ZEILINGER, A.: *Quantum cryptography with entangled photons*. Phys. Rev. Lett. **84**: 4729 (2000).
- [17] BENNETT, C.H.; BESSETTE, F.; BRASSARD, G.; SALVAIL, L.; and SMOLIN, J.: *Experimental quantum cryptography*. J. Cryptol. **5**: 3 (1992).
- [18] HISKETT, P.A.; ROSENBERG, D.; PETERSON, C.G.; HUGHES, R.J.; NAM, S.; LITA, A.E.; MILLER, A.J.; and NORDHOLT, J.E.: *Long distance quantum key distribution in optical fibre*. New J. Phys. **8**(9): 193 (2006).
- [19] KORZH, B.; LIM, C.C.W.; HOULMANN, R.; *et al.*: *Provably secure and practical quantum key distribution over 307 km of optical fibre*. Nat. Photonics **9**: 163 (2015).
- [20] YIN, H.L.; CHEN, T.Y.; YU, Z.W.; *et al.*: *Measurement-device-independent quantum key distribution over a 404 km optical fiber*. Phys. Rev. Lett. **117**: 190501 (2016).
- [21] YIN, J.; CAO, Y.; LI, Y.H.; *et al.*: *Satellite-based entanglement distribution over 1200 kilometers*. Sci. **356**(6343): 1140 (2017).
- [22] LIAO, S.K.; CAI, W.Q.; HANDSTEINER, J.; *et al.*: *Satellite-relayed intercontinental quantum network*. Phys. Rev. Lett. **120**: 030501 (2018).
- [23] LIU, H.Y.; TIAN, X.H.; GU, C.; *et al.*: *Drone-based entanglement distribution towards mobile quantum networks*. Natl. Sci. Rev. Nwz227 (2020).
- [24] WANG, H.; QIN, J.; DING, X.; *et al.*: *Boson sampling with 20 input photons and a 60-mode interferometer in a 10^{14} -dimensional hilbert space*. Phys. Rev. Lett. **123**: 250503 (2019).

-
- [25] BROD, D.J.; GALVÃO, E.F.; CRESPI, A.; OSELLAME, R.; SPAGNOLO, N.; and SCIA-RRINO, F.: *Photonic implementation of boson sampling: a review*. Adv. Photonics **1**(3): 1 (2019).
- [26] KNILL, E.; LAFLAMME, R.; and MILBURN, G.J.: *A scheme for efficient quantum computation with linear optics*. Nat. **409**: 46 (2001).
- [27] BRAUNSTEIN, S.L. and VAN LOOCK, P.: *Quantum information with continuous variables*. Rev. Mod. Phys. **77**: 513 (2005).
- [28] BLATT, R. and ROOS, C.F.: *Quantum simulations with trapped ions*. Nat. Phys. **8**: 277 (2012).
- [29] DURT, T.; ENGLERT, B.G.; BENGTTSSON, I.; and ŻYCKOWSKI, K.: *On mutually unbiased bases*. Int. J. Quant. Inf. **08**(04): 535 (2010).
- [30] TASCA, D.S.; SÁNCHEZ, P.; WALBORN, S.P.; and RUDNICKI, Ł.: *Mutual unbiasedness in coarse-grained continuous variables*. Phys. Rev. Lett. **120**: 040403 (2018).
- [31] CAVALCANTI, D. and SKRZYPCZYK, P.: *Quantum steering: a review with focus on semidefinite programming*. Reports on Prog. Phys. **80**(2): 024001 (2017).
- [32] DE VEGA, I. and ALONSO, D.: *Dynamics of non-Markovian open quantum systems*. Rev. Mod. Phys. **89**: 015001 (2017).
- [33] BREUER, H.P.; LAINE, E.M.; PILO, J.; and VACCHINI, V.: *Colloquium: Non-Markovian dynamics in open quantum systems*. Rev. Mod. Phys. **88**: 021002 (2016).
- [34] RIVAS, A.; HUELGA, S.F.; and PLENIO, M.B.: *Quantum non-Markovianity: characterization, quantification and detection*. Rep. Prog. Phys. **77**: 094001 (2014).
- [35] BUDINI, A.A.: *Quantum Non-Markovian Processes Break Conditional Past-Future Independence*. Phys. Rev. Lett. **121**: 240401 (2018).
- [36] BUDINI, A.A.: *Conditional past-future correlation induced by non-Markovian dephasing reservoirs*. Phys. Rev. A **99**: 052125 (2019).
- [37] TASCA, D.S.; GOMES, R.M.; TOSCANO, F.; RIBEIRO, P.H.S.; and WALBORN, S.P.: *Continuous-variable quantum computation with spatial degrees of freedom of photons*. Phys. Rev. A **83**: 052325 (2011).
- [38] LEMOS, G.B.; GOMES, R.M.; WALBORN, S.P.; SOUTO RIBEIRO, P.H.; and TOSCANO, F.: *Experimental observation of quantum chaos in a beam of light*. Nat. Commun. **3**: 1211 (2012).

-
- [39] SALEH, B.E.A. and TEICH, M.C.: *Fundamentals of Photonics*. John Wiley and Sons (1991).
- [40] GOODMAN, J.W.: *Introduction to Fourier optics*. McGraw-Hill, 2^aed. (1996).
- [41] OZAKTAS, H.M.; ZALEVSKY, Z.; and KUTAY, M.A.: *The Fractional Fourier Transform: with Applications in Optics and Signal Processing*. John Wiley and Sons Ltd, New York (2001).
- [42] MENDLOVIC, D. and OZAKTAS, H.M.: *Fractional fourier transforms and their optical implementation:i*. J. Opt. Soc. Am. A **10**: 1875 (1993).
- [43] LOHMANN, A.W.: *Image rotation, wigner rotation, and the fractional fourier transform*. J. Opt. Soc. Am. A **10**: 2181 (1993).
- [44] RODRIGO, J.A.; ALIEVA, T.; and CALVO, M.L.: *Programmable two-dimensional optical fractional fourier processor*. Opt. Express **17**(7): 4976 (2009).
- [45] MEIER, G.; SACKMANN, E.; and GRABMAIER, J.G.: *Application of liquid crystals*. Springer (1975).
- [46] JOHNSON, K.M.; MCKNIGHT, D.J.; and UNDERWOOD, I.: *Smart spatial light modulators using liquid crystals on silicon*. Quantum Electron. IEEE J. **29**(2): 699 (1993).
- [47] SILVA, T.L.; TAILLEBOIS, E.R.F.; GOMES, R.M.; WALBORN, S.P.; and AVELAR, A.T.: *Optical simulation of the free dirac equation*. Phys. Rev. A **99**: 022332 (2019).
- [48] DIRAC, P.A.M.: *The Quantum Theory of the Electron*. Proc. Royal Soc. Lond. **117**(778): 610 (1928).
- [49] ANDERSON, C.D.: *The positive electron*. Phys. Rev. **43**: 491 (1933).
- [50] Sitz. Preuss. Akad. Wiss. Phys.-Math. Kl. **24**: 418 (1930).
- [51] KLEIN, O.: *Die Reflexion von Elektronen an einem Potentialsprung nach der relativistischen Dynamik von Dirac*. Zeitschrift für Physik **53**: 157 (1929).
- [52] KREKORA, P.; SU, Q.; and GROBE, R.: *Relativistic electron localization and the lack of zitterbewegung*. Phys. Rev. Lett. **93**: 043004 (2004).
- [53] GERRITSMAN, R.; KIRCHMAIR, G.; ZÄHRINGER, F.; SOLANO, E.; BLATT, R.; and ROOS, C.F.: *Quantum Simulation of the Dirac Equation*. Nat. **463**: 68 (2010).
- [54] GERRITSMAN, R.; LANYON, B.P.; KIRCHMAIR, G.; *et al.*: *Quantum simulation of the klein paradox with trapped ions*. Phys. Rev. Lett. **106**: 060503 (2011).

- [55] ZHANG, X.: *Observing Zitterbewegung for photons near the Dirac point of a two-dimensional photonic crystal*. Phys. Rev. Lett. **100**: 113903 (2008).
- [56] OTTERBACH, J.; UNANYAN, R.G.; and FLEISCHHAUER, M.: *Confining stationary light: Dirac dynamics and Klein tunneling*. Phys. Rev. Lett. **102**: 063602 (2009).
- [57] KATSNELSON, M.I.; NOVOSELOV, K.S.; and GEIM, A.K.: *Chiral tunnelling and the Klein paradox in graphene*. Nat. Phys. **2**: 620 (2006).
- [58] DREISOW, F.; HEINRICH, M.; KEIL, R.; TÜNNERMANN, A.; NOLTE, S.; LONGHI, S.; and SZAMEIT, A.: *Classical simulation of relativistic Zitterbewegung in photonic lattices*. Phys. Rev. Lett. **105**: 143902 (2010).
- [59] SALGER, T.; GROSSERT, C.; KLING, S.; and WEITZ, M.: *Klein tunneling of a quasirelativistic Bose-Einstein condensate in an optical lattice*. Phys. Rev. Lett. **107**: 240401 (2011).
- [60] LEBLANC, L.J.; BEELER, M.C.; JIMÓNEZ-GARCÍA, K.; PERRY, A.R.; SUGAWA, S.; WILLIAMS, R.A.; and SPIELMAN, I.: *Direct observation of zitterbewegung in a Bose-Einstein condensate*. New J. Phys. **15**: 073011 (2013).
- [61] VAISHNAV, J.Y. and CLARK, C.W.: *Observing zitterbewegung with ultracold atoms*. Phys. Rev. Lett. **100**: 153002 (2008).
- [62] FOLDY, L.L. and WOUTHUYSEN, S.A.: *On the Dirac theory of spin 1/2 particles and its non-relativistic limit*. Phys. Rev. **78**: 29 (1950).
- [63] OBUKHOV, Y.N.: *Spin, gravity, and inertia*. Phys. Rev. Lett. **86**: 192 (2001).
- [64] QUACH, J.Q.: *Foldy-Wouthuysen transformation of the generalized Dirac Hamiltonian in a gravitational-wave background*. Phys. Rev. D **92**: 084047 (2015).
- [65] SCHWABL, F.: *Advanced Quantum Mechanics*. Springer, 4th ed. (2008).
- [66] THALLER, B.: *The Dirac Equation*. Springer, New York (1992).
- [67] DRAGOMAN, D. and DRAGOMAN, M.: *Quantum-classical analogies*. Springer (2013).
- [68] SABÍN, C.; CASANOVA, J.; GARCÍA-RIPOLL, J.J.; LAMATA, L.; SOLANO, E.; and LEÓN, J.: *Encoding relativistic potential dynamics into free evolution*. Phys. Rev. A **85**: 052301 (2012).
- [69] BOHR, N.: *The quantum postulate and the recent development of atomic theory*. Nat. **121**: 580 (1928).

-
- [70] TOSCANO, F.; TASCA, D.S.; RUDNICKI, L.; and WALBORN, S.P.: *Uncertainty relations for coarse-grained measurements: An overview*. Entropy **20**: 454 (2018).
- [71] AMARAL, B. and CUNHA, M.O.T., editors: *QOn Graph Approaches to Contextuality and their Role in Quantum Theory*. Springer, Berlin (2018).
- [72] BRUNNER, N.; CAVALCANTI, D.; PIRONIO, S.; SCARANI, V.; and WEHNER, S.: *Bell nonlocality*. Rev. Mod. Phys. **86**: 419 (2014).
- [73] HERRERO-COLLANTES, M. and GARCIA-ESCARTIN, J.C.: *Quantum random number generators*. Rev. Mod. Phys. **89**: 015004 (2017).
- [74] WOOTTERS, W.K. and FIELDS, B.D.: *Optimal state-determination by mutually unbiased measurements*. Annals Phys. **191**: 363 (1989).
- [75] BUTTERLEY, P. and HALL, W.: *Numerical evidence for the maximum number of mutually unbiased bases in dimension six*. Phys. Lett. A **369**(1): 5 (2007).
- [76] BRIERLEY, S. and WEIGERT, S.: *Maximal sets of mutually unbiased quantum states in dimension 6*. Phys. Rev. A **78**: 042312 (2008).
- [77] BRIERLEY, S. and WEIGERT, S.: *Mutually unbiased bases and semi-definite programming*. J. Physics: Conf. Ser. **254**: 012008 (2010).
- [78] RAYNAL, P.; LÜ, X.; and ENGLERT, B.G.: *Mutually unbiased bases in six dimensions: The four most distant bases*. Phys. Rev. A **83**: 062303 (2011).
- [79] BRIERLEY, S. and WEIGERT, S.: *Constructing mutually unbiased bases in dimension six*. Phys. Rev. A **79**: 052316 (2009).
- [80] PATEREK, T.; DAKIĆ, B.; and BRUKNER, i.c.v.: *Mutually unbiased bases, orthogonal latin squares, and hidden-variable models*. Phys. Rev. A **79**: 012109 (2009).
- [81] WEIGERT, S. and WILKINSON, M.: *Mutually unbiased bases for continuous variables*. Phys. Rev. A **78**: 020303 (2008).
- [82] PAUL, E.C.; WALBORN, S.P.; TASCA, D.S.; and RUDNICKI, L.: *Mutually unbiased coarse-grained measurements of two or more phase-space variables*. Phys. Rev. A **97**: 052103 (2018).
- [83] IVONOVIC, I.D.: *Geometrical description of quantal state determination*. J. Phys. A: Math. Gen. **14**(12): 3241 (1981).

-
- [84] BANDYOPADHYAY, S.; BOYKIN, P.; ROYCHOWDHURY, V.; and VATAN, F.: *A new proof of the existence of mutually unbiased bases*. *Algorithmica* **34**: 512 (2002).
- [85] A., K. and M., R.: *Constructions of mutually unbiased bases*. In M. G.L.; P. A.; and S. H., editors, *Finite Fields and Applications*. Springer, 137 (2003).
- [86] PAUL, E.C.; TASCIA, D.S.; RUDNICKI, L.; and WALBORN, S.P.: *Detecting entanglement of continuous variables with three mutually unbiased bases*. *Phys. Rev. A* **94**: 012303 (2016).
- [87] REVZEN, M.; MELLO, P.A.; MANN, A.; and JOHANSEN, L.M.: *Bell's inequality violation with non-negative wigner functions*. *Phys. Rev. A* **71**: 022103 (2005).
- [88] GILCHRIST, A.; DEUAR, P.; and REID, M.D.: *Contradiction of quantum mechanics with local hidden variables for quadrature phase amplitude measurements*. *Phys. Rev. Lett.* **80**: 3169 (1998).
- [89] BANASZEK, K. and WÓDKIEWICZ, K.: *Nonlocality of the einstein-podolsky-rosen state in the wigner representation*. *Phys. Rev. A* **58**: 4345 (1998).
- [90] BANASZEK, K. and WÓDKIEWICZ, K.: *Testing quantum nonlocality in phase space*. *Phys. Rev. Lett.* **82**: 2009 (1999).
- [91] WENGER, J.; HAFEZI, M.; GROSSHANS, F.; TUALLE-BROURI, R.; and GRANGIER, P.: *Maximal violation of bell inequalities using continuous-variable measurements*. *Phys. Rev. A* **67**: 012105 (2003).
- [92] CAVALCANTI, D.; BRUNNER, N.; SKRZYPCZYK, P.; SALLES, A.; and SCARANI, V.: *Large violation of bell inequalities using both particle and wave measurements*. *Phys. Rev. A* **84**: 022105 (2011).
- [93] WALBORN, S.P.; MONKEN, C.H.; PÀDUA, S.; and RIBEIRO, P.H.S.: *Spatial correlations in parametric down-conversion*. *Phys. Reports* **495**: 87 (2010).
- [94] KWIAT, P.G.; WAKS, E.; WHITE, A.G.; APPELBAUM, I.; and EBERHARD, P.H.: *Ultra-bright source of polarization-entangled photons*. *Phys. Rev. A* **60**: 773(R) (1999).
- [95] MANDEL, L. and WOLF, E.: *Optics coherence and quantum optics*. Cambridge University Press, New York (1995).
- [96] YARIV, A. and YEH, P.: *Optical waves in crystals*. Wiley (1984).
- [97] PAOLINO, P. and BELLON, L.: *Single beam interferometric angle measurement*. *Opt. Commun.* **280**(1): 1 (2007).

-
- [98] MACNEILLE, S.M.: *Beam splitter*. U.S. patent 2,403,731 (1946).
- [99] DAMASK, J.N.: *Polarization optics in telecommunications*. Springer-Verlag (2005).
- [100] TADDEI, M.M.; SILVA, T.L.; NERY, R.V.; AGUILAR, G.H.; WALBORN, S.P.; and AOLITA, L.: *Exposure of subtle multipartite quantum nonlocality*. arxiv e-prints : arxiv:1910.12884 (2019).
- [101] HORODECKI, R.; HORODECKI, P.; HORODECKI, M.; and HORODECKI, K.: *Quantum entanglement*. Rev. Mod. Phys. **81**(2): 865 (2009).
- [102] WEEDBROOK, C.; PIRANDOLA, S.; GARCÍA-PATRÓN, R.; CERF, N.J.; RALPH, T.C.; SHAPIRO, J.H.; and LLOYD, S.: *Gaussian quantum information*. Rev. Mod. Phys. **84**(2): 621 (2012).
- [103] REID, M.D.; DRUMMOND, P.D.; BOWEN, W.P.; CAVALCANTI, E.G.; LAM, P.K.; BACHOR, H.A.; ANDERSEN, U.L.; and LEUCHS, G.: *Colloquium : The Einstein-Podolsky-Rosen paradox: From concepts to applications*. Rev. Mod. Phys. **81**(4): 1727 (2009).
- [104] UOLA, R.; COSTA, A.C.S.; NGUYEN, H.C.; and GÜHNE, O.: *Quantum Steering* (2019).
- [105] BARRETT, J.; HARDY, L.; and KENT, A.: *No Signaling and Quantum Key Distribution*. Phys. Rev. Lett. **95**(1): 010503 (2005).
- [106] ACÍN, A.; Gisin, N.; and MASANES, L.: *From Bell's Theorem to Secure Quantum Key Distribution*. Phys. Rev. Lett. **97**(12): 120405 (2006).
- [107] ACÍN, A.; MASSAR, S.; and PIRONIO, S.: *Efficient quantum key distribution secure against no-signalling eavesdroppers*. New J. Phys. **8**(8): 126 (2006).
- [108] ACÍN, A.; BRUNNER, N.; Gisin, N.; MASSAR, S.; PIRONIO, S.; and SCARANI, V.: *Device-Independent Security of Quantum Cryptography against Collective Attacks*. Phys. Rev. Lett. **98**(23): 230501 (2007).
- [109] COLBECK, R.: *Quantum And Relativistic Protocols For Secure Multi-Party Computation* (2009).
- [110] COLBECK, R. and KENT, A.: *Private randomness expansion with untrusted devices*. J. Phys. A: Math. Theor. **44**(9): 095305 (2011).
- [111] PIRONIO, S.; ACÍN, A.; MASSAR, S.; *et al.*: *Random numbers certified by Bell's theorem*. Nat. **464**(7291): 1021 (2010).

-
- [112] ACÍN, A. and MASANES, L.: *Certified randomness in quantum physics*. Nat. **540**(7632): 213 (2016).
- [113] WISEMAN, H.M.; JONES, S.J.; and DOHERTY, A.C.: *Steering, Entanglement, Nonlocality, and the Einstein-Podolsky-Rosen Paradox*. Phys. Rev. Lett. **98**(14): 140402 (2007).
- [114] JONES, S.J.; WISEMAN, H.M.; and DOHERTY, A.C.: *Entanglement, Einstein-Podolsky-Rosen correlations, Bell nonlocality, and steering*. Phys. Rev. A **76**(5): 052116 (2007).
- [115] BRANCIARD, C.; CAVALCANTI, E.G.; WALBORN, S.P.; SCARANI, V.; and WISEMAN, H.M.: *One-sided device-independent quantum key distribution: Security, feasibility, and the connection with steering*. Phys. Rev. A **85**(1): 010301 (2012).
- [116] HE, Q.Y. and REID, M.D.: *Genuine Multipartite Einstein-Podolsky-Rosen Steering*. Phys. Rev. Lett. **111**(25): 250403 (2013).
- [117] SKRZYPCZYK, P. and CAVALCANTI, D.: *Maximal Randomness Generation from Steering Inequality Violations Using Qudits*. Phys. Rev. Lett. **120**(26): 260401 (2018).
- [118] KOGIAS, I.; XIANG, Y.; HE, Q.; and ADESSO, G.: *Unconditional security of entanglement-based continuous-variable quantum secret sharing*. Phys. Rev. A **95**(1): 012315 (2017).
- [119] XIANG, Y.; KOGIAS, I.; ADESSO, G.; and HE, Q.: *Multipartite Gaussian steering: Monogamy constraints and quantum cryptography applications*. Phys. Rev. A **95**(1): 010101 (2017).
- [120] HUANG, C.Y.; LAMBERT, N.; LI, C.M.; LU, Y.T.; and NORI, F.: *Securing quantum networking tasks with multipartite Einstein-Podolsky-Rosen steering*. Phys. Rev. A **99**(1): 012302 (2019).
- [121] PIANI, M. and WATROUS, J.: *Necessary and Sufficient Quantum Information Characterization of Einstein-Podolsky-Rosen Steering*. Phys. Rev. Lett. **114**(6): 060404 (2015).
- [122] GALLEGO, R. and AOLITA, L.: *Resource Theory of Steering*. Phys. Rev. X **5**(4): 041008 (2015).
- [123] KAUR, E. and WILDE, M.M.: *Relative entropy of steering: on its definition and properties*. J. Phys. A: Math. Theor. **50**(46): 465301 (2017).
- [124] BRANDÃO, F.G.S.L. and GOUR, G.: *Reversible Framework for Quantum Resource Theories*. Phys. Rev. Lett. **115**(7): 070503 (2015).

-
- [125] BRANDÃO, F.G.S.L. and GOUR, G.: *Erratum: Reversible Framework for Quantum Resource Theories* [*Phys. Rev. Lett.* **115**, 070503 (2015)]. *Phys. Rev. Lett.* **115**(19): 199901 (2015).
- [126] COECKE, B.; FRITZ, T.; and SPEKKENS, R.W.: *A mathematical theory of resources*. *Inf. Comput.* **250**: 59 (2016).
- [127] GALLEGO, R.; WÜRFLINGER, L.E.; ACÍN, A.; and NAVASCUÉS, M.: *Operational Framework for Nonlocality*. *Phys. Rev. Lett.* **109**(7): 070401 (2012).
- [128] DE VICENTE, J.I.: *On nonlocality as a resource theory and nonlocality measures*. *J. Phys. A: Math. Theor.* **47**(42): 424017 (2014).
- [129] GALLEGO, R. and AOLITA, L.: *Nonlocality free wirings and the distinguishability between Bell boxes*. *Phys. Rev. A* **95**(3): 032118 (2017).
- [130] WOLFE, E.; SCHMID, D.; SAINZ, A.B.; KUNJWAL, R.; and SPEKKENS, R.W.: *Bell Quantified: The Resource Theory of Nonclassicality of Common-Cause Boxes* (2019).
- [131] WINTER, A. and YANG, D.: *Operational Resource Theory of Coherence*. *Phys. Rev. Lett.* **116**(12): 120404 (2016).
- [132] CHITAMBAR, E. and GOUR, G.: *Critical Examination of Incoherent Operations and a Physically Consistent Resource Theory of Quantum Coherence*. *Phys. Rev. Lett.* **117**(3): 030401 (2016).
- [133] GRUDKA, A.; HORODECKI, K.; HORODECKI, M.; HORODECKI, P.; HORODECKI, R.; JOSHI, P.; KŁOBUS, W.; and WÓJCIK, A.: *Quantifying contextuality*. *Phys. Rev. Lett.* **112**(12): 1 (2013).
- [134] AMARAL, B.; CABELLO, A.; CUNHA, M.T.; and AOLITA, L.: *Noncontextual Wirings*. *Phys. Rev. Lett.* **120**(13): 130403 (2018).
- [135] TADDEI, M.M.; NERY, R.V.; and AOLITA, L.: *Quantum superpositions of causal orders as an operational resource* (2019).
- [136] BANCAL, J.D.; BARRETT, J.; GISIN, N.; and PIRONIO, S.: *Definitions of multipartite nonlocality*. *Phys. Rev. A* **88**(1): 14102 (2013).
- [137] SVETLICHNY, G.: *Distinguishing three-body from two-body nonseparability by a Bell-type inequality*. *Phys. Rev. D* **35**(10): 3066 (1987).

-
- [138] WOOD, C.J. and SPEKKENS, R.W.: *The lesson of causal discovery algorithms for quantum correlations: causal explanations of Bell-inequality violations require fine-tuning*. New J. Phys. **17**(3): 033002 (2015).
- [139] CAVALCANTI, E.G.; HE, Q.Y.; REID, M.D.; and WISEMAN, H.M.: *Unified criteria for multipartite quantum nonlocality*. Phys. Rev. A **84**(3): 032115 (2011).
- [140] ARMSTRONG, S.; WANG, M.; TEH, R.Y.; *et al.*: *Multipartite Einstein-Podolsky-Rosen steering and genuine tripartite entanglement with optical networks*. Nat. Phys. **11**(2): 167 (2015).
- [141] TADDEI, M.M.; NERY, R.V.; and AOLITA, L.: *Necessary and sufficient conditions for multipartite Bell violations with only one trusted device*. Phys. Rev. A **94**(3): 032106 (2016).
- [142] LI, C.M.; CHEN, K.; CHEN, Y.N.; ZHANG, Q.; CHEN, Y.A.; and PAN, J.W.: *Genuine High-Order Einstein-Podolsky-Rosen Steering*. Phys. Rev. Lett. **115**(1): 010402 (2015).
- [143] CAVALCANTI, D.; SKRZYPCZYK, P.; AGUILAR, G.H.; NERY, R.V.; RIBEIRO, P.S.; and WALBORN, S.P.: *Detection of entanglement in asymmetric quantum networks and multipartite quantum steering*. Nat. Commun. **6**(1): 7941 (2015).
- [144] SAINZ, A.B.; BRUNNER, N.; CAVALCANTI, D.; SKRZYPCZYK, P.; and VÉRTESI, T.: *Postquantum Steering*. Phys. Rev. Lett. **115**(19): 190403 (2015).
- [145] SAINZ, A.B.; AOLITA, L.; PIANI, M.; HOBAN, M.J.; and SKRZYPCZYK, P.: *A formalism for steering with local quantum measurements*. New J. Phys. **20**(8): 083040 (2018).
- [146] SAINZ, A.B.; HOBAN, M.J.; SKRZYPCZYK, P.; and AOLITA, L.: *Bipartite post-quantum steering in generalised scenarios* (2019).
- [147] SCHRÖDINGER, E.: *Discussion of Probability Relations between Separated Systems*. Math. Proc. Camb. Philos. Soc. **31**(04): 555 (1935).
- [148] POPESCU, S. and ROHRLICH, D.: *Quantum nonlocality as an axiom*. Foundations Phys. **24**(3): 379 (1994).
- [149] SAINZ, A.B.; AOLITA, L.; BRUNNER, N.; GALLEGO, R.; and SKRZYPCZYK, P.: *Classical communication cost of quantum steering*. Phys. Rev. A **94**(1): 012308 (2016).
- [150] FARÍAS, O.J.; AGUILAR, G.H.; VALDÉS-HERNÁNDEZ, A.; RIBEIRO, P.H.S.; DAVIDOVICH, L.; and WALBORN, S.P.: *Observation of the Emergence of Multipartite Entanglement Between a Bipartite System and its Environment*. Phys. Rev. Lett. **109**(15): 150403 (2012).

-
- [151] CLAUSER, J.F.; HORNE, M.A.; SHIMONY, A.; and HOLT, R.A.: *Proposed Experiment to Test Local Hidden-Variable Theories*. Phys. Rev. Lett. **23**(15): 880 (1969).
- [152] SILVA, T.d.L.; WALBORN, S.P.; SANTOS, M.F.; AGUILAR, G.H.; and BUDINI, A.A.: *Detection of quantum non-markovianity close to the born-markov approximation*. Phys. Rev. A **101**: 042120 (2020).
- [153] BREUER, H.P. and PETRUCCIONE, F.: *The theory of open quantum systems*. Oxford University Press (2002).
- [154] RIVAS, A.; HUELGA, S.F.; and PLENIO, M.B.: *Entanglement and non-markovianity of quantum evolutions*. Phys. Rev. Lett. **105**: 050403 (2010).
- [155] BASHARINA, G.P.; LANGVILLEB, A.N.; and NAUMOV, V.A.: *The life and work of A.A. Markov*. Linear Algebr. its Appl. **386**: 3 (2004).
- [156] A. JAMIOŁKOWSKI, Rep. Math. Phys. 3, 275 (1972); M.-D.CHOI, Lin. Alg. and Appl. 10, 285 (1975).
- [157] KRAUS, K.: *States, effects, and operations*. In *Lecture notes in Physics*, volume 190. Springer, Berlin (1993).
- [158] DOMINY, J.M.; SHABANI, A.; and LIDAR, D.A.: *A general framework for complete positivity*. Q. Info. Proc. **15**: 465 (2016).
- [159] VACCHINI, B.; SMIRNE, A.; LAINE, E.M.; PIILO, J.; and BREUER, H.P.: *Markovianity and non-Markovianity in quantum and classical systems*. New J. Phys. **13**: 093004 (2011).
- [160] HAIKKA, P.; CRESSER, J.D.; and MANISCALCO, S.: *Comparing different non-markovianity measures in a driven qubit system*. Phys. Rev. A **83**: 012112 (2011).
- [161] BREUER, H.P.; LAINE, E.M.; and PIILO, J.: *Measure for the degree of non-markovian behavior of quantum processes in open systems*. Phys. Rev. Lett. **103**: 210401 (2009).
- [162] SMIRNE, A.; MAZZOLA, L.; PATERNOSTRO, M.; and VACCHINI, B.: *Interaction-induced correlations and non-markovianity of quantum dynamics*. Phys. Rev. A **87**: 052129 (2013).
- [163] SCULLY, M.O. and ZUBAIRY, M.S.: *Quantum Optics*. Cambridge University Press, Cambridge (1997).

-
- [164] LEGGETT, A.J.; CHAKRAVARTY, S.; DORSEY, A.T.; FISHER, M.P.A.; GARG, A.; and ZWERGER, W.: *Dynamics of the dissipative two-state system*. Rev. Mod. Phys. **59**: 1 (1987).
- [165] ADDIS, C.; BYLICKA, B.; CHRUSCIŃSKI, D.; and MANISCALCO, S.: *Comparative study of non-Markovianity measures in exactly solvable one and two qubit models*. Phys. Rev. A **90**: 052103 (2014).
- [166] LAINE, E.M.; PIILO, J.; and BREUER, H.P.: *Measure for the non-Markovianity of quantum processes*. Phys. Rev. A **81**: 062115 (2010).
- [167] RUSKAI, M.B.; SZAREK, S.; and WERNER, E.: *An analysis of completely positive trace-preserving maps on \mathcal{M}_2* . Linear Algebr. its Appl. **347**: 159 (2002).
- [168] FANCHINI, F.F.; KARPAT, G.; ÇAKMAK, B.; *et al.*: *Non-markovianity through accessible information*. Phys. Rev. Lett. **112**: 210402 (2014).
- [169] FARÍAS, O.J.; AGUILAR, G.H.; VALDÉS-HERNÁNDEZ, A.; RIBEIRO, P.H.S.; DAVIDOVICH, L.; and WALBORN, S.P.: *Observation of the emergence of multipartite entanglement between a bipartite system and its environment*. Phys. Rev. Lett. **109**: 150403 (2012).
- [170] YU, S.; BUDINI, A.A.; WANG, Y.T.; *et al.*: *Experimental observation of conditional past-future correlations*. Phys. Rev. A **100**: 050301(R) (2019).
- [171] M. Bonifacio and A. A. Budini (unpublished).
- [172] CHOI, M.D.: *Completely positive linear maps on complex matrices*. Linear Algebr. its applications **10**: 285 (1975).
- [173] NIELSEN, M.A. and CHUANG, I.L.: *Quantum computation and quantum information*. Cambridge University Press (2000).
- [174] HORODECKI, M.; HORODECKI, P.; and HORODECKI, R.: *General teleportation channel, singlet fraction, and quasidistillation*. Phys. Rev. A **60**(3): 1888 (1999).
- [175] TERHAL, B.M.; CHUANG, I.L.; DIVINCENZO, D.P.; GRASSL, M.; and SMOLIN, J.A.: *Simulating quantum operations with mixed environments*. Phys. Rev. A **60**: 881 (1999).
- [176] WANG, D.S.; BERRY, D.W.; DE OLIVEIRA, M.C.; and SANDERS, B.C.: *Solovay-kitaev decomposition strategy for single-qubit channels*. Phys. Rev. Lett. **111**: 130504 (2013).
- [177] KING, C. and RUSKAI, M.: *Minimal entropy of states emerging from noisy quantum channels*. IEEE Trans. Inf. Theory **47**: 192 (2001).

-
- [178] KNOLL, L.T.; SCHMIEGELOW, C.T.; FARÍAS, O.J.; WALBORN, S.P.; and LAROTONDA, M.A.: *Entanglement-breaking channels and entanglement sudden death*. Phys. Rev. A **94**: 012345 (2016).
- [179] ALMEIDA, M.P.; DE MELO, F.; HOR-MEYLL, M.; SALLES, A.; WALBORN, S.P.; RIBEIRO, P.H.S.; and DAVIDOVICH, L.: *Environment-induced sudden death of entanglement*. Sci. **316**: 579 (2007).
- [180] FARÍAS, O.J.; LATUNE, C.L.; WALBORN, S.P.; DAVIDOVICH, L.; and RIBEIRO, P.H.S.: *Determining the dynamics of entanglement*. Sci. **324**: 1414 (2009).
- [181] HASELI, S.; KARPAT, G.; SALIMI, S.; *et al.*: *Non-markovianity through flow of information between a system and an environment*. Phys. Rev. A **90**: 052118 (2014).
- [182] SALLES, A.; DE MELO, F.; ALMEIDA, M.P.; HOR-MEYLL, M.; WALBORN, S.P.; SOUTO RIBEIRO, P.H.; and DAVIDOVICH, L.: *Experimental investigation of the dynamics of entanglement: Sudden death, complementarity, and continuous monitoring of the environment*. Phys. Rev. A **78**: 022322 (2008).
- [183] LU, H.; LIU, C.; WANG, D.S.; *et al.*: *Experimental quantum channel simulation*. Phys. Rev. A **95**: 042310 (2017).
- [184] MCCUTCHEON, W.; MCMILLAN, A.; RARITY, J.G.; and TAME, M.S.: *Experimental demonstration of a measurement-based realisation of a quantum channel*. New J. Phys. **20**(3): 033019 (2018).
- [185] CLIKEMAN, R.W.; LUBART, N.D.; and MAYFIELD, C.R.: *Device having reflective and transmissive properties*. U.S. patent 0088717 A1 (2005).
- [186] CHUANG, I.L. and NIELSEN, M.A.: *Prescription for experimental determination of the dynamics of a quantum black box*. J. Mod. Opt. **44**: 2455 (1997).
- [187] VERSTRAETE, F.; WOLF, M.M.; and IGNACIO CIRAC, J.: *Quantum computation and quantum-state engineering driven by dissipation*. Nat. Phys. **5**: 633 (2009).
- [188] HEGERFELDT, G.C.: *Remark on causality and particle localization*. Phys. Rev. D **10**: 3320 (1974).
- [189] HEGERFELDT, G.C.: *Violation of causality in relativistic quantum theory?* Phys. Rev. Lett. **54**: 2395 (1985).
- [190] KETTERER, A.; KELLER, A.; WALBORN, S.P.; COUDREAU, T.; and MILMAN, P.: *Quantum information processing in phase space: A modular variables approach*. Phys. Rev. A **94**: 022325 (2016).

- [191] ZANGWILL, A.: *Modern Electrodynamics*. Cambridge University Press (2012).
- [192] GALLEGO, R.; WÜRFLINGER, L.E.; ACÍN, A.; and NAVASCUÉS, M.: *Quantum Correlations Require Multipartite Information Principles*. Phys. Rev. Lett. **107**(21): 210403 (2011).
- [193] ROEHSNER, M.C.; KETTLEWELL, J.A.; BATALHÃO, T.B.; FITZSIMONS, J.F.; and WALTHER, P.: *Quantum advantage for probabilistic one-time programs*. Nat. Commun. **9**(1): 5225 (2018).